Switching of Degree of Interpenetration and its Effects on Porosity of Metal-Organic Frameworks (MOFs)

by

Himanshu Aggarwal

Supervisor: Prof. L. J. Barbour

Submitted in partial fulfilment of the requirements for the degree

Doctor of Philosophy

Department of Chemistry and Polymer Science

Faculty of Science

University of Stellenbosch

December 2015

DECLARATION

By submitting this dissertation electronically, I, Himanshu Aggarwal, hereby declare that the entirety of the work contained herein is my own, original work, that I am the owner of the copyright thereof (unless to the extent explicitly stated otherwise) and that I have not previously in its entirety or in part submitted it for obtaining any qualification.

_____

Signature

_____

Name in full

Date:

ABSTRACT

A number of metal-organic frameworks (MOFs) have been reported to lose porosity upon loss of solvent molecules from the channels. The primary objective of this work was to reinvestigate these systems in order to gain an understanding of the reasons behind loss of porosity in otherwise seemingly highly porous frameworks. The work provides a detailed account of switching of degree of interpenetration and its effects on porosity of MOFs.

The first section describes a well-known doubly-interpenetrated framework, **[$Zn_2(ndc)_2(bpy)$]** (ndc = 2,6-naphthalenedicarboxylate and bpy = 4,4′-dipyridyl) which has been studied for loss of porosity upon activation. The zinc-based pillared-layered structure possesses minimal porosity when activated and the framework was thought to collapse upon desolvation, leading to unexpected sorption results. In the present study, it is shown that the structure does not collapse, but converts to its triply-interpenetrated analogue upon desolvation and the transformation occurs in a single-crystal to single-crystal manner under ambient conditions. A mechanism has also been proposed for the conversion and is supported by computational methods.

In the second section, the work has been further extended to more robust and entirely different systems. Two known Cd(II) non-interpenetrated doubly-pillared MOFs, **[Cd(tp)(4,4′-bpy)]** (tp = terphthalate) and **[Cd(atp)(4,4′-bpy)]** (atp = 2-aminoterephthalate), have been studied for switching of degree of interpenetration. Both of these systems have been reported to form non-interpenetrated as well as doubly-interpenetrated structures. However, the possibility of inter-conversion has not been suggested. In the present study, these MOFs are shown to undergo a change in degree of interpenetration upon loss of solvent molecules from the channels. The transformation in these cases takes place at much higher temperatures as compared to the **[$Zn_2(ndc)_2(bpy)$]** case.

In the final section of this thesis, the effect of switching of degree of interpenetration on the porosity of MOFs is demonstrated using a previously reported system, **[$Co_2(ndc)_2(bpy)$]**, where an intermediate structure has been successfully isolated by modifying the activation conditions. This framework has also been reported to lose porosity upon desolvation. It has been found that the doubly-interpenetrated structure converts to its triply-interpenetrated form when activated at 120 °C, whereas the same material converts to an intermediate empty doubly-interpenetrated structure when activated under milder conditions. Sorption analysis using the intermediate twofold structure and the converted

threefold structure shows a clear difference in the porosities of the two forms. Interestingly, all the transformations occur in single-crystal to single-crystal fashion.

OPSOMMING

‘n Aantal metaal-organiese raamwerke (MOFs) wat poreusheid verloor wanneer oplosmiddel molekules die kanale verlaat, is gerapporteer. Die hoofdoel van hierdie werk was om hierdie stelsels te herondersoek om ‘n beter begrip te kry van die rede vir die verlies van poreusheid in ‘n raamwerk wat andersins skynbaar hoogs poreus is. Die werk verskaf ‘n gedetaileerde verslag van verandering in die graad van interpenetrasie en die effek daarvan op die poreusheid van MOFs.

Die eerste afdeling beskryf ‘n welbekende dubbel-geïnterpenitreerde raamwerk, **[Zn_2(ndc)$_2$(bpy)]** (ndc = 2,6-naphthalenedicarboxylate and bpy = 4,4′-dipyridyl) wat ondersoek is vir verlies van poreusheid na aktivering. Die geaktiveerde sink-gebaseerde pilaar-laag struktuur toon minimale poreusheid en daar is gemeen dat die struktuur inmekaar val wanneer die oplosmiddel molekules verwyder word. Dit het dan gelei tot onverwagse sorpsie resultate. In die huidige studie, word daar bewys dat die struktuur nie inmekaar val nie, maar omskakel na die trippel-geïnterpenitreerde vorm wanneer die oplosmiddel molekules verwyder word. Hierdie transformasie vind plaas op ‘n enkel-kristal na enkel-kristal wyse onder atmosferiese toestande. ‘n Meganisme is ook voorgestel vir die omskakeling en dit word ondersteun deur berekeningsmetodes.

In die tweede afdeling is die werk verder uitgebrei na meer robuuste en totaal verskillende stelsels. Twee bekende Cd(II) nie-geïnterpenetreerde dubbel-pilaar MOFs, **[Cd(tp)(4,4′-bpy)]** (tp = terphthalate) and **[Cd(atp)(4,4′-bpy)]** (atp = 2-aminoterephthalate), is ondersoek vir omskakeling van graad van interpenitrasie. Dit is gerapporteer dat beide stelsels nie-geïnterpenitreerde, sowel as dubbel-geïnterpenitreerde strukture vorm, hoewel die moontlikheid van omkeerbare omskakeling nie oorweeg is nie. In hierdie studie word gewys dat die MOFs ‘n verandering in die graad van interpenetrasie ondergaan, wanneer oplosmiddel molekules uit die kanale verwyder word. Die transformasie, in hierdie geval, vind plaas by veel hoër temperature as in die geval van **[Zn_2(ndc)$_2$(bpy)]**.

In die laaste afdeling van hierdie tesis word die effek van omskakeling van die graad van interpenetrasie op die poreusheid van MOFs gedemonstreer deur gebruik te maak van ‘n voorheen gerapporteerde stelsel, **[Co_2(ndc)$_2$(bpy)]**, waar ‘n oorgangstruktuur suksesvol geïsoleer is deur middel van aanpassing van die aktiveringstoestande. Dit is ook gerapporteer dat hierdie raamwerk poreusheid verloor wanneer die oplosmiddel molekules verwyder word. Daar is bevind dat die dubbel-geïnterpenitreerde struktuur omskakel na sy trippel-geïnterpenitreerde vorm wanneer dit geaktiveer word teen 120 °C, terwyl dieselfde material

omskakel na ‘n leë dubbel-geïnterpenitreerde struktuur as oorgangsproduk wanneer dit onder sagter toestande geaktiveer word. Sorpsie analise van die oorgangsproduk (tweevoudige struktuur) en die omgeskakelde drievoudige struktuur wys ‘n duidelike verskil in die poreusheid van die twee vorms. Dit is interessant dat al die transformasies op ‘n enkel-kristal na enkel-kristal wyse plaasvind.

ACKNOWLEDGEMENTS

I would like to acknowledge a number of people for their contributions to the research presented in this dissertation and to my learning experience as a postgraduate student as a whole:

Firstly, a sincere thanks to my supervisor, Prof. Len Barbour, for providing me the opportunity of working in his esteemed research group. He is an excellent mentor. He has created an exceptional research environment and always encourages new ideas. I was very fortunate to have access to a variety of state-of-art instruments for carrying out interesting experiments. I am also grateful to him for giving me an opportunity to present my work at various international conferences. These conferences not only gave me a platform to showcase my work, but also provided a chance for me to interact with well-known chemists from around the world.

Secondly, I would like to thank my parents and my family for supporting me throughout my PhD. Coming to South Africa and obtaining a PhD degree would never have been possible without their support and sacrifices.

I would like to thank all the people who have been a part of the Supramolecular Materials Research Group over the last three years: Prashant Bhatt, Vincent Smith, Raj Kumar Das, Prem Lama, Charl Bezuidenhout, Simon Herbert, Tia Jacobs, Emile Engel, Dawie de Villiers, Marike du Plessis, Lukman Alimi, Phumile Sikiti, Leigh Loots, Varia Nikolayenko, Dewald van Heerden, Laura Jane van Laeren, Helene Wahl, Agnieszka Janiak, Eustina Batisai, Prof. Delia Haynes, Prof. Catharine Esterhuysen and Dr. Tanya Le Roux.

I am grateful to Dr. Consiglia Tedesco for providing me an opportunity to work at the European Synchrotron Radiation Facility (ESRF) and Dr. Andy Fitch for teaching me structure solution from PXRD during my stay at the ESRF.

A special thanks to Prashant for his able guidance and support, Vincent for his productive discussions and motivation, Prem and Raj for their help with crystal structure solution and for helping me in compiling my results, Charl for help with the computational work, Simon for help with the synthesis, Dawie and Lukman for the sorption experiments on the IGA, and Marike for helping me submit all of the examination documents. I would also like to thank my friend Priyanka Manchanda for her immense support, and for proofreading my thesis. I am also thankful to my friends Kirti and Naba for being so helpful. Last but not the least, I would like to thank the NRF for financial support.

PUBLICATIONS

1. Direct Evidence for Single-Crystal to Single-Crystal Switching of Degree of Interpenetration in a Metal−Organic Framework.
H. Aggarwal, P. M. Bhatt, C. X. Bezuidenhout, and L. J. Barbour,
J. Am. Chem. Soc., **2014**, *136*, 3776.

2. Transformation from Non- to Double-Interpenetration in Robust Cd(II) Doubly-Pillared-Layered Metal–Organic Frameworks.
H. Aggarwal, P. Lama, and L. J. Barbour,
Chem. Commun., **2014**, *50*, 14543.

3. Isolation of a Structural Intermediate During Switching of Degree of Interpenetration in a Metal-Organic Framework.
H. Aggarwal, R. K. Das, P. M. Bhatt, and L. J. Barbour,
Chem. Sci., **2015**, *6*, 4986.

4. Anomalous Anisotropic Thermal Expansion in a One Dimensional Coordination Polymer Driven by Conformational Flexibility.
R. K. Das, **H. Aggarwal** and L. J. Barbour,
Inorg. Chem., **2015,** *54*, 8171. (not part of this work)

CONFERENCES

1. Attended Indaba 7: Insights from Structure, organised by the South African Crystallographic Society, September **2012**, held in Skukuza, Kruger National Park, South Africa.
2. Presented a poster at the 14th International Seminar on Inclusion Compounds (ISIC 14) August **2013**, held at Herriot Watt University, Edinburgh, Scotland.
3. Presented a poster at the 23rd Congress and General Assembly of the International Union of Crystallography (IUCr), August **2014**, held in Montreal, Canada.

ATOM COLOUR KEY

Colour	Element
	**Metal**
	**Oxygen**
	**Carbon**
	**Hydrogen**
	**Nitrogen**

ABBREVIATIONS

MOF	Metal-Organic Framework
SBU	Secondary Building Unit
SCSC	Single-Crystal to Single-Crystal
2f/2fa	Doubly-interpenetrated structure
3f/3fa	Triply-interpenetrated structure
2fa′	Intermediate doubly-interpenetrated structure
1D	One dimensional
2D	Two dimensional
3D	Three dimensional
SCD	Single-Crystal Diffraction
SCPT	Single-Crystal Phase Transformation
CPK	Corey-Pauling-Koltun
ndc	2,6-Naphthalenedicarboxylic acid
bpy	4,4′-Dipyridyl
bdc	Benzenedicarboxylic acid
bpe	1,2-Di(4-pyridyl)ethylene
tp	Terephthalic acid
atp	Aminoterephthalic acid
PXRD	Powder X-ray Diffraction
XRPD	X-ray Powder Diffraction
DSC	Differential Scanning Calorimetry
TGA	Thermogravimetric Analysis
SCXRD	Single-Crystal X-ray Diffraction

This dissertation is dedicated to my parents...

Table of Contents

DECLARATION		ii
ABSTRACT		iii-iv
OPSOMMING		v-vi
ACKNOWLEDGEMENTS		vii
PUBLICATIONS		viii
CONFERENCES		viii
ATOM COLOUR KEY		ix
ABBREVIATIONS		x
TABLE OF CONTENTS		xii–xiii
Chapter 1	**INTRODUCTION TO METAL-ORGANIC FRAMEWORKS**	**1–51**
1	Metal-Organic Frameworks	2
1.1	Synthesis of MOFs	3
1.2	Design of MOFs	5
1.2.1	One Dimensional Coordination Polymers	6
1.2.2	Two Dimensional Coordination Polymers	9
1.2.3	Three Dimensional Coordination Polymers	11
1.2.4	Classification of Porous Coordination Polymers	14
1.3	Applications of MOFs	15
1.3.1	Gas Sorption	15
1.3.2	MOFs for Gas Sorption and Separation	17
1.4	Interpenetration	25
1.4.1	Interpenetration Based on One Dimensional Chains	26
1.4.2	Interpenetration Based on Two Dimensional Layers	27
1.4.3	Interpenetration in Three Dimensional MOFs	28
1.5	Methods of Controlling Interpenetration	31
1.5.1	Temperature and Concentration Control	31
1.5.2	Template Effects	33
1.5.3	Ligand Design/Modification	35
1.5.4	Liquid Epitaxy	37
1.6	Single-Crystal to Single-Crystal Transformations	38
1.7	Aims and Objectives	42
1.8	Thesis Outline	42
1.9	References	44

Chapter 2	**EXPERIMENTAL TECHNIQUES**	**52–57**
2.1	Single-Crystal X-Ray Diffraction (SCXRD)	52
2.2	X-Ray Powder Diffraction (XRPD)	52
2.3	Thermogravimetric Analysis (TGA)	53
2.4	Differential Scanning Calorimetry (DSC)	53
2.5	Gravimetric gas sorption	53
2.6	Environmental Gas Cell for Collection of Single Crystal Data Under Controlled Atmospheres	54
2.7	High Pressure Differential Scanning Calorimetry (HPDSC)	56
2.8	Electron Density Studies	56
2.9	References	57
Chapter 3	**DIRECT EVIDENCE FOR SINGLE-CRYSTAL TO SINGLE-CRYSTAL SWITCHING OF DEGREE OF INTERPENETRATION IN A METAL-ORGANIC FRAMEWORK**	**58–78**
Chapter 4	**TRANSFORMATION FROM NON- TO DOUBLE-INTERPENETRATION IN ROBUST Cd(II) DOUBLY-PILLARED LAYERED METAL-ORGANIC FRAMEWORKS**	**79–95**
Chapter 5	**ISOLATION OF A STRUCTURAL INTERMEDIATE DURING SWITCHING OF INTERPENETRATION IN A METAL-ORGANIC FRAMEWORK**	**96–121**
CONCLUSIONS		**122–123**
APPENDIX		**124**

CHAPTER 1

INTRODUCTION TO METAL-ORGANIC FRAMEWORKS

Porous solids have gained much attention due to their wide potential applications in sorption, chemical separations and catalysis. The ability of any porous material to perform a desired function depends on the size and the nature of its pores. For instance, if the pores are small and uniform, as in the case of zeolites,[1] then such a material can be used to selectively separate small guest molecules from a mixture. Also, depending on the nature of the atoms lining the pores, either hydrophobic or hydrophilic guest molecules can be absorbed. Porous materials have been divided into three categories on the basis of their pore sizes: microporous (<15 Å), mesoporous (15-500 Å) and macroporous (>500 Å).[2,3] Conventionally, porous solids were known as materials with permanent pores that would allow guest molecules to pass through them reversibly without affecting the nature of the pores. Porosity[3] (ε) has been defined as the ratio of the total pore volume to the apparent volume of the material (excluding interparticle voids).

Zeolites are archetypal microporous materials with permanent porosity.[4] They are 3D crystalline, hydrated alkaline or alkaline-earth aluminosilicates with the general formula $M^{n+}_{x/n}[(AlO_2)_x(SiO_2)_y]^{x-}\cdot wH_2O$[5–7] (M = metal). The water molecules in the channels can be eliminated to generate rigid porous frameworks. The word zeolite comes from two Greek words, "zeo" meaning "to boil" and "lithos" meaning "a stone". In 1756 the Swedish mineralogist Cronstedt discovered the first zeolite mineral, stilbite. In 1862 St. Claire Deville reported the first hydrothermal synthesis of the zeolite, leyvinite.[8] Since then hundreds of zeolites have been reported and it was soon realized that zeolites can act as promising materials for sorption due to their high stability and uniformity in pore size. Because of their unique porous properties, zeolites are used in a variety of applications with a global market of several million tonnes per annum. However, a major drawback with zeolites is their high affinity for the guest molecules, which are difficult to remove.[9]

Activated carbons are another class of highly porous materials. They have high specific surface areas and relatively moderate strength of adsorption for gases, which makes desorption easier.[9] The essential structural feature is a twisted network of hexagonal carbon

layers, cross-linked by aliphatic bridging groups. The non-uniformity of the pores in activated carbons limits their use as efficient materials for selective sorption and separation of guests.

Conventional porous materials such as zeolites and activated carbons have high thermal stability and permanent porosity owing to strong Si-O or C-C bonds. However, it is very challenging to design new frameworks with different topologies having various pore sizes and shapes. In this regard porous coordination polymers or metal-organic frameworks (MOFs)[10] have emerged as promising materials for sorption as they offer relatively easier methods of designing new frameworks by using different metal ion or metal cluster nodes and different sizes and shapes of organic bridging ligands (Figure 1). This class of porous materials will be discussed in detail in the following sections.

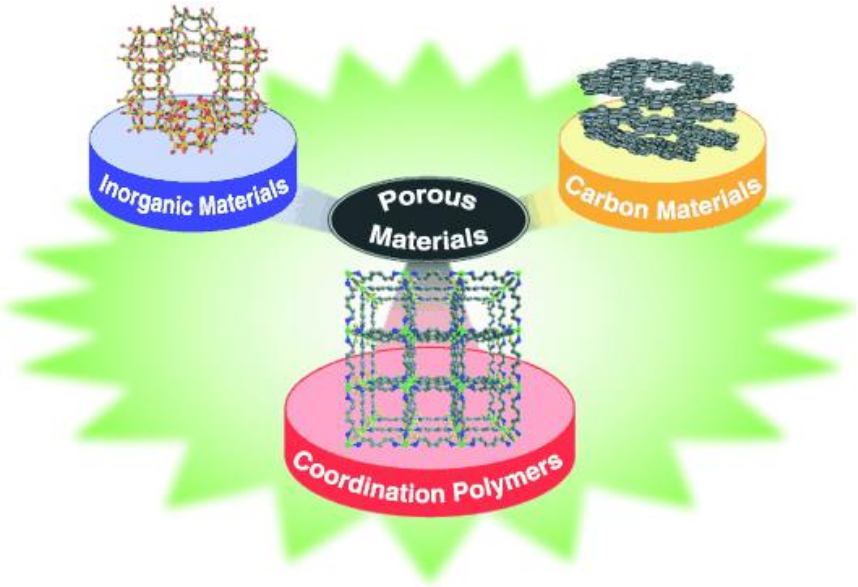

Figure 1. Classes of porous materials.[12b]

1. Metal-Organic Frameworks

Metal-organic frameworks are porous compounds consisting of metal ions or metal clusters connected together by organic bridging ligands to give two or three dimensional networks.[11] For a coordination polymer to be termed as a MOF it should display properties such as strong bonding that provides robustness, linking units that are available for modification by organic synthesis and a geometrically well-defined structure.[11] MOFs are now well known for their applications in separation, storage and catalysis.[12] In 1990 Robson *et al*. reported a porous coordination polymer capable of anion exchange.[13] In 1994 Fujita *et al*. reported the heterogeneous catalytic properties of the two-dimensional (2D) coordination polymer

$[Cd^{II}(4,4'\text{-bpy})_2]_n$ (4,4′-bpy = bipyridine).[14] However, it was in 1995 that adsorption of guest molecules by MOFs was first studied independently by the groups of Yaghi[15] and Moore.[16] A significant breakthrough was achieved when Kitagawa reported the high pressure gas sorption isotherms[17] of $[M_2(4,4'\text{-bpy})_3(NO_3)]_4$ (M = Co) in 1997 and Yaghi studied the gas sorption properties of $[Zn(bdc)]_n$ (MOF-2) in 1998 (bdc = benzenedicarboxylic acid).[18] In the following year Yaghi reported MOF-5, also known as isoreticular metal-organic framework 1 (**IRMOF-1**), which displayed extremely high porosity with a Brunauer-Emmett-Teller (BET) surface area of over 3000 $m^2\ g^{-1}$.[19] The discovery of MOF-5 was a great success for chemists working in this field as it showed that MOFs have enormous potential for gas sorption. Thereafter the quest to produce more metal-organic frameworks began.

1.1 Synthesis of MOFs

The synthesis of MOFs is generally carried out in the solution phase, either by using a single solvent or an appropriate combination of solvents. The self-assembly of the structural components leads to the formation of a crystalline structured network of metal-ligand coordinate bonds. MOFs are commonly prepared by solvothermal reaction, which can be defined as "a heterogeneous chemical reaction in the presence of a solvent above room temperature and at an autogeneous pressure greater than 1 atm in a closed system".[20] The synthesis generally involves addition of highly soluble metal salts such as nitrates, sulfates or acetates along with organic components that are generally mono-, di-, tri- or tetracarboxylic acids in a polar organic solvent such as dimethylformamide (DMF) or diethylformamide (DEF). The choice of solvent may vary depending upon the solubility of the metal salts and organic linkers. The resultant solution is then stirred and heated at temperatures ranging from 25 °C to 200 °C, followed by slow cooling to obtain suitable single crystals of the desired framework.

Besides solvothermal methods, there are various other methods for the preparation of MOFs such as the use of non-miscible solvents,[21] electrochemical routes,[22] and a high-throughput approach.[23] Another important alternative is microwave irradiation, which takes less time for crystallization while controlling face morphology and particle size distribution.[24] A serious limitation of this approach, however, is the general lack of formation of crystals large enough to obtain good structural data.

Although there are various ways of synthesising MOFs, solvothermal synthesis remains the most frequently used method. Using solvothermal synthesis, Yaghi and co-workers reported the well-known MOF-5 structure[19] where octahedral $Zn_4O(COO)_6$ clusters are connected by phenylene struts to form a cubic framework. The same approach was later extended to strategically reticulate metal ions and organic linkers to generate a series of porous structures with systematically increased pore sizes. This methodology is also known as isoreticular synthesis of MOFs.[25] Using MOF-5 (IRMOF-1) as a reference, its functionality was varied with organic groups such as –Br, $-NH_2$, $-OC_3H_7$, $-OC_5H_{11}$, $-C_2H_4$, and $–C_4H_4$ and its pore size was increased by using longer linkers such as biphenyl, pyrene, terphenyl and tetrahyropyrene to generate a total of 15 new IRMOFs (Figure 2).[11,25]

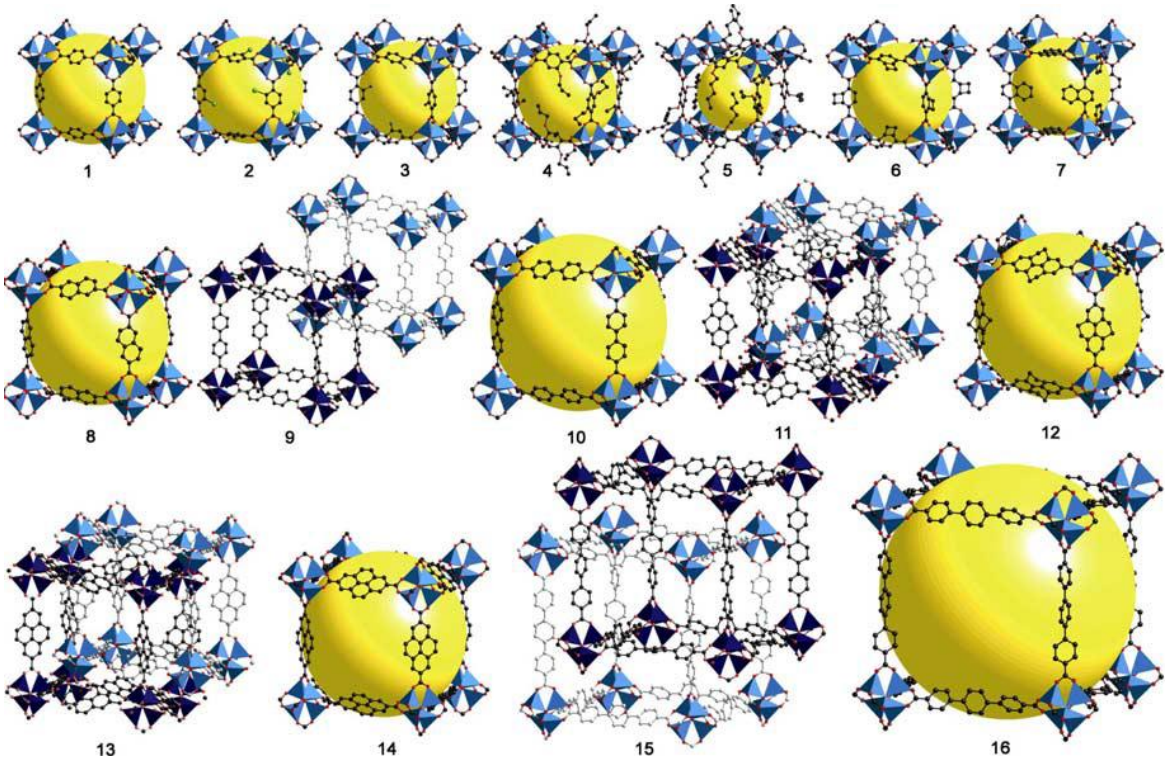

Figure 2. Isoreticular series of MOFs.[11]

In IRMOF-2 through IRMOF-7, bdc is functionalised with bromo, amino, *n*-propoxy, *n*-pentoxy, cyclobutyl and fused benzene groups to reticulate into the desired structure. In each of these frameworks the functional groups point into the voids. Furthermore, pore expansion is illustrated by the structure of IRMOF-8 through IRMOF-16 in which progressively longer linkers have been used. In some cases, expansion of the linkers resulted in interpenetrated frameworks. The isoreticular series is an extraordinary example of tuning structure-function properties in MOFs, while retaining their thermal stability.

1.2 Design of MOFs

The basic idea of constructing a MOF lies in selecting rigid/flexible organic linkers that act as pillars, along with inflexible metal ions or clusters that serve as joints connecting these pillars (Figure 3). This is also known as the "node and spacer" approach.[26]

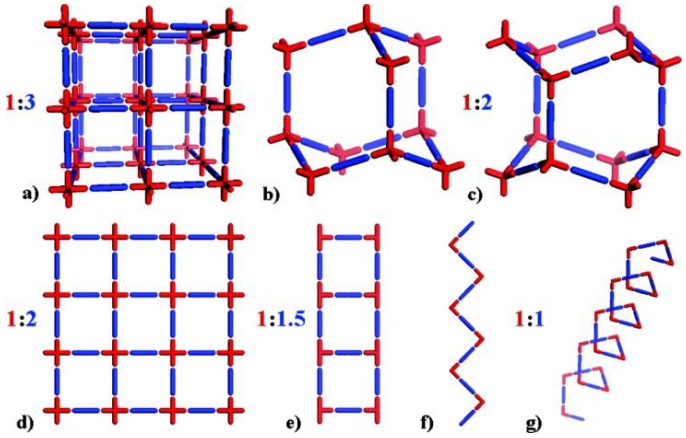

Figure 3. Schematic representation for using metal "nodes" (red) and organic "spacers" (blue) to construct 1D, 2D and 3D metal-organic networks: (a) cubic, (b) cubic diamond, (c) hexagonal diamond, (d) square grid, (e) ladder, (f) zigzag and (g) helix.[26]

Both linkers and connectors can have various orientations and total number of binding sites (Figure 4).[24,27] Depending on the coordination number of the metal ion and the nature of the linker, MOFs with different geometries can be synthesised. These are broadly divided into two- and three-dimensional frameworks and several high profile reviews also include 1D coordination polymers.[28]

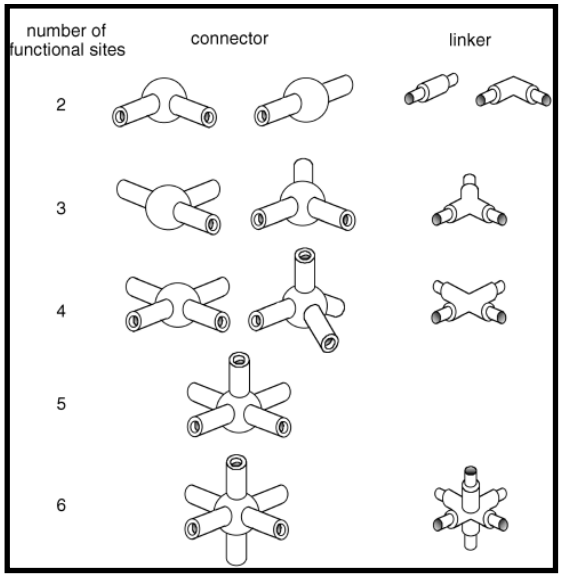

Figure 4. Different orientations of linkers and connectors.[24]

1.2.1 One Dimensional Coordination Polymers

One dimensional (1D) coordination polymers (CPs) have been recognised for their interesting electrical, magnetic, optical and mechanical properties. A wide variety of 1D coordination polymers have been reported in the literature.[29-33] They have simple topologies and their ease of formation enables modification of their functional properties at the metal centers or in the organic linkers that act as the backbone of the framework. 1D polymers can have various types of architectures such as *linear chains*, *zigzag chains*, *ladders*, *ribbons*, etc. (Figure 5).

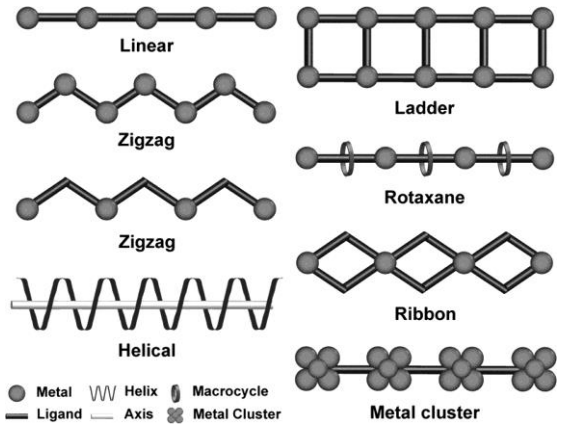

Figure 5. Various conformations for 1D coordination polymers.[29]

Jacobson and coworkers reported various 1D coordination polymeric structures $[Ni(bdc)(1,10\text{-phen})]_n$, $\{[Ni(bdc)(2,2'\text{-bpy})]\cdot 0.75H_2bdc\}_n$, $[Ni(bdc)(1,10\text{-phen})(H_2O)]_n$, $\{[Ni(bdc)(1,10\text{-phen})(H_2O)]\cdot 0.5H_2bdc\}_n$ and $[Ni(bdc)(2,2'\text{-bpy})(H_2O)]_n$ [2,2'-bpy = 2,2'-bipyridine and 1,10-phen = 1,10-phenanthroline].[34] All of these structures have the same topology but their geometries are quite different from one another due to different types of packing arrangements (Figure 6).

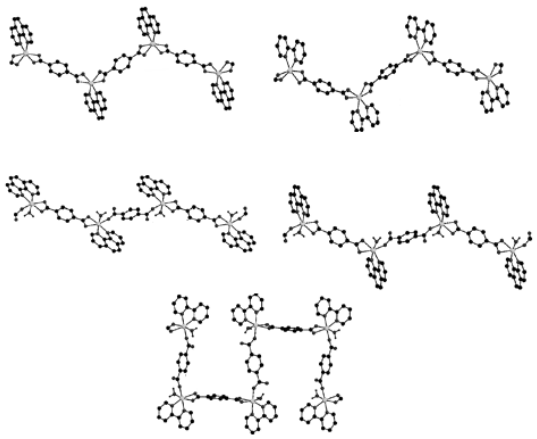

Figure 6. Structures of different 1D coordination polymers.[34]

Cheetham *et al*. reported an interesting example of a ribbon type packing arrangement in the case of $[Cu(H_3hip)_2(4,4'\text{-bpy})]_n$ (H_3hip = 5-hydroxyisophthalic acid).[35] The $[Cu(4,4'\text{-bpy})]_n$ linear strands in this case are hydrogen-bonded through the H_2hip ligands to form ribbons (Figure 7).[29,35]

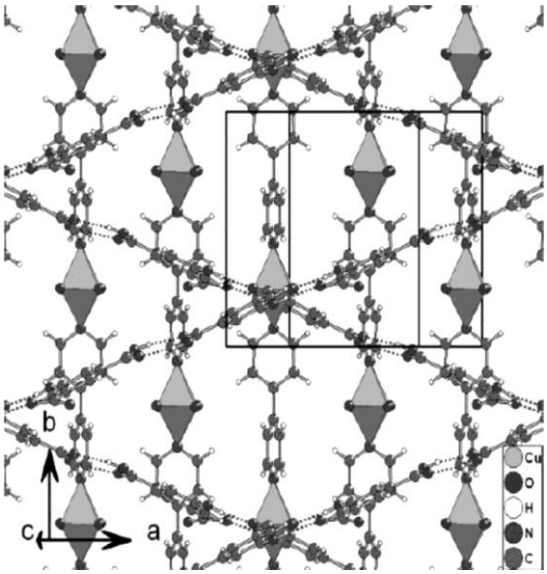

Figure 7. Packing of linear ribbon chains in $[Cu(H_3hip)_2(4,4'\text{-bpy})]_n$.[29]

Various zigzag 1D coordination polymers have been reported by different research groups.[36-40] An interesting example of a zigzag framework was described by Proserpio and co-workers[36] where two types of bridging bpmbp ligands with different conformations alternately form a framework with cobalt metal ions, $[Co(bpmbp)(NO_3)_2]_n$ [bpmbp = 4,4′-bis(pyridin-4-ylmethoxy)biphenyl]. The aromatic rings of one type of ligand are almost perpendicular, whereas those of the second type are almost parallel to the plane of the zigzag chain (Figure 8).[29,36]

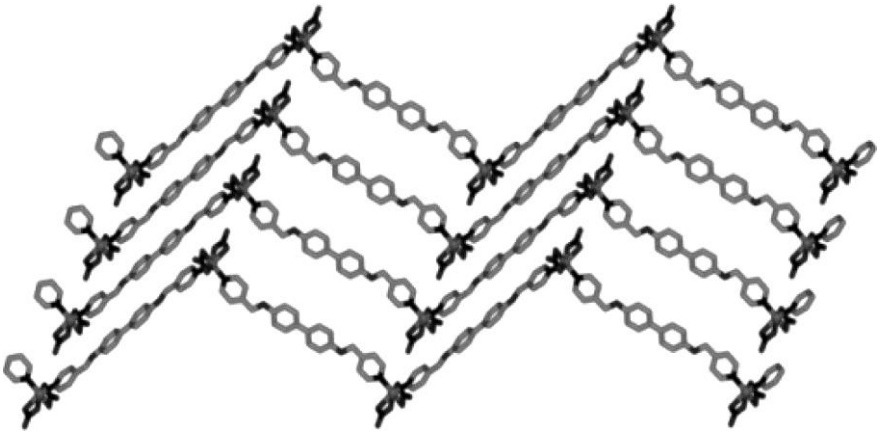

Figure 8. Zigzag arrangement in $[Co(bpmbp)(NO_3)_2]_n$ framework.[29]

Zaworotko and co-workers synthesised homochiral helical CP {[Ni(4,4′-bipy)$(PhCOO)_2(MeOH)_2$]·*x*(guest)}$_n$ from the linear spacers 4,4′-bpy bonded to Ni(II) ions in a *cis* geometry.[28,41] They demonstrated the ability of helical frameworks with large chiral channels to host a series of organic guest molecules and showed that chiral crystals can be obtained from achiral components (Figure 9). Besides this there have been many more reports on helical 1D coordination frameworks.[42-45]

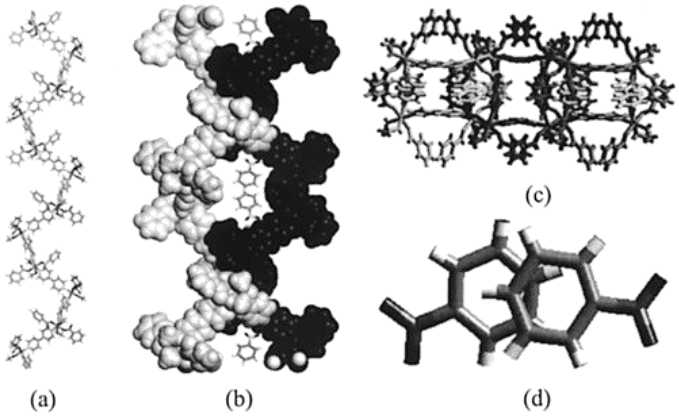

Figure 9. (a) Portion of a single helical chain of {[Ni(bipy)$(PhCOO)_2(MeOH)_2$]·$PhNO_2$}$_n$, (b) space-filling model showing the packing of adjacent helices and the resulting cavities occupied by $(nitrobenzene)_2$ adducts, (c) overhead view of packing of helices, and (d) illustration of the dissymmetric nitrobenzene dimer.[28]

The same group also synthesised the ladder like coordination polymer {[Zn(4,4'-bpy)$_{1.5}(NO_3)_2$]·0.5pyrene·MeOH}$_n$ utilising Zn(II) as a T-shaped node and 4,4′-bipyridine as linkers.[46] In this case pyrene molecules become sandwiched between two ladders through $\pi\cdots\pi$ stacking interactions (Figure 10).

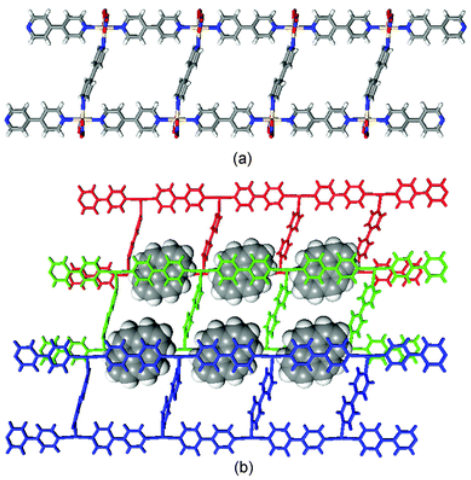

Figure 10. (a) Schematic representation of a ladder-shaped coordination polymer and (b) encapsulation of pyrene molecules between the ladder-shaped chains.[46]

1.2.2 Two Dimensional Coordination Polymers

The strategy of using known coordination geometries of metals with linear bifunctional ligands has yielded many 2D structures with various architectures. The ratio of metal and ligand are the primary factors that determine the topology of the network. Also, the nature of the coordination of terminal ligands (i.e. degree of chelation) plays an important role in the overall structure of the framework.[47] Commonly known 2D frameworks include herringbone, brick wall, square grid, honeycomb and bilayer (Figure 11).[47] Square grids and honeycombs are the simplest examples of 2D frameworks. Square grids are formed by 1:2 metal:ligand complexes with linear bifunctional ligands. They were first reported using cyano ligands[48] and have more recently been based on *N,N′*-bipyridine-type ligands.[49]

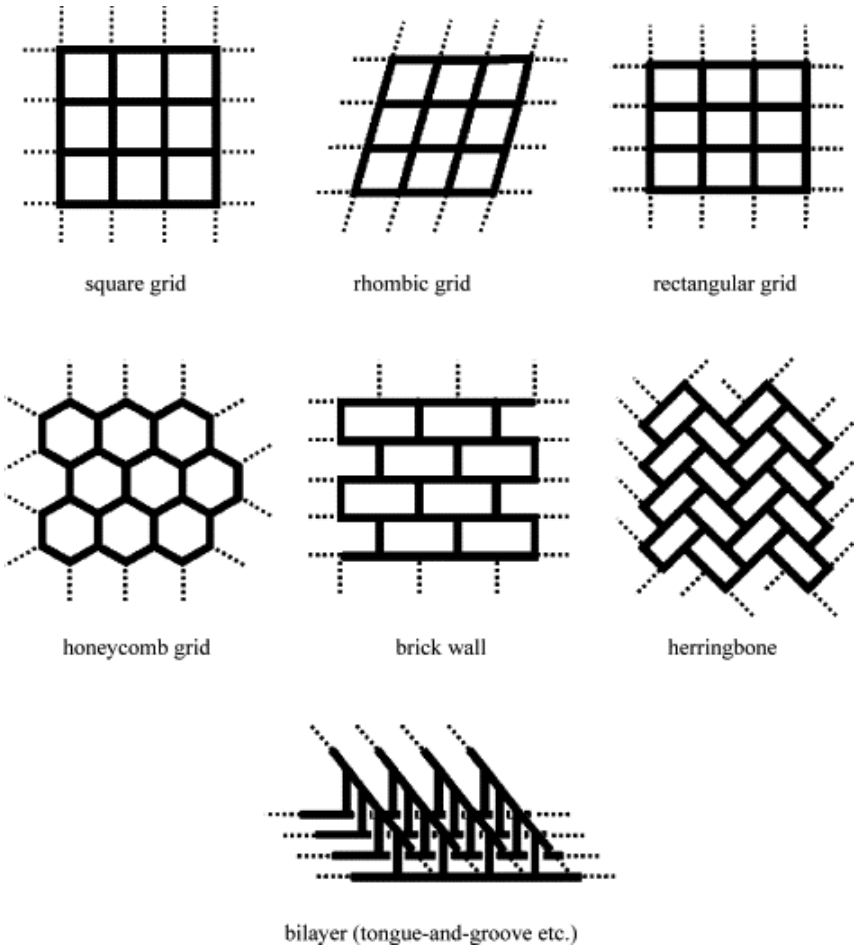

Figure 11. Different topologies of 2D coordination polymers.[47]

Zur Loye and co-workers made use of a chiral fluorene-based *N,N′*-bipyridine-type ligand (9,9-bis[(*S*)-2-methylbutyl]-2,7-bis(4-pyridylethynyl)fluorine (L) with a Cu(II) salt to synthesise first chiral non-interpenetrating square-grid coordination polymer (Figure 12).[50]

Similarly, many derived motifs such as rhombic or rectangular grids can be found in the literature.[51-54] In these cases the metal centers are also linked by four ligand molecules.

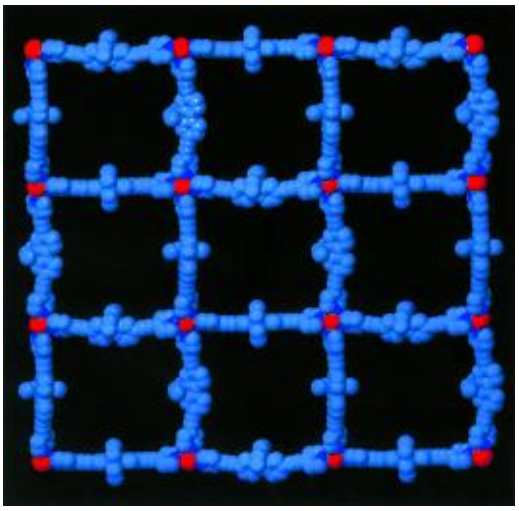

Figure 12. Square-grid structure of $[Cu(L)_2(NO_3)_2]$, L= 9,9-diethyl-2,7-bis(4-pyridylethynyl)fluorine.[50]

If the metal ions are coordinated to three ligand molecules to give a "T-shaped" node, layers are formed and the resulting structures are honeycomb grids, brick walls or herringbone type structures.[55-57] An interesting example of honeycomb structure has been reported by Suh *et al*., who generated a 2D coordination polymer $\{[Cu(C_{10}H_{26}N_6)]_3[C_6H_3(COO)_3]_2 \cdot 18H_2O\}_n$ (**1**), which has 1D channels perpendicular to the 2D layers.[56] The framework affords large honeycomb channels (~8.1 Å) where phenol molecules can be accommodated within the channels *via* H-bonding interactions (**2**) (Figure 13). The solid **1** binds guest molecules such as MeOH, EtOH and PhOH with different binding constants and capacities.

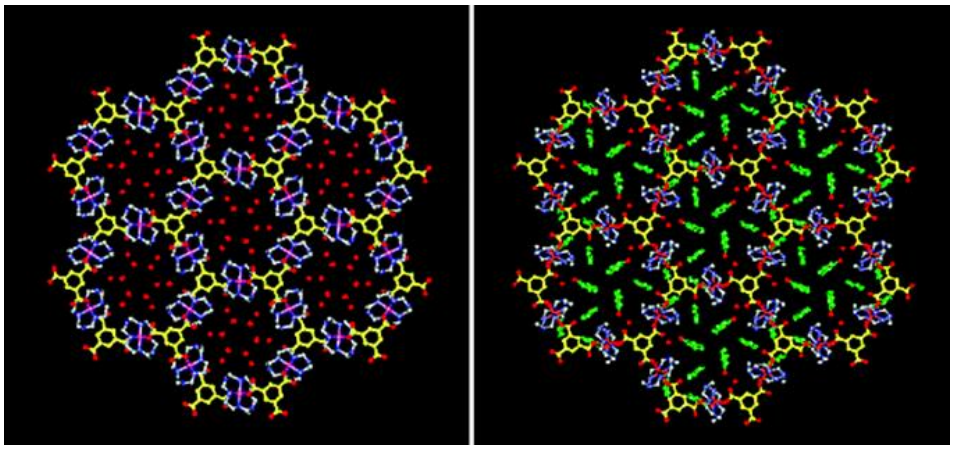

Figure 13. Packing diagram showing 1D channels (left) and filling of 1D channels by phenol molecules (right).[56]

1.2.3 Three Dimensional Coordination Polymers

The extension of ligand connectors in all the three dimensions results in 3D polymers. Various combinations of connectors and linkers have afforded a wide range of 3D MOFs.[28] Due to their high stability and porosity, 3D polymers find many useful applications in gas sorption and separation. The synthesis of such polymers generally involves the use of anionic ligands in order to compensate for metal ion charge. A common problem encountered with the early MOFs was their inability to support permanent porosity and to avoid collapse upon removal of the guest molecules. This problem was overcome by the use of multidentate linkers such as carboxylates that allow for the formation of more rigid 3D frameworks due to their ability to aggregate metal ions into M–O–C clusters commonly known as secondary building units (SBUs).[58] A well-known example of this approach is MOF-5 reported by Yaghi (Figure 14).[19]

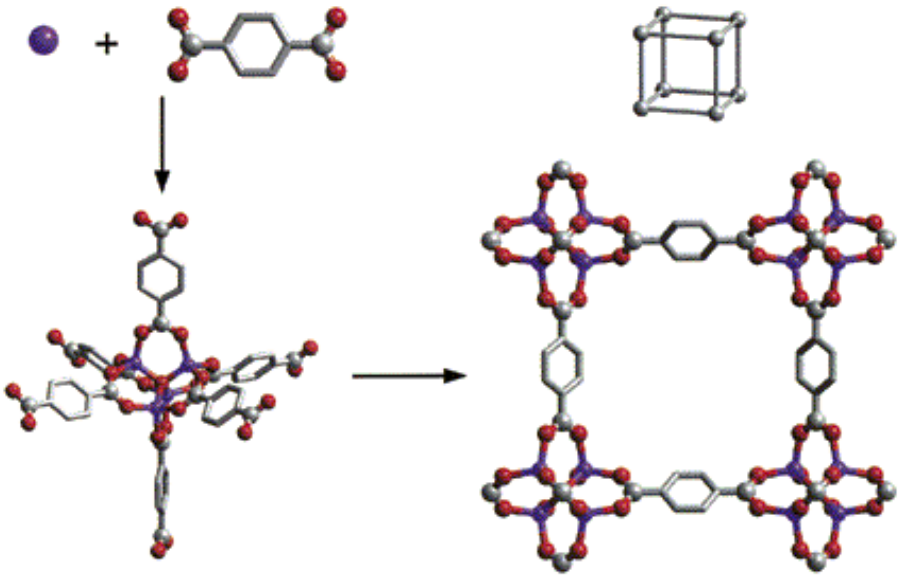

Figure 14. View of rigid metal-carboxylate clusters (Zn_4O) that can be linked by phenylene spaces to form rigid extended frameworks.[58]

Thereafter, the use of SBUs has been a common strategy to produce new MOFs. Once the synthesis of the SBU is established, it could be used to direct the assembly of ordered frameworks with rigid or flexible organic linkers.[59] The SBUs not only provide sufficient rigidity to the structure by locking the metal ions into their positions with the help of carboxylates but they also ensure overall neutrality of the framework, thus obviating the need for counter ions in the cavities. Overall, it is the combination of both SBUs (as nodes) and organic ligands (as linkers) that determines the final framework-topology. A number of

different topologies of 3D polymers using such an approach have been reported, of which the most common networks are shown in Figure 15.

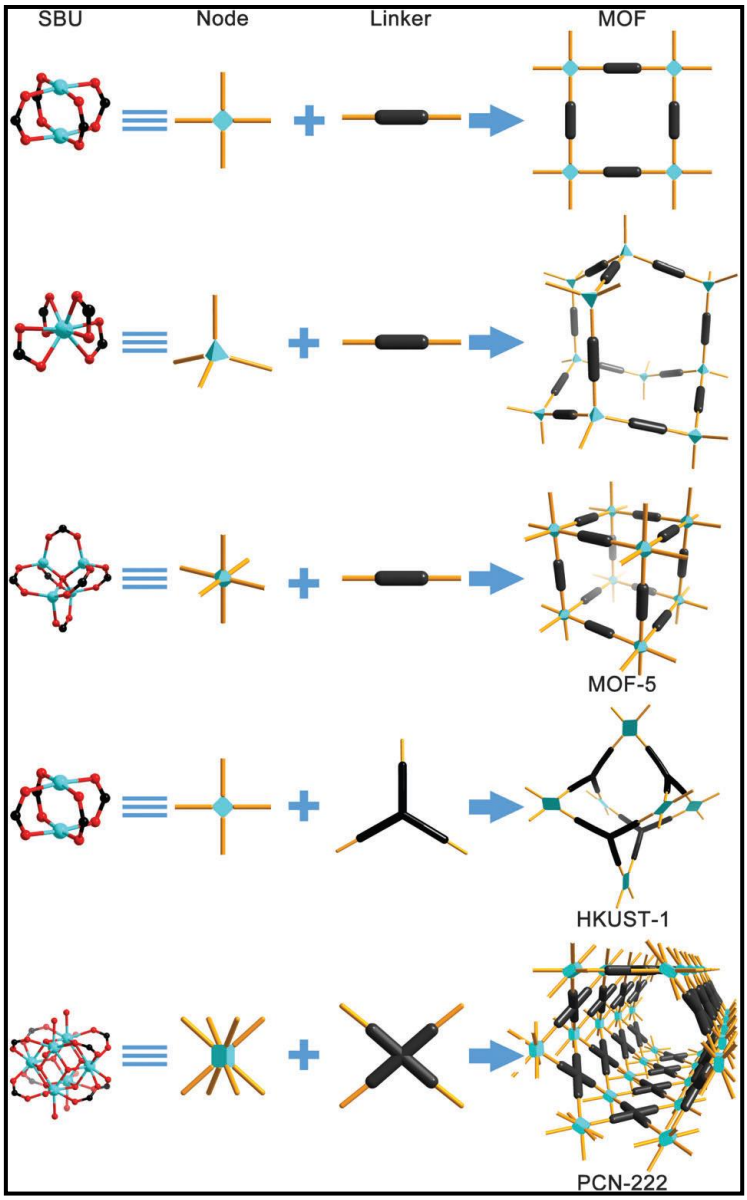

Figure 15. Schematic illustration of the construction of some well-known MOFs from SBUs and rigid linkers.[59]

Another very common approach for producing 3D MOFs involves the use of bipyridyl linkers as pillars. The metal ion is coordinated to the dicarboxylate ligands to produce stable 2D layered structures, which are further extended in three dimensions by the use of linear bipyridyl linkers (Figure 16).[60] These type of MOFs will be discussed in more detail in the following sections.

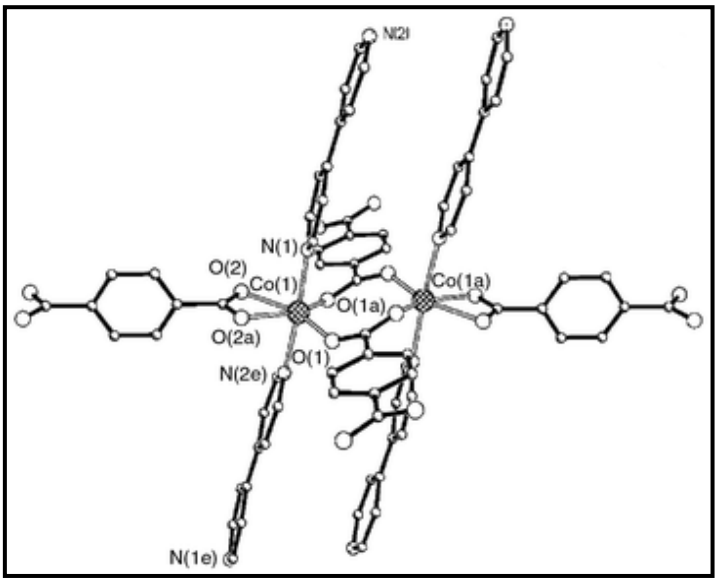

Figure 16. Coordination environment of the cobalt binuclear unit in $\{[Co(terephthalate)(4,4'\text{-bpy})]\}_n$[60]

A stable pillared and double-walled Zn(II) polymer with regular nanochannels prepared by the solvothermal reaction of zinc(II) nitrate, *dl*-lactic acid and 4-(pyridin-4-yl)benzoic acid (pybz) in DMF was reported recently.[61] This compound $\{[Zn_3(dl\text{-}lac)_2(pybz)_2]\cdot 2.5DMF\}_n$ built around infinite pillars of $\{[Zn_3(dl\text{-}lac)_2]^{2+}\}_n$, undergoes single-crystal to single-crystal (SCSC) transformation upon desolvation and has the ability to take up a large quantity of iodine with controlled release (Figure 17).

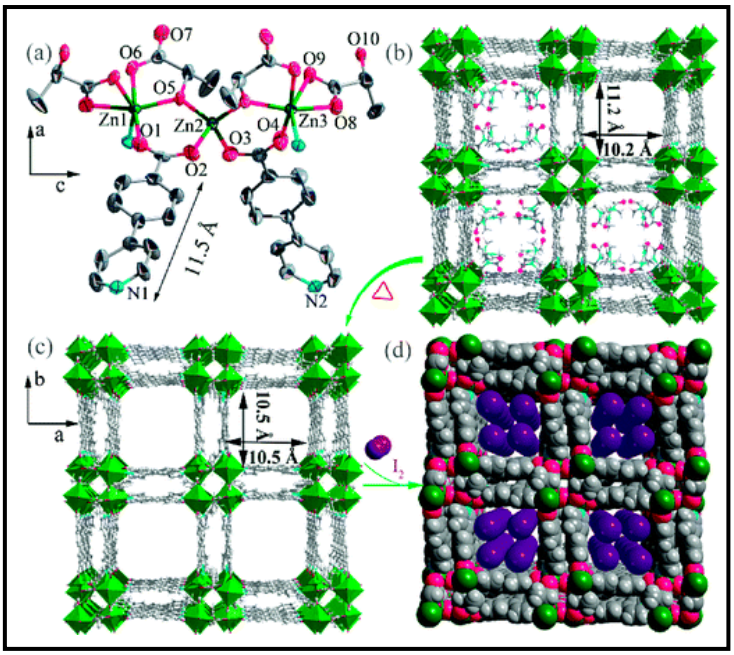

Figure 17. (a) Coordination environment of Zn ions, (b) View of the 3D open framework with 1D channel, the guest DMF molecules being shown in channels, (c) desolvated framework and (d) sketch of I_2 molecules occupying the channels.[61]

1.2.4 Classification of Porous Coordination Polymers

Porous coordination compounds have been classified into three categories on the basis of the stability of the framework upon removal of the guest (Figure 18).[12] *First generation* compounds have microporous frameworks that are stable only in the presence of the guest molecules and show irreversible framework collapse on guest removal. *Second generation* compounds have stable and robust porous frameworks with permanent porosity even after removal of guest molecules from the pores. *Third generation* compounds have flexible and dynamic frameworks that respond to external stimuli such as light, electric field, guest molecules and change their channels or pores reversibly.

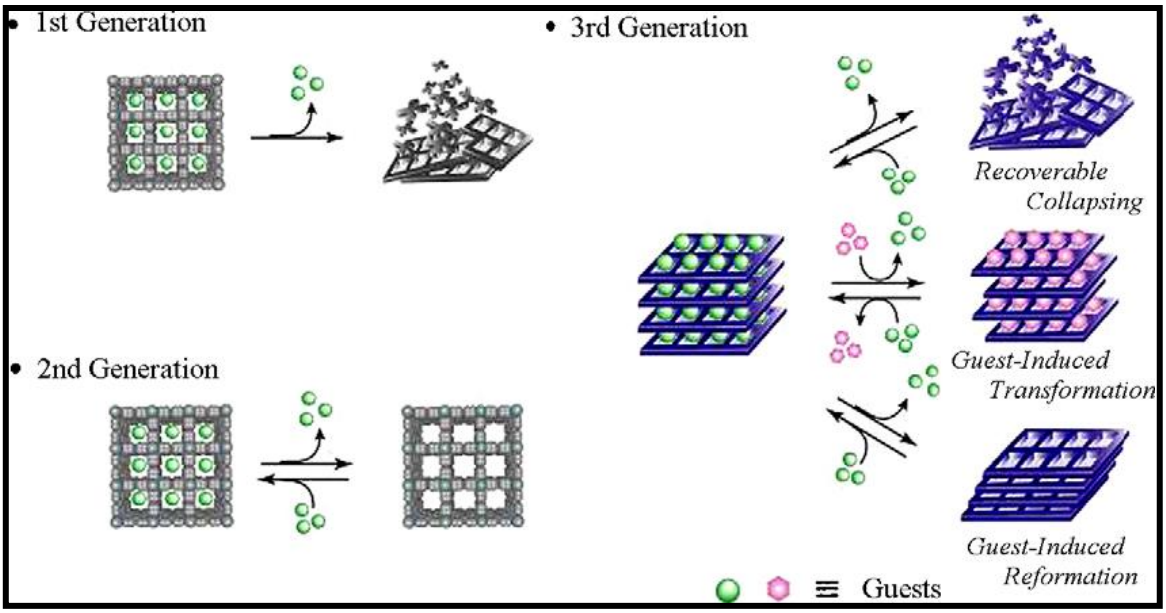

Figure 18. Classification of porous compounds as 1st, 2nd, and 3rd generation.[12b]

Porous coordination polymers comprise both robust 2nd generation compounds as well as flexible and dynamic 3rd generation compounds. The 3rd generation PCPs are further subdivided into three types. Type I frameworks lose crystallinity upon guest removal due to network collapse but are regenerated under the initial conditions. Type II frameworks undergo structural shifts in their networks due to simultaneous exchange of guest molecules. Finally, Type III undergoes structural changes of the networks into a different structure upon removal of the guest molecules, but the new structure reverts back to the original under initial conditions. Also, unlike Type I porous coordination compounds, Type II and III retain their crystal singularity while undergoing such structural transformations.

1.3 Applications of MOFs

In the early 1990s, research was mainly focused on the syntheses, X-ray crystal structures and topological validation of coordination polymers (CPs), along with their potential applications for molecular sieving and ion exchange.[13] However, it took a long time to establish their permanent porosity due to difficulty in stabilising the frameworks in the absence of the guest molecules.[16,17] It was very important to demonstrate the integrity of an open framework in order to successfully use it as a storage material.[10] Various research groups carried out solvent exchange experiments to provide evidence of the accessibility of the void spaces in several PCPs/MOFs. These experiments showed that the optical, electronic or magnetic properties of the MOF could be altered by the nature of the guest molecules. With proper tailoring of the framework structure and pore surfaces, MOFs were later exploited as highly selective catalysts and sensors. However, one of the most promising applications of MOFs is their ability to store gases.[12] In recent times MOFs have emerged as one of the most important materials for gas sorption due to their exceptionally high surface areas as well as chemically-tunable structures.[10] In the following section the general concept for the application of MOF materials in gas sorption and separation will be discussed in detail.

1.3.1 Gas Sorption

Sorption behaviour is divided into two types, namely *adsorption* and *absorption*. *Adsorption* involves enrichment of one or more components in an interfacial layer comprised of *surface layer* and the *adsorption space* in which enrichment of the adsorptive can occur. In *absorption*, molecules penetrate the surface layer and enter the bulk. Thus, adsorption is essentially a surface phenomenon whereas absorption is a bulk phenomenon.[2] In some cases the distinction between adsorption and absorption becomes difficult or irrelevant and a more general term *sorption* is used, which embraces both the phenomena. The counterpart of adsorption is *desorption*, denoting the converse process in which the amount adsorbed decreases. When adsorption and desorption curves do not coincide we observe *adsorptive hysteresis*. Further distinction should be made between two sorptive processes, namely *physisorption* and *chemisorption*, depending on the type and strength of interactions. *Physisorption* occurs when a gas (the *adsorbate*) makes contact with the surface of a solid (the *adsorbent*) and the interaction between *adsorbent* and *adsorbate* is very weak, with the corresponding enthalpy of adsorption being less than *ca* 10 kcal mol^{-1}. On the other hand

chemisorption normally occurs with the formation of significant chemical bonds and the enthalpy of adsorption is in the range of *ca* 25 – 95 kcal mol^{-1}.

A sorption isotherm is used to illustrate the sorption and desorption of a gas on a solid at constant temperature and relates the amount of gas sorbed (in moles, grams, cm^3 etc) to the equilibrium pressure of the gas. The IUPAC has divided sorption isotherms into six types (Figure 19).[2]

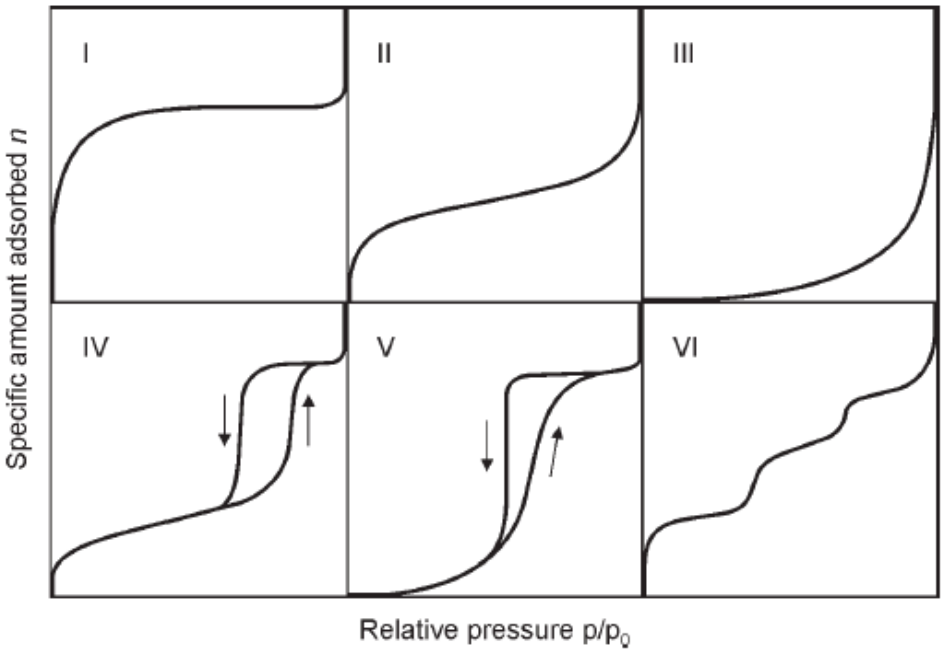

Figure 19. Types of sorption isotherms categorized by the IUPAC.[2]

Type I isotherms are reversible, with a concave shape. Such isotherms are characteristic of microporous materials having relatively small external surfaces such as activated carbons and molecular sieve zeolites. *Type II* isotherms are also reversible and represent unrestricted monolayer-multilayer adsorption. Such isotherms are observed with a non-porous or macroporous adsorbent. *Type III* isotherms (also reversible) have a convex shape and are uncommon. In such cases, the adsorbate-adsorbent interactions play an important role. *Type IV* isotherms display hysteresis loops associated with capillary condensation taking place in mesopores while the initial shape of the isotherm is attributed to monolayer-multilayer adsorption. *Type V* isotherms are also uncommon and are obtained with certain porous adsorbents. Such isotherms involve weak adsorbate-adsorbent interactions. *Type VI* isotherms are obtained for uniform non-porous surfaces where the steps represent stepwise multilayer adsorption.[2]

1.3.2 MOFs for Gas Sorption and Separation

The impending decline in fossil fuel reserves and increase in global warming have forced the world to look for alternative sources of clean energy. Due to the ready availability of fossil fuels, over 85% of our current global energy demand is supported by burning fossil fuels, which releases large amounts of CO_2 into the atmosphere. A significant challenge thus lies in developing materials that can store gases such as carbon dioxide, hydrogen and methane in a confined space for various applications. Porous materials have received much attention in this regard. Pure organic materials such as activated carbons and pure inorganic materials such as zeolites were the first to emerge as favourable materials for gas sorption.[9] However, they have their own limitations as they suffer from the lack of diversity. In order to exploit the properties of both organic and inorganic materials, hybrid materials or MOFs have been generated that are stable, diverse and ordered porous materials with high surface areas.[12a] Porous MOFs have some interesting features such as extremely high surface areas, tunable framework structures and porosities, and rationally immobilized functional sites and pore surfaces.[62]

The first significant work on hydrogen storage was reported by Yaghi and co-workers in 1999 when they reported the structure of **MOF-5**.[19] **MOF-5** has a cubic three dimensional extended porous structure which is stable upon desolvation and when heated up to 300 °C. The rigid and divergent character of the added linker allowed the articulation of the clusters into a three-dimensional framework, resulting in a structure with higher apparent surface area and pore volume than most porous crystalline zeolites (Figure 20).

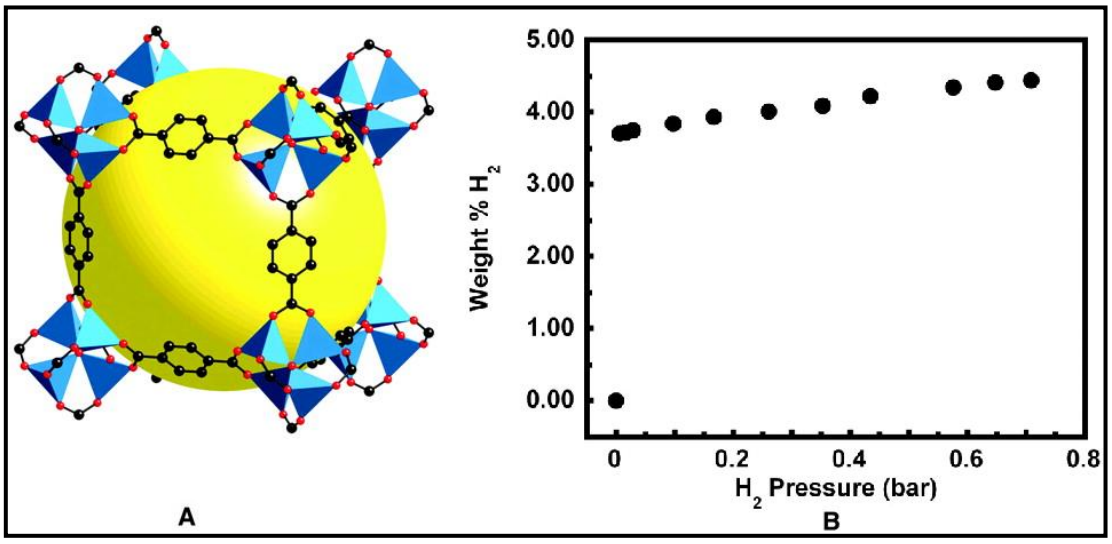

Figure 20. (**a**) Crystal structure of **MOF-5** and (**b**) H_2 sorption isotherm for **MOF-5** at 78 K.[19]

MOF-5 immediately attracted wide attention because of its extremely high porosity, with a BET surface area over 3000 m^2 g^{-1}. The hydrogen uptake was 4.5 weight percent (wt%), equal to 17.2 hydrogen molecules per formula unit at 78 K.[63] The 3D rigid framework $[Cu(SiF_6)(4,4'\text{-bpy})_2]_n$ reported by Kitagawa and co-workers can adsorb far more CH_4 than zeolite 5A at room temperature and relatively low pressure. Both of these frameworks are second generation porous materials.[64]

Hexacarboxylates have been widely used to construct porous frameworks with high surface areas. In this series of MOFs the surface areas and pore volumes can be progressively enhanced by increasing the length of the organic linkers. Notable examples include **NOTT-112**, **PCN-68/NOTT-116**, **PCN-69/NOTT-119**, **NU-100/PCN-610** and **NU-111**.[65] Schröder and co-workers made use of a triangular hexacarboxylate ligand (Figure 21) with $Cu(NO_3)_2 \cdot 3H_2O$ to yield **NOTT-112,** which comprises three types of cages.[66] The fully evacuated sample shows a high BET surface area of 3800 m^2 g^{-1} as well as excellent gravimetric H_2 adsorption capacities of 10.0 wt% at 77 bar and 77 K (Figure 21).

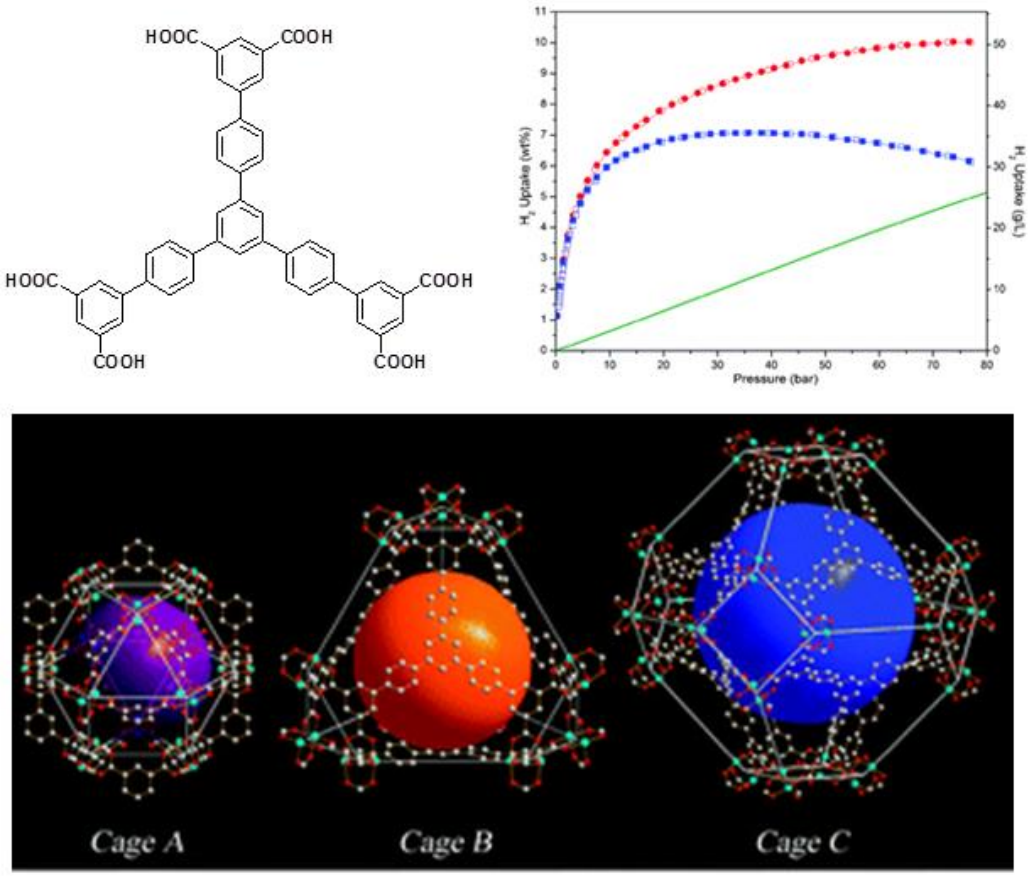

Figure 21. Structure of hexacarboxylate ligand used for the synthesis of **NOTT-112** along with high pressure H_2 adsorption isotherm at 77 K for **NOTT-112** (top), three different cages in **NOTT-112** (bottom).[65]

Later Hupp *et al.* synthesised a new framework, known as **NU-111** using triple bond spacers to replace the phenyl spacers of hexacarboxylate ligand used in **NOTT-112**.[67] This framework showed a high BET surface area of 4930 m^2 g^{-1} and a total H_2 gravimetric uptake of 13.5 wt% at 77 K, which is much higher than that of **NOTT-112** (Figure 22).

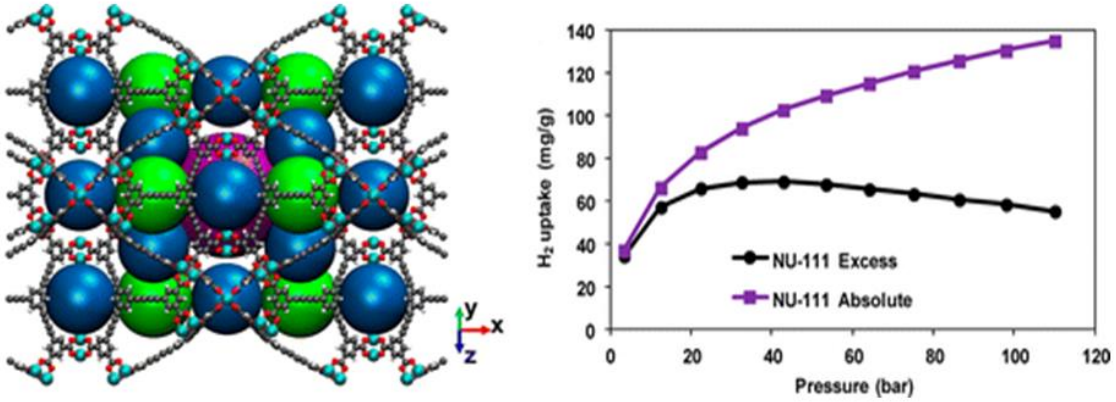

Figure 22. Different types of cages in **NU-111** (left), and high pressure H_2 adsorption isotherm at 77 K for **NU-111** (right).[67]

Recently Yaghi *et al.* reported an ultra-high porous coordination polymer **MOF-210**, which is composed of Zn_4O secondary building units joined by two types of organic linkers.[68] **MOF-210** shows a record total H_2 gravimetric uptake of 17.6 wt% at 80 bar and 77 K with an exceptionally high BET surface area exceeding 6200 m^2 g^{-1} (Figure 23).

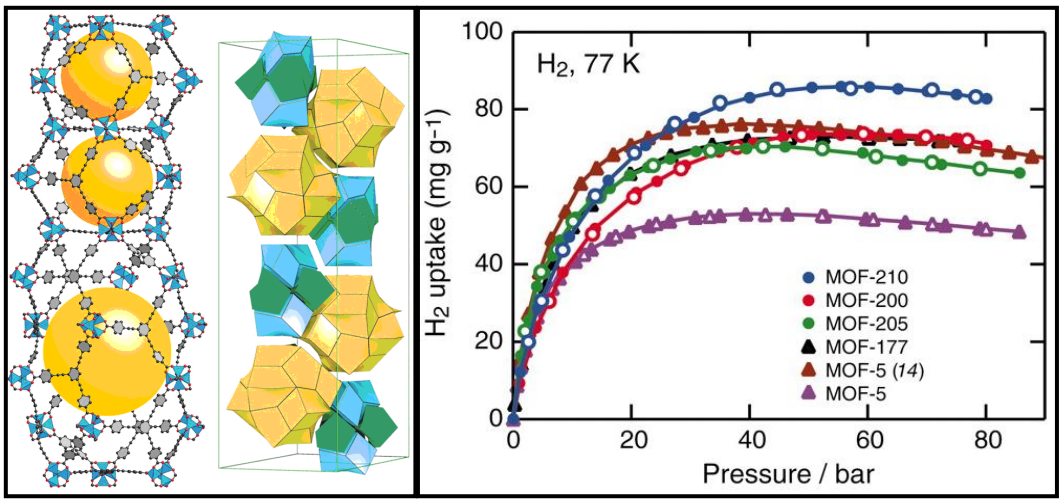

Figure 23. Crystal structure and high-pressure H_2 sorption isotherms for **MOF-210**.[68]

The well-known MOF **HKUST-1**, first reported by Chui *et al.*, has been widely studied for high pressure methane storage.[69] The 3D framework contains three different types of cages of ~4, 10, and 11 Å in diameter for the recognition of methane molecules (Figure

24). Although it has the moderate BET surface area of 1850 m^2 g^{-1} and low gravimetric CH_4 storage capacity of 0.216 g g^{-1}, this material exhibits an exceptionally high volumetric methane storage capacity of 267 cm^3 (STP) cm^{-3} at 298 K and 65 bar (Figure 23), which is the highest reported value so far.[62,70]

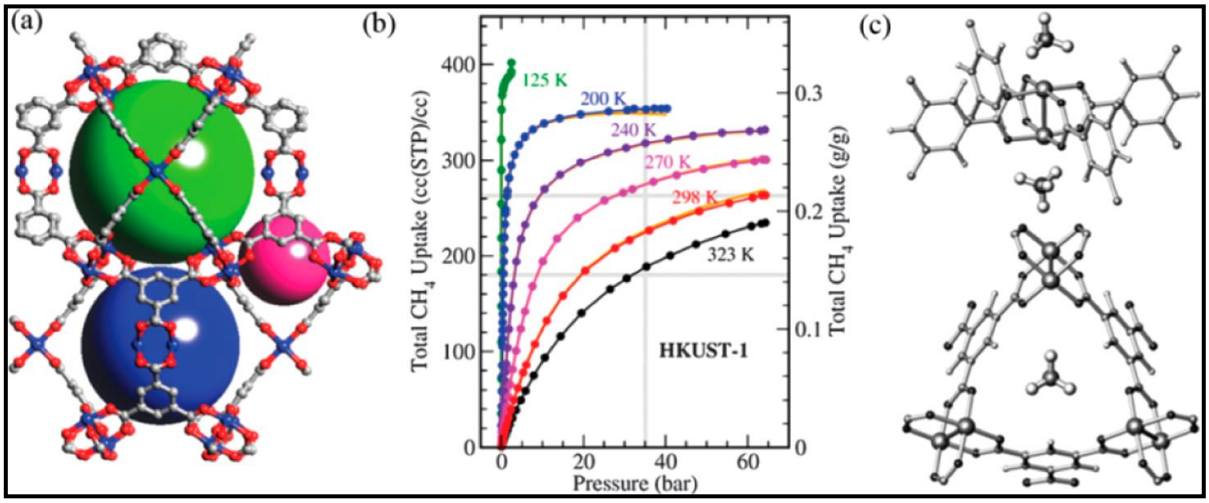

Figure 24. (a) Three different types of cages in **HKUST-1**. (b) Methane adsorption isotherms for **HKUST-1** at various temperatures. (c) Two primary adsorption sites for methane: open copper site (upper) and the small cage window site (down) in **HKUST-1**.[62]

MOFs have attracted wide attention as porous materials for CO_2 sorption and separation. Chen and co-workers recently examined a series of porous MOFs having different pore structures, surface areas and pore surface functionalities for their performance on post combustion CO_2 capture.[71] It was observed that the incorporation of functional sites within MOFs leads to significant improvement in their post combustion CO_2 capture and separation capacities.[71-76] Of the various MOFs studied, **Mg-MOF-74** with an extremely high density of open Mg^{2+} sites had the highest gravimetric and volumetric adsorption capacity[75] while another MOF **UTSA-16** exhibited high volumetric uptake of CO_2 at ambient conditions (Figure 25).[71] The results indicated that the immobilization of specific sites such as open metal sites and $-NH_2$ sites can induce strong interactions with CO_2 molecules and then enhance the capacity of CO_2 capture and separation. Recently Yaghi and co-workers reported three hydrophobic MOF materials namely **ZIF-300**, **ZIF-301** and **ZIF-302**. All three MOFs are capable of separation of CO_2 from N_2 even under humid conditions without any loss of performance.[77]

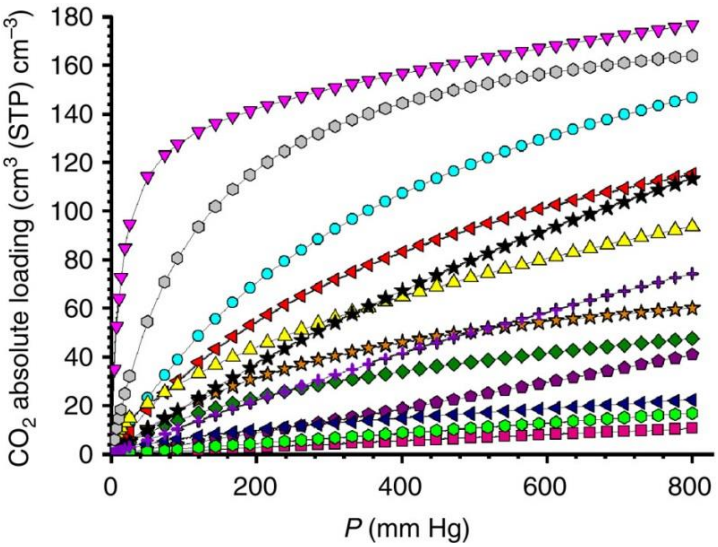

Figure 25. (a) Comparison of the absolute loading of CO_2 at 296 K on selected MOFs. From top to bottom, **Mg-MOF-74** (magenta down triangle), **UTSA-16** (gray hexagon), **Zn-MOF-74** (cyan circle), **bio-MOF-11** (red left triangle), **Cubtc** (black star), **Cutdpat** (yellow up triangle), **UTSA-20** (violet cross), **ZIF-78** (orange star), **$Zn_5(bta)_6(tda)_2$** (olive diamond), **Zn(bdc)(dabco)** (purple pentagon), **MIL-101** (navy left triangle), **Yb(bpt)** (green hexagon) and **MOF-177** (pink square).[71]

Although 2nd generation materials have been used extensively for gas storage and separation, the most interesting class of porous materials are the 3rd generation compounds that can alter their frameworks in response to guest molecules. These structures are also known as *dynamic/flexible* frameworks as they frequently undergo structural transformation (Figure 26).[78] Since these porous structures can reversibly change their channel structures to accommodate guest molecules, they have found useful applications in selective sorption, specific sensing and as actuators.[12b] In general, gas sorption in flexible MOFs is more complicated than that in rigid MOFs since the sorption isotherm generally shows hysteretic behaviour due to structural rearrangement during the adsorption-desorption process.

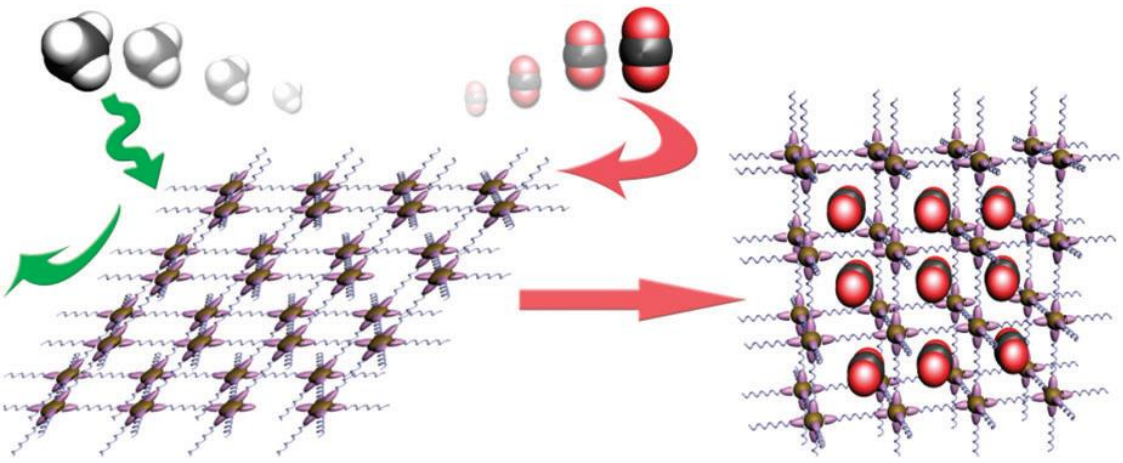

Figure 26. Schematic representation of selective gas adsorption in a flexible MOF.[78]

The selective gas sorption behaviour in some flexible MOFs can be due to the size/shape exclusion effect, despite the change in pore size/shape upon adsorption.[79-81] The $[Cd(pzdc)(bpee)]_n$ [pzdc = pyrazinedicarboxylic acid and bpee = 1,2-Di(4-pyridyl)ethylene] pillared layered MOF reported by Kitagawa *et al.* exhibits such a property.[82] The framework absorbs H_2O and MeOH, accompanied by channel expansion, but not EtOH, THF, and Me_2CO, suggesting that sorption selectivity arises from the molecular sieving effect. Another classic example of size/shape exclusion was presented by Chen and co-workers who systematically tuned the pore void space of three 3D doubly interpenetrated MOFs, $[Cu(FMA)(Pyz)_{0.5}]_n$, $\{[Cu(FMA)(4,4'\text{-}Bipy)_{0.5}]\cdot 0.25H_2O\}_n$, and $\{[Cu(FMA)(4,4'\text{-}Bpe)_{0.5}]\cdot 0.5H_2O\}_n$ (FMA = fumaric acid, Pyz = pyrazine) by simply increasing the length of the pillar linker.[62,83] The sorption studies show that activated $[Cu(FMA)(4,4'\text{-}bpy)_{0.5}]_n$ does not take up either H_2 or N_2 at 77 K due to the pore apertures being much smaller than the sizes of H_2 and N_2 molecules, whereas $[Cu(FMA)(4,4'\text{-}bpe)_{0.5}]_n$ with larger pores shows selective sorption behaviour with respect to different gas molecules (Figure 27). This MOF can thus selectively adsorb H_2 while excluding Ar, N_2 and CO at 77 K. Furthermore, this framework also exhibits dynamic behaviour to some extent at the higher temperature of 195 K, where pore apertures can be enlarged leading to selective sorption of CO_2 over CH_4 and N_2.

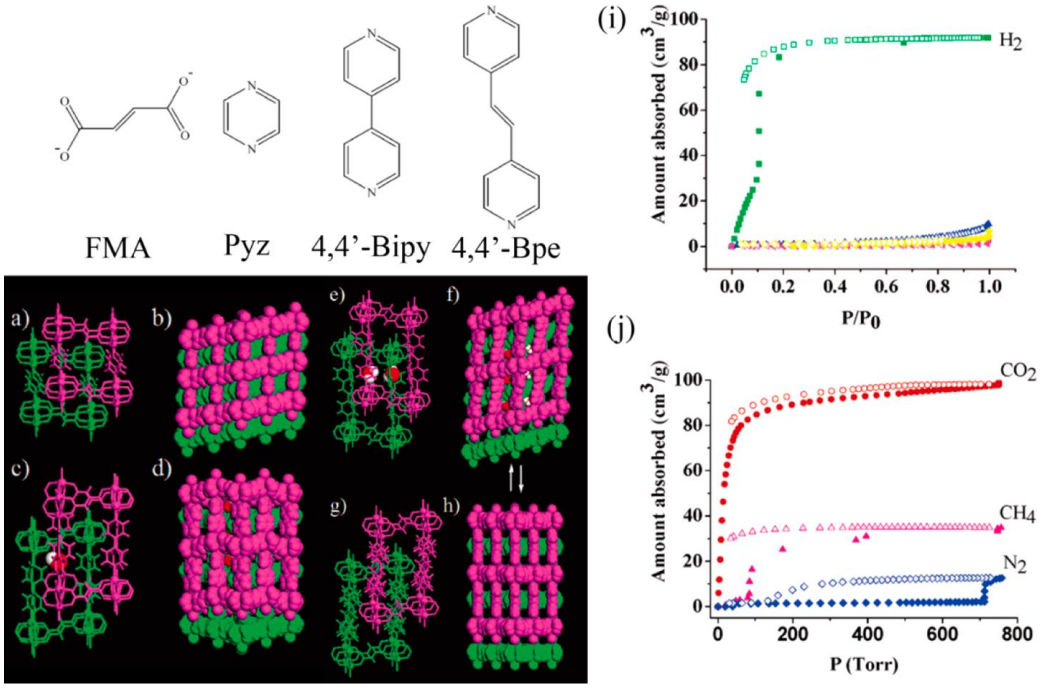

Figure 27. Crystal structures of frameworks $[Cu(FMA)(Pyz)_{0.5}]_n$ (a, b), $\{[Cu(FMA)(4,4'\text{-}bpy)_{0.5}]\cdot 0.25H_2O\}_n$ (c, d), $\{[Cu(FMA)(4,4'\text{-}bpe)_{0.5}]\cdot 0.5H_2O\}_n$ (e, f), and $[Cu(FMA)(4,4'\text{-}bpe)_{0.5}]_n$ (g, h) as well as gas sorption isotherms for $[Cu(FMA)(4,4'\text{-}bpe)_{0.5}]_n$ at (i) 77 K and (j) 195 K.[62]

Another interesting class of flexible MOFs that display selective adsorption for different gases are the (**MIL**) compounds.[84-87] These compounds show adsorption selectivity based on adsorbate-surface interactions accompanied by pore size/shape change. This has been observed in the case of chromium (III) dicarboxylate, **MIL-53**, which has a 3D structure with 1D diamond shaped channels.[84] The framework undergoes a *breathing* phenomenon upon hydration-dehydration. At room temperature **MIL-53$_{HT}$** quickly adsorbs atmospheric water to give $[Cr^{III}(OH)\cdot\{O_2C\text{-}C_6H_4\text{-}CO_2\}\cdot H_2O]_n$ or **MIL-53$_{LT}$** (LT: low-temperature form; **HT**: high-temperature form). The transition between the hydrated form (**MIL-53$_{LT}$**) and the anhydrous form (**MIL-53$_{HT}$**) is completely reversible with a very strong breathing effect of more than 5 Å (Figure 28). The same phenomenon was also observed in the case of aluminium **MIL-53**.

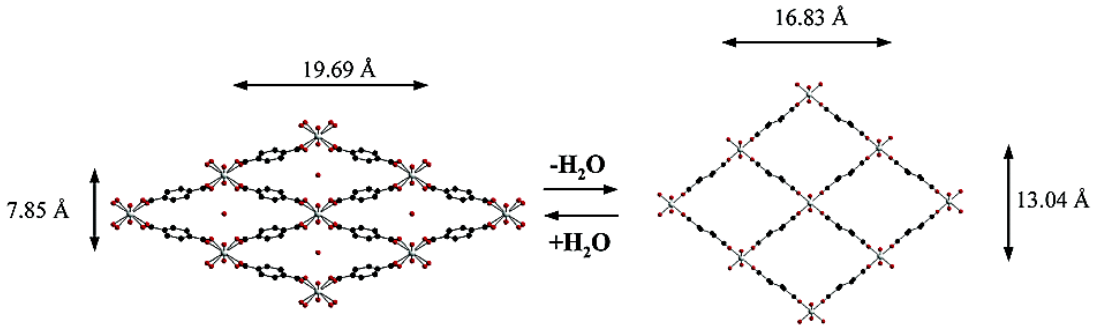

Figure 28. Breathing phenomenon in **MIL-53** (Al, Cr). (Left) **MIL-53$_{LT}$** (hydrated). (Right) **MIL-53$_{HT}$** (dehydrated).[84]

The dehydrated forms of aluminium and chromium **MIL-53** compounds were later studied for their gas sorption properties.[85] Both forms show two step adsorption isotherms for CO_2 whereas no steps are observed in the case of CH_4 (Figure 29). The difference in the sorption trend was attributed to the quadrupole moment of the CO_2 molecules. Besides **MIL-53**, there are various other **MIL** compounds that show similar behaviour.[86,87]

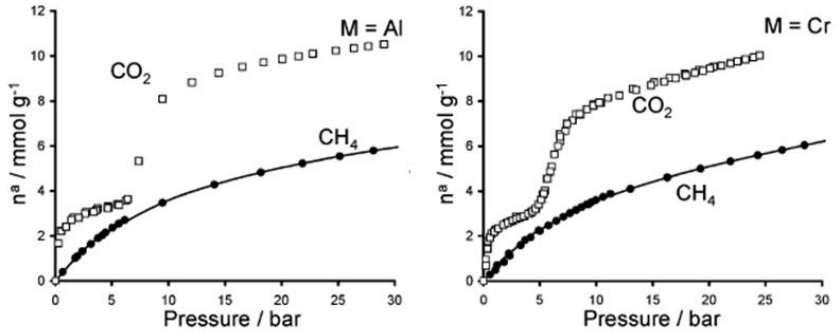

Figure 29. (a) Framework structure of **MIL-53**. (b) Gas sorption isotherms of **MIL-53(Cr)** at 304 K (inset, schematic illustration of the ‘‘breathing’’ effect in **MIL-53(Cr)**).[85]

Some flexible MOFs do not allow guest molecules to enter the framework in their closed state due to the presence of small pores. However, the pores expand when the framework is exposed to certain gases. This phenomenon is known as the *gate-opening effect*.[88] The selective sorption of CO_2 over CH_4 in **ZIF-20** has been attributed to gate-opening process.[88] The 3D structure consists of large cages connected by small windows. At 273 K the uptake of CO_2 is five times greater than that of CH_4, suggesting stronger interactions between the pore surface and CO_2 molecules. Since the maximum pore aperture of **ZIF-20** is smaller than the kinetic diameter of CO_2 and CH_4, it was believed that the small windows expand, making large cage space accessible to gas molecules.

The gate-opening effect does not only depend on the adsorbate-surface interactions but also on the specific gas pressure known as the gate-opening pressure. For a certain flexible MOF each gas has its own gate-opening pressure. Thus several types of gases may be separated at different pressures by just one adsorbent. The [Cu(dhbc)$_2$(4,4′-bpy)] (dhbc = 2,5-dihydroxybenzoic acid) framework reported by Kitagawa and co-workers displays such a gate-opening process with different gases at different pressures.[89] The N_2, O_2, CH_4 and CO_2 adsorption isotherms initially show a flat curve in the low pressure region, followed by an abrupt jump at a specific gate-opening pressure in each case, along with broad hysteresis (Figure 30).

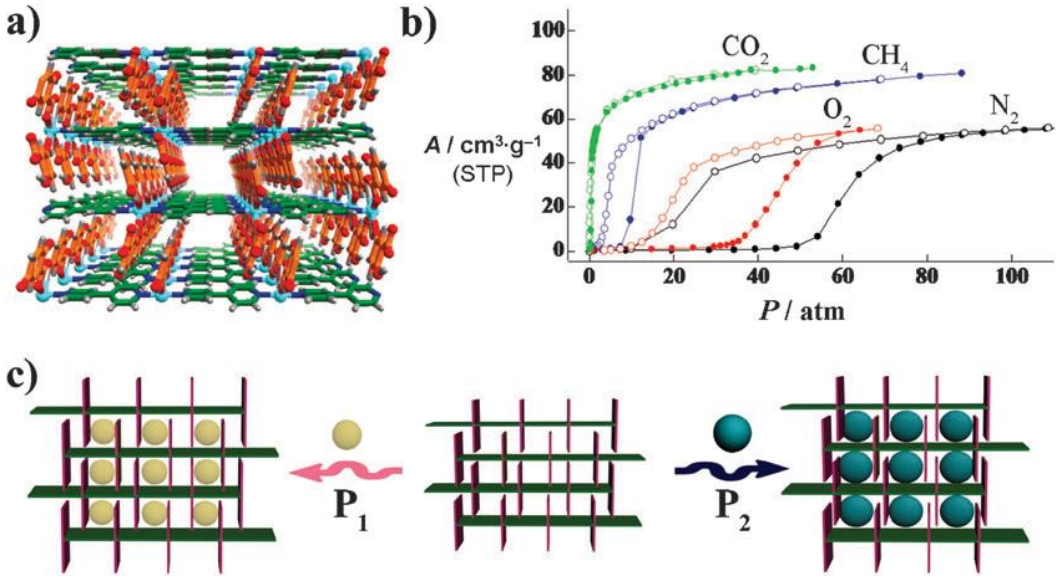

Figure 30. (a) 3D structure of [Cu(dhbc)$_2$(4,4′-bpy)]$_n$. (b) Gas sorption (filled circles) and desorption (open circles) isotherms at 298 K. (c) Schematic representation showing that gap open size depends on the guest molecules at specific pressures.[89]

1.4 Interpenetration

MOFs are rationally designed by keeping in mind their structure-property relationships. When MOFs are synthesised, they generate spacious voids, cavities and channels that are usually occupied by solvent molecules. In certain cases voids associated with one framework are sufficiently large to accommodate one or more independent networks, leading to interpenetration.[90] Interpenetration can be expressed as the polymeric analogue of catenanes and rotaxanes (Figure 31).[91]

Figure 31. Schematic representaion of catenanes (left) and rotaxanes (right).[91]

Interpenetration or catenation in MOFs is an intriguing phenomenon with effects on their structures, porosity and functional applications (Figure 32). It significantly enhances the stability of the frameworks by minimising large empty void spaces, thus preventing the structure from possible collapse in the absence of the solvent molecules. The use of elongated linkers in an attempt to synthesize MOFs with large pores often results in interpenetrated frameworks and this may be preferred to provide increased stability of the framework.[90] Besides providing stability to the structure, interpenetration also provides flexibility and guest selectivity. However, such frameworks have their own drawbacks such as reduced surface areas and void volumes.

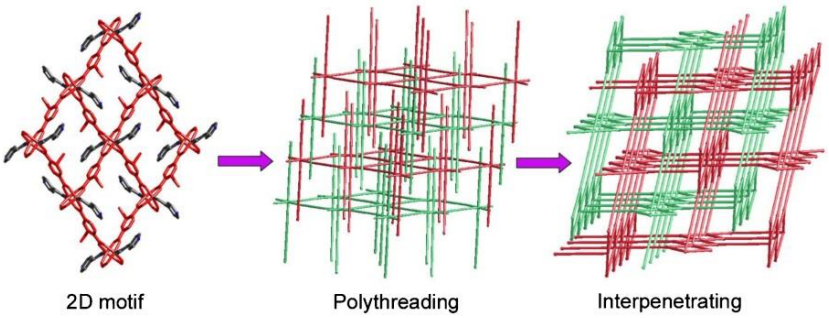

Figure 32. Schematic representation of interpenetration.[90]

The formation of interpenetrated frameworks is generally not anticipated but rather discovered serendipitously. The phenomenon is now well known in 1D, 2D and 3D structures. Since the scope of the current work is confined to 3D frameworks, 1D and 2D structures will be discussed in less detail.

1.4.1 Interpenetration Based on One Dimensional Chains

Interpenetration in one dimensional frameworks is quite uncommon. 1D chains containing rings and rods form interpenetrated structures similar to those of catenanes and rotaxanes. The entanglement of both parallel and inclined 1D chains leads to higher dimensional frameworks. A zinc complex $\{[Zn_2(bix)_3(SO_4)_2].8H_2O\}_n$, [bix = 1,4-bis(imidazole-1-ylmethyl)benzene], with 1D chains reported by Proserpio and co-workers was constructed by alternating rings and rods to form 2D sheets (Figure 33).[90,92]

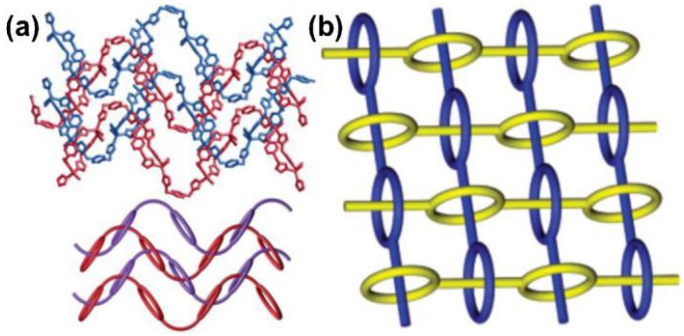

Figure 33. Parallel interlacing of the chains in $\{[Zn_2(bix)_3(SO_4)_2].8H_2O\}_n$ (top) and a schematic illustration of the chain entanglement (bottom). (b) Schematic view of two inclined polyrotaxane motifs involving a 1D infinite polymer that results in a 2D polythreaded layer.[90]

The same ligand was also used by Robson to form $\{[Ag_2(bix)_3](NO_3)_2\}$ in which inclined 1D chains are interpenetrated to give 2D square sheets.[93] Besides these, various complicated interpenetrated structures based on 1D chains or sheets have been reported to produce 3D networks.[94-97] Most of these networks are formed through 2-fold inclined catenation with each square entangled by the other two ladders. Based on same idea, Fujita *et al.* reported a Cd based coordination polymer in which 1D ladder-like chains are interpenetrated to give a 3D network (Figure 34).[91,98]

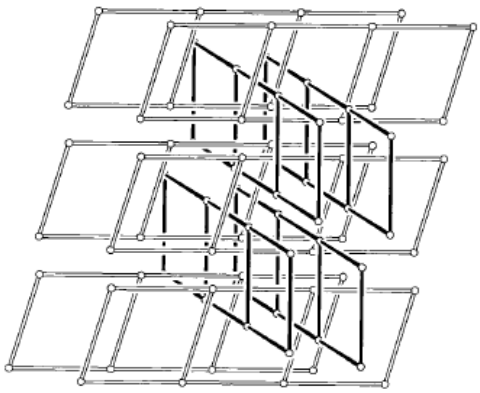

Figure 34. Interpenetrating ladder like chains in Cd based coordination polymer.[91]

1.4.2 Interpenetration Based on Two Dimensional Layers

The interpenetration between two layers, like 1D chains, can be divided into two types: parallel[99] and inclined (Figure 35).[91,100] Parallel interpenetration gives rise to either 2D layered structures or 3D structures, whereas inclined interpenetration always leads to 3D frameworks. For parallel interpenetration, the individual 2D networks must be corrugated or possess some element of undulation. For inclined interpenetration, one stack of sheets is often inclined perpendicular to the other.

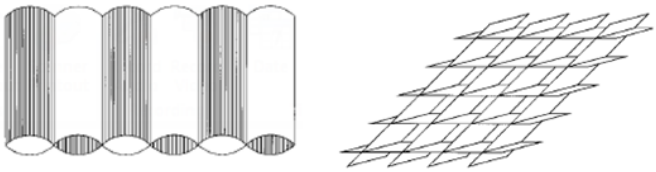

Figure 35. Parallel (left) and inclined (right) interpenetration of sheets.[91]

A layered MOF, $[Cu(hfipbb)(H_2O)]_n$ (H_2hfipbb = 4,4′-(hexa-fluoroisopropylidene)bis(benzoic acid) reported by Xu and co-workers shows 2-fold parallel interpenetration of 2D layers.[101] The structure has each Cu(II) paddle-wheel SBU connected to four neighbouring SBUs by bent hfipbb ligands (Figure 36a). Another framework assembled by two long V-shaped ligands of 1,3-bis(4-carboxy-phenoxy)propane and 1,3-bis(4-pyridyl)propane to provide 3-fold parallel interpenetration provides 2D to 3D motifs (Figure 36b).[90,102] The layered structure of $\{[Cu(bpp)_2Cl]Cl\cdot 1.5H_2O\}_n$ reported by Rizzato consists of five-coordinated copper ions in a square-pyramidal geometry. The three similar but crystallographically independent sets of layers (shown in red, green and blue in Figure. 36c), presents inclined interpenetration to give an overall 3D architecture.[103]

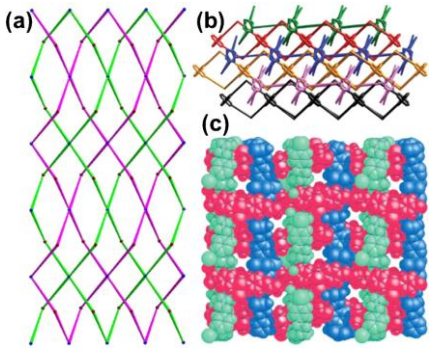

Figure 36. (a) Schematic representation of the 2-fold parallel interpenetration between 2D layered structures. (b) Side-on view of the 3-fold parallel interpenetration from 2D to 3D. (c) 3D array fabricated by interpenetration of the three sets of layers with different colours.[90]

1.4.3 Interpenetration in Three Dimensional MOFs

The construction of MOFs with long linkers generally results in large voids, which makes them unstable. This leads to interpenetration, which reduces the pore size and at the same time provides stability to the framework. Interpenetration in 3D MOFs is quite common as compared to 1D and 2D MOFs. Different degrees of interpenetration such as **2-fold**,[104] **3-fold**,[105] **4-fold**,[106] **5-fold**,[107] **6-fold**,[108] **7-fold**,[109] **8-fold**,[110] **10-fold**,[111] and even **54-fold**[112] have been reported to date (Figure 37).

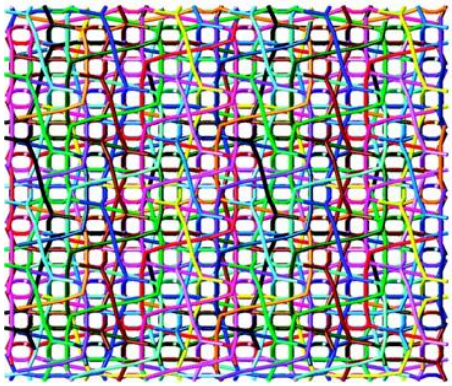

Figure 37. Fifty-four fold interpenetrated structure.[112]

The doubly interpenetrated structure of the well-known **MOF-5** was recently reported by Kimoon Kim and co-workers.[113] The phase pure interpenetrated **MOF-5** was prepared by carefully controlling the pH of the reaction medium between 4.0 and 4.5. Compared to **MOF-5**, this framework shows higher stability towards heat and moisture. Due to interpenetration the surface area is much smaller than that of **MOF-5**, but it exhibits higher hydrogen uptake capacity than **MOF-5** at 77 K and 1 atm pressure (Figure 38).[113]

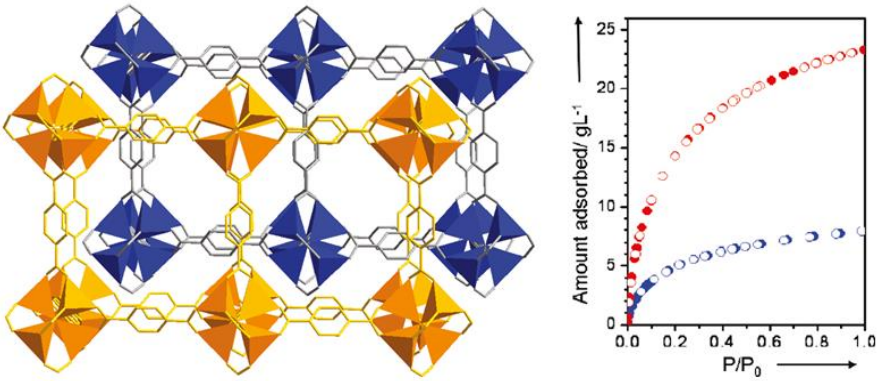

Figure 38. Structure of interpenetrated **MOF-5** (left) and hydrogen sorption isotherm of MOF-5 (blue) and interpenetrated **MOF-5** (red) at 77 K (right).[113]

An unusual but interesting case of interpenetration was reported by Schröder *et al.* who managed to synthesise a partially interpenetrated MOF for selective sorption of carbon dioxide.[114] The partially interpenetrated structure **NOTT-202** consists of a dominant net A and a secondary net B in the ratio 1:0.75, affording the overall complex $\{(Me_2NH_2)_{1.75}[In(L)]_{1.75}(DMF)_{12}(H_2O)_{10}\}_n$, [L = biphenyl-3,3′,5,5′-tetra-(phenyl-4-carboxylic acid)]. The CO_2 sorption isotherm of **NOTT-202** exhibits three distinct steps at P/P_0 = 0.07, 0.52 and 0.95 with uptake capacities of ~7, 14 and 20 mmol g^{-1}, respectively (Figure 39).

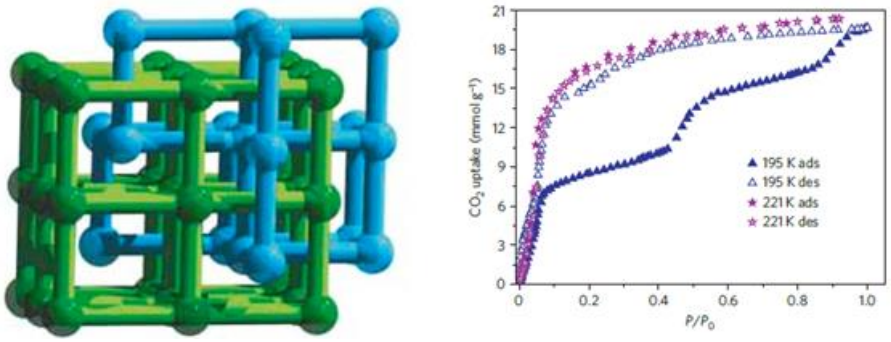

Figure 39. Partially interpenetrated **NOT-202** (left) and CO_2 sorption isotherm at 195 K (right).[114]

The degree of interpenetration can be varied by changing temperature, concentration, nature of the solvent or the length of the organic linkers. Generally, a bulkier solvent results in a lower level of interpenetration whereas a longer linker results in higher degree of entanglement. Hong and co-workers recently investigated the effect of solvent on the degree of interpenetration. They prepared three Zn(II) frameworks $[Zn(H_2L)(bdc)]\cdot 1.4DEF\cdot 0.6H_2O$ (**1**) H_2L = 1,4-di(1H-imidazol-4-yl)benzene, H_2bdc = terephthalic acid), $[Zn(H_2L)(bdc)]\cdot 1.5DMF\cdot 1.2H_2O$ (**2**), and $[Zn(H_2L)(L)0.5(bdc)0.5]\cdot formamide\cdot H_2O$ (**3**) under solvothermal conditions in DEF/H_2O, DMF/H_2O, and formamide/H_2O, respectively (Figure 40).[115]

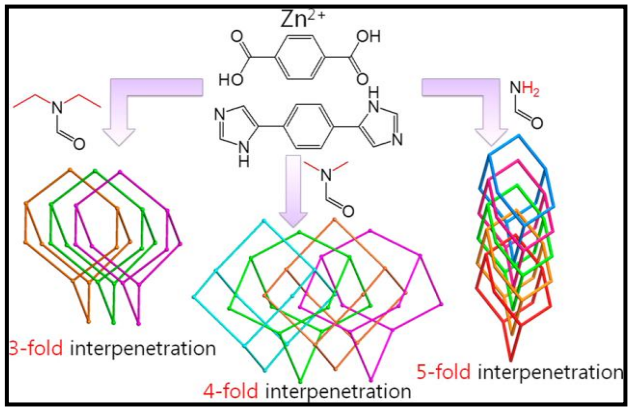

Figure 40. Schematic representation for the synthesis of frameworks **1**, **2** and **3**.[115]

All frameworks are based on admantanoid three dimensional networks. The reaction time, temperature and reactant ratio were the same for all the three compounds. The bulkier solvent DEF resulted in a 3-fold interpenetrated structure whereas the smallest solvent, formamide, resulted in 5-fold interpenetrated structure.

Kim and co-workers systematically modulated organic linkers connecting Zn-based paddle-wheel motifs to generate a series of three dimensional isomorphous MOFs having different degrees of interpenetration.[116] Aromatic dicarboxylates such as 1,4-benzenedicarboxylate (1,4-bdc), tetramethylterephthalate (tmbdc), 1,4-naphthalenedicarboxylate (1,4-ndc), tetrafluoroterephthalate (tfbdc), or 2,6-naphthalenedicarboxylate (2,6-ndc) are linear linkers used to form two-dimensional layers with Zn^{2+} ions and the diamine ligands, 4-diazabicyclo[2.2.2]octane (dabco) or 4,4′-dipyridyl (bpy) act as vertical pillars (Figure 41). It was found that the shorter linker such as 1,4-bdc and substituted bdc linkers form non-interpenetrated structures with dabco (**1-5**) whereas the with bpy and 1,4-bdc form doubly interpenetrated framework (**6**). When ndc was used in place of bdc, the resulting structure was threefold interpenetrated (**7**).[116]

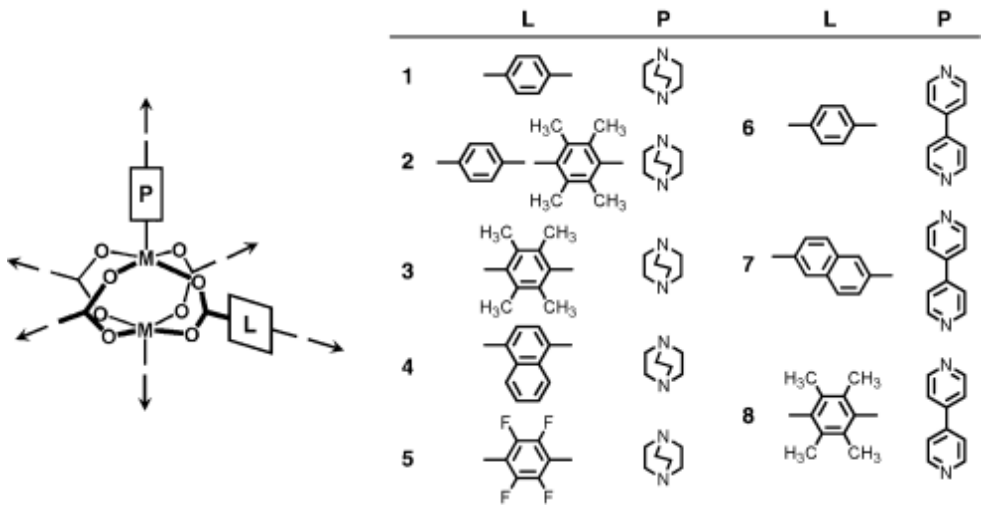

Figure 41. Linkers (L) and pillars (P) used to synthesise frameworks 1-8.[116]

1.5 Methods of Controlling Interpenetration

Interpenetrated frameworks can be quite useful for selective guest capture,[117] photoluminescence control,[118] and guest responsive porosity,[119] whereas non-interpenetrated frameworks are desirable for applications such as high pressure gas storage[120] and chemical catalysis.[121] Since interpenetration leads to decrease in surface area, various research groups proposed different ways of controlling interpenetration. These methods will be discussed one by one in detail.

1.5.1 Temperature and Concentration Control

Temperature and concentration are two important parameters of any chemical reaction, including the synthesis of MOFs. It has been observed that higher temperatures and concentrations often result in interpenetrated or denser structures, whereas lower temperatures and more dilute reaction mixtures lead to non-interpenetrated structures.[122,123] Zaworotko and co-workers investigated the effect of reaction temperature and concentration of reactants on the degree of interpenetration of a pillared layered Cd(II) based MOF. The previously reported twofold interpenetrated $[Cd(4,4'\text{-bpy})(bdc)]_n$[60] MOF was re-synthesised by solvothermal reaction of $Cd(NO_3)_2 \cdot 4H_2O$, 4,4′-bpy, and H_2bdc in a 1:1:1 molar ratio in DMF/DEF (2:1, v/v) at 85 °C which resulted in the non-interpenetrated $\{[Cd(4,4'\text{-bpy})(bdc)] \cdot 3DMF \cdot H_2O\}_n$ framework.[122] The temperature and concentration parameters were systematically altered and it was found that both of these factors affected the interpenetration as well as the phase purity of the product (Figure 42).

	0.2M	0.1M	0.05M	0.025M	0.0125 M	0.0062 5M
85°C	?	1	1	1	1	?
95°C	?	1	1	1	1	?
105°C	?	1+2	1+2	1	1	?
115°C	?	2	2	1+2	1	?
125°C	?	2	2	1+2	?	?

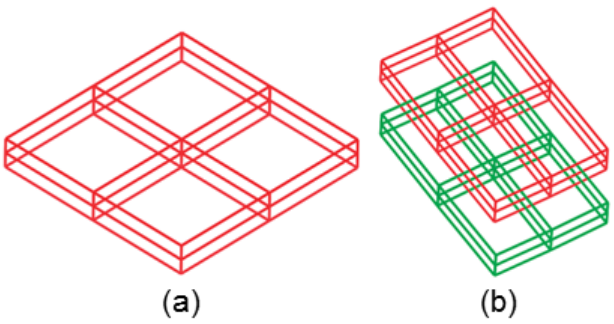

Figure 42. Table showing isolation of non-interpenetrated (**1**, a) and doubly interpenetrated (**2**, b) products at different temperatures and concentration.[122]

Based on the same approach, Xu and co-workers later reported nonporous, microporous, and mesoporous MOFs from the same starting materials.[123] The microporous MOF was prepared by interpenetration control from the same reactants by decreasing the reaction temperature and the micropores were further enlarged to mesopores by simply reducing reactant concentrations. The solvothermal reactions of the same amounts of $Cd(NO_3)_2 \cdot 4H_2O$, 4,4′-bipyridyl, and 2-amino-1,4-benzenedicarboxylic acid in DMF yielded $[Cd(abdc)(4,4'\text{-bpy})]_n$ (**3**), $\{[Cd(abdc)(4,4'\text{-bpy})] \cdot 4H_2O \cdot 2.5DMF\}_n$ (**4**), and $\{[Cd(abdc)(4,4'\text{-bpy})] \cdot 4.5H_2O \cdot 3DMF\}_n$ (**5**). These structures have the same framework formula but different guest solvents. Framework **3** is doubly interpenetrated whereas frameworks **4** and **5** are non-interpenetrated and highly porous (Figure 43).[90,123]

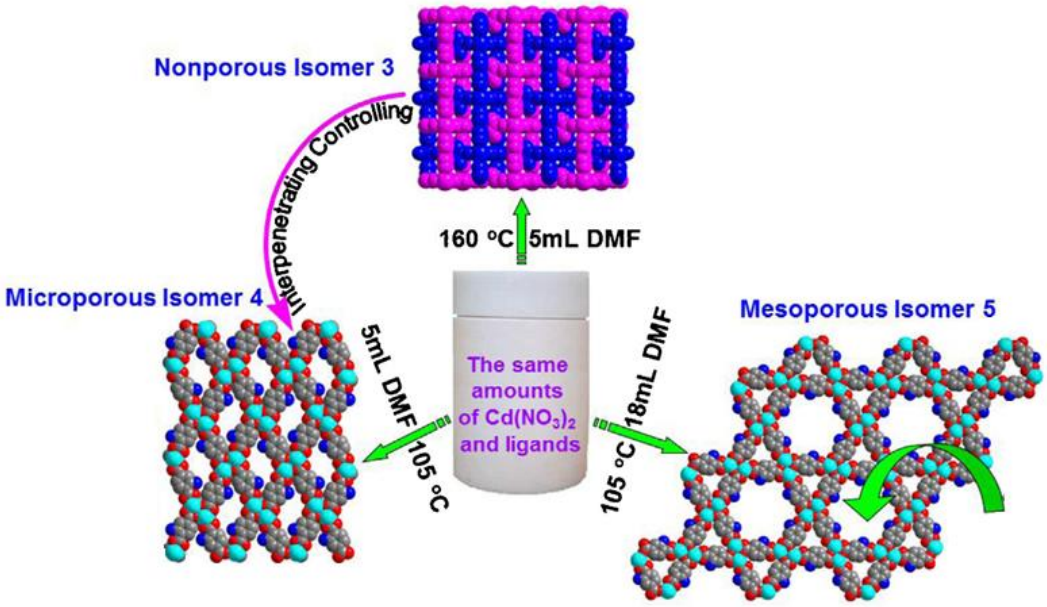

Figure 43. Schematic representation of non-, micro- and mesorporous $[Cd(abdc)(4,4'\text{-bpy})]_n$ frameworks.[90]

These studies clearly suggest that high temperature and concentration leads to interpenetrated frameworks while low temperature and concentration favours non-interpenetrated structures. It is reasonable to assume that due to the faster rate of crystallization at higher temperatures, more independent nets may self-assemble to give interpenetrated frameworks. Upon lowering the temperature, the rate of deprotonation of acid linkers and the process of nucleation slows down, which may decrease the possibility of ascending of multiple independent nets, at the same time resulting in non-interpenetrated structures. However, the exact reasons behind the formation of different degrees of catenated frameworks remain unknown.

1.5.2 Template Effects

Templates such as solvents and organic linkers have been extensively used for constructing porous MOFs.[90] When a template is used, it is expected that the MOF will grow around the surface of the template, thus preventing interpenetration of various independent nets. The utility of templates in controlling degree of interpenetration was first shown by Zhou and co-workers.[124] They first synthesised the interpenetrated structure of the well-known twofold interpenetrated MOF **PCN-6**, $[Cu_3(tatb)_2(H_2O)_3]_n$, (tatb = 4,4′,4″-s-triazine-2,4,6-triyltribenzoate), which consists of dicopper tetracarboxylate paddle-wheel SBUs with aqua ligands linked by tatb bridges in the equatorial plane. After that they introduced oxalate as a template to produce the non-interpenetrated isomer $\{[Cu_6(H_2O)_6(tatb)_4]\cdot DMA\cdot 12H_2O\}_n$ (**PCN-6′**) (Figure 44).[90,124] Also, **PCN-6′** has a higher solvent-accessible volume (86%) than **PCN-6** (74%). The hydrogen uptake was studied for both isomers and **PCN-6** was found to take up more H_2 than **PCN-6′** due to smaller pore size.

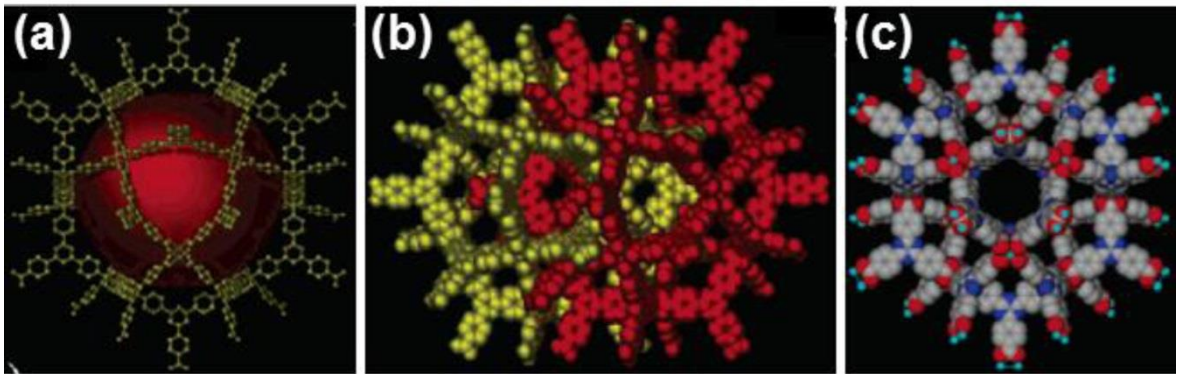

Figure 44. (a) Cuboctahedral cage with the inner void highlighted with a large red sphere. (b) Space-filling model of **PCN-6** and (c) **PCN-6′**.[90]

Kitagawa *et al.* used solvent molecules as templates to control the level of interpenetration in a Zn-based porous coordination polymer.[125] A reaction between $Zn(NO_3)_2\cdot 6H_2O$, 2,2′-bithiophene-5,5′-dicarboxylic acid (H_2btdc) and 4,4′-bpy with DMF yielded a 3-fold interpenetrated structure, whereas the same mixture in the presence of mixed DMF/benzene (1:1) formed a 2-fold interpenetrated structure (Figure 45a). The larger benzene played a templating role by preventing denser packing of the frameworks. Benzene was then replaced by other solvents such as toluene and cyclohexane and the resulting structure was still doubly interpenetrated. This confirmed the role of solvent molecules as templates in controlling the degree of interpenetration. Both of these MOFs were further

studied for their gas sorption properties. The CO_2 sorption isotherm of the 3-fold version indicated that it is a rigid structure whereas the 2-fold interpenetrated structure shows dynamic features (Figures 45b and c).[90,125]

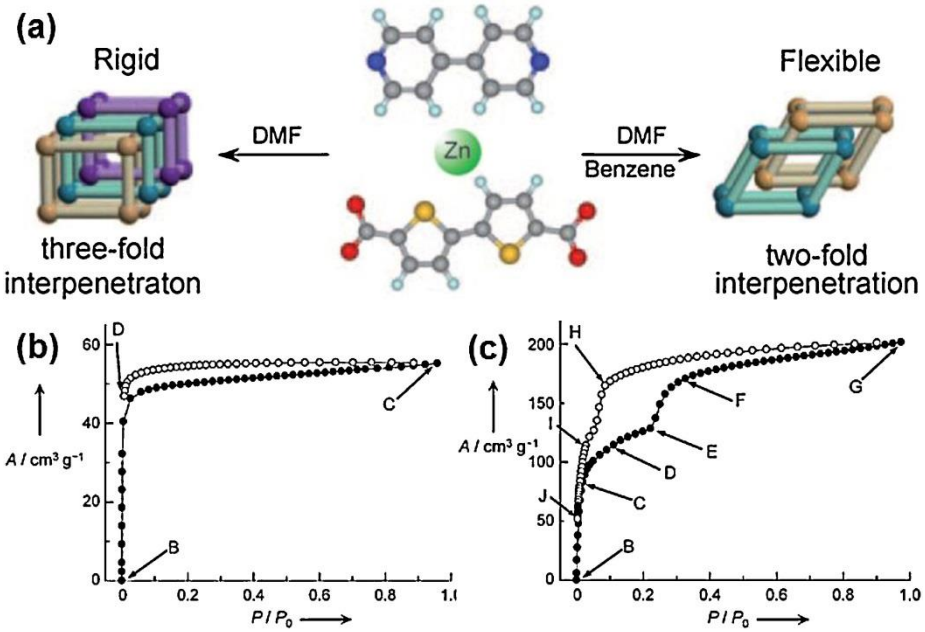

Figure 45. (a) Control of degree of interpenetration using solvent as a template, (b) CO_2 sorption for the 3-fold at 195 K and (c) CO_2 sorption of 2-fold at 195 K.[90]

Guo and Sun have reported two 3D Zn-based MOFs using a similar approach. Both of the MOFs have the the same framework formula $[Zn_3(L_1)(L_2)]_n$ [L_1 = 4-[3-(4-carboxyphenoxy)-2-[(4-carboxyphenoxy)methyl]-2-methyl-propoxy]benzoate, L_2 = 1,4-bis(1-imidazolyl)benzene] under same reaction conditions. 2-fold and 3-fold interpenetrated structures were formed in the presence of DMF and acetonitrile, respectively.[126]

Interpenetration modulation has also been investigated by Su *et al.* by using a long rigid ligand, 2,5-bis(4′-(imidazol-1-yl)benzyl)-3,4-diaza-2,4-hexadiene (ImBNN), and $M(CF_3SO_3)_2$ (M = Cd or Mn) in the absence or presence of aromatic molecules.[127] In the absence of aromatic guest molecules, 3-fold interpenetrated networks were formed with closely packed layered structures while in the presence of aromatic guest molecules such as *o*-xylene, naphthalene, phenanthrene, benzene, *p*-xylene and pyrene the resultant structure had 2-fold interpenetrated networks with inclusion of the aromatic molecules. Similarly, Lin and co-workers have made extensive use of solvent as templates to control degree of interpenetration in various MOFs.[128]

1.5.3 Ligand Design/Modification

The design of new bulkier ligands and the modification of the ligands with pendant groups has been an effective method of controlling interpenetration.[90] Generally, a secondary functional group or a side chain is introduced on the linker to block the spacious voids of the framework, thus not permitting the structure to accommodate another net passing through it. A remarkable example of suppressing interpenetration by simple ligand design has been reported by Hupp's group who prepared a series of interpenetrated and non-interpenetrated isomers (Figure 46).[90,129]

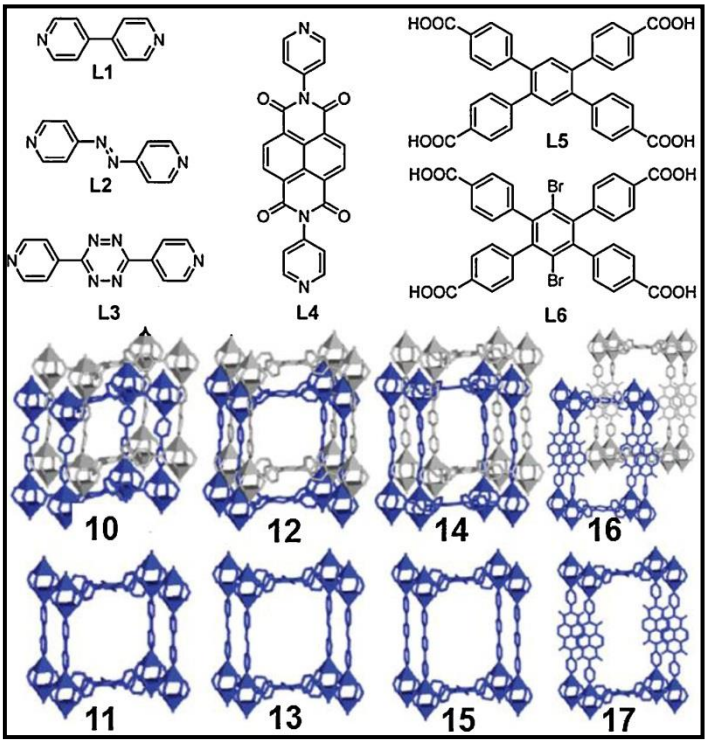

Figure 46. (Top) Organic linkers involved in the syntheses of MOFs. (Bottom) 2-fold interpenetrated structures (**10**, **12**, **14,** and **16**) with building block H_4**L5** and non-interpenetrated structures (**11**, **13**, **15**, and **17**) with building block H_4**L6**.[90]

The various pillared-layer frameworks comprise a combination of **L5** or **L6** acid linkers with different dipyridyl pillars such as **L1**, **L2**, **L3** and **L4**. Interestingly, all MOFs formed by **L5** are interpenetrated whereas those formed by **L6** are non-interpenetrated under identical reaction conditions. Interpenetration has been avoided by simple modification of **L5** from aryl-H to aryl-Br where Br groups act as steric blocks in the *xy* plane. This approach was further extended to produce two more Zn-based MOFs with standard biphenyl dicarboxylate linkers with one or two pendant azolinium moieties.[130]

Recently, Suh and co-workers presented another interesting example of controlling interpenetration by simply controlling the presence of carbon-carbon single or double bonds in an otherwise identical organic building block.[131] Non-interpenetrated (**SNU-70**) and doubly interpenetrated (**SNU-71**) frameworks were prepared by the solvothermal reaction of $[Zn(NO_3)_2]\cdot 6H_2O$ in *N*,*N*′-diethylformamide (DEF) with 4-(2-carboxyvinyl)-benzoic acid and 4-(2-carboxyethyl)-benzoic acid, respectively (Figure 47).[90,131] The non-interpenetrated structure has a much larger pore size than does the interpenetrated framework.

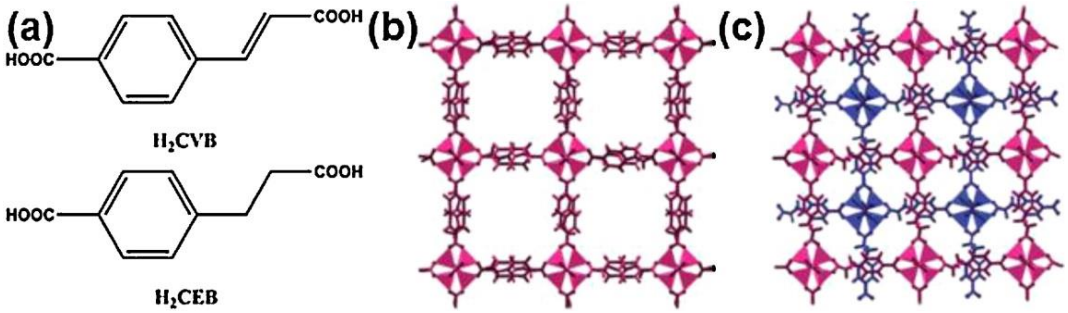

Figure 47. (a) Ligands used for the MOF synthesis and crystal structures of (b) non-interpenetrated and (c) 2-fold interpenetrated MOFs.[90]

The introduction of a functional group such as the amino moiety is another convenient way of controlling catenation. Xue *et al.* introduced an amino group on bdc to generate porous doubly pillared-layer framework $\{[Co_2(abdc)_2(bpy)_2]\cdot 8DMF\}_n$ with permanent porosity (Figure 48).[132] These results have further shown that introduction of a bulky group on a linker is an effective way of controlling catenation. Besides these, there are various other reports on control of interpenetration by ligand modification.[133]

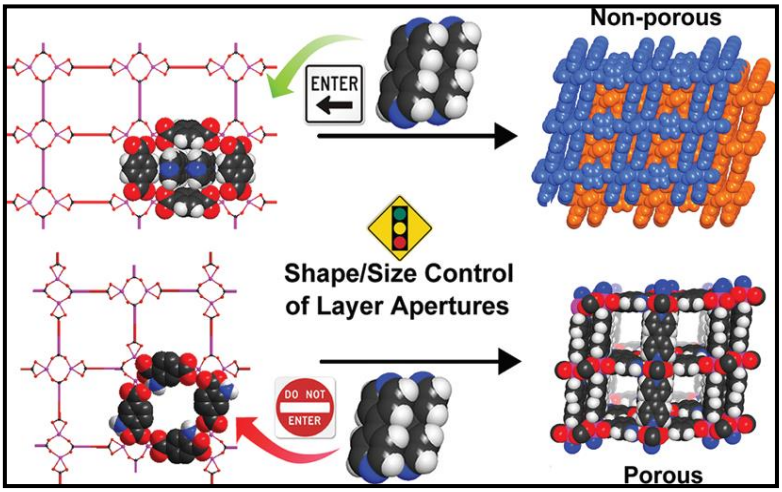

Figure 48. (top) Doubly interpenetrated and (bottom) non-interpenetrated MOFs produced by using benzenedicarboxylic acid and 2-amino-1,4-benzene dicarboxylate as respective linkers.[132]

1.5.4 Liquid Epitaxy

Interpenetration can also be suppressed by using liquid-phase epitaxy on an organic monolayer followed by layer-by-layer growth. This method demonstrates the potential of step-by-step synthesis of new MOFs that cannot be synthesised by conventional solvothermal methods. Wöll and co-workers used liquid epitaxy to synthesise the non-interpenetrated structure[134] of **MOF-508**, $[Zn(bdc)\text{-}(4,4'\text{-bipy})_{0.5}]_n$, which otherwise forms a 2-fold interpenetrated structure[135] by solvothermal synthesis (Figure 49).[90,134]

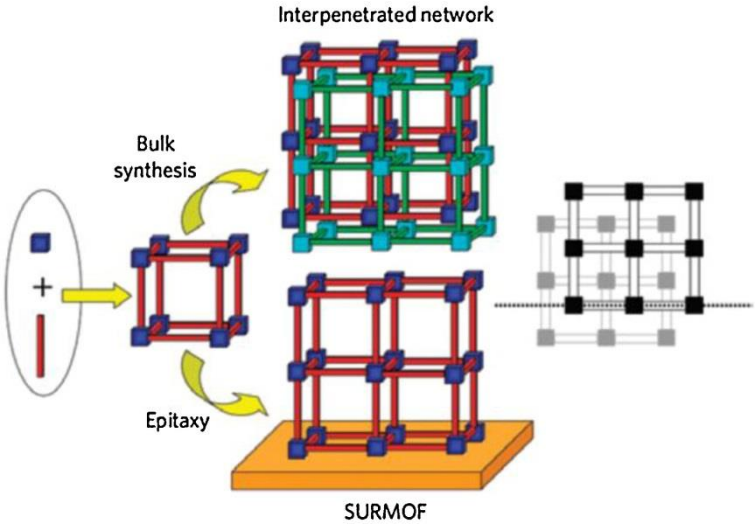

Figure 49. Schematic representation of (top) identical interpenetrated networks (coloured red and green) usually formed by conventional synthesis, while (bottom) using liquid phase epitaxy the equivalence of these two networks is lifted by the presence of the substrate (dotted line in the schematic diagram on the right) and the formation of interpenetrated networks is suppressed generating SURMOFs with only one net.[90]

To prepare this MOF, separate ethanolic solutions of zinc acetate and the mixture of the organic ligands (H_2bdc and 4,4′-bipy) were kept in two different beakers and an appropriately functionalized organic surface was immersed alternately in the two different solutions with intermittent rinsing. The organic surface was prepared by fabricating a self-assembled monolayer (SAM) from 4,4-pyridyl-benzenemethanethiol (PBMT) on an Au substrate. The surface of this SAM mimics the upper rim of a layer of 4,4′-bipyridine `poles' in the **MOF-508a** structure and thus permits the epitaxial growth of this material. Also, an interpenetrating network in the surface mounted MOF (SURMOF) cannot match the pyridine-terminated organic surface that acts as a nucleation template, therefore the second lattice cannot nucleate at the surface and the interpenetration can be successfully suppressed.

1.6 Single-Crystal to Single-Crystal Transformations

One of the most important properties of some MOFs is the flexibility provided by organic linkers and metal ions/clusters. The *flexible/dynamic* nature of these frameworks is crucial for selective sorption and sensor devices. It also allows the framework to undergo extreme structural transformations without any significant loss of crystal singularity also known as a single-crystal to single-crystal transformation,[136] upon exposure to solvents,[137] gases,[138] and elevated temperatures.[139] The understanding of structure-property relationships is very important in order to rationalise the various factors involved during these transformations and to design new materials with tailor-made properties. Though there are various spectroscopic techniques to study the various aspects of single-crystal transformations,[140] crystallography is still the most expedient and effective method for direct visualisation of changes at the molecular level.

Amongst the various types of single-crystal transformations recorded in the case of MOFs, structural rearrangements due to guest solvent molecules is the most common type. Such changes can occur either due to removal of lattice solvent molecules (by heating) or due to exchange of solvent molecules with a different guest. Kitagawa *et al.* recently reported an interesting example of reversible metal-ligand bond breaking/formation upon removal and restoration of lattice solvent molecules.[141] When the as-synthesised crystals of $\{[Zn_2(bdc)_2(bpb)]\cdot 2.5DMF\cdot 0.5H_2O\}_n$ (bpb = 2,3-difluoro-1,4-bis(4-pyridyl)benzene) were heated at 115 °C under dynamic vacuum to give guest-free $[Zn_2(bdc)_2(bpb)]$, the coordination environment of Zn(II) centers changed from square pyramidal to tetrahedral (Figure 50). Besides that, one of the two carboxylate groups changed from bidentate to monodentate with the Zn–O distances being changed from 2.043 to 5.164 Å.

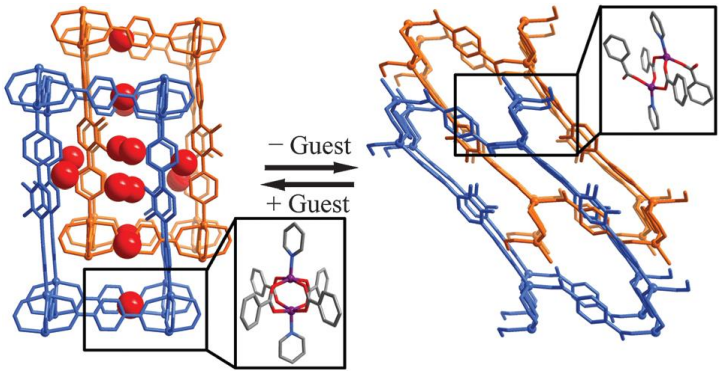

Figure 50. Interconversion between $\{[Zn_2(bdc)_2(bpb)]\cdot 2.5DMF\cdot 0.5H_2O\}_n$ and $[Zn_2(bdc)_2(bpb)]_n$ induced by removal and restoration of the lattice solvent molecules.[136b]

Another interesting example of a structural change upon removal of guest molecules has been reported by Du *et al.* who showed that the removal of lattice solvent molecules by different methods can lead to completely different types of single-crystal transformations.[142] The as-synthesised 3D PCP $\{[Cu(iba)_2]\cdot 2H_2O\}_n$ (Hiba = 4-(1H-imidazol-1-yl)benzoic acid) with a 3-fold interpenetrated structure can be dehydrated to form two isomeric guest-free phases $[Cu(iba)_2]_n$, either with the original topology or transforming to a different network. The structure with the same topology results by heating at 160 °C for 12 h, while exposing the as-synthesised crystal in air at room temperature for about two months resulted in a different topology (Figure 51).

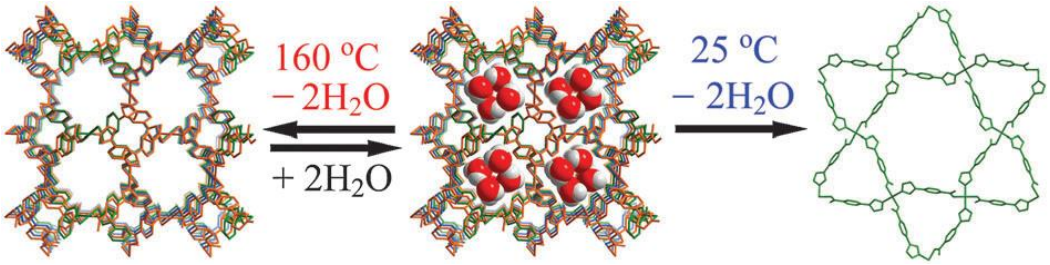

Figure 51. Conversion of 3D $\{[Cu(iba)_2]\cdot 2H_2O\}_n$ to $[Cu(iba)_2]_n$ isomers either with the original lvt topology (left) or a 2D *kgm* topology (right).[142]

The inclusion of large guest molecules in a porous coordination polymer has been well documented by Fujita and co-workers.[143] With the help of X-ray crystallography they have monitored the SCSC guest exchange of triphenylene in the 3D coordination network $[(ZnI_2)_3(\mathbf{1})_2]_n$, where **1** is 2,4,6-tris(4-pyridyl)triazine. The 3D network forms a nitrobenzene clathrate, $\{[(ZnI_2)_3(\mathbf{1})2]\cdot 5.5(\text{nitrobenzene})\}_n$, whose crystals are immersed in cyclohexane solution of triphenylene (**3a**) to give $\{[(ZnI_2)_3(\mathbf{1})_2]\cdot 1.5(\mathbf{3a})\cdot 2.5(\text{cyclohexane})\}_n$ at room temperature (Figure 52). Despite the inclusion of large guest, the 3D net remains unchanged.

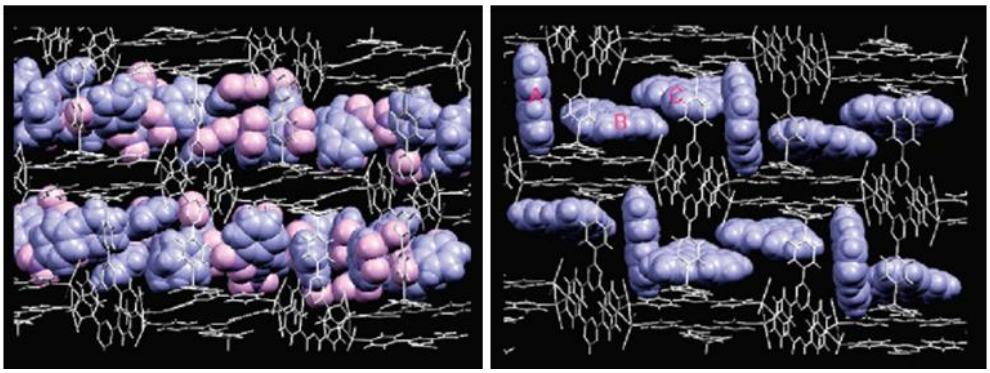

Figure 52. Crystal structures of 3D network accommodating nitrobenzene molecules (left) and triphenylene molecules (right).[143]

The removal/addition or exchange of coordinated solvent molecules may also give rise to interesting structural changes. Generally, such a change leads to complete rearrangement of framework connectivity. In a recent example, Kim *et al.* showed that removal/addition of coordinated solvent molecules can change the degree of interpenetration of a porous coordination polymer (PCP).[144] A 3D PCP $[Zn_7O_2(nbd)_5(DMF)_2]_n$ (**MOF-123**; H_2nbd = 2-nitrobenzene-1,4-dicarboxylic acid) with a non-interpenetrated structure, when heated at 300 °C, loses the coordinated DMF resulting in a nonporous crystal $[Zn_7O_2(nbd)_5]_n$ (**MOF-246**) with a 2-fold interpenetrated structure (Figure 53). The coordination environment around the central Zn atom changes from 6-coordinate to 4-coordinate upon loss of the DMF molecules.

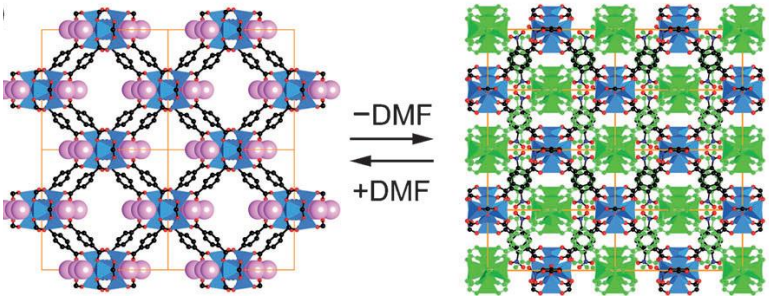

Figure 53. Change from non- to doubly-interpenetrated structure on loss of coordinated DMF.[136b]

Besides removal of coordinated solvent, the structure of a MOF can also change upon exchange of coordinated solvent. Lin *et al.* reported a 2D PCP $\{[Zn_2(mtc)(DMF)_4]\cdot 2DMF\cdot 4H_2O\}_n$ (H_4mtc = methanetetra(biphenyl-p-carboxylic acid)) with 4-fold interpenetrated hinged-layer structure and a BET surface area of 177 $m^2\ g^{-1}$.[145] Soaking the as-synthesized crystal in CH_2Cl_2 at room temperature for 8 h yielded a 4-fold interpenetrated 3D structure $\{[Zn_2(mtc)(H_2O)_2]\cdot G\}_n$ (G = uncertain guest molecules) with large BET surface area of 1170 $m^2\ g^{-1}$ (Figure 54).[136b,145]

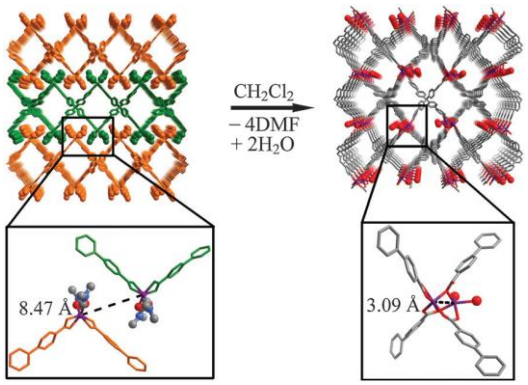

Figure 54. Conversion of 2D $[Zn_2(mtc)(DMF)_4]\cdot 2DMF\cdot 4H_2O$ to 3D $[Zn_2(mtc)(H_2O)_2]\cdot G$ in CH_2Cl_2 by replacement of coordinated DMF with H_2O molecules.[136b]

Gas-induced structural transformations are another important area of study in the case of PCPs. Such transformations are crucial for understanding adsorption mechanisms in detail. Since gas molecules are more energetic as compared to solvent molecules, it is more difficult to monitor gas-induced changes in a SCSC fashion. Takamizawa *et al.* have used SCXRD to study the sorption behaviours of different gases in flexible PCPs $[M^{II}{}_2(bza)_4\text{-}(Rpyz)]_n$ (M = Cu, Rh; Hbza = benzoic acid; Rpyz = pyrazine derivatives).[146-148] $[Rh_2(bza)_4(pyz)]_n$ consisting of 1D chains showed a two-step CO_2 sorption isotherm at 195 K. The guest-free structure with void volume 16.2% crystallised in the monoclinic system (*C*2/*c* < 90 K and *C*2/*m* > 298 K). The single-crystal data for the CO_2 loaded crystal at 90 K showed an increase of 4% in void volume along with the change of space group from *C*2/*c* to $P\bar{1}$ (Figure 55). Later they also observed the precise location of H_2 molecules in the same MOF.[149]

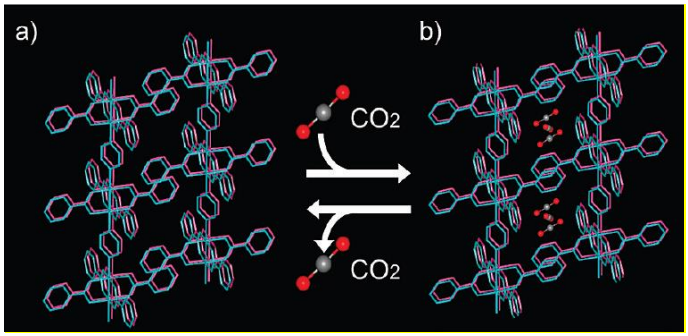

Figure 55. Schematic diagram of channel transformation by CO_2 adsorption.[147]

Recently Barbour *et al.* reported large anisotropic thermal expansion in the MOF, $[Zn(L)_2(OH)_2]_n{\cdot}nCH_3OH$ (L = 4-(1H-naphtho[2,3-d]imidazol-1-yl)benzoic acid, with 1D channels in the presence of different guests (MeOH, EtOH, n-PrOH, i-PrOH).[150] This study revealed the variation of thermal expansion coefficients with the change in size of the guest used (Figure 55).

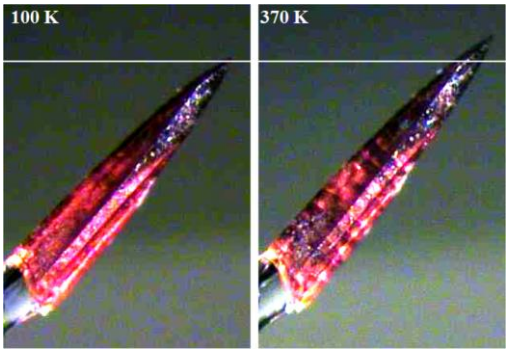

Figure 56. Photomicrographs of a crystal of $[Zn(L)_2(OH)_2]_n{\cdot}nCH_3OH$, recorded at 100 and 370 K.[150]

1.7 Objective of this Study

Owing to their wide applications, MOFs are considered an important class of porous materials. Thousands of MOFs have been synthesised to date and efforts are ongoing to design new MOFs with better sorption and storage properties. In order to synthesise highly porous frameworks researchers have often used long linkers, which commonly leads to interpenetration. Since interpenetration is often considered undesirable, various methods have been reported to control it. When a less interpenetrated/more porous form of a MOF is reported, it is often assumed that the structure will retain its identity upon activation. But there are various reports in the literature where researchers have lamented the loss of porosity in MOF structures upon activation/desolvation of solvent molecules from channels. The aim of this study is to revisit those systems and closely investigate the factors that lead to loss of porosity upon activation. All the structures described in the following chapters are three dimensional MOFs.

1.8 Thesis Outline

In order to extensively study the systems reported in this dissertation, various techniques such as single-crystal X-ray diffraction, powder X-ray diffraction, thermogravimetric analysis, differential scanning calorimetry, gas sorption, etc. have been used. **Chapter 2** of this thesis contains a detailed account of all such techniques as well as the instruments that have been used during the course of the present work.

Chapter 3 describes an already reported Zn-based doubly interpenetrated system which has been considered to lose porosity upon activation. It was assumed that the doubly interpenetrated structure collapses upon loss of lattice solvent molecules but in the present work it is clearly shown that the doubly interpenetrated structure converts to its triply interpenetrated form as a result of loss of solvent molecules from the channels. Further, to rule out any possibility of conversion from crystalline to amorphous phase, the transformation has been recorded in single-crystal to single-crystal fashion. A mechanism has also been proposed in order to explain this dramatic change.

In **chapter 4**, the work is extended to entirely different frameworks that are considered to be more robust. Both these Cd-based MOFs have been reported to form non- as well as doubly-interpenetrated structures. However, they have not been presumed to convert from one

form to the other under any circumstances. It has now been shown that, upon heating at elevated temperatures, both of these non-interpenetrated MOFs convert to their respective twofold interpenetrated structures, which are non-porous. Once again a plausible mechanism has been given for the transformations.

In **Chapter 5**, another doubly interpenetrated Co-based paddle-wheel framework, similar to the Zn framework reported in Chapter 3, is described. A more robust system was selected this time in order to isolate an intermediate phase that would help in understanding such transformations in detail. The Co framework has been reported to form both doubly- and triply-interpenetrated structures. The present work shows that this MOF also changes from its doubly- to triply-interpenetrated form upon loss of solvent molecules from the channels. Besides that, a structural intermediate (empty twofold interpenetrated structure) has been successfully isolated for the first time for such a change.

This dissertation highlights the importance of studying structure-property relationships in MOFs. Although synthesising new MOFs for gas sorption is no doubt an important aspect of MOF research, studying the already reported systems in greater detail is equally important. The present work also draws our attention towards the fact that a less interpenetrated structure may not retain its identity upon activation, therefore synthesising less interpenetrated frameworks is not always a guarantee of obtaining permanently porous systems. Since as-synthesized MOFs often lose crystal singularity upon activation, many such changes go unnoticed. Finally, this study also highlights the fact that it is very critical to use proper activation conditions for gas sorption studies. Use of different activation conditions might lead to entirely different products and thus result in incorrect interpretation of sorption results.

1.9 References

1. http://www.bza.org/zeolites.html accessed on 15-05-2015.
2. K. S. W. Sing, D. H. Everett, R. A. W. Haul, L. Moscou, R. A. Pierotti, J. Rouquerol, T. Siemieniewska, *Pure Appl. Chem.* **1985**, *57*, 603.
3. J. Rouquerol, D. Avnir, C. W. Fairbridge, D. H. Everett, J. H. Haynes, N. Pernicone, J. D. F. Ramsay, K. S. W. Sing, K. K. Unger, *Pure Appl. Chem.* **1994**, *66*, 1739.
4. D. W. Breck, *Zeolite Molecular Sieves: Structure, Chemistry, and Use*, Wiley, New York, **1974**.
5. Z. Alothman, *Materials* **2012**, *5*, 2874.
6. W. M. Meier, D. H. Olsen, C. Baerlocher, *Atlas of Zeolite Structure Types*, Elsevier, London, **1996**.
7. P. B. Venuto, *Microporous Mater*. **1994**, *2*, 297.
8. H. de St Claire Deville, *Compt. Rend. Séances Acad. Sci*. **1862**, *54*, 324.
9. S. Sircar, T. C. Golden, M. B. Rao, *Carbon* **1996**, *34*, 1.
10. H. Furukawa, K. E. Cordova, M. O'Keeffe, O. M. Yaghi, *Science* **2013**, *341*, 6149.
11. J. L. C. Rowsell, O. M. Yaghi, *Microporous Mesoporous Mater*. **2004**, *73*, 3.
12. (a) S. Kitagawa, R. Kitaura, S.-I. Noro, *Angew. Chem. Int. Ed.* **2004**, *43*, 2334; (b) S. Kitagawa, R. Matsuda, *Coord. Chem. Rev.* **2007**, *251*, 2490.
13. B. F. Hoskins, R. Robson, *J. Am. Chem. Soc*. **1990**, *112*, 1546.
14. M. Fujita, Y. J. Kwon, S.Washizu, K. Ogura, *J. Am. Chem. Soc*. **1994**, *116*, 1151.
15. O. M. Yaghi, G. Li, H. Li, *Nature* **1995**, *378*, 703.
16. D. Venkataraman, G. B. Gardner, S. Lee, J. S. Moore, *J. Am. Chem. Soc.* **1995**, *117*, 11600.
17. M. Kondo, T. Yoshitomi, K. Seki, H. Matsuzaka, S. Kitagawa, *Angew. Chem. Int. Ed. Engl.* **1997**, *36*, 1725.
18. H. Li, M. Eddaoudi, T. L. Groy, O. M. Yaghi, *J. Am. Chem. Soc.* **1998**, *120*, 8571.
19. H. Li, M. Eddaoudi, M. O'Keeffe, O. M. Yaghi, *Nature* **1999**, *402*, 276.
20. K. Byrappa, M. Yoshimura, *Handbook of Hydrothermal Chemistry*; William Andrew Publishing, New York.
21. P. M. Foster, P. M. Thomas, A. K. Cheetham, *Chem. Mater*. **2002,** *14*, 17.
22. U. Mueller, M. Schubert, F. Teich, H. Puetter, K. Scheirle-Arndt, J. Pastre, *J. Mater. Chem.* **2006**, *16*, 626.

23. E. Biemmi, S. Christian, N. Stock, T. Bein, *Microporous Mesoporous Mater.* **2009**, *117*, 111.
24. (a) G. A. Tompsett, W. C. Conner, K. S. Yngvesson, *ChemPhysChem* **2006**, *7*, 296; (b) S. H. Jhung, J. W. Yoon, J.-S. Hwang, A. K. Cheetham, J.-S. Chang, *Chem. Mater.* **2005**, *17*, 4455.
25. M. Eddaoudi, J. Kim, N. L. Rosi, D. T. Vodak, J. Wachter, M. O'Keeffe, O. M. Yaghi, *Science* **2002**, *295*, 469.
26. J. J. Perry IV, J. A. Perman, M. J. Zaworotko, *Chem. Soc. Rev.* **2009**, *38*, 1400.
27. S. Kitagawa, R. Kitaura, S-i Noro, *Angew. Chem. Int. Ed.* **2004**, *43*, 2334.
28. B. Moulton, M. J. Zaworotko, *Chem. Rev.* **2001**, *101*, 1629.
29. W. L. Leong, J. J. Vittal, *Chem. Rev.* **2011**, *111*, 688.
30. M.-C. Brandys, R. J. Puddephatt, *J. Am. Chem. Soc.* **2001**, *123*, 4839.
31. L. Cunha-Silva, R. Ahmad, M. J. Hardie, *Aus. J. Chem.* **2006**, *59*, 40.
32. L. F. Szczepura, C. P. Galloway, Y. Zheng, P. Han, A. L. Rheingold, S. R. Wilson, T. B. Rauchfuss, *Angew. Chem. Int. Ed. Engl.* **1995**, *34*, 1890.
33. Y. Zheng, J.- R. Li, M. Du, R.-Q. Zou, X.-H. Bu, *Cryst. Growth Des.* **2005**, *5*, 215.
34. Y. Go, X. Wang, E. V. Anokhina, A. J. Jacobson, *Inorg. Chem.* **2004**, *43*, 5360.
35. R. K. Feller, A. K. Cheetham, *Dalton Trans.* **2008**, 2034.
36. S. Banfi, L. Carlucci, E. Caruso, G. Ciani, D. M. Proserpio, *J. Chem. Soc., Dalton Trans.* **2002**, 2714.
37. M. G. Amiri, G. Mahmoudi, A. Morsali, A. D. Hunter, M. Zeller, *CrystEngComm* **2007**, *9*, 686.
38. C.-B. Ma, C.-N. Chen, Q.-T. Liu, *CrystEngComm* **2005**, *7*, 650.
39. L. Carlucci, G. Ciani, A. Gramaccioli, D. M. Proserpio, S. Rizzato, *CrystEngComm* **2000**, *2*, 154.
40. A.-L. Cheng, N. Liu, Y.-F. Yue, Y.-W. Jiang, E.-Q. Gao, C.-H. Yan, M.-Y. He, *Chem. Commun.* **2007**, 407.
41. K. Biradha, C. Seward, M. J. Zaworotko, *Angew. Chem. Int. Ed*. **1999**, *38*, 492.
42. T. Ezuhara, K. Endo, Y. Aoyama, *J. Am. Chem. Soc.* **1999**, *121*, 3279.
43. C. A. Wheaton, R. J. Puddephatt, *Angew. Chem. Int. Ed*. **2007**, *46*, 4461.
44. X.-D. Chen, T. C. W. Mak, *Dalton Trans*. **2005**, 3646.
45. O. Mamula, A. V. Zelewsky, T. Bark, G. Bernardinelli, *Angew. Chem. Int. Ed*. **1999**, *38*, 2945.

46. B. D. Wagner, G. J. McManus, B. Moulton, M. J. Zaworotko, *Chem. Commun.* **2002**, 2176.
47. A. Y. Robin, K. M. Fromm, *Coord. Chem. Rev*. **2006**, *250*, 2127.
48. (a) S. Nishikiori, T. Iwamoto, *Inorg. Chem.* **1986**, *25*, 788; (b) S. Nishikiori, T. Iwamoto, *J. Inclusion Phenom.* **1984**, *2*, 341; (c) S. Nishikiori, T. Iwamoto, *Bull. Chem. Soc. Jpn.* **1983**, *56*, 3246.
49. M. J. Zaworotko, *Chem. Commun.* **2001**, 1.
50. N. G. Pschirer, D. M. Ciurtin, M. D. Smith Dr., U. H. F. Bunz, H.-C. zur Loye, *Angew. Chem. Int. Ed.* **2002**, *41*, 583.
51. Y.-R. Xie, H. Zhao, X.-S. Wang, Z.-R. Qu, R.-G. Xiong, X. Xue, Z. Xue, X.-Z. You, *Eur. J. Inorg. Chem.* **2003**, 3712.
52. K. Uemura, S. Kitagawa, K. Fukui, K. Saito, *J. Am. Chem. Soc.* **2004**, *126*, 3817.
53. Z. Spichal, M. Necas, J. Pinkas, J. Novosad, *Inorg. Chem*. **2004**, *43*, 2776.
54. X.-M. Ouyang, B.-L. Fei, T.-A. Okamura, H.-W. Bu, W.-Y. Sun, W.-X. Tang, N. Ueyama, *Eur. J. Inorg. Chem*. **2003**, 618.
55. Z. Spichal, M. Necas, J. Pinkas, *Inorg. Chem.* **2005**, *44*, 2074.
56. J. W. Ko, K. S. Min, M. P. Suh, *Inorg. Chem.* **2002**, *41*, 2151.
57. K.-T. Youm, S. Huh, Y. J. Park, S. Park, M.-G. Choi, M.-J. Jun, *Chem. Commun.* **2004**, 2384.
58. M. Eddaoudi, D. B. Moler, H. Li, B. Chen, T. M. Reineke, M. O'Keefe, O. M. Yaghi, *Acc. Chem. Res*. **2001,** *34*, 319.
59. W. Lu, Z. Wei, Z.-Y. Gu, T.-F. Liu, J. Park, J. Park, J. Tian, M. Zhang, Q. Zhang, T. Gentle III, M. Boscha, H.-C. Zhou, *Chem. Soc. Rev.* **2014**, *43*, 5561.
60. J. Tao, M.-L. Tong, X.-M. Chen, *J. Chem. Soc. Dalton Trans*. **2000**, 3669.
61. M.-H. Zeng, Q.-X. Wang, Y.-X. Tan, S. Hu, H.-X. Zhao, L.-S. Long, M. Kurmoo, *J. Am. Chem. Soc.* **2010**, *132*, 2561.
62. B. Li, H.-M. Wen, W. Zhou, B. Chen, *J. Phys. Chem. Lett.* **2014**, *5*, 3468.
63. N. L. Rosi, J. Eckert, M. Eddaoudi, D. T. Vodak, J. Kim, M. O'Keeffe, O. M. Yaghi, *Science* **2003**, *300*, 1127.
64. S.-I. Noro, S. Kitagawa, M. Kondo, K. Seki, *Angew. Chem. Int. Ed*. **2000**, *39*, 2081.
65. Y. He, B. Li, M. O'Keeffe, B. Chen, *Chem. Soc. Rev*. **2014**, *43*, 5618.
66. Y. Yan, X. Lin, S. Yang, A. J. Blake, A. Dailly, N. R. Champness, P. Hubberstey, M. Schröder, *Chem. Commun*. **2009**, 1025.

67. O. K. Farha, C. E. Wilmer, I. Eryazici, B. G. Hauser, P. A. Parilla, K. O'Neill, A. A. Sarjeant, S. T. Nguyen, R. Q. Snurr, J. T. Hupp, *J. Am. Chem. Soc.* **2012**, *134*, 9860.
68. H. Furukawa, N. Ko, Y. B. Go, N. Aratani, S. B. Choi, E. Choi, A. O. Yazaydin, R. Q. Snurr, M. O'Keeffe, J. Kim, O. M. Yaghi, *Science* **2010**, *329*, 424.
69. S. S. Y. Chui, S. M. F. Lo, J. P. H. Charmant, A. G. Orpen, I. D. Williams, *Science* **1999**, 283, 1148.
70. Y. Peng, V. Krungleviciute, I. Eryazici, J. T. Hupp, O. K. Farha, T. Yildirim, *J. Am. Chem. Soc.* **2013**, *135*, 11887.
71. S. Xiang, Y. He, Z. Zhang, H. Wu, W. Zhou, R. Krishna, B. Chen, *Nat. Commun*. **2012**, *3*, 954.
72. K. Sumida, D. L. Rogow, J. A. Mason, T. M. McDonald, E. D. Bloch, Z. R. Herm, T.-H. Bae, J. R. Long, *Chem. Rev*. **2012**, *112*, 724.
73. Z. Zhang, Z.-Z. Yao, S. Xiang, B. Chen, *Energy Environ. Sci*. **2014**, *7*, 2868.
74. Q. Lin, T. Wu, S.-T. Zheng, X. Bu, P. Feng, *J. Am. Chem. Soc.* **2012**, *134*, 784.
75. A. Ö. Yazaydın, R. Q. Snurr, T.-H. Park, K. Koh, J. Liu, M. D. LeVan, A. I. Benin, P. Jakubczak, M. Lanuza, D. B. Galloway, J. J. Low, R. R. Wills, *J. Am. Chem. Soc*. **2009**, *131*, 18198.
76. A. Demessence, D. M. D'Alessandro, M. L. Foo, J. R. Long, *J. Am. Chem. Soc.* **2009**, *131*, 8784.
77. N. T. T. Nguyen, H. Furukawa, F. Gándara, H. T. Nguyen, K. E. Cordova, O. M. Yaghi, *Angew. Chem. Int. Ed*. **2014**, *53*, 10645.
78. S. Kitagawa, M. Kondo, *Bull. Chem. Soc. Jpn*. **1998**, *71*, 1739.
79. B. Chen, S. Q. Ma, E. J. Hurtado, E. B. Lobkovsky and H.-C. Zhou, *Inorg. Chem.* **2007**, 46, 8490.
80. S. Q. Ma, X. S. Wang, E. S. Manis, C. D. Collier, H.-C. Zhou, *Inorg. Chem*. **2007**, *46*, 3432.
81. S. K. Ghosh, S. Bureekaew, S. Kitagawa, *Angew. Chem. Int. Ed*. **2008**, *47*, 3403.
82. T. K. Maji, K. Uemura, H. C. Chang, R. Matsuda, S. Kitagawa, *Angew. Chem. Int. Ed*. **2004**, *43*, 3269.
83. B. Chen, S. Q. Ma, F. Zapata, F. R. Fronczek, E. B. Lobkovsky, H.-C. Zhou, *Inorg. Chem.* **2007**, *46*, 1233.
84. C. Serre, F. Millange, C. Thouvenot, M. Noguès, G. Marsolier, D. Louër, G. Férey, *J. Am. Chem. Soc.* **2002**, 124, 13519.

85. S. Bourrelly, P. L. Llewellyn, C. Serre, F. Millange, T. Loiseau, G. Férey, *J. Am. Chem. Soc.* **2005**, *127*, 13519.
86. F. Salles, G. Maurin, C. Serre, P. L. Llewellyn, C. Knöfel, H. J. Choi, Y. Filinchuk, L. Oliviero, A. Vimont, J. R. Long, G. Férey, *J. Am. Chem. Soc.* **2010**, *132*, 13782.
87. P. L. Llewellyn, P. Horcajada, G. Maurin, T. Devic, N. Rosenbach, S. Bourrelly, C. Serre, D. Vincent, S. Loera-Serna, Y. Filinchuk, G. Férey, *J. Am. Chem. Soc.* **2009**, *131*, 13002.
88. H. Hayashi, A. P. Côté, H. Furukawa, M. O'Keeffe, O. M. Yaghi, *Nat. Mater.* **2007**, *6*, 501.
89. R. Kitaura, K. Seki, G. Akiyama, S. Kitagawa, *Angew. Chem. Int. Ed.* **2003**, *42*, 428.
90. H.-L. Jianga, T. A. Makal, H.-C. Zhou, *Coord. Chem. Rev.* **2013**, *257*, 2232.
91. S. R. Batten, R. Robson, *Angew. Chem. Int. Ed.* **1998**, *37*, 1460.
92. L. Carlucci, G. Ciani, D. M. Proserpio, *Cryst. Growth Des.* **2005**, *5*, 37.
93. B. F. Hoskins, R. Robson, D. A. Slizys, *J. Am. Chem. Soc.* **1997**, *119*, 2952.
94. L. Carlucci, G. Ciani, D. M. Proserpio, *Dalton Trans.* **1999**, 1799.
95. M. A. Withersby, A. J. Blake, N. R. Champness, P. A. Cooke, P. Hubberstey, M. Schröder, *J. Am. Chem. Soc.* **2000**, *122*, 4044;
96. C.-Y. Su, A. M. Goforth, M. D. Smith, H.-C. zur Loye, *Chem. Commun.* **2004**, 2158;
97. G.-P. Yang, J.-H. Zhou, Y.-Y. Wang, P. Liu, C.-C. Shi, A.-Y. Fu, Q.-Z. Shi, *CrystEngComm* **2011**, *13*, 33.
98. M. Fujita, Y. J. Kwon, O. Sasaki, K. Yamaguchi, K. Ogura, *J. Am.Chem. Soc.* **1995**, *117*, 7287.
99. Y.-Q. Lan, S.-L. Li, J.-S. Qin, D.-Y. Du, X.-L. Wang, Z.-M. Su, Q. Fu, *Inorg. Chem.* **2008**, *47*, 10600.
100. J. Yang, J.-F. Ma, S. R. Batten, Z.-M. Su, *Chem. Commun.* **2008**, 2233.
101. H.-L. Jiang, Q. Xu, *CrystEngComm* **2010**, *12*, 3815.
102. J.-Q. Liu, Y.-Y. Wang, P. Liu, Z. Dong, Q.-Z. Shi, S. R. Batten, *CrystEngComm* **2009**, *11*, 1207.
103. L. Carlucci, G. Ciani, M. Moret, D. M. Proserpio, S. Rizzato, *Chem. Mater.* **2002**, *14*, 12.
104. (a) B. Chen, S. Ma, F. Zapata, F. R. Fronczek, E. B. Lobkovsky, H.-C. Zhou, *Inorg. Chem.* **2007**, *46*, 1233; (c) K. L. Mulfort, O. K. Farha, C. D. Malliakas, M. G. Kanatzidis, J. T. Hupp, *Chem. Eur. J.* **2010**, *16*, 276.

105.(a) M. H. Mir, S. Kitagawa, J. J. Vittal, *Inorg. Chem.* **2008**, *47*, 7728; (b) F. Luo, J.-M. Zheng, S. R. Batten, *Chem. Commun.* **2007**, 3744; (c) M. Xue, S. Ma, Z. Jin, R. M. Schaffino, G.-S. Zhu, E. B. Lobkovsky, S.-L. Qiu, B. Chen, *Inorg. Chem.* **2008**, *47*, 6825.

106.(a) J. Yang, J.-F. Ma, S. R. Batten, S. W. Ng, Y.-Y. Liu, *CrystEngComm* **2011**, *13*, 5296. (b) Y. E. Cheon, M. P. Suh, *Chem. Eur. J.* **2008**, *14*, 3961.

107.(a) X.-L. Wang, C. Qin, E.-B. Wang, Y.-G. Li, Z.-M. Su, *Chem. Commun.* **2005**, 5450; (b) H.-J. Hao, D. Sun, F.-J. Liu, R.-B. Huang, L.-S. Zheng, *Cryst. Growth Des.* **2011**, *11*, 5475.

108.L.-H. Xie, M. P. Suh, *Chem. Eur. J.* **2011**, *17*, 13653.

109.M. K. Sharma, P. Lama, P. K. Bharadwaj, *Cryst. Growth Des.* **2011**, *11*, 1411.

110.(a) X.-S. Wang, H. Zhao, Z.-R. Qu, Q. Ye, J. Zhang, R.-G. Xiong, X.-Z. You, H.-K. Fun, *Inorg. Chem*. **2003**, *42*, 5786; (b) H. Kim, M. P. Suh, *Inorg. Chem.* **2005**, *44*, 810.

111.L.-L. Dang, J.-Q. Li, S.-J. Liu, M.-B. Luo, F. Luo, *Inorg. Chem. Commun*. **2014**, *45*, 30.

112.H. Wu, J. Yang, Z.-M. Su, S. R. Batten, J.-F. Ma, *J. Am. Chem. Soc*. **2011**, *133*, 11406.

113.H. Kim, S. Das, M. G. Kim, D. N. Dybtsev, Y. Kim, K. Kim, *Inorg. Chem.* **2011**, *50*, 3691.

114.S. Yang, X. Lin, W. Lewis, M. Suyetin, E. Bichoutskaia, J. E. Parker, C. C. Tang, D. R. Allan, P. J. Rizkallah, P. Hubberstey, N. R. Champness, K. M. Thomas, A. J. Blake, M. Schröder, *Nat. Mater.* **2012**, *11*, 710.

115.J. H. Park, W. R. Lee, Y. Kim, H. J. Lee, D. W. Ryu, W. J. Phang, C. S. Hong, *Cryst. Growth Des*. **2014**, *14*, 699.

116.H. Chun, D. N. Dybtsev, H. Kim, K. Kim, *Chem. Eur. J.* **2005**, *11*, 3521.

117.H. Kim, M. P. Suh, *Inorg. Chem.* **2005**, *44*, 810.

118.Y. Takashima, V. M. Martinez, S. Furukawa, M. Kondo, S. Shimomura, H. Uehara, M. Nakahama, K. Sugimoto, S. Kitagawa, *Nat. Commun.* **2011**, *2*, 168.

119.T. K. Maji, R. Matsuda, S. Kitagawa, *Nat. Mater.* **2007**, *6*, 142−148.

120.(a) O. K. Farha, O. Yazaydin, I. Eryazici, C. Malliakas, B. Hauser, M. G. Kanatzidis, S. T. Nguyen, R. Q. Snurr, J. T. Hupp, *Nat. Chem.* **2010**, *2*, 944; (b) H. Furukawa, N. Ko, Y. B. Go, N. Aratani, S. B. Choi, E. Choi, A. Ö. Yazaydin, R. Q. Snurr, M. O'Keeffe, J. Kim, O. M. Yaghi, *Science* **2010**, *329*, 424.

121.(a) J. Lee, O. K. Farha, J. Roberts, K. A. Scheidt, S. T. Nguyen, J. T. Hupp, Chem. Soc. Rev. **2009**, *38*, 1450; (b) L. Ma, C. Abney, W. Lin, *Chem. Soc. Rev.* **2009**, *38*, 1248.

122. J. Zhang, L. Wojtas, R. W. Larsen, M. Eddaoudi and M. J. Zaworotko, *J. Am. Chem. Soc.* **2009**, *131*, 17040.

123. H.-L. Jiang, Yo. Tatsu, Z.-H. Lu and Q. Xu, *J. Am. Chem. Soc.* **2010**, *132*, 5586.

124. (a) D. Sun, S. Ma, Y. Ke, D. J. Collins, H.-C. Zhou, *J. Am. Chem. Soc.* **2006**, *128*, 3896; (b) S. Ma, D. Sun, M. Ambrogio, J. A. Fillinger, S. Parkin, H.-C. Zhou, *J. Am. Chem. Soc.* **2007**, *129*, 1858; (c) S. Ma, J. Eckert, P. M. Forster, J. W. Yoon, Y. K. Hwang, J.-S. Chang, C. D. Collier, J. B. Parise, H.-C. Zhou, *J. Am. Chem. Soc.* **2008**, *130*, 15896.

125. S. Bureekaew, H. Sato, R. Matsuda, Y. Kubota, R. Hirose, J. Kim, K. Kato, M. Takata, S. Kitagawa, *Angew. Chem. Int. Ed.* **2010**, *49*, 7660.

126. M. Guo, Z.-M. Sun, *J. Mater. Chem.* **2012**, *22*, 15939.

127. Q. Wang, J. Zhang, C.-F. Zhuang, Y. Tang, C.-Y. Su, *Inorg. Chem.* **2009**, *48*,287.

128. (a) L. Ma, W. Lin, *J. Am. Chem. Soc.* **2008**, *130*, 13834; (b) F. Song, C. Wang, J. M. Falkowski, L. Ma, W. Lin, *J. Am. Chem. Soc.* **2010**, *132*, 15390;

129. O. K. Farha, C. D. Malliakas, M. G. Kanatzidis, J. T. Hupp, *J. Am. Chem. Soc.* **2010**, *132*, 950.

130. J. M. Roberts, O. K. Farha, A. A. Sarjeant, J. T. Hupp, K. A. Scheidt, *Cryst. Growth Des.* **2011**, *11*, 4747.

131. T. K. Prasad, M. P. Suh, *Chem. Eur. J.* **2012**, *18*, 8673.

132. X.-F. Wang, Y.-B. Zhang, W. Xue, *Cryst. Growth Des.* **2012**, *12*, 1626.

133. (a) M. Dincă, A. Dailly, C. Tsay, J. R. Long, *Inorg. Chem.* **2008**, *47*, 11; (b) R. K. Deshpande, J. L. Minnaar, S. G. Telfer, *Angew. Chem. Int. Ed.* **2010**, *49*, 4598.

134. O. Shekhah, H. Wang, M. Paradinas, C. Ocal, B. Schupbach, A. Terfort, D. Zacher, R. A. Fischer, C. Wöll, *Nat. Mater.* **2009**, *8*, 481.

135. B. Chen, C. Liang, Y. Jun, D. S. Contreras, Y. L. Clancy, E. B. Lobkovsky, O. M. Yaghi, S. Dai, *Angew. Chem. Int. Ed.* **2006**, *45*, 1390.

136. (a) L. J. Barbour, *Aust. J. Chem.* **2006**, *59*, 595; (b) J.-P. Zhang, P.-Q. Liao, H.-L. Zhou, R.-B. Lin, X.-M. Chen, *Chem. Soc. Rev.* **2014**, 43, 5789; (c) M. P. Suh, Y. E. Cheon, *Aust. J. Chem.* **2006**, *59*, 605.

137. (a) R. Medishetty, D. Jung, X. K. Song, D. Kim, S. S. Lee, M. S. Lah, J. J. Vittal, *Inorg. Chem.* **2013**, *52*, 2951; (b) K. Biradha, Y. Hongo and M. Fujita, *Angew. Chem. Int. Ed.* **2002**, *41*, 3395.

138. J.-P. Zhang, X.-M. Chen, *J. Am. Chem. Soc.* **2009**, *131*, 5516; (b) R. Vaidhyanathan, S. S. Iremonger, G. K. Shimizu, P. G. Boyd, S. Alavi, T. K. Woo, *Science* **2010**, *330*, 650.

139. B. A. Demessence, J. R. Long, *Chem. Eur. J.* **2010**, *16*, 5902; (b) M.-H. Zeng, X.-L. Feng, X.-M. Chen, *Dalton Trans.* **2004**, 2217.

140. Y. Kubota, M. Takata, R. Matsuda, R. Kitaura, S. Kitagawa, K. Kato, M. Sakata, T.C. Kobayashi, *Angew. Chem. Int. Ed.* **2005**, *44*, 920; (b) G. Férey, C. Serre, C. Mellot-Draznieks, F. Millange, S. Surble, J. Dutour, I. Margiolaki, *Angew. Chem. Int. Ed.* **2004**, *43*, 6296.

141. J. Seo, C. Bonneau, R. Matsuda, M. Takata, S. Kitagawa, *J. Am. Chem. Soc.* **2011**, *133*, 9005.

142. X.-D. Chen, X.-H. Zhao, M. Chen, M. Du, *Chem. Eur. J.* **2009**, *15*, 12974.

143. O. Ohmori, M. Kawano, M. Fujita, *J. Am. Chem. Soc.* **2004**, *126*, 16292.

144. S. B. Choi, H. Furukawa, H. J. Nam, D. Y. Jung, Y. H. Jhon, A. Walton, D. Book, M. O'Keeffe, O. M. Yaghi, J. Kim, *Angew. Chem. Int. Ed.* **2012**, *51*, 8791.

145. L. Wen, P. Cheng, W. Lin, *Chem. Commun.* **2012**, *48*, 2846.

146. S. Takamizawa, T. Hiroki, E. Nakata, K. Mochizuki, W. Mori, *Chem. Lett.* **2002**, 1208.

147. S. Takamizawa, E.-I. Nataka, T. Akatsuka, R. Miyake, Y. Kakizaki, H. Takeuchi, G. Maruta, S. Takeda, *J. Am. Chem. Soc.* **2010**, *132*, 3783.

148. S. Takamizawa, Y. Takasaki, R. Miyake, *Chem. Commun.* **2009**, 6625.

149. S. Takamizawa, E.-I. Nakata, *CrystEngComm* **2005**, *7*, 476.

150. I. Grobler, V. J. Smith, P. M. Bhatt, S. A. Herbert, L. J. Barbour, J. *Am. Chem. Soc.* **2013**, *135*, 6411.

CHAPTER 2

EXPERIMENTAL TECHNIQUES

The work described in this thesis required the use of various instrumental techniques and methodologies. All these techniques are discussed in detail in this chapter and additional instrumental and synthetic protocols are discussed in the relevant chapters that follow.

2.1 Single-Crystal X-Ray Diffraction (SCXRD)

Intensity data were collected on two different instruments: A Bruker SMART Apex-2 diffractometer[1] and a Bruker Apex-2 DUO diffractometer. Mo K_α radiation (λ= 0.71073 Å) was selected for the experiments. The temperature of the crystals was controlled using an Oxford Cryostream 700 Plus cooler. Data reduction was carried out by means of a standard procedure using the Bruker software package SAINT[2] while correction for of absorption and other systematic errors was performed using SADABS.[3,4] The structures were solved by direct methods using SHELXS-97 and refined using SHELXL-97.[5] X-Seed[6] was used as the graphical interface for the SHELX program suite. All ordered nonhydrogen atoms were refined anisotropically by means of full-matrix least squares calculations on F^2 using SHELXL-97[5] within the X-Seed[6] environment. Hydrogen atoms were placed in calculated positions using riding models and assigned isotropic thermal parameters 1.2 or 1.5 times the U_{eq} of their parent atoms.

2.2 X-Ray Powder Diffraction (XRPD)

X-ray powder diffraction patterns were recorded with a Bruker D2 PHASER equipped with a Lynxeye 1D detector and Ni-filtered Cu K_α radiation (30 kV, 10 mA generator parameters; restricted by a 1.0 mm divergence slit and a 2.5° Soller collimator) with a 0.02° step width. All samples were first ground into a powder (with a mortar and pestle) and loaded onto zero-background sample holders. Diffractograms were also measured on a PANalytical X'Pert PRO instrument with Bragg-Brentano geometry, using Cu K_α radiation (λ = 1.5418 Å). Intensity data were recorded using an X'Celerator detector and 2θ scans in the range of 5-40° were carried out. The sample was spun at 15 rotations per minute to minimise preferred orientation contributions to intensity data. Variable temperature XRPD patterns were obtained by sealing the powdered sample within a Lindemann glass capillary (outer diameter of 0.5

mm) and the capillary spinner configuration of the instrument was used. The capillary spinner configuration allows for more accurate temperature control using a short-nozzle Oxford Cryostream 700+ cryostat. The patterns were plotted using the X'Pert Highscrore Plus and Origin software[7] packages.

2.3 Thermogravimetric Analysis (TGA)

Thermogravimetric analyses were carried out using a TA Instruments Q500 thermogravimetric analyser to record the weight loss of the metal-organic frameworks as a function of temperature. TGA analyses are important for determining the activation conditions for a particular compound. The balance and sample were purged with dry N_2 gas flowing at rates of 50 and 70 cm^3 min^{-1}, respectively. Samples typically ranged between 2-7 mg and were heated at a constant rate of 10 ºC min^{-1} from 25 °C to 600 °C. Thermograms were analysed using the TA Instruments Universal Analysis program and figures were prepared using Origin.[7]

2.4 Differential Scanning Calorimetry (DSC)

Differential Scanning Calorimetry is based on measuring the heat flow into or out of a sample, relative to a reference (empty pan), as a function of time or temperature in a controlled atmosphere.[8] A difference in temperature between the sample and the reference pan signifies that a thermal event (endo- or exothermic) has occurred. DSC studies are very important for examining the physical and chemical changes in a material. The measurements were carried out using a TA Instruments Q100 differential scanning calorimeter with sample sizes of typically 2-10 mg. Samples were enclosed in a pan and lid that were crimped together, after which a pinhole was made in the lid. Both the reference and the sample pans were prepared in the same way. N_2 gas, flowing at a rate of 50 ml min^{-1} was used to purge the furnace and a heating rate of 10 °C min^{-1} was used. The resulting thermograms were analysed using the TA Instruments Universal Analysis program and plotted with Origin.[7]

2.5 Gravimetric Gas Sorption

Gravimetric sorption isotherms were measured using an Intelligent Gravimetric Analyser (IGA-002) (Figure 1) supplied by Hiden Analytical (Ltd), Warrington, UK.[9] The instrument records the change in mass of sample under controlled pressure and temperature conditions. It

is equipped with an advanced pressure rating that allows measurements up to 20 bar gas pressure.

Figure 1: Images of the Hiden Intelligent Gravimetric Analyser (IGA-002).

The pressure is monitored using a pressure transducer with a range of 0-20 bar and buoyancy effects are corrected for automatically by the control software. An accurate estimate of the sample density is required for the buoyancy correction. Densities are generally estimated from the single-crystal structure or in the absence of a structure, by means of a buoyancy scan under helium pressure. Ultra high purity gases were used for the measurements and the system was outgassed after a new sample was introduced, or when the gas cylinders were changed. Temperature control was maintained to an accuracy of ± 0.05 °C using a Grant refrigerated recirculation bath.

Sorption data are monitored by real-time software that analyses the pressure and weight equilibrium using least-squares regression to extrapolate a value for the asymptote.[10-16] A Linear Driving Force (LDF) relaxation model was used and each point was recorded once a 99% fit to the model was achieved, or a pre-set time-out was reached (set at 120 minutes). Although there are various options for reporting data, the data were exported as values of mmol of gas per gram of host, which can easily be converted to a host:guest (H:G) ratio or occupancy (by using the molar masses of the guest and host) and comparing it to the expected H:G ratio derived from SCXRD structures.

2.6 Environmental Gas Cell for Collection of Single Crystal Data Under Controlled Atmospheres

An environmental gas cell has been developed by the *Barbour* group at the University of Stellenbosch in order to record single-crystal X-ray diffraction data for crystals under controlled atmospheres (Figure 2). The gas cell allows exposure of a single crystal to desired

gas pressures and equilibration under given conditions. The gas cell was used extensively used during this project to study single-crystal to single-crystal transformations (in order to preserve the quality of the crystals).

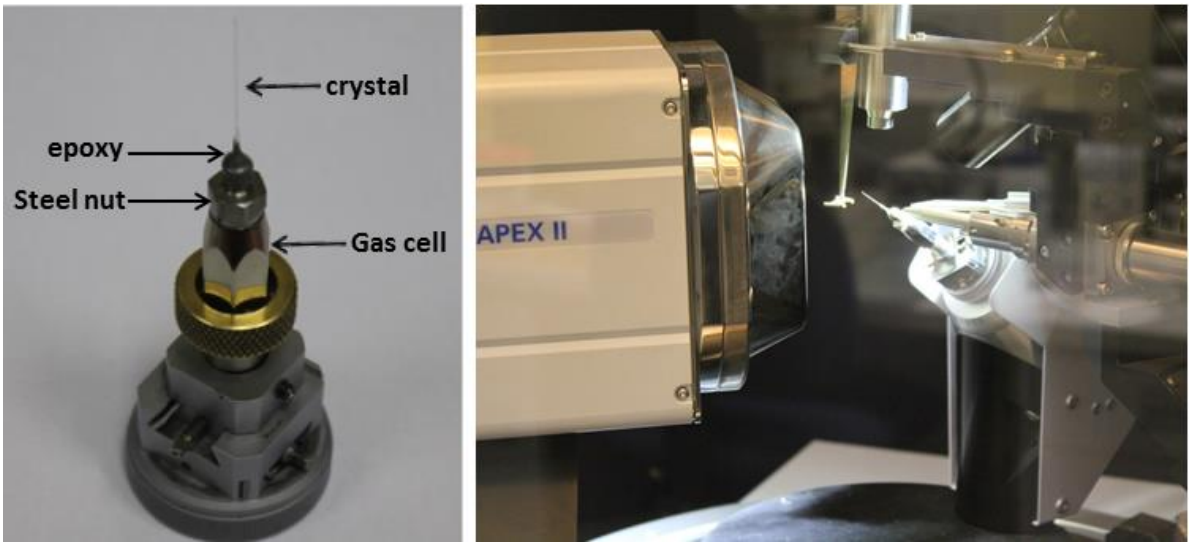

Figure 2: (left) Environmental gas cell for measuring SCXRD data under controlled atmospheres and (right) gas cell mounted on single-crystal X-ray diffractometer.

The gas cell consists of:

i) A stainless steel fitting to which a glass capillary containing the crystal is attached with epoxy resin;

ii) A nickel-coated brass cell

First, a crystal is selected and glued to the end of a glass microfiber, which is then inserted and glued into a 0.3 mm glass capillary that is flame-sealed at the narrow end. The open end of the capillary is then attached to the steel fitting with epoxy resin and left to set for about an hour. The steel fitting is screwed onto the gas cell, and an embedded rubber O-ring ensures a gas-tight seal. During gas loading the detachable gas inlet arm connects the gas cell to a gas cylinder through a regulator adjusted to the required pressure. The valve stem opens/closes the gas cell during/after gas loading. After removal of the inlet arm, the pressurised cell is then mounted on the X-ray diffractometer using a commercial goniometer head (Figure 2).

2.7 High Pressure Differential Scanning Calorimetry (HPDSC)

HPDSC measurements were carried out using a Setaram μDSC7 Evo module equipped with a high pressure sample holder. The instrument measures heat flow (like a conventional DSC) as

a function of pressure. For a constant-gradient pressure measurement with a default rate of 0.1 bar min^{-1}, the DSC was coupled to a Teledyne ISCO 260D syringe pump (Figure 3), which was controlled with software developed by L. J. Barbour. For stepwise pressure increase, the DSC was connected to a PCTPro-2000 gas sorption analyser to supply the required pressure doses. Data were collected and analysed using the Calisto software supplied by Setaram.

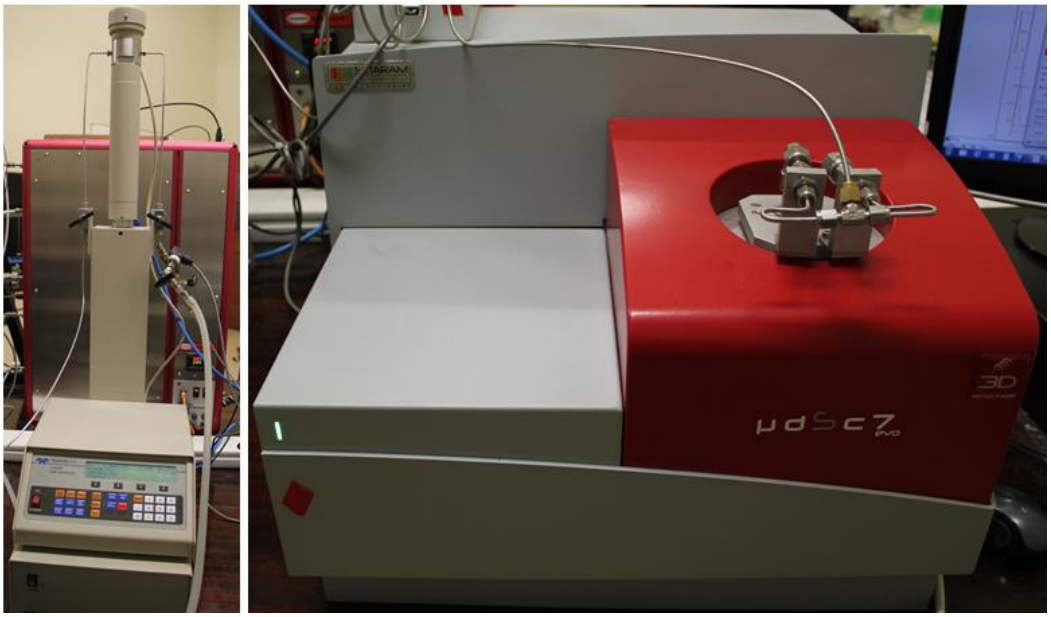

Figure 3: High Pressure Differential Scanning Calorimeter.

2.8 Electron Density Studies

The guest occupancies of the single-crystal structures were determined using PLATON /SQUEEZE[17,18] which calculates the electron contributions of molecules omitted from the model. The final occupancy can then be determined from the electron count calculated by SQUEEZE – by comparison with the known number of electrons in the guest molecule(s). According to the SQUEEZE manual: "The SQUEEZE procedure takes care of the contribution of a (heavily) disordered solvent to the calculated structure factors by back-Fourier transformation of the continuous density found in a masked region of the difference map. The masked region is defined as the solvent accessible region left by the ordered part of the structure." The calculation yields, among other values, the void volume and the number of electrons in the void. Under normal circumstances one would expect this electron count to match that expected for the presumed solvent. It is noted however, that the method relies on high resolution data and that if the dataset does not fulfil this requirement, the accuracy of the results may be questionable. SQUEEZE calculations were carried out for structures with the included *N,N′*-dimethylformamide (DMF) deleted as appropriate.

2.9 References

1. *SMART Data Collection Software*, Version 5.629, Bruker AXS Inc., Madison, WI, **2003**.
2. *SAINT Data Reduction Software*, Version 6.45, Bruker AXS Inc., Madison, WI, **2003**.
3. *SADABS*, Version 2.05, Bruker AXS Inc., Madison, WI, **2002**.
4. R. H. Blessing, *Acta Crystallogr., Sect. A: Found. Crystallogr.* **1995**, *51*, 33.
5. G. M. Sheldrick, *Acta Crystallogr., Sect. A: Found. Crystallogr.* **2008**, *64*, 112.
6. L. J. Barbour, *Supramol. Chem.*, **2001**, *1*, 189.
7. OriginPro 8 SRO downloaded from http://www.originlab.com
8. M. A. White, Thermal Analysis and Calorimetry Methods. In *Comprehensive Supramolecular Chemistry*, J. E. Davies; J. A. Ripmeester, Eds. Pergamon: Oxford, 1996; Vol. 8, pp 179.
9. M. J. Benham, D. K. Ross, *Z. Phys. Chem. (Muenchen, Ger.)* **1989**, *163*, 25.
10. A. J. Fletcher, K. M. Thomas, *Langmuir* **1999**, *15*, 6908.
11. A. J. Fletcher, K. M. Thomas, *Langmuir* **2000**, *16*, 6253.
12. A N. J. Foley, K. M. Thomas, P. L. Forshaw, D. Stanton, P. R. Norman, *Langmuir* **1997**, *13*, 2083.
13. A A. W. Harding, N. J. Foley, P. R. Norman, D. C. Francis, K. M. Thomas, *Langmuir* **1998**, *14*, 3858.
14. I. P. Okoye, M. Benham, K. M. Thomas, *Langmuir* **1997**, *13*, 4054.
15. C. R. Reid, I. P. O'Koye, K. M. Thomas, *Langmuir* **1998**, *14*, 2415.
16. C. R. Reid, K. M. Thomas, *Langmuir* **1999**, *15*, 3206.
17. (a) *PLATON, A Multipurpose Crystallographic Tool*, Utrecth University, Utrecht, The Netherlands, **2008,** (b) A. L. Spek, *J. Appl. Crystallogr.* **2003**, *36*, 7-13.
18. P. van der Sluis, A. L. Spek, *Acta Crystallogr., Sect. A: Found. Crystallogr.* **1990**, *46*, 194.

CHAPTER 3

DIRECT EVIDENCE FOR SINGLE-CRYSTAL TO SINGLE-CRYSTAL SWITCHING OF DEGREE OF INTERPENETRATION IN A METAL-ORGANIC FRAMEWORK

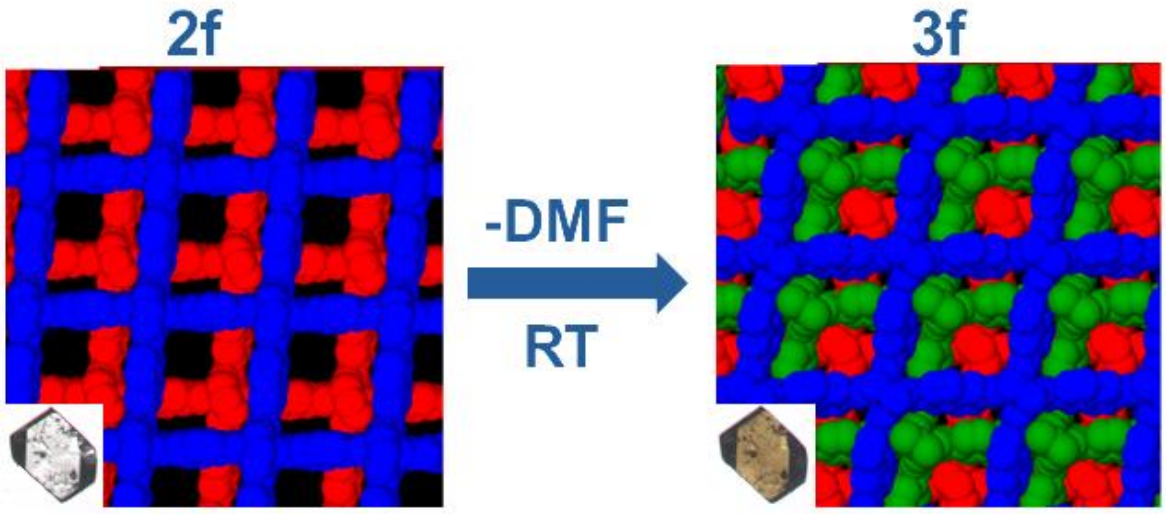

Author's Contribution

- Designing the project.
- Synthesis of $[Zn_2(ndc)_2(bpy)]$ crystals and carrying out supporting studies involving PXRD and TGA.
- Recording of single-crystal transformation with help from Prashant M. Bhatt.
- Discussion and evaluation of results with co-authors.
- Compiled the result with help of Prashant M. Bhatt and Charl X. Bezuidenhout.

JACS
JOURNAL OF THE AMERICAN CHEMICAL SOCIETY

Communication

pubs.acs.org/JACS

Direct Evidence for Single-Crystal to Single-Crystal Switching of Degree of Interpenetration in a Metal–Organic Framework

Himanshu Aggarwal, Prashant M. Bhatt, Charl X. Bezuidenhout, and Leonard J. Barbour*

Department of Chemistry and Polymer Science, University of Stellenbosch, Matieland 7602, Stellenbosch, South Africa

Supporting Information

ABSTRACT: A known doubly interpenetrated metal–organic framework with the formula $[Zn_2(ndc)_2(bpy)]$ possesses minimal porosity when activated. We show not only that the material converts to its triply interpenetrated analogue upon desolvation, but also that the transformation occurs in a single-crystal to single-crystal manner under ambient conditions. The mechanism proposed for the conversion is supported by computational methods and by analogy with the solid-state behavior of an analogous system.

One of the primary goals of crystal engineering is to understand structure–function relationships at the molecular level,[1] with a view to establishing protocols for the development of designer materials. Some of these materials might be exploited as single-crystal devices, in which case it would generally be desirable for a crystal to undergo nondestructive internal changes in order to perform a specific function.[2,3] For example, a single crystal of a porous framework has recently been used for structural characterization of nanogram quantities of scarce natural products, thereby establishing a new approach to the characterization of very small quantities of compound that cannot be characterized by means of conventional analytical techniques.[4] Owing to the requirement for three-dimensional packing periodicity of their components, crystals usually crack or crumble as a result of the long-range strain introduced when the internal periodicity is disrupted. Therefore, we refer to crystals as being brittle unless the internal changes can be effected in a concerted fashion that preserves molecular-level continuity throughout the single-crystal phase transformation (SCPT). Discrete crystals have been shown to tolerate considerable dynamic behavior at the molecular level while maintaining their single-crystal character. Examples that are common in the literature include bond formation/cleavage,[5] guest uptake,[6,7] release,[6] or exchange[8] as well as polymorphic phase transformations.[9] Although occurrences of SCPTs are usually anecdotal, it has become interesting to probe the extent to which structural changes might occur within crystals without destroying their macroscopic integrity.

Because of their numerous potential applications, metal–organic frameworks (MOFs) and related materials are of considerable interest in chemistry and materials science.[10−12] Accordingly, much effort has been devoted to structural aspects of MOFs with a view to gaining better understanding and control of their properties. In particular, the use of structurally robust secondary building units (SBUs) that are based on metal clusters is a common approach toward the reticular synthesis of MOF materials that maintain their framework connectivity after solvent removal, often even surviving as single crystals.[13] Indeed, this strategy has become routine for the preparation of numerous porous materials. Framework interpenetration is a well-known structural feature in MOFs and related structures;[11,14−16] when the open spaces of a network are large enough, one or more additional (usually identical) networks can be accommodated within these spaces such that there are no formal bonds between the different networks. This means that the networks cannot be separated without breaking numerous chemical bonds,[15] and the degree of interpenetration may be 2-fold or greater, subject to the grid dimensions. Whether interpenetration is welcomed or unwanted depends upon the desired properties of the material. For example, interpenetration can promote flexibility in MOFs, resulting in dynamic phenomena that can be exploited for selective guest capture and separation.[14,16] On the other hand, interpenetration reduces the guest-accessible volume, and it is one of the major obstacles to preparing MOFs with large surface areas.[15,17,18] Either way, interpenetration cannot be ignored, and a better understanding of this important phenomenon would be helpful in designing dynamic materials with tailor-made properties.

As part of our exploration of pillared-layer structures, we have reinvestigated a system composed of naphthalene dicarboxylic acid (ndc), 4,4′-bipyridine (bpy), and the zinc paddlewheel SBU. There have been two independent reports of this system based on single-crystal diffraction (SCD) analysis—one describing a 2-fold (**2f**)[19] and the other a 3-fold (**3f′**)[20] interpenetrated structure, both with the network formula $[Zn_2(ndc)_2(bpy)]$. The crystal structure of **2f** (Figure 1a,b) possesses 44% guest-accessible volume and contains dimethylformamide (DMF) and water molecules in channels, although the guest solvent could not be modeled. In contrast, the structure of **3f′** possesses much less guest-accessible space (18%) and thus fewer solvent molecules (also not modeled).[20] We prepared crystals of **2f**, and thermogravimetric analysis (TGA) shows a 25% weight loss in the temperature range 40–140 °C, which corresponds to three DMF molecules and one H_2O molecule per formula unit (see Supporting Information (SI), Figure S10a). In order to remove the solvent from **2f** for subsequent porosity studies, crystals were subjected to dynamic vacuum at 120 °C for 24 h. Although many of the crystals

Received: January 17, 2014
Published: February 20, 2014

dx.doi.org/10.1021/ja500530y | J. Am. Chem. Soc. 2014, 136, 3776−3779

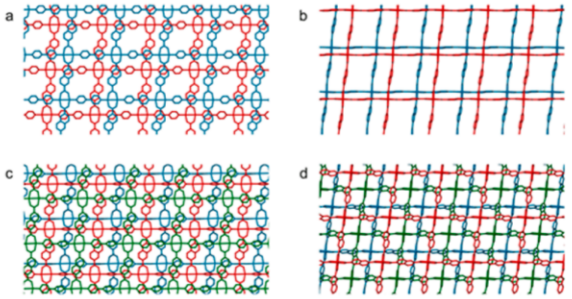

Figure 1. Structure of doubly interpenetrated [Zn2(ndc)2(bpy)] (**2f**) viewed perpendicular to the (a) (100) and (b) (001) planes converts in single-crystal to single-crystal fashion to **3f** viewed perpendicular to the (c) (110) and (d) (001) planes. Guest DMF molecules, hydrogen atoms and disordered components have been omitted for clarity. The independent frameworks are colored red and blue for **2f** and red, green, and blue for **3f**. In all cases the ligands propagating the frameworks in the direction of the projection have been omitted.

became opaque upon desolvation, several SCD-quality crystals remained intact.

Remarkably, SCD analysis of these crystals revealed a new 3-fold interpenetrated structure **3f** (Figure 1c,d), which is different from that reported in the literature (i.e., **3f′**).[20] The structure of **3f** is reminiscent of **3f′**, having the same SBU and metal to ligand connectivity, but it possesses 17% guest-accessible volume within which it was still possible to model DMF guest molecules (0.4 molecule of DMF per formula unit). A comparison of the powder X-ray diffraction (PXRD) patterns of the simulated structures of **3f** and **3f′** shows that these two phases are easily distinguishable from each other (Figure S17). There are also small differences in dihedral angles of the ligands and the coordination angles, and the crystallographic symmetry is also different for the two structures. PXRD analysis of the desolvated bulk sample matched the pattern simulated from the SCD structure (see SI) of as-synthesized **3f**. Indeed, the desolvation experiment was repeated several times and under different conditions, and in each case PXRD analysis confirmed full conversion of **2f** to **3f** (see SI). We also observed that **2f** converts to **3f** upon standing under ambient conditions (i.e., in the absence of mother liquor), as verified by unit cell determinations (see SI). This implies that the transformation follows a relatively low energy pathway as compared to a previous report of a change in interpenetration resulting from extreme heating of the material.[21] Moreover, in this particular case the change in interpenetration results from spontaneous loss of DMF guest molecules from the channels which, in turn, leads to spontaneous conversion of the structure from **2f** to **3f**. The previously reported example involved complete removal of the ligand upon heating, leading to a change in the coordination environment around the metal atom, whereas in the present case the coordination environment remains the same even after conversion.

In order to show unequivocally that the conversion occurs as a SCPT, it is highly desirable to carry out complete SCD structural analyses of the same crystal both before and after transformation. A single crystal of **2f** was glued to a glass fiber and inserted into a Lindeman glass capillary with an outer diameter of 0.3 mm and a wall thickness of 10 μm. The crystal was thermostated at 200 K while X-ray intensity data were collected, yielding the structure of **2f**. The temperature was then increased to 298 K at a rate of 120 K h^{-1} and kept constant while the unit cell was determined repeatedly. After approximately 6 h at 298 K, unit cell determination indicated that the transformation to **3f** had occurred to near completion (i.e., the unit cell could only be indexed as that of **3f**). The temperature was then decreased back to 200 K, and X-ray diffraction data were collected once again, yielding the structure of **3f**. It is noteworthy that the crystal quality did not deteriorate as a result of the SCPT, as verified by visual inspection and measurement of its mosaicity (see SI). Conversion of **2f** to **3f** was also investigated using other techniques. Optical microscopy revealed substantial reduction in the crystal size upon desolvation over time, which is consistent with conversion of **2f** to **3f** (Figure S14). Time-lapse solid-state UV−visible spectroscopy also indicated a gradual change from **2f** to **3f** upon desolvation—a reflectance band around 225 nm started appearing after 2 h and gradually increased in intensity over time. After 24 h the spectrum did not change any further and matched that of **3f** prepared by heating **2f** under vacuum (Figures S12 and S13). In order to investigate the reversibility of the transformation **2f**→**3f**, a transformed crystal of **3f** was immersed in DMF at room temperature for 24 h. Determination of the unit cell parameters did not indicate reversion to **2f**. When the experiment was then repeated at 120 °C, the same result was obtained. Similar experiments were carried out using powdered material (see SI), and it does not appear that the transformation is reversible under the conditions investigated.

The well-studied benzene dicarboxylic acid (bdc) analogue of the $[Zn_2(ndc)_2(bpy)]$ system may offer clues toward suggesting a plausible mechanism for the conversion of the latter from **2f** to **3f**. $[Zn_2(bdc)_2(bpy)]$ is also formed as a DMF solvate ($\mathbf{1}_{DMF}$) under solvothermal conditions. On heating under dynamic vacuum, $\mathbf{1}_{DMF}$ converts to the desolvated nonporous phase (**1**).[22] The most conspicuous difference between $\mathbf{1}_{DMF}$ and **1** involves the coordination geometry of the bpy ligand: the (Zn···Zn)−N bond angle in $\mathbf{1}_{DMF}$ is almost linear (ca. 176°), and in **1** it becomes considerably bent (ca. 153°). It appears that this angular distortion occurs in order to minimize the empty space in the desolvated structure. The structure of **2f** is quite similar to that of $\mathbf{1}_{DMF}$, except that ndc is longer than bdc, and hence the grid spacing and channel sizes are larger in the case of **2f**. Extending the analogy, upon desolvation of **2f**, the corresponding coordination angle of the bpy linker should also distort in order to reduce the amount of empty space. Indeed, it is reasonable to expect even more severe distortion of the (Zn···Zn)−N_{bpy} angle in the case of **2f**→**3f** owing to the greater solvent-accessible volume of **2f** relative to that of **1**. We therefore postulate a transformation mechanism based on the assumption that the ndc carboxylate-linked layers are able to slide laterally while maintaining their connectivity during the conversion, whereas the bpy pillars can undergo Zn−N bond cleavage and re-formation (see video file in SI).

With reference to Figure 2, the two frameworks in the structure of **2f** are offset with respect to each other such that they contain guest-accessible space (1), with the guest molecules playing a structure-supporting role. With respect to the stacking direction (i.e., the vertical direction in Figure 2), pairs of proximate adjacent layers (i.e., bilayers) from the two distinct networks slide laterally and in unison as the guest molecules are driven from the crystals (2). This transverse displacement is facilitated by the ability of the bpy pillars to become distorted until they reach the limit at which the Zn−N

dx.doi.org/10.1021/ja500530y | J. Am. Chem. Soc. 2014, 136, 3776−3779

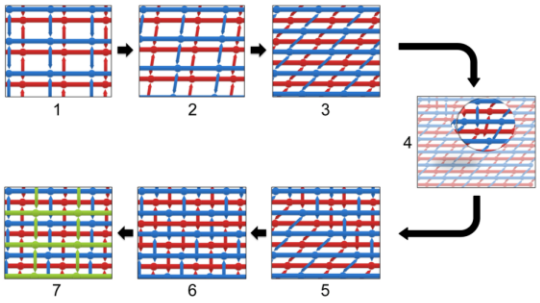

Figure 2. Schematic representation of the suggested mechanism governing the conversion from **2f** to **3f**. Independent frameworks are colored red, green, and blue. The Zn_2 cluster SBUs are represented by circles, the ndc linkages by solid lines, and the bpy linkages by double-ended arrows. In the projections shown, the ndc-linked layers form horizontal planes that are pillared in the vertical direction by means of bpy ligands.

coordination bonds can still be maintained (3). Since the bilayers are tethered to their neighboring bilayers by means of the bpy pillars, this sliding motion brings the bilayers closer together until all of the ndc-linked planes are approximately evenly spaced. Owing to enforced instability of the distorted Zn−N linkages, the bpy ligands each begin to detach from one of their associated Zn ions and reattached to a more favorably located metal site to once again form an almost linear (Zn···Zn)−bpy−(Zn···Zn) pillared connection (4, inset). Ultimately this mechanism should cascade through the crystal (5) until all of the bpy connections have been reassigned (6). The final result of this process is that the doubly interpenetrated ***...ababab...*** layers of ndc-linked SBUs in **2f** (shown respectively as ***a*** = red and ***b*** = blue in 1−3) become triply interpenetrated ***...abcabc...*** layers (red, blue, and green in 7) as a result of the new interconnections by means of the bpy pillars. We note that a SCPT involving substantial lateral translation (by approximately 6 Å) of layers relative to one another has previously been observed in an organic crystal.[23] The zinc paddlewheel SBU is generally considered to be flexible, but still sufficiently robust not to undergo bond cleavage or rearrangement during crystal desolvation, and a recent report[24] describing the internal rearrangement of a paddlewheel SBU represents by far the most dramatic distortion observed heretofore. However, to date there has been no unequivocal report describing a change in network connectivity involving metal-cluster SBUs as a SCPT. That such a process can occur throughout a single crystal without causing fracturing is surprising since it requires a high degree of internal cooperativity to be maintained throughout the transformation process.

The proposed mechanism is also supported by computational methods; the model used to investigate the relationship between a bpy pillar and a zinc-ndc paddlewheel node is shown in Figure 3a. Using the geometry in **2f** as the starting point, an angular scan was carried out by incrementally tilting the bpy molecule (i.e., by manipulating its angle ϕ, Figure 3b). The system was allowed to optimize after each step using the positions of each preceding step as a starting point, and plots of the resulting Zn1−N1 coordination bond length, the bpy inclination angles (θ and ϕ), and the corresponding energy of the system are shown in Figure 3c,d. The angle θ decreases with decreasing ϕ (Figure 3d), with concomitant lengthening of the Zn−N bond, as evidenced by the increasing relative

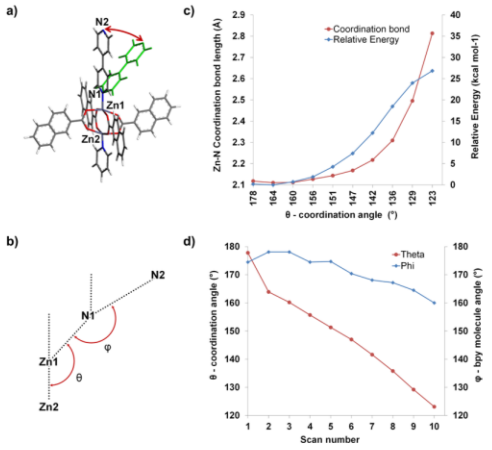

Figure 3. Change in the energy of the system with deformation of the $(Zn\cdots Zn)-N_{bpy}$ orientation. (a) The model used for an angular scan of the $(Zn\cdots Zn)-N_{bpy}$ bond angle by rotating the bpy molecule in steps of 2.5° over 20 steps. (b) Diagrammatic representation of the bpy coordination (θ) and ligand orientation (φ) angles. (c) Plot of the change in the N1−Zn1 coordination bond length and the energy of the system with decreasing θ. (d) Change in the coordination and ligand angles θ and φ with scan step number.

energy of the system (Figure 3c). Moreover, as φ deviates further from linearity, the $(N\cdots N)_{bpy}$ axis gradually points away from the metal, thus further destabilizing the coordination bond. Since the relative energy of the system increases approximately exponentially, it seems reasonable to assume that distortion of the (Zn···Zn)−bpy−(Zn···Zn) geometry will ultimately result in bond cleavage, followed by formation of a more favorable connection between the freed extremity of the bpy ligand and a different metal center.

Although a few recent reports have mentioned changes in the degree of interpenetration of MOFs upon desolvation, the transformations have always occurred with concomitant polycrystalline degradation of single crystals.[25,26] However, to our knowledge the present study is the first unequivocal description of a change in the degree of interpenetration occurring as a single-crystal to single-crystal phase transformation, as verified by structural analysis of the same crystal both pre- and post-conversion. The relative ease with which **2f** converts to **3f** suggests that many more such conversions might be possible, but they have most likely not been reported because the crystal structure of the desolvated phase has not yet been determined; i.e., in most of the cases single crystals do not survive substantial rearrangement during such conversions, making structural analysis difficult to accomplish. Researchers in this area often encounter instances in which the surface area of a material is much lower than expected from SCD analysis of the original open framework,[19,27−30] or the material irreversibly converts to an unknown nonporous (or collapsed) phase upon desolvation. A report by Hupp and co-workers on **2f** and its sorption properties stated that "N_2 adsorption measurements on framework **3** [evacuated **2f**] yields a lower than anticipated surface area due to possible channel collapse".[19] We have now established that the evacuated "framework **3**" is actually **3f** and that the channels do not merely collapse; instead, complete transformation of the structure takes place from the highly porous doubly interpenetrated **2f** to the considerably less porous triply interpenetrated **3f**, the structure of which was not

previously known. Another report[31] compared the PXRD patterns of evacuated **2f** with analogous structures that are 3-fold interpenetrated but provided no evidence for the transformation of **2f** to **3f** as a SCPT. The present study not only provides direct evidence for a change in degree of interpenetration but also emphasizes that this phenomenon should also be considered as a very plausible possibility when explaining the loss of porosity in MOFs upon desolvation. Indeed, in this context we examined the previously reported[28] doubly interpenetrated *trans*-1,2-bis(4-pyridyl)ethylene (bpe) analogue of **2f**, since it has been reported that the surface area of $[Zn_2(ndc)_2(bpe)]$ is much lower than expected from the crystal structure of the solvated framework.[28] Comparison of powder patterns of solvated and activated $[Zn_2(ndc)_2(bpe)]$ with simulated powder patterns from single-crystal structures suggests that doubly interpenetrated $[Zn_2(ndc)_2(bpe)]$ converts to a triply interpenetrated structure upon activation (Figure S9), but the transformation does not appear to proceed as a SCPT.

When single-crystal to polycrystalline-phase transformations occur as the result of solvent removal, it is difficult to argue that the mechanism does not involve partial dissolution and regrowth of the components. However, such processes can be discounted in the case of single-crystal to single-crystal transformations, especially when the same crystal is used to determine the structures before and after conversion. We have shown that it is possible to change the degree of interpenetration of a three-dimensional MOF as a SCPT, and we have postulated a mechanism involving a concerted process of coordination bond cleavage and re-formation facilitated by transverse sliding of pillared layers. This study probes the limits to which a single-crystal material can undergo structural rearrangement while still maintaining the macroscopic integrity of the crystal a discrete entity.

■ ASSOCIATED CONTENT

Supporting Information

Synthetic procedure, thermal analysis, detailed crystallographic information, additional figures, and an animation explaining the mechanism. This material is available free of charge via the Internet at http://pubs.acs.org.

■ AUTHOR INFORMATION

Corresponding Author

ljb@sun.ac.za

Notes

The authors declare no competing financial interest.

■ ACKNOWLEDGMENTS

We thank the National Research Foundation and the Claude Leon Foundation for financial support.

■ REFERENCES

(1) Tiekink, E. R. T., Vittal, J. J. *Frontiers in Crystal Engineering*; John Wiley & Sons, Ltd.: Chichester, 2006.

(2) Kobatake, S.; Takami, S.; Muto, H.; Ishikawa, T.; Irie, M. *Nature* **2007**, *446*, 778.

(3) Papaefstathiou, G. S.; Zhong, Z.; Geng, L.; MacGillivray, L. R. *J. Am. Chem. Soc.* **2004**, *126*, 9158.

(4) Inokuma, Y.; Yoshioka, S.; Ariyoshi, J.; Arai, T.; Hitora, Y.; Takada, K.; Matsunaga, S.; Rissanen, K.; Fujita, M. *Nature* **2013**, *495*, 461.

(5) Bernini, M. C.; Gándara, F.; Iglesias, M.; Snejko, N.; Gutiérrez-Puebla, E.; Brusau, E. V.; Narda, G. E.; Monge, M. Á. *Chem.—Eur. J.* **2009**, *15*, 4896.

(6) Jacobs, T.; Lloyd, G. O.; Gertenbach, J.-A.; Müller-Nedebock, K. K.; Esterhuysen, C.; Barbour, L. J. *Angew. Chem., Int. Ed.* **2012**, *51*, 4913.

(7) Takamizawa, S.; Nakata, E.-i.; Yokoyama, H.; Mochizuki, K.; Mori, W. *Angew. Chem., Int. Ed.* **2003**, *42*, 4331.

(8) Das, M. C.; Bharadwaj, P. K. *J. Am. Chem. Soc.* **2009**, *131*, 10942.

(9) Das, D.; Engel, E.; Barbour, L. J. *Chem. Commun.* **2010**, *46*, 1676.

(10) Li, H.; Eddaoudi, M.; O'Keeffe, M.; Yaghi, O. M. *Nature* **1999**, *402*, 276.

(11) Horike, S.; Shimomura, S.; Kitagawa, S. *Nat. Chem.* **2009**, *1*, 695.

(12) MacGillivray, L. R. *Metal–Organic Frameworks: Design and Application*; John Wiley & Sons, Inc.: New York, 2010.

(13) Yaghi, O. M.; O'Keeffe, M.; Ockwig, N. W.; Chae, H. K.; Eddaoudi, M.; Kim, J. *Nature* **2003**, *423*, 705.

(14) Maji, T. K.; Matsuda, R.; Kitagawa, S. *Nat. Mater.* **2007**, *6*, 142.

(15) Shekhah, O.; Wang, H.; Paradinas, M.; Ocal, C.; Schupbach, B.; Terfort, A.; Zacher, D.; Fischer, R. A.; Woll, C. *Nat. Mater.* **2009**, *8*, 481.

(16) Yang, S.; Lin, X.; Lewis, W.; Suyetin, M.; Bichoutskaia, E.; Parker, J. E.; Tang, C. C.; Allan, D. R.; Rizkallah, P. J.; Hubberstey, P.; Champness, N. R.; Mark Thomas, K.; Blake, A. J.; Schröder, M. *Nat. Mater.* **2012**, *11*, 710.

(17) Zhang, J.; Wojtas, L.; Larsen, R. W.; Eddaoudi, M.; Zaworotko, M. J. *J. Am. Chem. Soc.* **2009**, *131*, 17040.

(18) Prasad, T. K.; Suh, M. P. *Chem.—Eur. J.* **2012**, *18*, 8673.

(19) Ma, B.-Q.; Mulfort, K. L.; Hupp, J. T. *Inorg. Chem.* **2005**, *44*, 4912.

(20) Chun, H.; Dybtsev, D. N.; Kim, H.; Kim, K. *Chem.—Eur. J.* **2005**, *11*, 3521.

(21) Choi, S. B.; Furukawa, H.; Nam, H. J.; Jung, D.-Y.; Jhon, Y. H.; Walton, A.; Book, D.; O'Keeffe, M.; Yaghi, O. M.; Kim, J. *Angew. Chem., Int. Ed.* **2012**, *51*, 8791.

(22) Chen, B.; Liang, C.; Yang, J.; Contreras, D. S.; Clancy, Y. L.; Lobkovsky, E. B.; Yaghi, O. M.; Dai, S. *Angew. Chem., Int. Ed.* **2006**, *45*, 1390.

(23) Atwood, J. L.; Barbour, L. J.; Jerga, A.; Schottel, B. L. *Science* **2002**, *298*, 1000.

(24) Seo, J.; Bonneau, C.; Matsuda, R.; Takata, M.; Kitagawa, S. *J. Am. Chem. Soc.* **2011**, *133*, 9005.

(25) Zhang, J.-P.; Lin, Y.-Y.; Zhang, W.-X.; Chen, X.-M. *J. Am. Chem. Soc.* **2005**, *127*, 14162.

(26) Ohara, K.; Martí-Rujas, J.; Haneda, T.; Kawano, M.; Hashizume, D.; Izumi, F.; Fujita, M. *J. Am. Chem. Soc.* **2009**, *131*, 3860.

(27) Chen, B.; Ma, S.; Hurtado, E. J.; Lobkovsky, E. B.; Liang, C.; Zhu, H.; Dai, S. *Inorg. Chem.* **2007**, *46*, 8705.

(28) Chen, B.; Ma, S.; Zapata, F.; Lobkovsky, E. B.; Yang, J. *Inorg. Chem.* **2006**, *45*, 5718.

(29) Dybtsev, D. N.; Yutkin, M. P.; Peresypkina, E. V.; Virovets, A. V.; Serre, C.; Férey, G.; Fedin, V. P. *Inorg. Chem.* **2007**, *46*, 6843.

(30) Henke, S.; Schneemann, A.; Kapoor, S.; Winter, R.; Fischer, R. A. *J. Mater. Chem.* **2012**, *22*, 909.

(31) Liu, H.; Zhao, Y.; Zhang, Z.; Nijem, N.; Chabal, Y. J.; Zeng, H.; Li, J. *Adv. Funct. Mater.* **2011**, *21*, 4754.

Supporting Information

Direct Evidence for Single-Crystal to Single-Crystal Switching of Degree of Interpenetration in a Metal-Organic Framework

Himanshu Aggarwal, Prashant M. Bhatt, Charl X. Bezuidenhout and Leonard J. Barbour*

Department of Chemistry and Polymer Science, University of Stellenbosch, Matieland 7602, Stellenbosch, South Africa

1. Methods and materials

All chemicals were obtained commercially and used as received without further purification.

2. Solvothermal synthesis of $[Zn_2(ndc)_2(bpy)]$ (2f)

The metal-organic framework $[Zn_2(ndc)_2(bpy)]$ **2f** was prepared by mixing $Zn(NO_3)_2.6H_2O$ (30 mg, 0.1 mmol), 2,6-naphthalene dicarboxylic acid (21.6 mg, 0.1 mmol) and bipyridine (7.8 mg, 0.05 mmol) in 10 ml of DMF and heating the mixture at 70 °C for 24 hours. Colourless crystals of **2f** were obtained and washed with fresh DMF before further study.

Solvothermal synthesis of $[Zn_2(ndc)_2(bpy)]$ (3f)

The triply interpenetrated metal-organic framework $[Zn_2(ndc)_2(bpy)]$ **3f** was prepared by mixing $Zn(NO_3)_2.6H_2O$ (300 mg, 1 mmol), 2,6-naphthalene dicarboxylic acid (216 mg, 1 mmol) and bipyridine (78 mg, 0.5 mmol) in 5 ml of DMF and heating the mixture at 120 °C for 24 hours. Colourless crystals of **3f** were washed with fresh DMF before further study.

3. Preparation of $[Zn_2(ndc)_2(bpy)]$ (3f) by activation of 2f

Crystals of the triply interpenetrated structure **3f** were prepared by activating **2f** under dynamic vacuum at 120 degrees in a Büchi glass oven. Crystals of **3f** were also obtained when **2f** crystals were removed from mother liquor and left standing under ambient conditions for approximately one day.

4. Packing diagrams of 2f and 3f

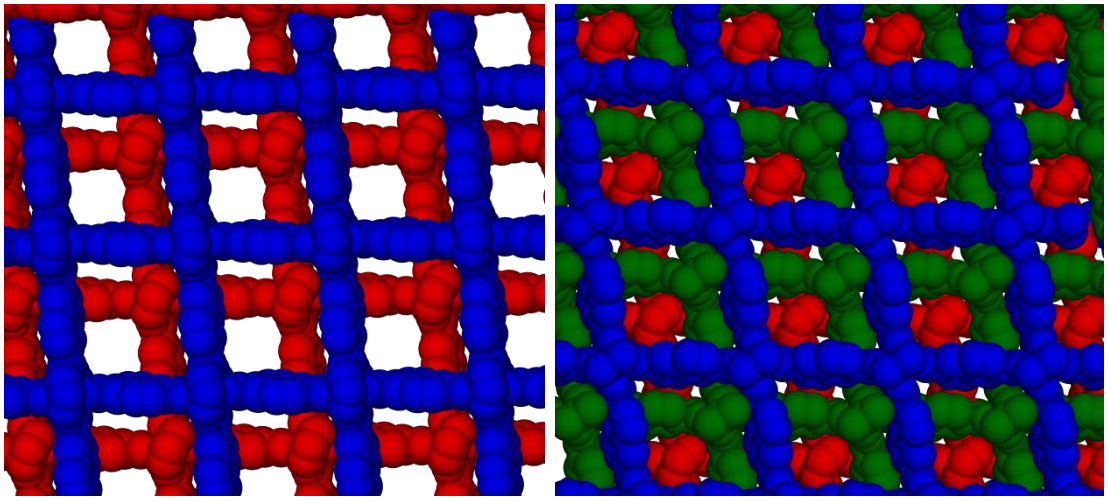

(a) (b)

Figure S1. Space filling model of (a) **2f** and (b) **3f** viewed along the direction of the bpy pillars.

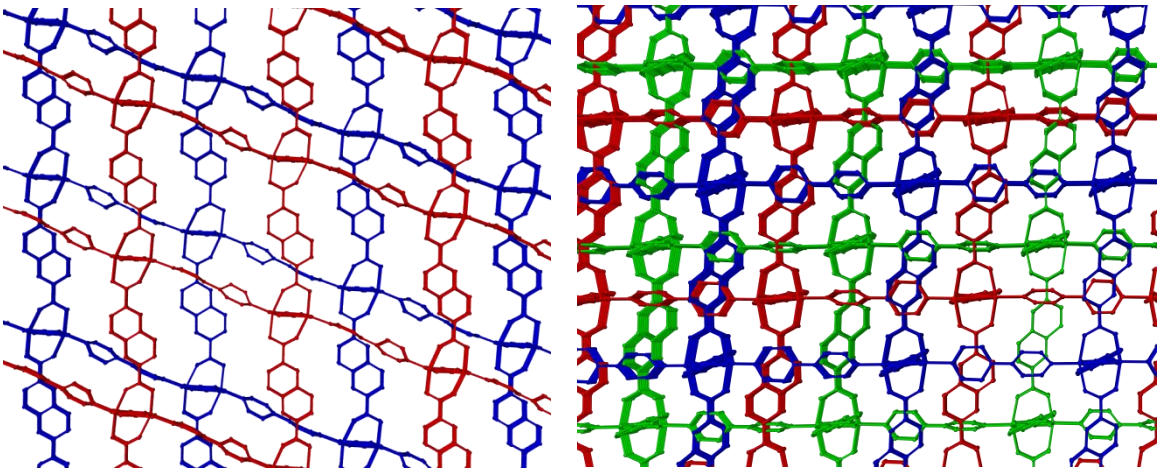

(a) (b)

Figure S2. Packing of (a) **2f** and (b) **3f** viewed perpendicular to the ndc layers.

5. Single Crystal X-ray Diffraction (SCD)

Intensity data were collected on a Bruker Apex II DUO CCD diffractometer with a multilayer monochromator. Mo K_α radiation (λ= 0.71073 Å) was used for the experiments. The temperature of the crystal was controlled using an Oxford Cryostream 700 Plus. Data reduction was carried out by means of standard procedures using the Bruker software package SAINT[1] while absorption corrections and correction of other systematic errors were carried out using SADABS.[2] The structures were solved by direct methods using SHELXS-97 and refined using SHELXL-97.[3] X-Seed[4] was used as the graphical interface for the SHELX program suite. Hydrogen atoms were placed in calculated positions using riding models.

6. Disorder and modelling of solvent molecules

For the structure of **2f** it was not possible to model all of the solvent crystallographically. However, it was possible to model two DMF molecules with site occupancies of 80% and 50%. The site occupancies of the DMF molecules were determined by refining the site occupancy factors and then fixing them to a common value for each unique molecule. The remaining electron density within the channel was removed using the SQUEEZE routine of PLATON. However, according to TGA there should be three DMF molecules and one water molecule per formula unit of fully solvated **2f** ($C_{34}H_{20}N_2O_8Zn_2$).

For **3f** it was possible to model a DMF solvent molecule with 40% occupancy per formula unit of **3f** ($C_{34}H_{20}N_2O_8Zn_2 \cdot C_{17}H_{10}NO_4Zn$)

In **2f** the atoms C19 and C20 of a naphthalene ring are disordered over two positions with 60% and 40% occupancy. C25, C26, C28, C29 and C30, C31, C33, C34 of the bipyridyl rings were modelled as disordered over two positions with occupancies (54:46) and (52:48). In all cases the disordered positions were obtained from difference Fourier maps and site occupancy factors were allowed to refine such that the sum of the disordered component = 1. The occupancy of DMF molecules was determined by refining SOF and then fixing it to a common value for all of the atoms.

7. Table S1. Crystal Data and Structure Refinement

Identification code	**2f**	**3f converted**	**3f synthesised**
Empirical formula	$C_{34}H_{20}N_2O_8Zn_2 \cdot 1.3(C_3H_7NO)$	$C_{34}H_{20}N_2O_8Zn_2 \cdot C_{17}H_{10}NO_4Zn \cdot 0.4(C_3H_7NO)$	$C_{34}H_{20}N_2O_8Zn_2 \cdot C_{17}H_{10}NO_4Zn \cdot 0.32(C_3H_7NO)$
Formula weight	808.97	1102.13	1095.96
Temperature (K)	200 (2)	200(2)	200(2)
Wavelength (Å)	0.71073	0.71073	0.71073
Crystal system	Triclinic	Monoclinic	Monoclinic
Space Group	*P*-1	*C*2	*C*2
a/Å	13.0126(4)	17.0963(3)	17.1323(14)
b/Å	13.1146(4)	19.9054(3)	19.8444(16)
c/Å	13.9071(4)	14.0678(2)	14.0625(12)
$\alpha/^o$	84.956(1)	90.00	90.00
$\beta/^o$	69.273(1)	95.978(1)	96.159(1)
$\gamma/^o$	84.608(1)	90.00	90.00
Volume ($Å^3$), Z	2206.08(11) , 2	4761.36(13) , 4	4753.4(7) , 4
Density (calculated) (g/cm^3)	1.218	1.537	1.531
Absorption coefficient (mm^{-1})	1.137	1.568	1.570

F(000)	825	2236	2222
Theta range for data collection (^{o})	1.56 to 26.72	1.46 to 27.92	1.46 to 26.56
Limiting indices	-16<h<16, -16<k<16, -17<l<17	-22<h<21, -25<k<26, -18<l<18	-21<h<21, -24<k<24, -17<l<17
Reflections collected/unique	50155/9350	41287/11153	31578/9843
Goodness of fit on F^2	1.078	1.065	1.026
R_{int}	0.0524	0.0473	0.0667
Absolute structure parameter	-	0.0(7)	0.0(7)
Final R indices [I>2sigma(I)]	R_1 = 0.0470 wR_2 = 0.1360	R_1 = 0.0408 wR_2 = 0.0889	R_1 = 0.0504 wR_2 = 0.1134
R indices (all data)	R_1 = 0.0574 wR_2 = 0.1414	R_1 = 0.0594 wR_2 = 0.0968	R_1 = 0.0795 wR_2 = 0.1254
Largest diffraction peak and hole (e/Å^{-3})	1.147/-0.506	0.461/-0.378	0.704/-1.062
Mosaicity	0.36	0.39	0.37

8. Single-crystal to single-crystal conversion of 2f to 3f

A single crystal of **2f** was glued to a glass fibre and inserted into a Lindeman glass capillary with an outer diameter of 0.3 mm and a wall thickness of 10 µm. The crystal was thermostated at 200 K while X-ray intensity data were collected, yielding the structure of **2f**. The temperature was then increased to 298 K at a rate of 120 K h^{-1}, kept constant for 6 hours (unit cells were determined until conversion to **3f** was unequivocal) and then decreased back to 200 K. X-ray diffraction data were collected again, yielding the structure of **3f**.

9. Unit cell parameters:

Unit cell of **2f** crystal at 200 K

a = 13.0126(4) Å, b = 13.1146(4) Å, c = 13.9071(4) Å

α= 84.956(1)°, β = 69.273(1)°, γ = 84.608(1)°

Space Group = *P*-1

Unit cell volume = 2206.08(11) $Å^3$

Crystal mosaicity: 0.36°

Unit cell of **3f** crystal after conversion from **2f** at 200 K (same crystal as above)

a = 17.0963(3) Å, b = 19.9054(3) Å, c = 14.0678(2) Å

α = 90°, β = 95.978(1) °, γ = 90°,

Space Group = *C*2

Unit cell volume = 4761.36(13) $Å^3$

Crystal mosaicity: 0.39°

10. Representative diffraction patterns of 2f and 3f (same crystal in same orientation)

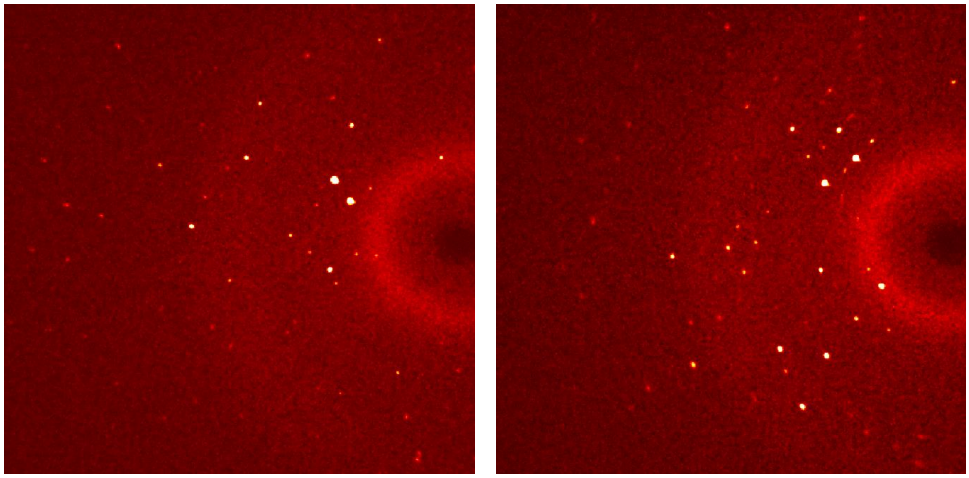

(a) (b)

Figure S3. Diffraction patterns of (a) **2f** before conversion and (b) after conversion to **3f**. These patterns were recorded using the same crystal in the same orientation.

11. Monitoring the transformation from 2f to 3f during RT data collection of 2f (crystal 2)

Run 1 (50 frames)

a= 13.194(8) Å, *b*=13.268(7) Å, *c*= 14.105(7) Å, *α*=85.24(2) Å, *β*=72.90(2) Å, *γ*=82.51(2) Å, V=2233(3) Å^3

Run 2 (50 frames)

a=13.055(26) Å, *b*=13.190(21) Å, *c*=14.080(21) Å, *α*=85.07(4) Å, *β*=72.49(5) Å, *γ*=82.56(7) Å, V=2290(8) Å^3

Run 3 (50 frames)

a=17.212(52) Å, *b*=19.972(87) Å, *c*=14.107(40) Å, *α*=90, *β*=96.22(5), *γ*=90, V=4821(29) Å^3

Run 4 (50 frames)

a= 17.357(59) Å, *b*= 19.927(42) Å, *c*= 14.125(30) Å, *α*=90, *β*=96.18(8), *γ*=90, V= 4857(20) Å^3

12. Powder X-ray diffraction (PXRD)

Experiments were carried out on a PANalytical X'Pert PRO instrument using Bragg-Brentano geometry. Intensity data were collected using an X'Celerator detector and 2θ scans (Cu K_α radiation, λ = 1.5418 Å) were carried out in the range of 5-40°. The phase purity of the as-

synthesised **2f** and the activated form **3f** was confirmed by comparison of experimental PXRD with the simulated PXRD patterns from the respective crystal structures. PXRD was used to study conversion of **2f** to **3f** under different conditions.

Heating at 120 °C under dynamic vacuum for 12 hours

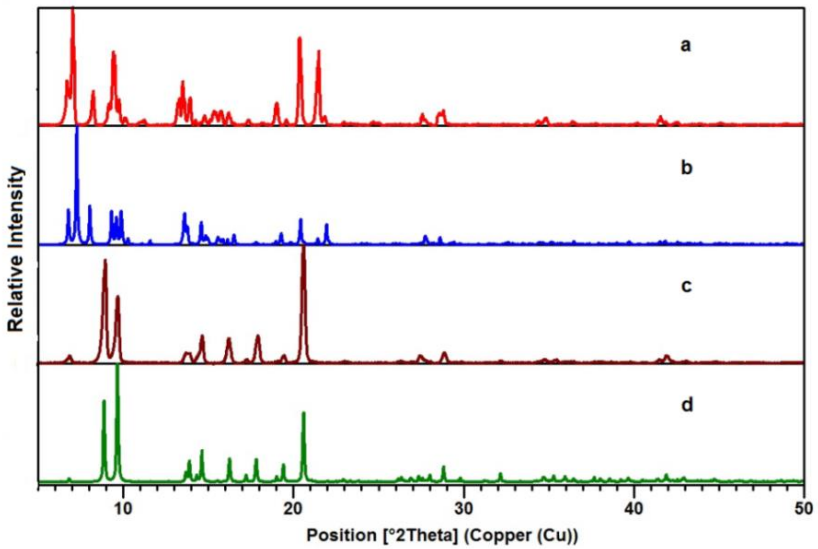

Figure S4. (a) PXRD patterns of as-synthesised **2f**, (b) simulated PXRD pattern of **2f** from crystal structure, (c) PXRD pattern of activated sample and (d) simulated PXRD pattern of **3f** from crystal structure.

13. Dichloromethane (DCM) exchanged 2f crystals on exposure to ambient conditions after 2 hours

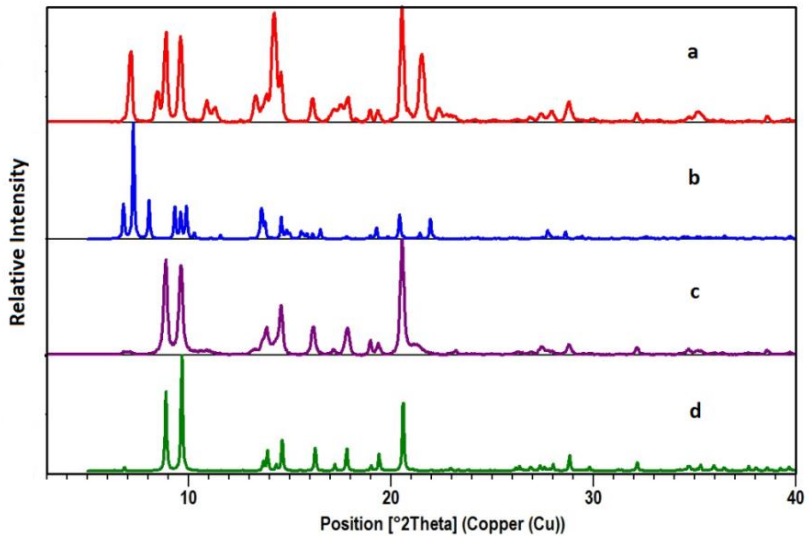

Figure S5. (a) PXRD patterns of DCM exchanged crystals, (b) simulated PXRD pattern of **2f** from crystal structure, (c) DCM exchanged crystals on exposure to ambient conditions after 2 hours and (d) simulated PXRD pattern of **3f** from crystal structure.

14. 2f crystals under ambient conditions for 12 hours

The conversion of **2f** crystals to **3f** also took place at the room temperature by keeping crystals under ambient conditions for 12 hours.

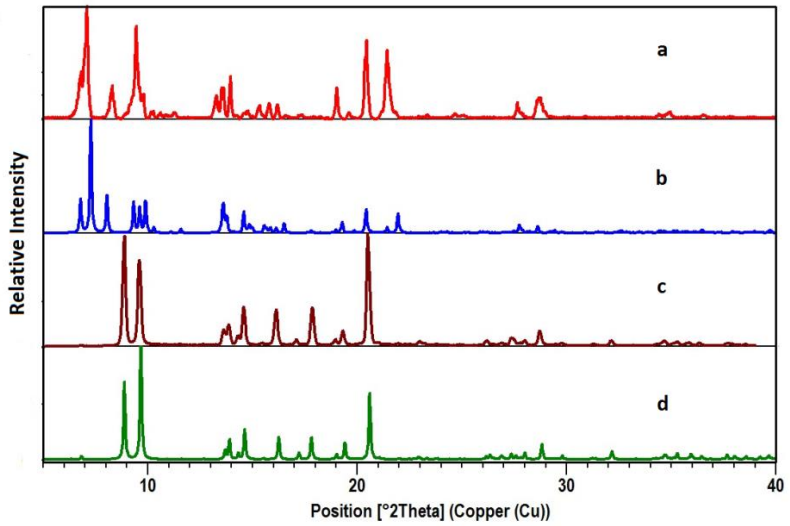

Figure S6. (a) PXRD patterns of as-synthesised **2f**, (b) simulated PXRD pattern of **2f** from crystal structure, (c) PXRD pattern of sample after keeping it under ambient conditions for 12 hours and (d) simulated PXRD pattern of **3f** from crystal structure.

15. Treatment of 2f with supercritical CO_2

The as-synthesised crystals of **2f** were exposed to supercritical CO_2 for activation. The PXRD pattern of these crystals was recorded after 3 hours and then again after 2 days. The PXRD pattern after 2 days of treatment with supercritical CO_2 is very similar to that of **3f**.

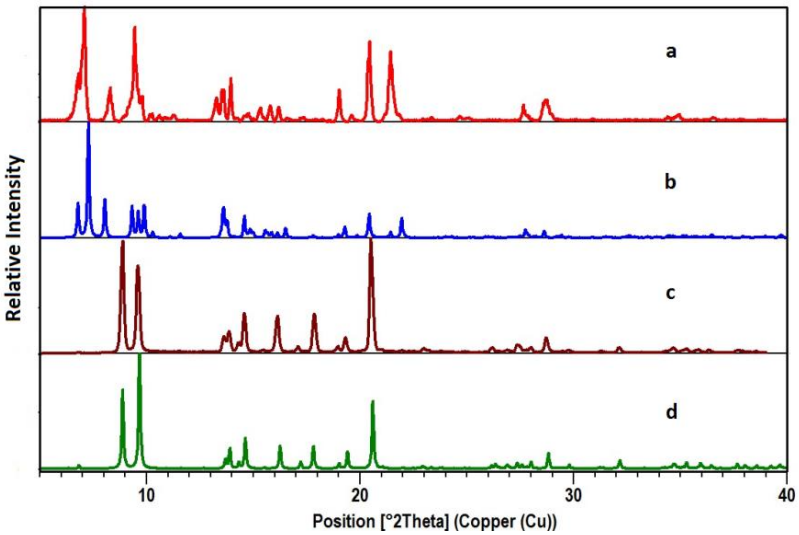

Figure S7. (a) PXRD patterns of crystals kept in supercritical CO_2 for 2 hours, (b) simulated PXRD pattern of **2f** from the SCD crystal structure, (c) PXRD patterns of crystals kept in supercritical CO_2 for 2 days and (d) simulated PXRD pattern of **3f** from crystal structure.

16. Variable temperature powder x-ray diffraction (VTPXRD) of 2f

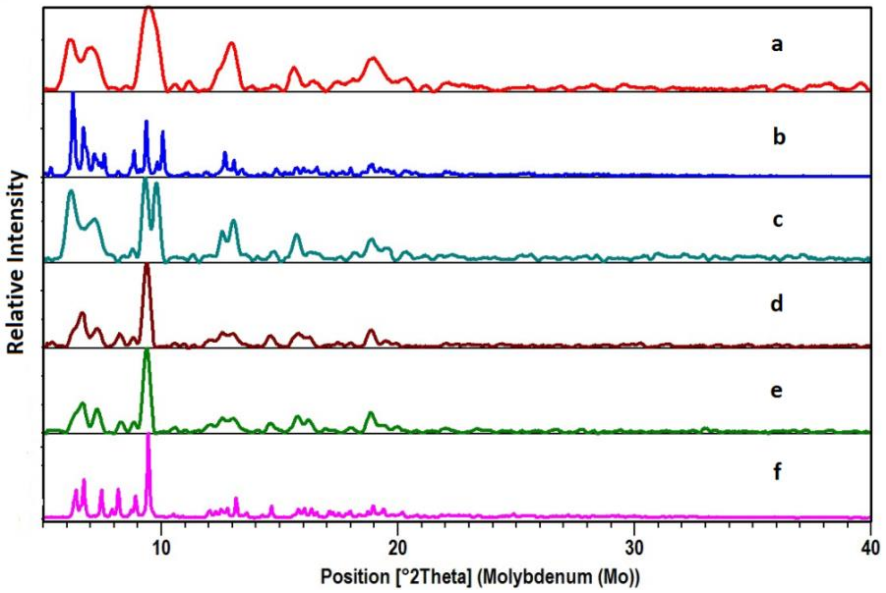

Figure S8. PXRD patterns collected using a Mo K_α source (a) PXRD pattern of crystals of **2f** at 25 ^oC, (b) simulated PXRD pattern of **2f** from the crystal structure, (c) PXRD pattern at 100 ^oC, (d) PXRD pattern at 120 ^oC, (e) PXRD pattern at 150^o C and (f) simulated PXRD pattern of **3f** from crystal structure.

17. Powder X-Ray Diffraction patterns for [Zn(ndc)$_2$(bpe)]

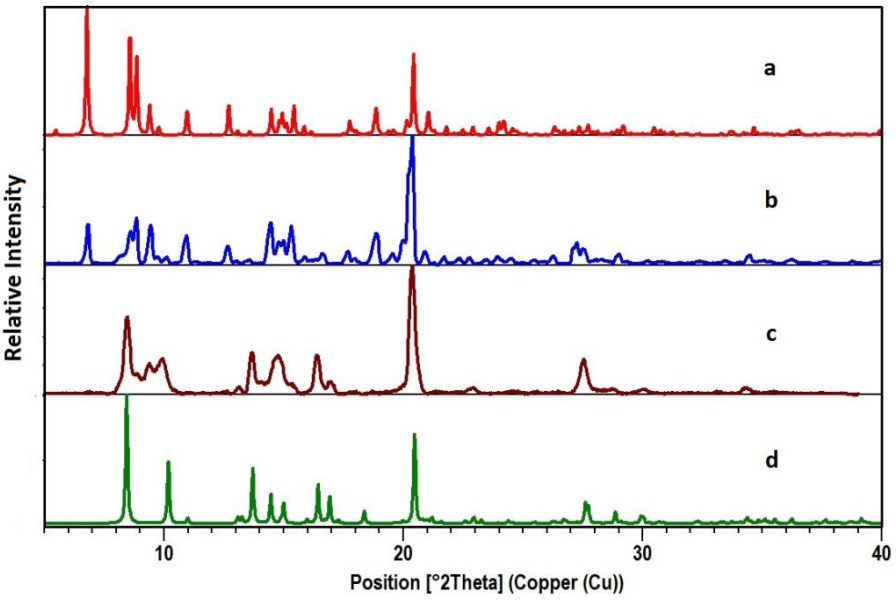

Figure S9. (a) Simulated PXRD patterns from reported doubly-interpenetrated [Zn(ndc)$_2$(bpe)] crystal structure, (b) PXRD pattern of as-synthesised [Zn(ndc)$_2$(bpe)], (c) PXRD pattern of activated sample and (d) simulated PXRD patterns from reported triply interpenetrated [Zn(ndc)$_2$(bpe)] crystal structure

18. Thermogravimetric Analysis (TGA)

Thermal analyses were carried out using a TA Instruments Q500 thermogravimetric analyser. The activated crystals of **2f** were kept in DMF for 24 h in an attempt to regenerate the as-synthesised form **2f** and the TGA for these crystals was recorded. The TGA showed only 2.4% weight loss below 200 ^{o}C, followed by single step decomposition of the product around 400 ^{o}C.

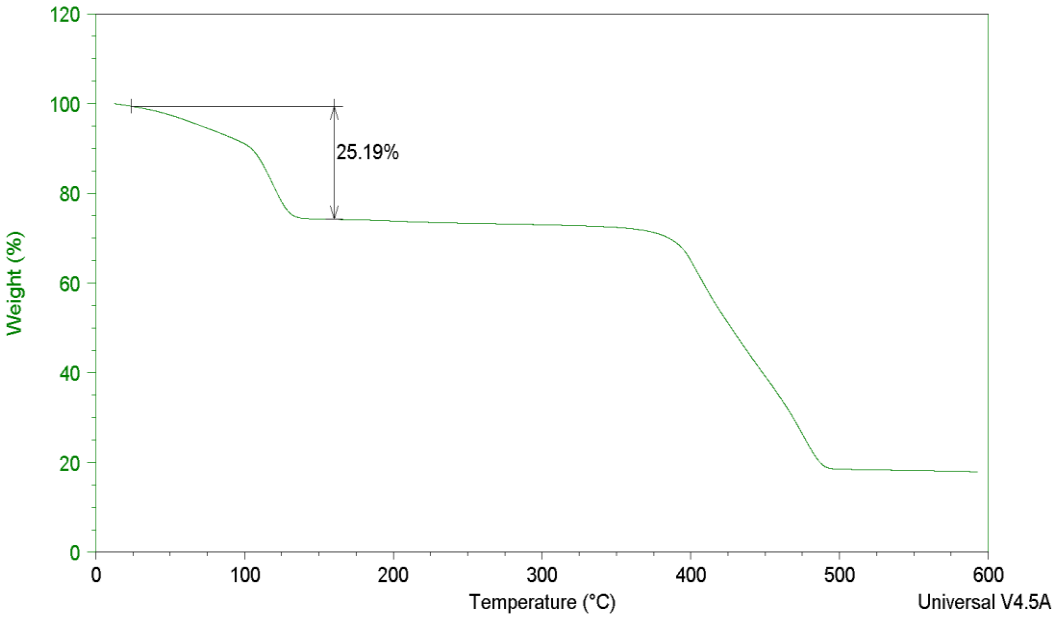

(a)

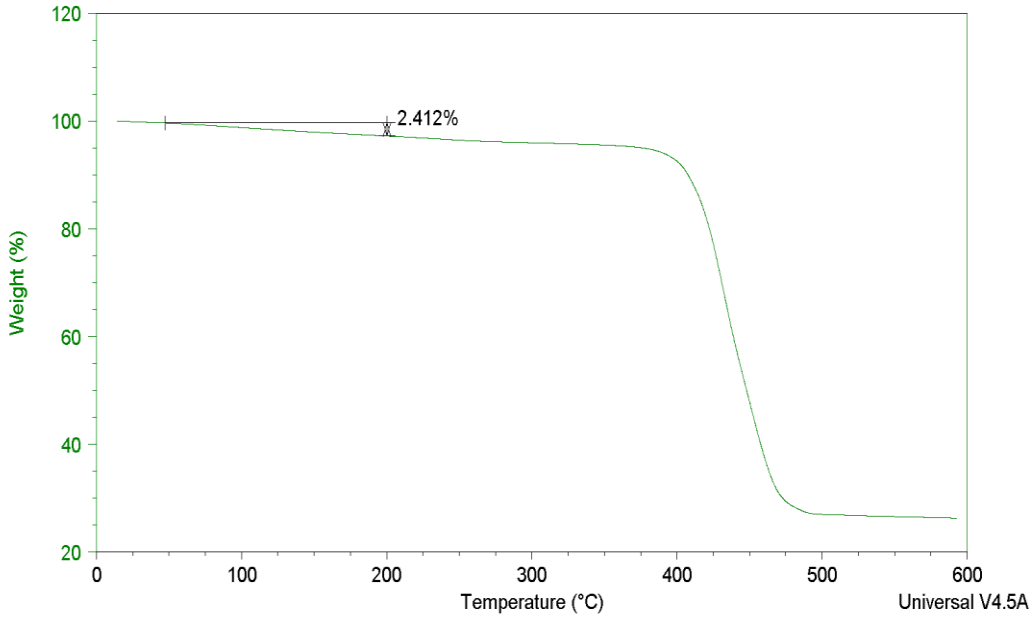

(b)

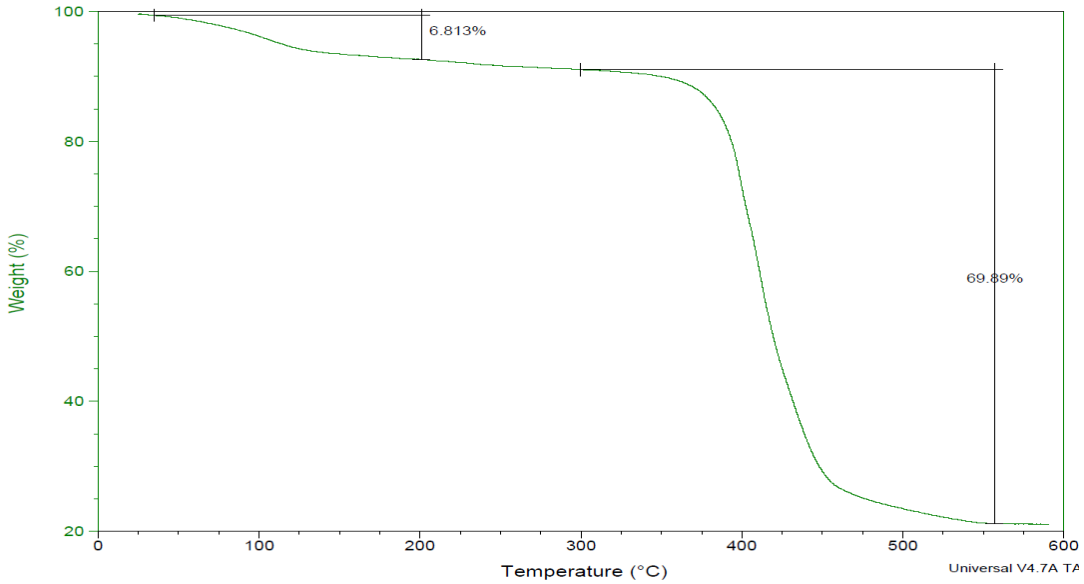

(c)

Figure S10. (a) The TGA analysis of the as-synthesised crystals of **2f**, (b) TGA analysis of DMF-regenerated activated crystals (transformed **3f**) and (c) TGA analysis of as-synthesised **3f**.

19. Differential Scanning Calorimetry (DSC)

DSC analysis was carried out using a TA Instruments Q100 differential scanning calorimeter.

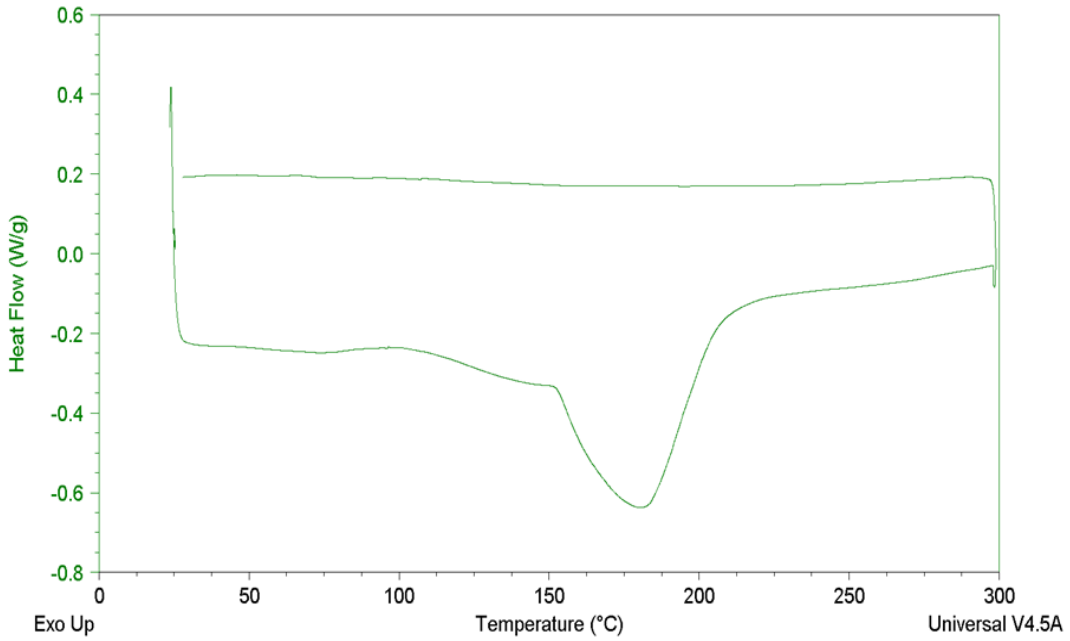

Figure S11. DSC analysis of as-synthesised **2f** crystals; the broad endotherm around 170 °C corresponds to solvent loss.

20. Solid-state UV-visible spectroscopy

Solid state UV-visible spectroscopy was carried out on Analytik Jena SPECORD 210 plus spectrometer equipped with an integrating sphere for solid samples.

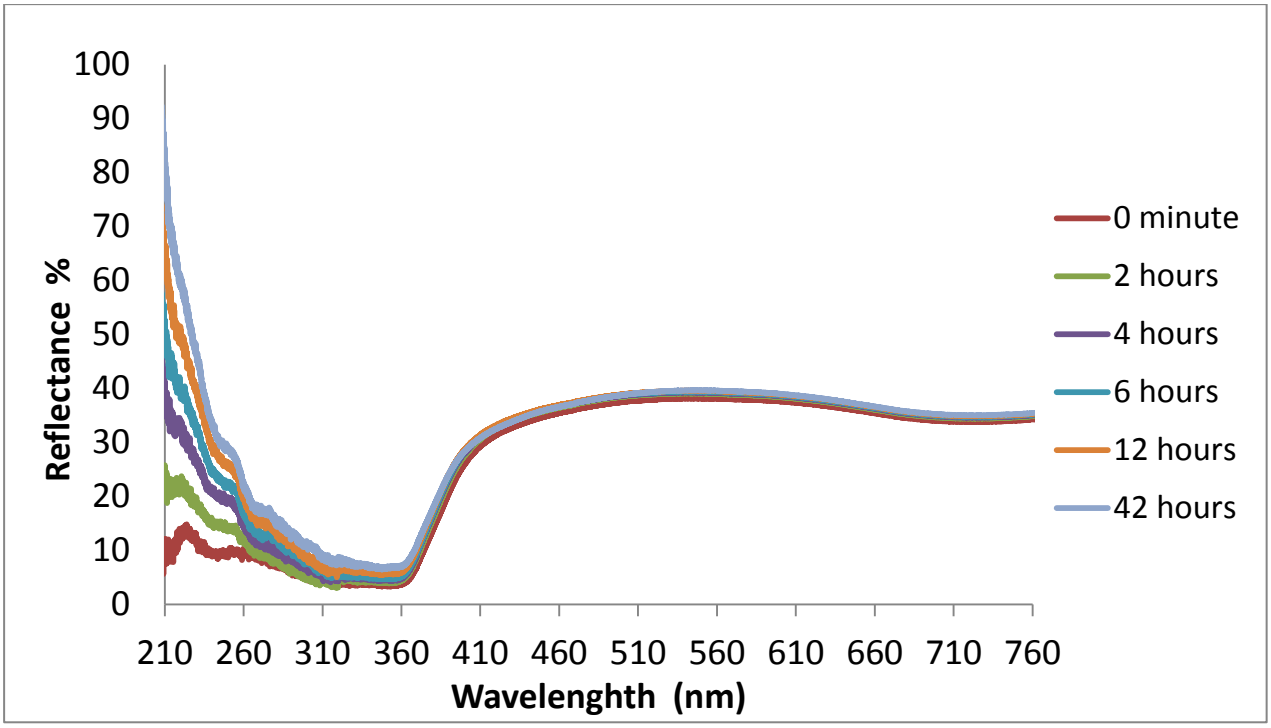

Figure S12. Time-lapse solid-state UV-visible spectrum of **2f**. The reflectance spectrum slowly changes over a time and after 12 hours resembles that of **3f**.

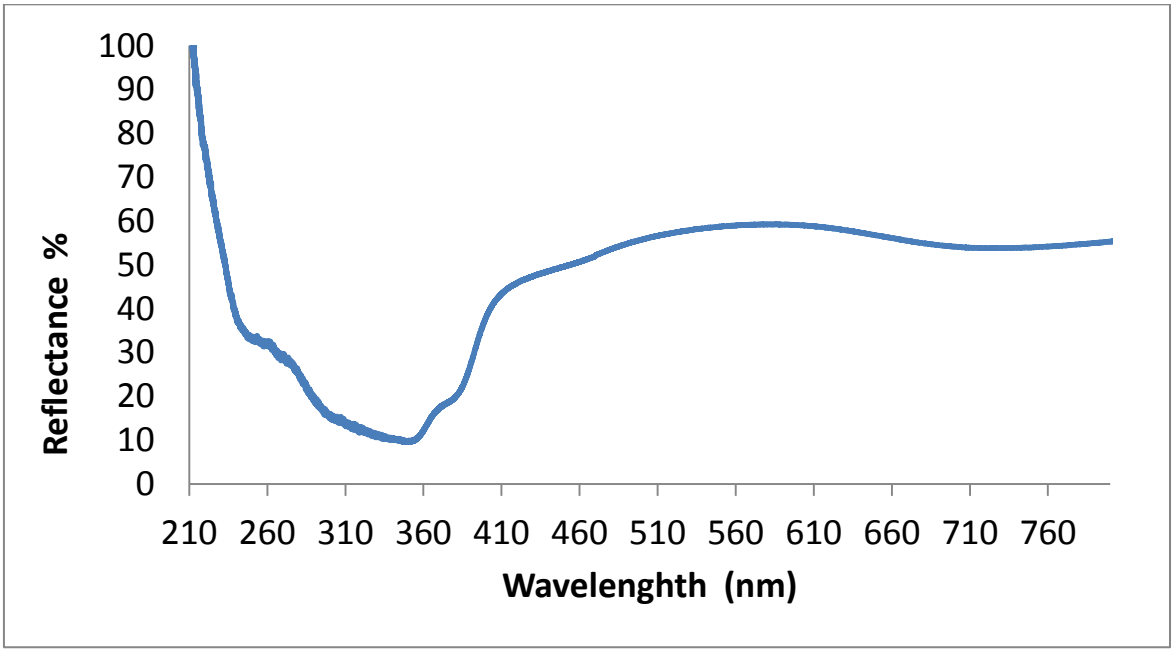

Figure S13. Solid-state UV-visible spectrum of **3f**.

21. Conversion of 2f to 3f followed by optical microscopy.

Optical microscopy was carried out on Leica microscope equipped with a Leica camera DFC290 HD.

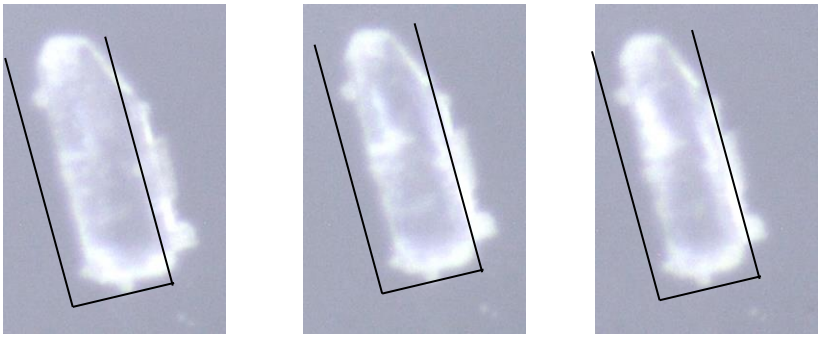

(a) **(b)** **(c)**

Figure S14.Time-lapse photographs of single-crystal to single-crystal conversion from **2f** to **3f**. (a) Crystal of **2f** from mother liquor (0 hours), (b) after 6 hours and (c) after 24 hours.

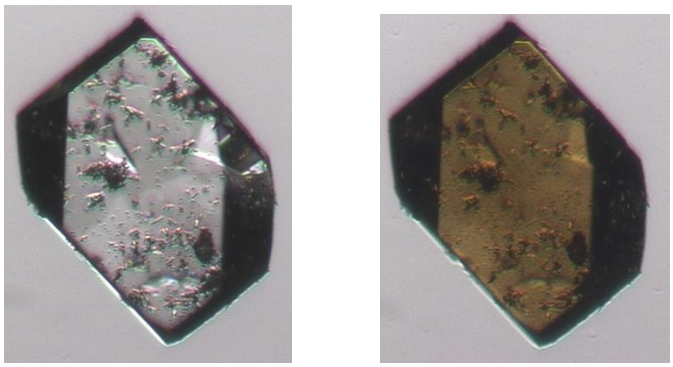

(a) (b)

Figure S15. (a) Initial photomicrograph of a crystal and (b) photomicrograph of the same crystal after 24 hours under ambient conditions. The change in the size cannot be observed from this view of the crystals.

22. Computational methodology

The optimisations was carried out using the PW1PW91 functional, the 6-31G basis set with a single polarisation function and LANL2 pseudo potentials on the Zn atoms. The scan was performed by tilting the bpy molecule by manipulating one of its dihedral angles. The optimisation was performed using internal coordinates with only the scan parameter fixed at each of the scan points. The coordination angle (θ) and bpy molecule angle (φ) were measured as indicated in Fig. 3b and plotted against the coordination bond distance and relative energy of the system.

23. Irreversibility of the transformation

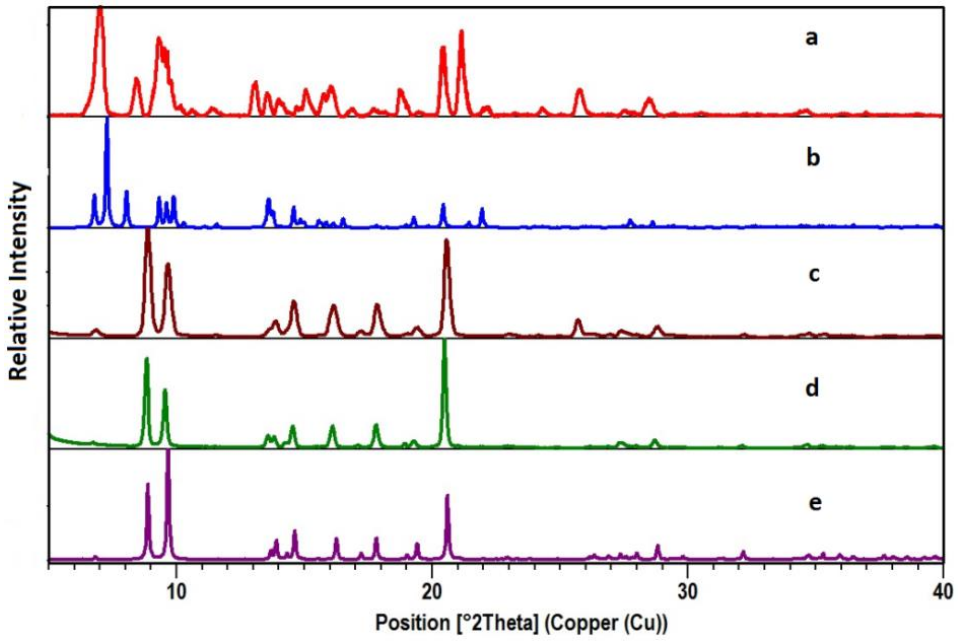

Figure S16: (a) PXRD pattern of as synthesised **2f**, (b) Simulated PXRD pattern of **2f** from the SCD structure, (c) PXRD pattern of the material after activation by heating under dynamic vacuum (i.e. **3f**), (d) PXRD pattern of **3f** after immersion in fresh DMF at 120 °C for 24 hours and (e) simulated PXRD pattern of **3f** from SCD data.

24. Comparison of the simulated PXRD patterns of 3f′ and 3f

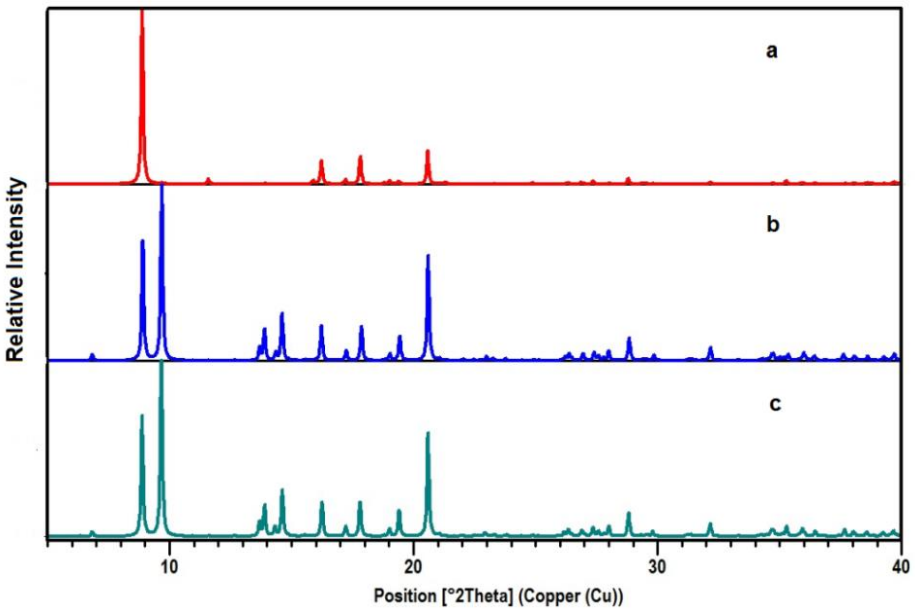

Figure S17: (a) Simulated PXRD pattern of reported **3f**', (b) Simulated PXRD pattern of as synthesised **3f**, (c) Simulated PXRD pattern of **3f** obtained after transformation from **2f**.

References

1. SAINT Data Reduction Software, Version 6.45; Bruker AXS Inc., Madison, WI, 2003.

2. (a) SADABS, Version 2.05; Bruker AXS Inc., Madison, WI, 2002; (b) R. H. Blessing, *Acta Crystallogr.*, Sect. A: Found. Crystallogr. **1995**, 51, 33.

3. G. M. Sheldrick, *Acta Crystallogr.*, Sect. A: Found. Crystallogr. **2008**, 64, 112.

4. L. J. Barbour, *J. Supramol. Chem*. **2001**, 1, 189.

CHAPTER 4

TRANSFORMATION FROM NON- TO DOUBLE-INTERPENETRATION IN ROBUST Cd(II) DOUBLY-PILLARED LAYERED METAL-ORGANIC FRAMEWORKS

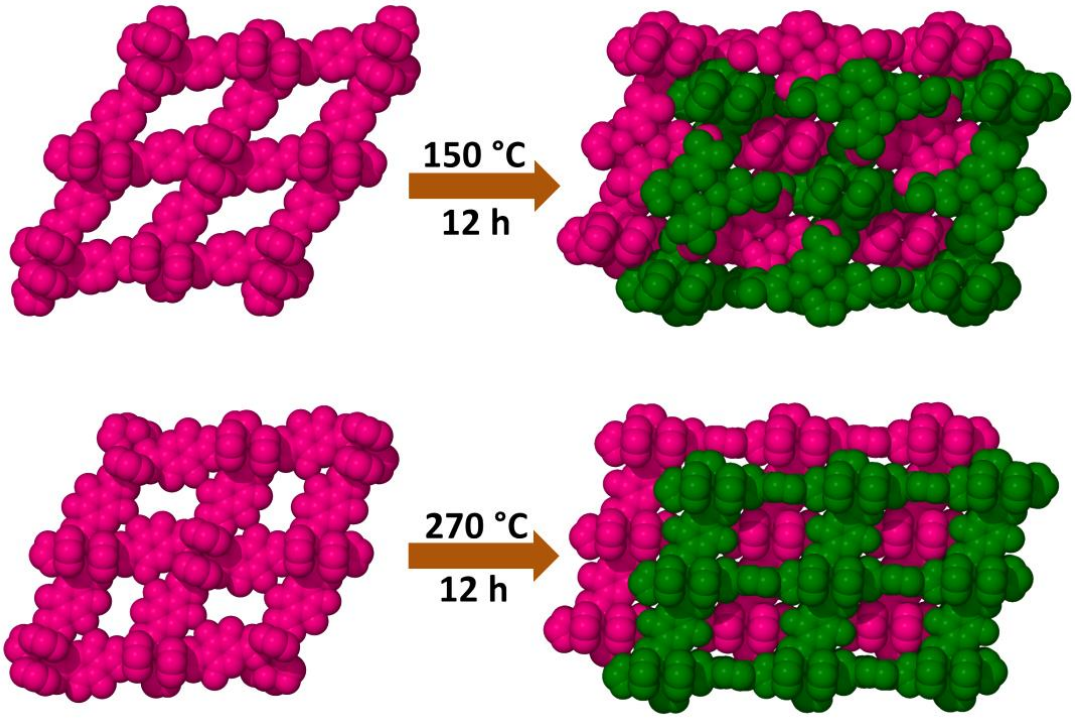

Author's Contribution

- Designed the project.
- Synthesised [Cd(tp)(4,4′-bpy)] and [Cd(atp)(4,4′-bpy)] crystals.
- Performed all additional studies such as PXRD, TGA and Rietveld refinements.
- Discussed and evaluated results with co-authors.
- Wrote manuscript with inputs from Prem Lama.

ChemComm

COMMUNICATION

View Article Online
View Journal | View Issue

Transformation from non- to double-interpenetration in robust Cd(II) doubly-pillared-layered metal–organic frameworks†

Himanshu Aggarwal, Prem Lama and Leonard J. Barbour*

Cite this: *Chem. Commun.*, 2014, 50, 14543

Received 9th September 2014,
Accepted 28th September 2014

DOI: 10.1039/c4cc07112c

www.rsc.org/chemcomm

Two known Cd(II) non-interpenetrated doubly-pillared metal organic frameworks are shown to undergo a change of degree of interpenetration upon loss of lattice solvent molecules to yield doubly-interpenetrated frameworks. The conversion is inferred from powder X-ray diffraction (PXRD) patterns and supported by additional evidence from single-crystal diffraction (SCD) data.

We[1] and others[2] have long been interested in solid–solid phase transformations resulting from guest insertion/removal into/from inclusion compounds. Indeed, such phenomena are particularly important for the utility of porous crystalline systems such as metal–organic frameworks (MOFs). Some of the most important attributes of a MOF include its rigidity, free volume and surface area. Typically, a MOF would be prepared[3] (usually under solvothermal conditions) and then 'activated' by removal of the solvent molecules. In ideal cases the material would retain its framework connectivity without collapse or distortion of the network – MOFs with metal cluster nodes (*i.e.* secondary building units) are generally thought to be more robust to the activation process.[4]

Interpenetration[5] or catenation of MOFs[6] is a well-known phenomenon; when the geometry of the system allows, two or more independent frameworks can become interwoven to yield double-, triple- or even higher-order interpenetration. For a given framework the free volume and surface area depend on the total number of nets involved. Since gas sorption[7] is considered one of the major applications of MOFs, interpenetration is usually undesirable because it results in reduction of the guest-accessible space[8] (*i.e.* less porosity). To overcome this problem, several groups have tried to control the degree of interpenetration using various techniques such as liquid epitaxy,[9] variation of temperature[10,11] and concentration,[11] and the use of bulkier solvents for crystallisation.[12] As a result of these strategies, a number of MOFs have been reported that exhibit less interpenetration than their network topologies can allow.[13] However, the phenomenon of dynamic conversion between different orders of interpenetration has received little attention to date.

We recently reported how a highly porous doubly-interpenetrated MOF converts to a less porous triply-interpenetrated form upon loss of solvent molecules from the channels.[14] Since it seems that switching of degree of interpenetration upon activation is generally assumed to be improbable, we became interested in investigating whether such occurrences are restricted to only a handful of specific systems, or if the phenomenon might be more general. We thus expanded our study to include a supposedly more robust system, and its analogue.

Here we report on our investigation of two closely-related non-interpenetrated MOFs which have previously been described by other groups. Frameworks **1** and **2** have the formulae [Cd(tp)-(4,4′-bpy)][11,15] and [Cd(atp)(4,4′-bpy)],[10] respectively (Scheme 1, tp = terephthalate; 4,4′-bpy = 4,4′-bipyridine and atp = 2-aminoterephthalate).

These frameworks are comprised of Cd(II) ions coordinated to carboxylate linkers to form two dimensional networks, which are further linked by means of 4,4′-bipyridine ligands to yield infinite three-dimensional doubly-pillared structures. Both systems have been reported to form non-interpenetrated as well as doubly-interpenetrated structures (Fig. 1). However, the possibility has not been suggested that the corresponding structures might interconvert by switching their degrees of interpenetration.

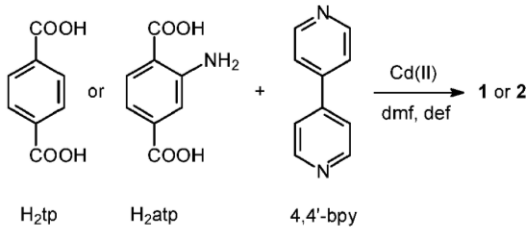

Scheme 1 Synthetic scheme for the preparation of frameworks **1** and **2**.

Department of Chemistry and Polymer Science, University of Stellenbosch, Private Bag X1, Matieland, 7602, South Africa. E-mail: ljb@sun.ac.za

† Electronic supplementary information (ESI) available: PXRD patterns, thermal analysis, crystallographic information, Rietveld refinement parameters and additional figures. See DOI: 10.1039/c4cc07112c

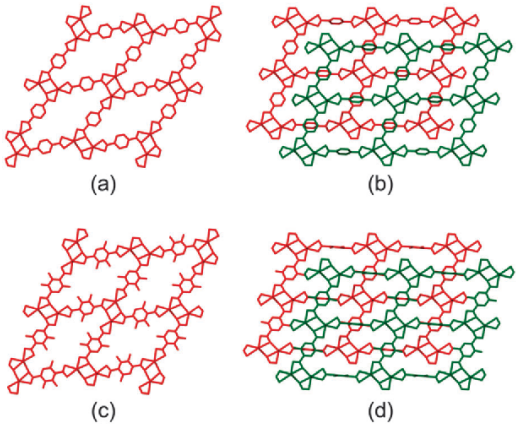

Fig. 1 Packing diagrams of (a) non-interpenetrated **1**, (b) doubly-interpenetrated **1**, (c) non-interpenetrated **2** and (d) doubly-interpenetrated **2**.

As expected, the non-interpenetrated structures are more porous than their corresponding doubly-interpenetrated forms. As part of our investigation we prepared the non-interpenetrated form of framework **1** using the reported procedure.[11] The crystal structure possesses free volume of 59.3% of the unit cell[11,16] with dimethyl formamide (dmf) and water molecules occupying the channels. Thermogravimetric analysis (TGA) shows continuous weight loss up to 160 °C, which corresponds to the loss of all the solvent molecules. The PXRD pattern of the bulk material was compared with that simulated from the reported SCD structure[11] to establish phase purity of the crystals. In order to completely remove the solvent molecules from the channels, the as-synthesised crystals were evacuated at 150 °C under dynamic vacuum for 12 hours. The crystals remained transparent upon desolvation, yielding a PXRD pattern different from that of the as-synthesised material but matching that simulated from the reported twofold-interpenetrated crystal structure of **1**[15] (Fig. 2). This finding indicates that the as-synthesised non-interpenetrated framework transforms to its doubly-interpenetrated form upon activation.

This result is consistent with our previous observation that the loss of solvent from MOF channels can result in switching of degree of interpenetration, showing that the phenomenon is not limited to only one system. Although we attempted to record SCD intensity data for the activated crystals, they had been subjected to a relatively high activation temperature and the quality of the data was therefore insufficient for acceptable structure solution and refinement. Nevertheless, comparison of the unit cell parameters of the activated crystals with those of the reported twofold-interpenetrated structure confirmed that the crystals had indeed undergone a change in degree of interpenetration (ESI†). It seems reasonable to propose that the change in interpenetration occurs as a result of the empty space created upon solvent removal – the architecture of the framework can accommodate interpenetration and the coordination linkages are sufficiently labile to allow the process to proceed once the space becomes available.

As a continuation of this study, we also investigated the closely analogous system **2**, where terephthalate is replaced by

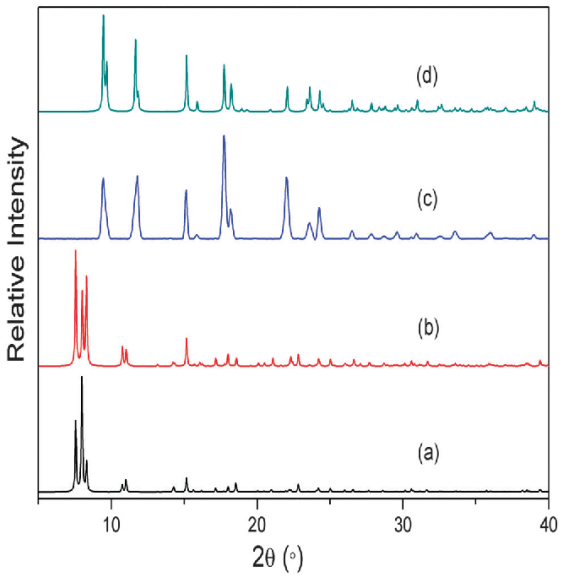

Fig. 2 (a) Simulated PXRD pattern of non-interpenetrated **1**, (b) experimental PXRD pattern of as-synthesised **1**, (c) experimental PXRD pattern of **1** activated at 150 °C and (d) simulated PXRD pattern of the reported crystal structure of doubly-interpenetrated **1**.

2-aminoterephthalate, but the overall coordination environment around the central metal atoms remains the same. We prepared crystals of non-interpenetrated [Cd(atp)(4,4′-bpy)] by following the reported procedure;[10] the PXRD pattern of the as-synthesised crystals was compared with the simulated PXRD pattern for the known structure in order to confirm phase purity of the bulk material. The free volume in framework **2** is 61.2% of the unit cell[10,16] and TGA shows continuous weight loss until 220 °C, corresponding to the complete loss of dmf and water molecules from the channels. Similar to the treatment of **1**, as-synthesised bulk crystals of **2** were evacuated at 150 °C under dynamic vacuum for 12 hours. The PXRD pattern of the resulting material differed considerably from that of the as-synthesised crystals (ESI†) but it did not match that simulated for the reported doubly-interpenetrated SCD structure of **2**.[10] Further activation was carried out at 270 °C, after which the PXRD pattern matched that of **2** (Fig. 3). The harsher conditions required for the activation of **2** can be attributed to the presence of the amino groups directed towards the framework channels; *i.e.* more energy is required for the process of solvent removal and concomitant disassembly/reassembly of the framework. As noted for the transformation of **1**, it was possible to determine the unit cell parameters of **2** by means of SCD data, but the diffraction record was of insufficient quality for rigorous crystal structural analysis (ESI†).

Based on our previous report on the change in mode of interpenetration of $[Zn_2(ndc)_2(4,4'\text{-bpy})]$,[14] we can postulate a possible mechanism for the transformations experienced by **1** and **2**. It is well known that molecular crystal solvates are generally stabilised by the presence of the solvent molecules.

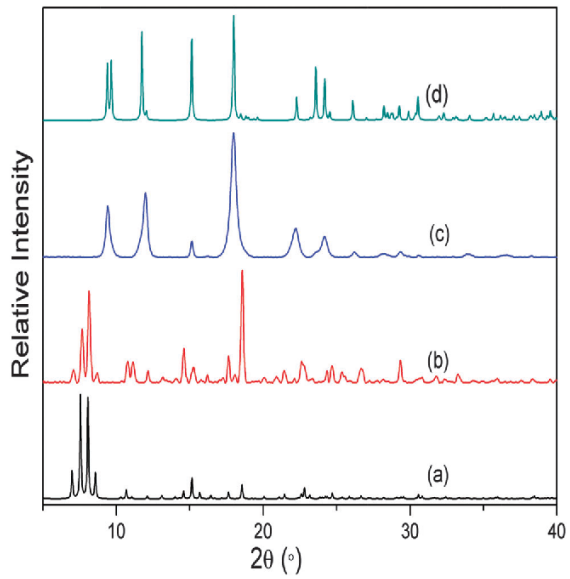

Fig. 3 (a) Simulated PXRD pattern of non-interpenetrated **2**, (b) experimental PXRD pattern of as-synthesised **2**, (c) experimental PXRD pattern of **2** activated at 270 °C and (d) simulated PXRD pattern of the reported crystal structure of doubly-interpenetrated **2**.

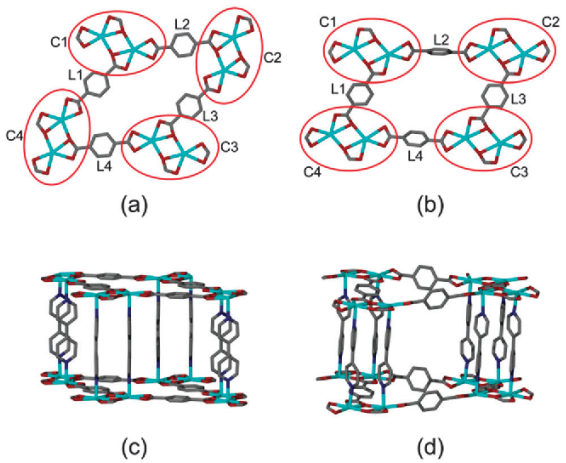

Fig. 4 Comparison of corresponding parts of an individual network representing framework **1** in both its non-interpenetrating and doubly-interpenetrating forms: arrangement of metal clusters and tp units in the (a) non-interpenetrated and (b) doubly-interpenetrated forms and arrangement of the 4,4′-bpy ligands in the (c) non-interpenetrated and (d) doubly-interpenetrated forms.

That is, the solvent molecules play a structural role until they are removed, whereupon the host molecules rearrange to form a closely-packed apohost phase. We believe that the same holds true for some MOF structures; *i.e.* that the frameworks are partially supported by the solvent molecules. When an attempt is made to activate the crystals by removing the solvent molecules, the vacant spaces thus created allow the coordination bonds to become distorted. In extreme cases, the coordination environment about the metal centre can undergo modification.[17] In even more severe cases, the secondary building units may disassemble and reassemble, which could also involve changes in entanglement of the coordination networks.[14,18] Such a process involves rapid bond dissociation and formation to yield a thermodynamically more stable structure with a higher degree of interpenetration. It is interesting to note the differences between the current systems and our previously reported examples where the change of interpenetration was from doubly- to triply- in singly-pillared-layered paddlewheel structures. Systems **1** and **2** are more robust owing to their doubly-pillared-layered structures and the change in interpenetration is from non- to doubly-. Moreover, in the case of $[Zn_2(ndc)_2(4,4'\text{-bpy})]$[14] the conversion took place under ambient conditions whereas the transformation requires elevated temperatures for **1** and **2**.

Close inspection of the non-interpenetrated [Cd(tp)(4,4′-bpy)] structure shows that four dinuclear Cd(II) clusters along with four tp units form a cyclic metallo-organic unit with cluster C1 in the same orientation as C3 and cluster C2 in the same orientation as C4 (Fig. 4). All of the aromatic units of the terephthalate ligands (L1 to L4) are in the metal–carboxylate plane – *i.e.* parallel to (001) and the doubly-pillaring bipyridyl linkers are parallel to [001], with a dihedral angle of 2.1(1)° between the two pyridyl rings. Upon activation of non-interpenetrated **1** at 150 °C, rotation of two of the four terephthalate linkers (L2 and L4) takes place. This is concomitant with coordination bond breaking and formation within the metal cluster, thereby altering the orientations of the diagonally placed metal-cluster nodes C2 and C4. In the non-interpenetrated structure all four tp units have one carboxylate coordinated to the metal centre in chelating mode whereas the second carboxylate group is coordinated in both bridging and chelating fashion. However, in the corresponding doubly-interpenetrated structure, both of the carboxylate groups of L2 and L4 are coordinated to the metal centre in chelating fashion only, whereas both of the carboxylate groups of L1 and L3 are coordinated in bridging as well as chelating mode. Furthermore, the pyridyl rings of the 4,4′-bpy ligands are twisted relative to one another with a dihedral angle of 38.7(8)°. Owing to the changes in metal cluster nodes C2 and C4, all four dinuclear Cd(II) clusters (C1 to C4) assume the same general orientation in the twofold-interpenetrated framework. During the transformation of **1** from being non-interpenetrated to doubly-interpenetrated the diagonal distances between the metal cluster centres (*i.e.* the Cd···Cd centroid) changes from 21.29(7) × 12.95(7) Å to 20.17(4) × 16.11(3) Å (ESI†). We also note that the originally planar geometry of the ring C1–C4 becomes distorted as a result of the transformation.

A similar rearrangement of the metal clusters and ligand coordination mode occurs during the transformation of **2** (Fig. 5). The diagonal distances between the metal clusters change from 21.10(3) × 13.70(2) Å to 20.48(6) × 15.95(2) Å on conversion from non-interpenetrated to twofold interpenetrated **2** (ESI†).

We have shown that robust doubly-pillared structures can also undergo change in degree of interpenetration upon loss of solvent molecules from the channels. The transformation occurs at 150 °C in the case of framework **1**, whereas the analogous

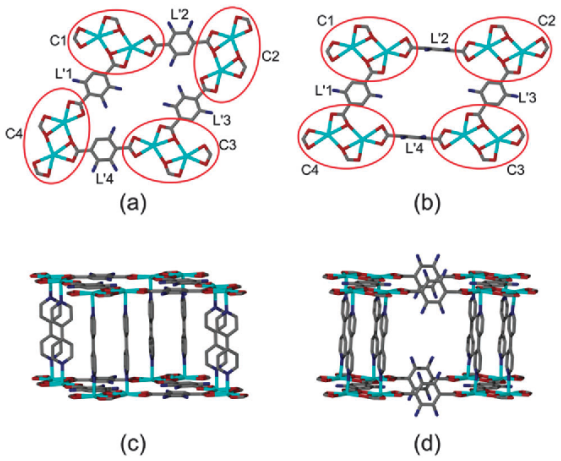

Fig. 5 Comparison of corresponding parts of an individual network representing framework **2** in both its non-interpenetrating and doubly-interpenetrating forms: arrangement of metal clusters and atp units in the (a) non-interpenetrated and (b) doubly-interpenetrated forms and arrangement of the 4,4′-bpy ligands in the (c) non-interpenetrated and (d) doubly-interpenetrated forms.

conversion of framework **2** requires a much higher temperature. This is due to the presence of the amino group in **2**, which most likely obstructs the channels, thereby making it more difficult for the system to accommodate another network. Over the past few years there has been significant interest[19] in the post-synthetic modification (PSM) of MOFs and, in this regard, a change in the degree of interpenetration can be considered to be a new form of PSM. We believe that similar transformations are possible in other MOF systems and that a more detailed study is required in order to better understand such phenomena.

We are grateful to the SARChI Programme of the Department of Science and Technology and the National Research Foundation (South Africa) for financial support. P. L thanks the Claude Leon Foundation for financial support.

Notes and references

1 (*a*) L. J. Barbour, M. R. Caira, A. Coetzee and L. R. Nassimbeni, *J. Chem. Soc., Perkin Trans. 2*, 1995, 1345–1349; (*b*) J. L. Atwood, L. J. Barbour, A. Jerga and B. L. Schottel, *Science*, 2002, **298**, 1000–1002; (*c*) J. L. Atwood, L. J. Barbour and A. Jerga, *Chem. Commun.*, 2002, 2952–2953; (*d*) L. J. Barbour, M. R. Caira, T. le Roex and L. R. Nassimbeni, *J. Chem. Soc., Perkin Trans. 2*, 2002, 1973–1979; (*e*) L. Dobrzańska, G. O. Lloyd, C. Esterhuysen and L. J. Barbour, *Angew. Chem., Int. Ed.*, 2006, **45**, 5856–5859; (*f*) D. Das, E. Engel and L. J. Barbour, *Chem. Commun.*, 2010, **46**, 1676–1678; (*g*) T. Jacobs, J.-A. Gertenbach, D. Das and L. J. Barbour, *Aust. J. Chem.*, 2010, **63**, 573–577; (*h*) M. Lusi and L. J. Barbour, *Angew. Chem., Int. Ed.*, 2012, **51**, 3928–3931; (*i*) M. Lusi and L. J. Barbour, *Chem. Commun.*, 2013, **49**, 2634–2636; (*j*) M. Lusi and L. J. Barbour, *CrystEngComm*, 2014, **16**, 36–38; (*k*) M. du Plessis, V. J. Smith and L. J. Barbour, *CrystEngComm*, 2014, **16**, 4126–4132.

2 (*a*) D. Bradshaw, J. E. Warren and M. J. Rosseinsky, *Science*, 2007, **315**, 977–980; (*b*) L. R. Nassimbeni, *Acc. Chem. Res.*, 2003, **36**, 631–637; (*c*) A. Schneemann, V. Bon, I. Schwedler, I. Senkovska, S. Kaskel and R. A. Fischer, *Chem. Soc. Rev.*, 2014, **43**, 6062–6096; (*d*) M. Kawano and M. Fujita, *Coord. Chem. Rev.*, 2007, **251**, 2592–2605; (*e*) J. J. Vittal, *Coord. Chem. Rev.*, 2007, **251**, 1781–1795.

3 (*a*) B. Chen, M. Eddaoudi, S. T. Hyde, M. O'Keeffe and O. M. Yaghi, *Science*, 2001, **291**, 1021–1023; (*b*) D. Han, F.-L. Jiang, M.-Y. Wu, L. Chen, Q.-H. Chen and M.-C. Hong, *Chem. Commun.*, 2011, **47**, 9861–9863; (*c*) H. Kim, S. Das, M. G. Kim, D. N. Dybtsev, Y. Kim and K. Kim, *Inorg. Chem.*, 2011, **50**, 3691–3696.

4 O. M. Yaghi, M. O'Keeffe, N. W. Ockwig, H. K. Chae, M. Eddaoudi and J. Kim, *Nature*, 2003, **423**, 705–714.

5 (*a*) H.-L. Jiang, T. A. Makala and H.-C. Zhou, *Coord. Chem. Rev.*, 2013, **257**, 2232–2249; (*b*) J. L. C. Rowsell and O. M. Yaghi, *J. Am. Chem. Soc.*, 2006, **128**, 1304–1315.

6 (*a*) H. Li, M. Eddaoudi, M. O'Keeffe and O. M. Yaghi, *Nature*, 1999, **402**, 276–279; (*b*) S. Kitagawa and K. Uemura, *Chem. Soc. Rev.*, 2005, **34**, 109–119; (*c*) R. K. Das, A. Aijaz, M. K. Sharma, P. Lama and P. K. Bharadwaj, *Chem. – Eur. J.*, 2012, **18**, 6866–6872; (*d*) C. Dey and R. Banerjee, *Chem. Commun.*, 2013, **49**, 6617–6619.

7 (*a*) S. Horike, S. Shimomura and S. Kitagawa, *Nat. Chem.*, 2009, **1**, 695–704; (*b*) T. Jacobs, G. O. Lloyd, J.-A. Gertenbach, K. K. Müller-Nedebock, C. Esterhuysen and L. J. Barbour, *Angew. Chem., Int. Ed.*, 2012, **124**, 4997–5000.

8 H. Chun, D. N. Dybtsev, H. Kim and K. Kim, *Chem. – Eur. J.*, 2005, **11**, 3521–3529.

9 O. Shekhah, H. Wang, M. Paradinas, C. Ocal, B. Schüpbach, A. Terfort, D. Zacher, R. A. Fischer and C. Wöll, *Nat. Mater.*, 2009, **8**, 481–484.

10 H.-L. Jiang, Yo. Tatsu, Z.-H. Lu and Q. Xu, *J. Am. Chem. Soc.*, 2010, **132**, 5586–5587.

11 J. Zhang, L. Wojtas, R. W. Larsen, M. Eddaoudi and M. J. Zaworotko, *J. Am. Chem. Soc.*, 2009, **131**, 17040–17041.

12 (*a*) H. M. Guo and Z.-M. Sun, *J. Mater. Chem.*, 2012, **22**, 15939–15946; (*b*) L. Ma and W. Lin, *J. Am. Chem. Soc.*, 2008, **130**, 13834–13835.

13 (*a*) L. J. Murray, M. Dinca and J. R. Long, *Chem. Soc. Rev.*, 2009, **38**, 1294–1314; (*b*) T. K. Prasad and M. P. Suh, *Chem. – Eur. J.*, 2012, **18**, 8673–8680.

14 H. Aggarwal, P. M. Bhatt, C. X. Bezuidenhout and L. J. Barbour, *J. Am. Chem. Soc.*, 2014, **136**, 3776–3779.

15 J. Tao, M.-L. Tongand and X.-M. Chen, *J. Chem. Soc., Dalton Trans.*, 2000, 3669–3674.

16 The free volume values given are those reported in the original publications. Using Mercury (C. F. Macrae, P. R. Edgington, P. McCabe, E. Pidcock, G. P. Shields, R. Taylor, M. Towler and J. van de Streek, *J. Appl. Crystallogr.*, 2006, **39**, 453–457), we have calculated guest-accessible volumes of 30.4% and 28.3% for frameworks **1** and **2**, respectively.

17 J. Seo, C. Bonneau, R. Matsuda, M. Takata and S. Kitagawa, *J. Am. Chem. Soc.*, 2011, **133**, 9005–9013.

18 S. B. Choi, H. Furukawa, H. J. Nam, D.-Y. Jung, Y. H. Jhon, A. Walton, D. Book, M. O'Keeffe, O. M. Yaghi and J. Kim, *Angew. Chem., Int. Ed.*, 2012, **51**, 8791–8795.

19 (*a*) M.-H. Zeng, Z. Yin, Y.-X. Tan, W.-X. Zhang, Y.-P. He and M. Kurmoo, *J. Am. Chem. Soc.*, 2014, **136**, 4680–4688; (*b*) M. Kim, J. F. Cahill, H. Fei, K. A. Prather and S. M. Cohen, *J. Am. Chem. Soc.*, 2012, **134**, 18082–18088; (*c*) S. M. Cohen, *Chem. Rev.*, 2012, **112**, 970–1000; (*d*) K. K. Tanabe and S. M. Cohen, *Chem. Soc. Rev.*, 2011, **40**, 498–519; (*e*) R. K. Deshpande, J. L. Minnaar and S. G. Telfer, *Angew. Chem., Int. Ed.*, 2010, **49**, 4598–4602.

Supplementary Information

Transformation from Non- to Double-Interpenetration in Robust Cd(II) Doubly-Pillared-Layered Metal-Organic Frameworks

Himanshu Aggarwal,[a] Prem Lama[a] and Leonard J. Barbour[a]*

*Department of Chemistry and Polymer Science, University of Stellenbosch, Stellenbosch 7600, South Africa

Synthesis

Both [Cd(tp)(4,4′-bipy)] and [Cd(atp)(4,4′-bipy)] non-interpenetrated frameworks were synthesised following previously reported procedures.[1,2]

Single Crystal Parameters

Table S1. Comparison of unit cell parameters of non-interpenetrated, activated and twofold interpenetrated [Cd(tp)(4,4′-bipy)]**.**

Non-interpenetrated [Cd(tp)(4,4′-bipy)] (CCDC REFCODE CUHPUR)	**Activated [Cd(tp)(4,4′-bipy)] (this study)**	**Twofold interpenetrated [Cd(tp)(4,4′-bipy)] CCDC REFCODE LOTXIB**
Space Group = *Pbam*	Space Group = *C2/c*	Space Group = *C2/c*
Temperature (K) = 100	Temperature (K) = 100	Temperature (K) = 294
a (Å) = 12.949(<1)	*a* (Å) = 15.902(3)	*a* (Å) = 16.108(3)
b (Å) = 21.290(<1)	*b* (Å) = 11.664(3)	*b* (Å) = 11.675(2)
c (Å) = 11.683(<1)	*c* (Å) = 20.202(2)	*c* (Å) = 20.171(4)
α (º) = 90	α (º) = 90	α (º) = 90
β (º) = 90	β (º) = 112.093(3)	β (º) = 111.99(3)
γ (º) = 90	γ (º) = 90	γ(º) = 90
V (Å^3) = 3220.82(4)	*V* (Å^3) = 3472.04(3)	*V*(Å^3) = 3517.4(11)

Table S2. Comparison of unit cell parameters of non-interpenetrated, activated and twofold interpenetrated [Cd(atp)(4,4′-bipy)].

Non-interpenetrated [Cd(atp)(4,4′-bipy)] CCDC REFCODE YUXQOY	**Activated [Cd(atp)(4,4′-bipy)] (this study)**	**Twofold interpenetrated [Cd(atp)(4,4′-bipy)] CCDC REFCODE YUXQUE**
Space Group = *Pbam*	Space Group = *C2/m*	Space Group = *C2/m*
Temperature (K) = 293	Temperature (K) = 100	Temperature (K) = 293
a (Å) = 13.700(3)	*a* (Å) = 16.202(2)	*a* (Å) = 15.950(3)
b (Å) = 21.050(4)	*b* (Å) = 11.921(3)	*b* (Å) = 11.700(2)
c (Å) = 11.720(2)	*c* (Å) = 10.438(3)	*c* (Å) = 10.210(2)
α (º) = 90	*α* (º) = 90	*α* (º) = 90
β (º) = 90	*β* (º) = 112.683(3)	*β* (º) = 112.77(3)
γ (º) = 90	*γ* (º) = 90	*γ*(º) = 90
V (Å^3) = 3379.87(5)	*V* (Å^3) = 1860.13(3)	*V*(Å^3) = 1756.8(6)

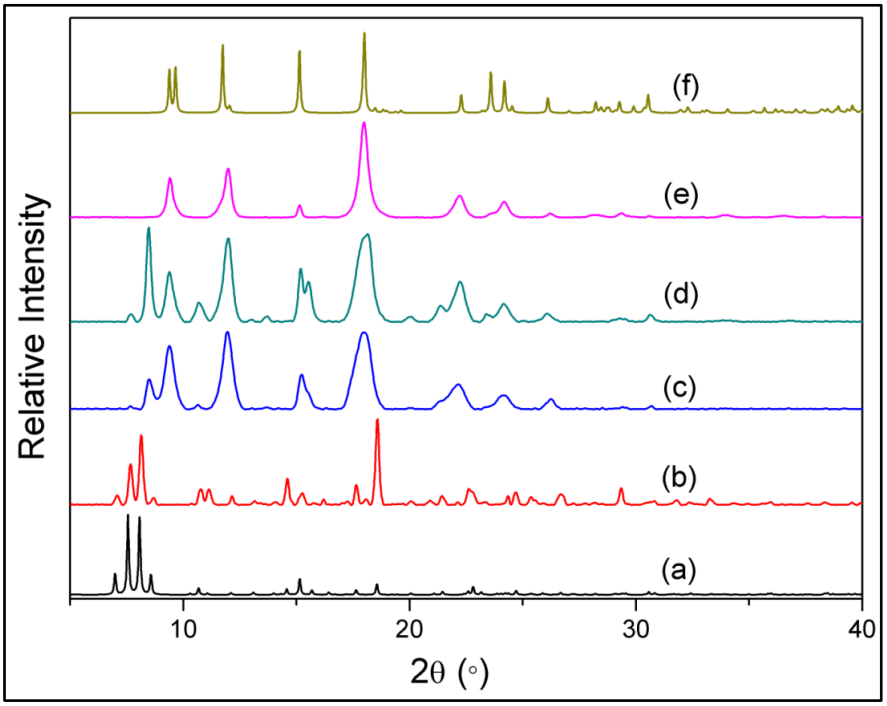

Figure S1: PXRD patterns of (a) simulated non-interpenetrated **2**, (b) as-synthesised non-interpenetrated **2**, (c) activated **2** at 150 °C, (d) activated **2** at 200 °C, (e) activated **2** at 270 °C and (f) (a) simulated doubly-interpenetrated **2**.

Thermogravimetric Analysis (TGA)

Thermogravimetric analysis was carried out using a TA Instruments Q500 analyser. The sample was heated at 40 °C/min from room temperature to decomposition.

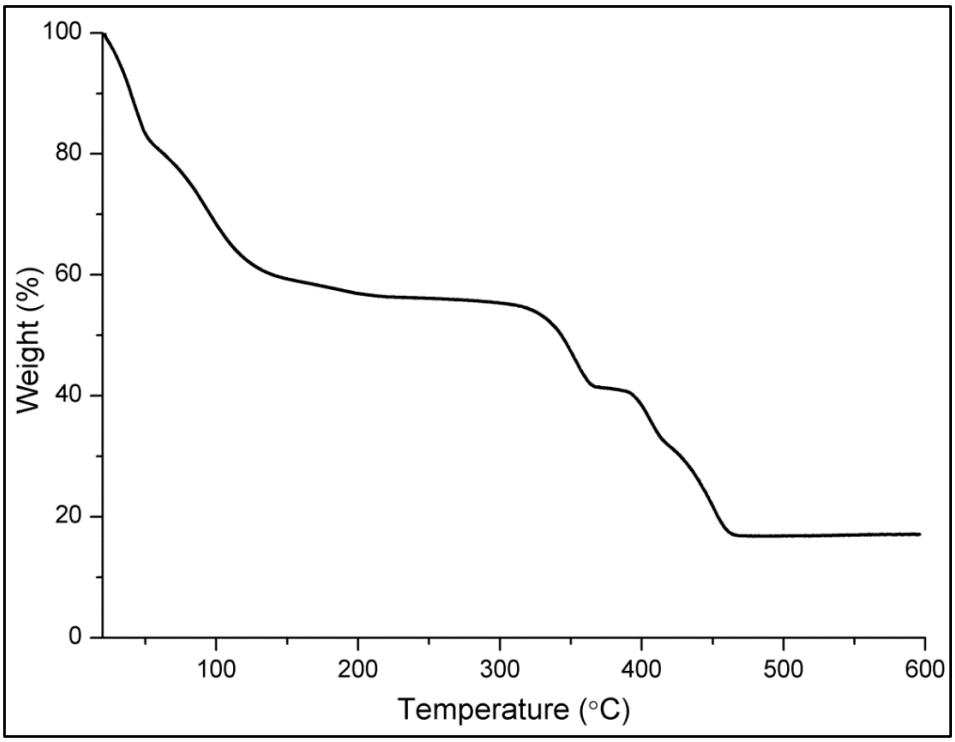

Figure S2: TGA for **1**.

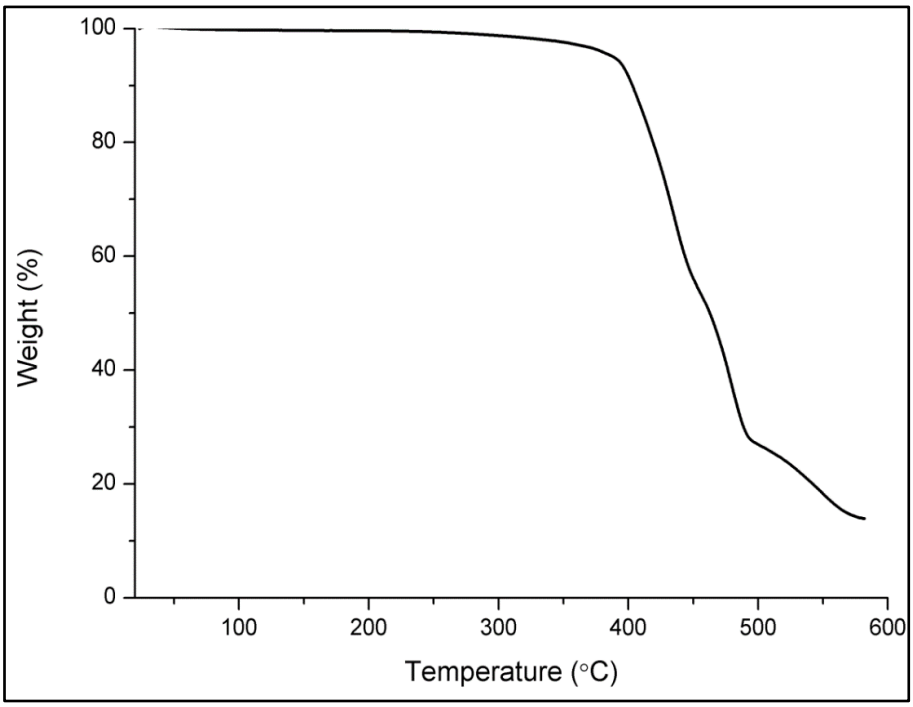

Figure S3: TGA for activated **1**.

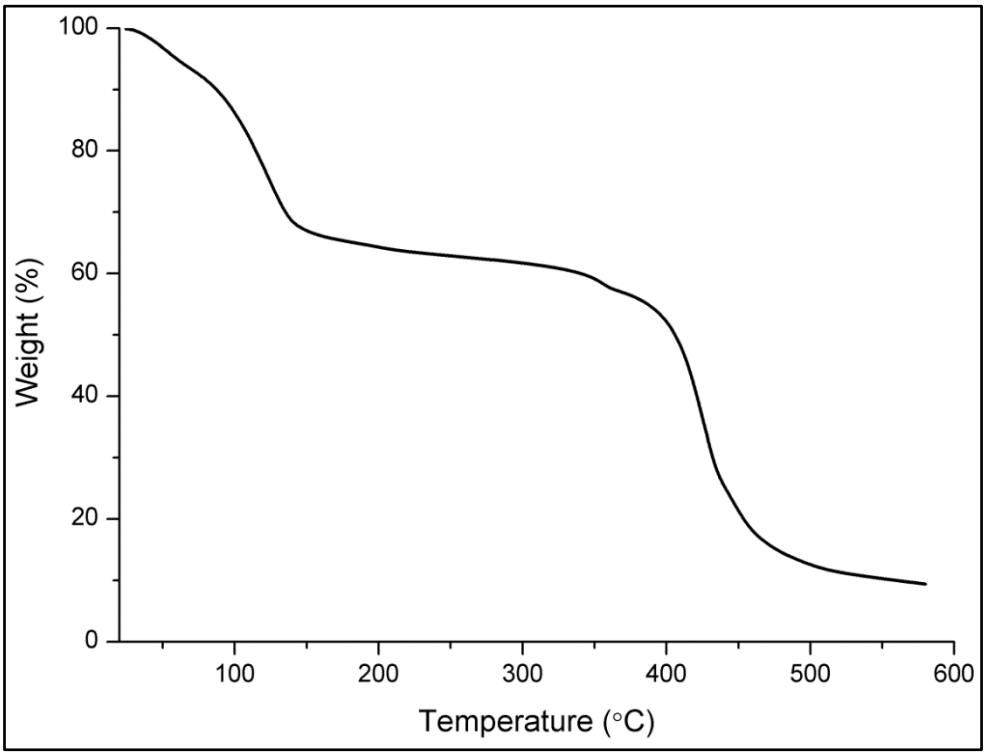

Figure S4: TGA for **2**.

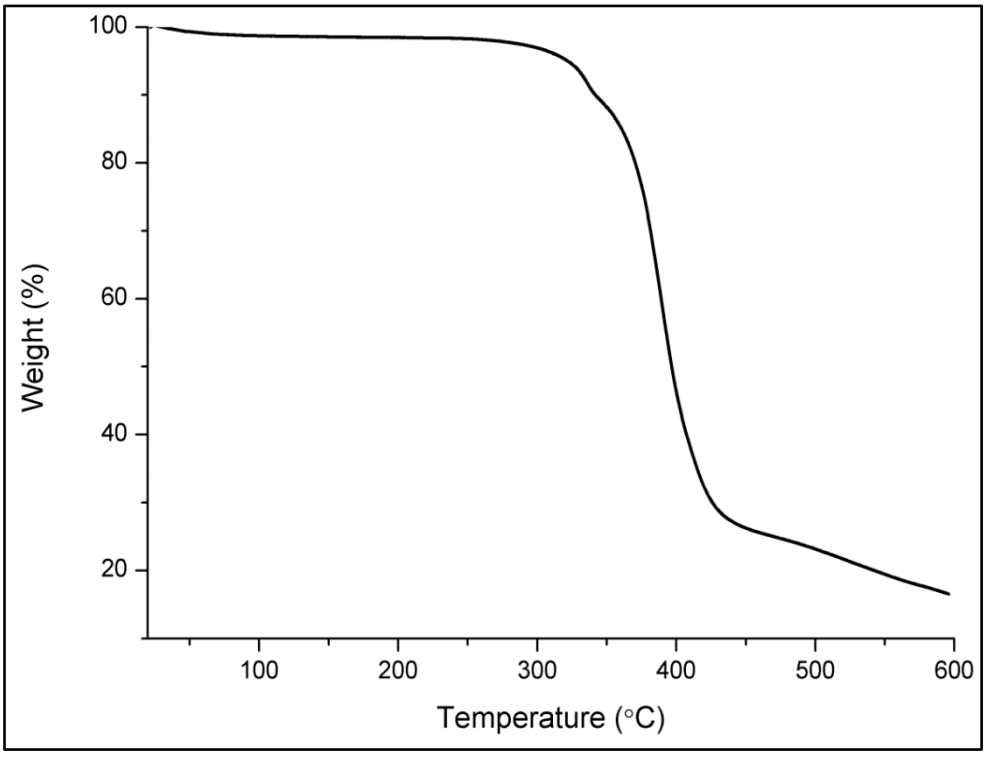

Figure S5: TGA for activated **2**.

Differential Scanning Calorimetry (DSC)

DSC experiments were carried out on a TA Instruments Q100 with the sample heated to 270 °C at a rate of 40 °C/min.

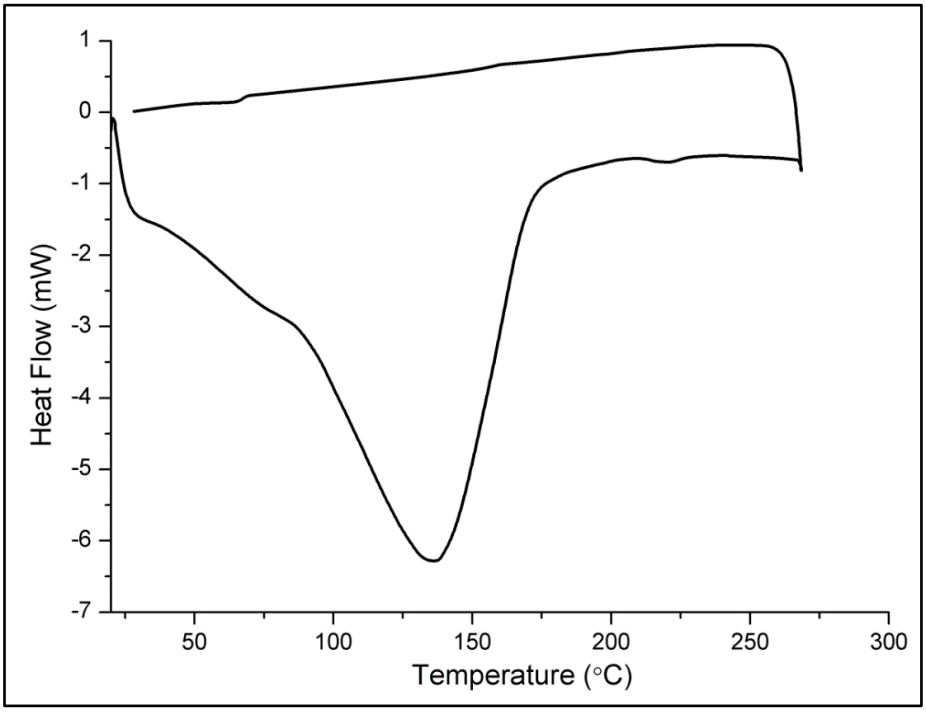

Figure S6: DSC for **1**.

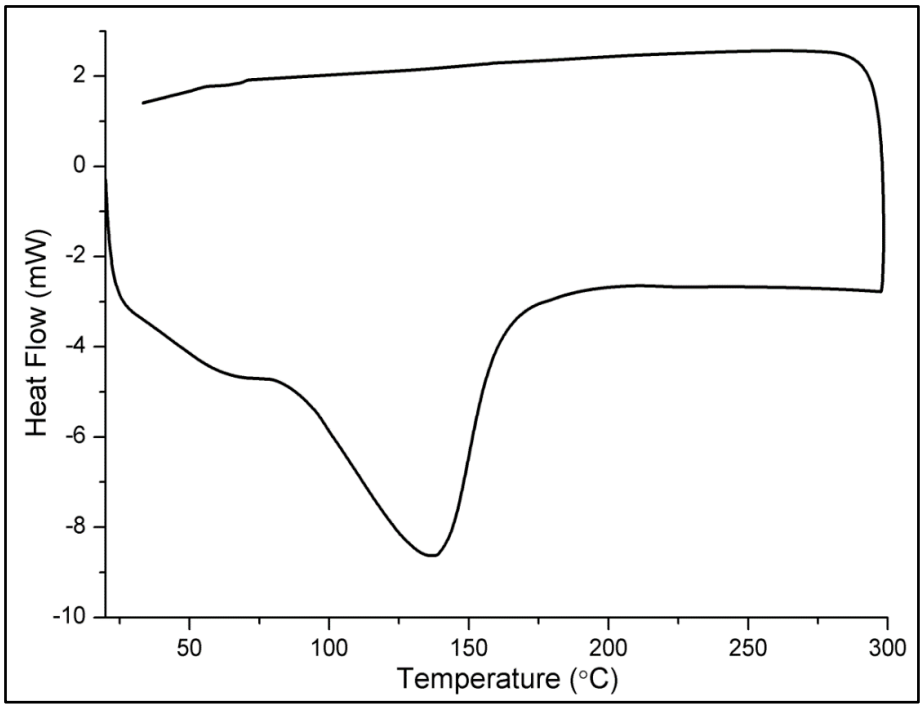

Figure S7: DSC for **2**.

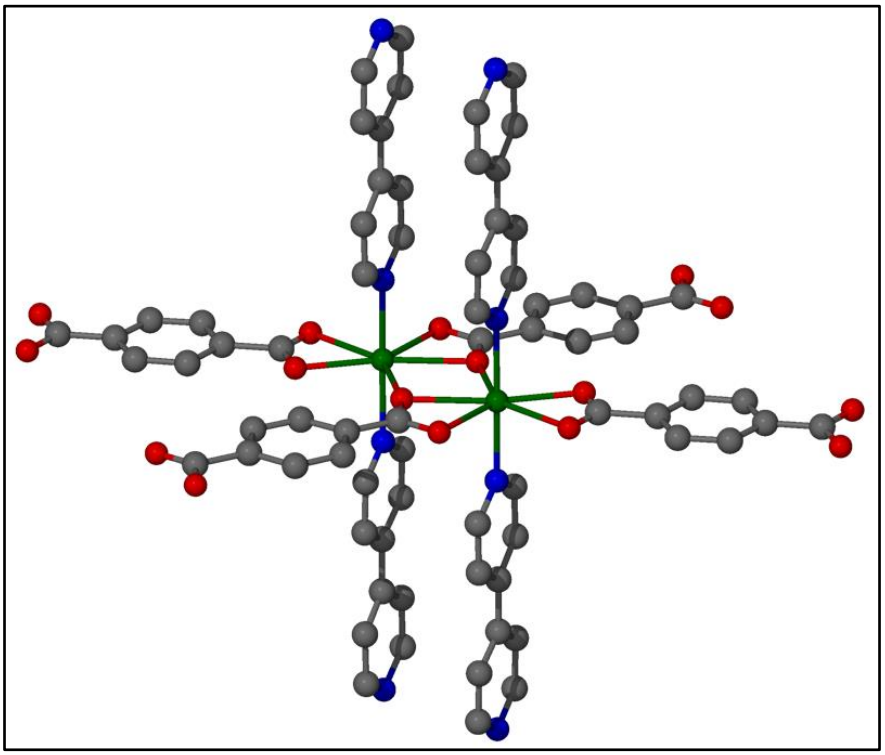

Figure S8: Dinuclear unit in **1**.

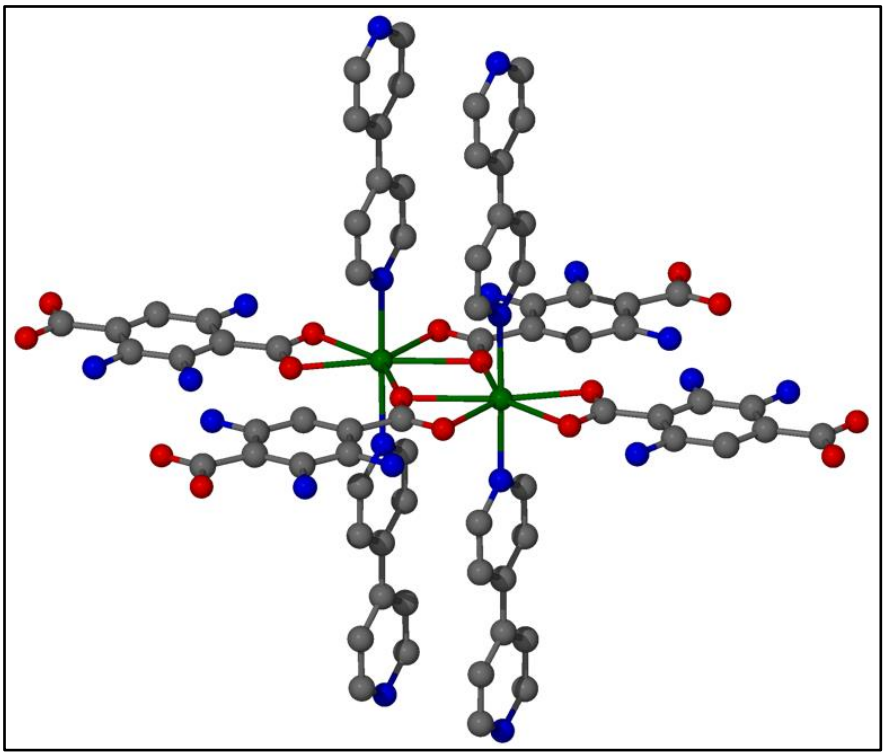

Figure S9: Dinuclear unit in **2**.

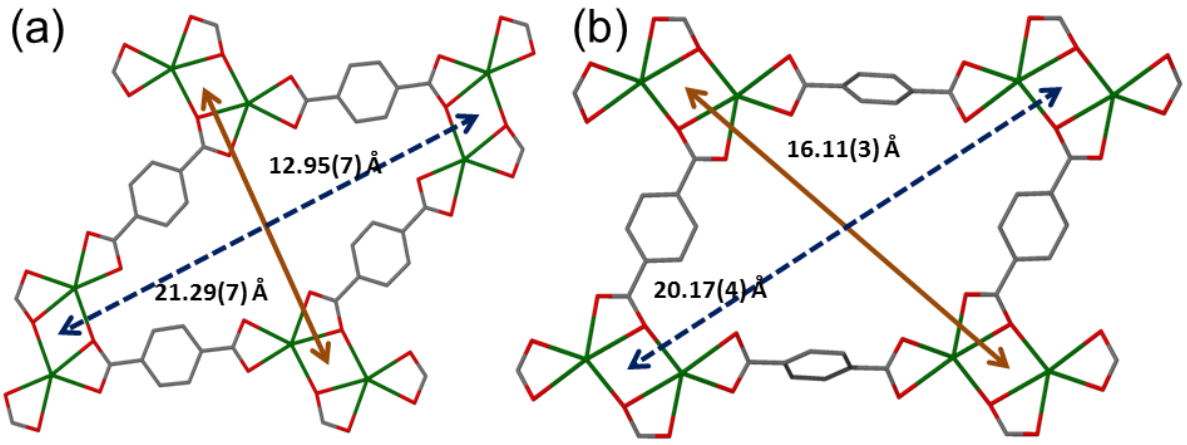

Figure S10: Packing diagram showing the diagonal distances between metal cluster centres (i.e. the Cd···Cd centroid) in (a) non-interpenetrated **1** and (b) doubly interpenetrated **1**.

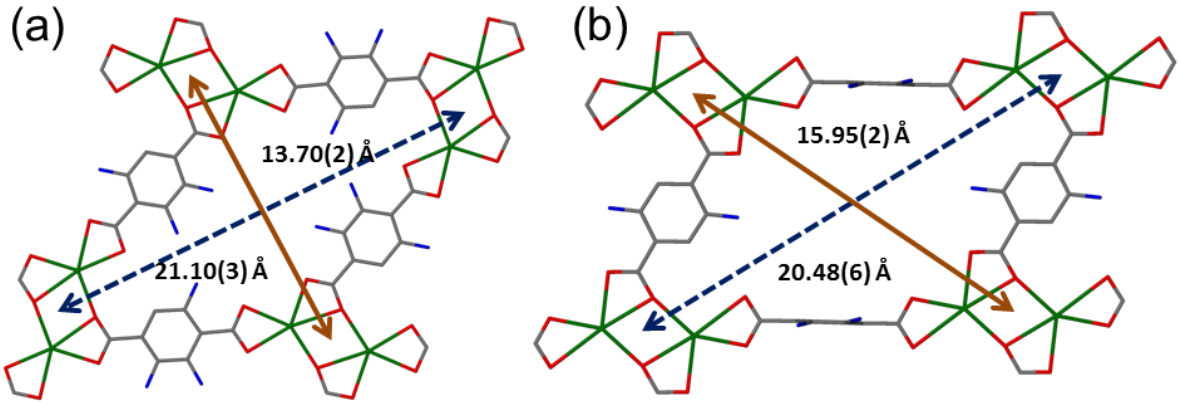

Figure S11: Packing diagram showing the diagonal distances between metal cluster centres (i.e. the Cd···Cd centroid) in (a) non-interpenetrated **2** and (b) doubly interpenetrated **2**.

Rietveld Refinement

The observed X-ray powder patterns were refined using the Rietveld[3] method. We employed the program TOPAS[3] using the corresponding published single-crystal X-ray structures as starting models. The resultant difference plots thus generated are given below.

Table S3 Final Rietveld refinement parameters for the four structures:

Compound	**1** Non-interpenetrated	**1** Doubly-interpenetrated	**2** Non-interpenetrated	**2** Doubly-interpenetrated
$R_p$fitted	0.074	0.037	0.043	0.024
$_wR_p$fitted	0.101	0.051	0.056	0.031
Bragg R-factor	2.20	0.79	0.47	0.56
GoF (χ)	3.05	3.71	2.00	1.51
Temperature (K)	298(2)	298(2)	298(2)	298(2)
Space group	*Pbam*	*C*2/*c*	*Pbam*	*C*2/*m*
a (Å)	12.9018(5)	15.8442(3)	13.4882(6)	16.1576(7)
b (Å)	21.3502(6)	11.6038(2)	21.1458(3)	11.6540(9)
c (Å)	11.6964(4)	20.0921(3)	11.5206(8)	10.1833(13)
α, γ (°)	90	90	90	90
β (°)	90	112.461(12)	90	113.403(15)
No. of parameters	1612	369	2749	402

Table S4: Comparison of Rietveld parameters with the reported unit cell parameters for Non-interpenetrated and doubly-interpenetrated compound **1**.

Compound	Non-interpenetrated **1**		Doubly-interpenetrated **1**	
	Rietveld	Reported	Rietveld	Reported
Temperature (K)	298	100	298	294

Space group	*P*bam	*P*bam	*C*2/c	*C*2/*c*
a (Å)	12.901(5)	12.949(5)	15.844(3)	16.108(3)
b (Å)	21.350(6)	21.290(6)	11.603(2)	11.675(2)
c (Å)	11.696(4)	11.682(5)	20.092(3)	20.171(4)
α, γ (°)	90.00	90.00	90.00	90.00
β (°)	90.00	90.00	112.46(12)	111.99(3)

Table S5: Comparison of Rietveld parameters with the reported unit cell parameters for non-interpenetrated and doubly-interpenetrated compound **2**.

Compound	Non-interpenetrated **2**		Doubly-interpenetrated **2**	
	Rietveld	Reported	Rietveld	Reported
Temperature (K)	298	293	298	293
Space group	*P*bam	*P*bam	*C*2/m	*C*2/*m*
a (Å)	13.488(6)	13.700(3)	16.157(7)	15.950(3)
b (Å)	21.145(3)	21.050(4)	11.654(9)	11.700(2)
c (Å)	11.520(8)	11.720(2)	10.183(13)	10.210(2)
α, γ (°)	90.00	90.00	90.00	90.00
β (°)	90.00	90.00	113.40(15)	112.77(3)

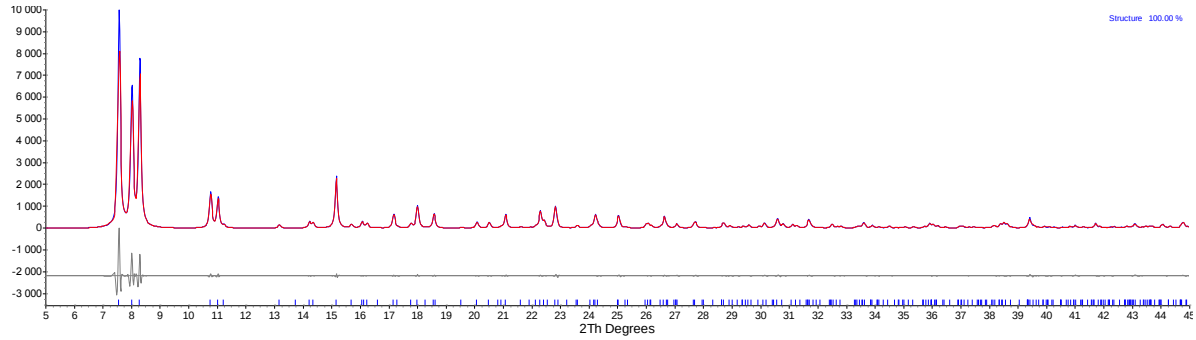

Figure S12: Observed (blue) and simulated (red) X-ray powder diffractograms (the latter obtained from Rietveld refinement) as well as the difference plot (grey) for non-interpenetrated compound **1**.

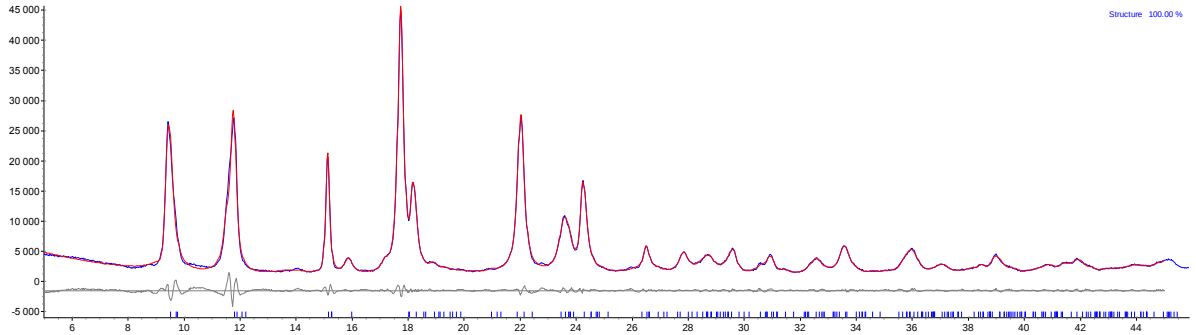

Figure S13: Observed (blue) and simulated (red) X-ray powder diffractograms (the latter obtained from Rietveld refinement) as well as the difference plot (grey) for doubly-interpenetrated compound **1**.

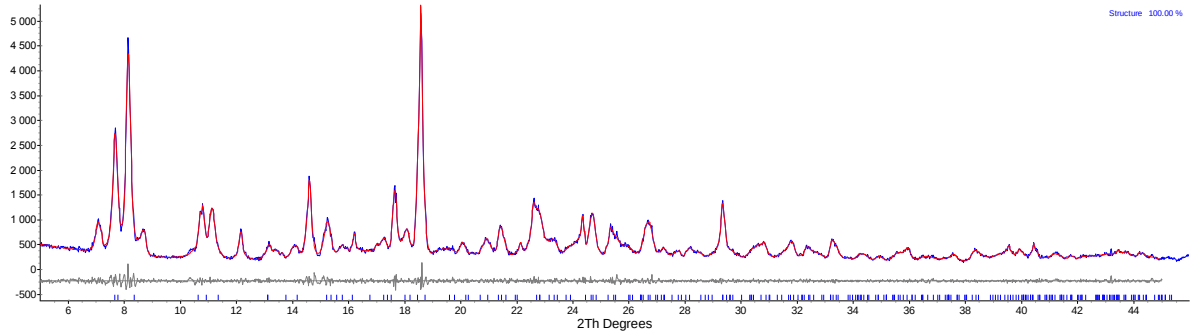

Figure S14: Observed (blue) and simulated (red) X-ray powder diffractograms (the latter obtained from Rietveld refinement) as well as the difference plot (grey) for non-interpenetrated compound **2**.

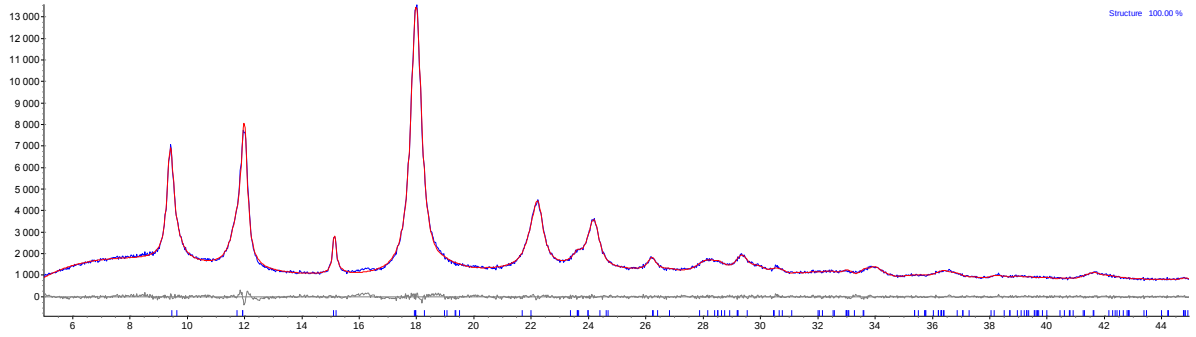

Figure S15: Observed (blue) and simulated (red) X-ray powder diffractograms (the latter obtained from Rietveld refinement) as well as the difference plot (grey) for doubly-interpenetrated compound **2**.

The as-synthesised and activated PXRD patterns for both compounds **1** and **2** were compared with the non-interpenetrated and doubly interpenetrated CIF data of **1** and **2,** respectively by using X'Pert Highscore Plus[4] to identify the phase purity of the compounds.

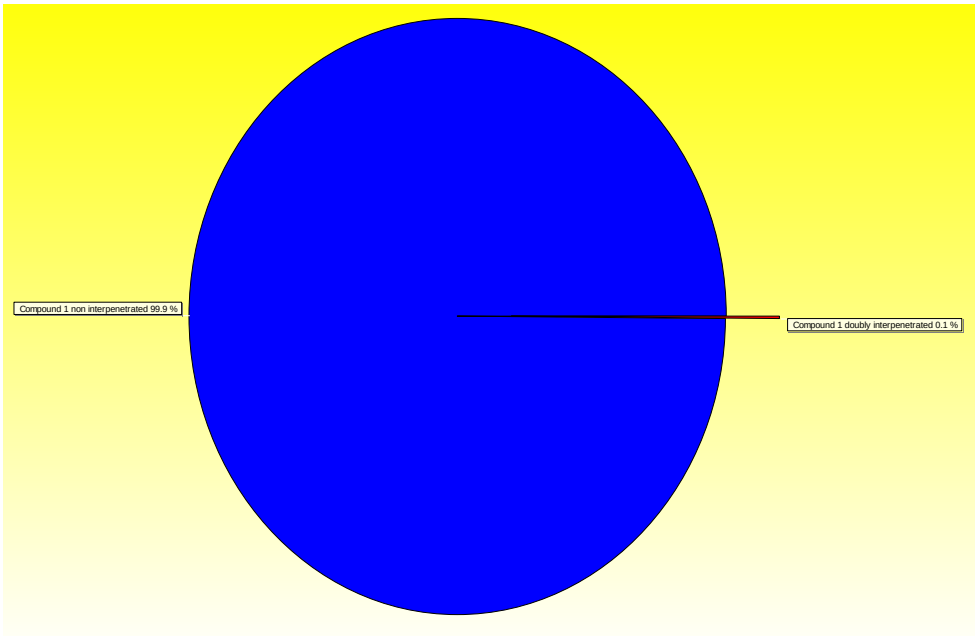

Figure S16: Quantification plot for as-synthesised **1** generated by X'Pert Highscore Plus after comparison with the non-interpenetrated (blue) and doubly interpenetrated (red) CIF data of **1**.

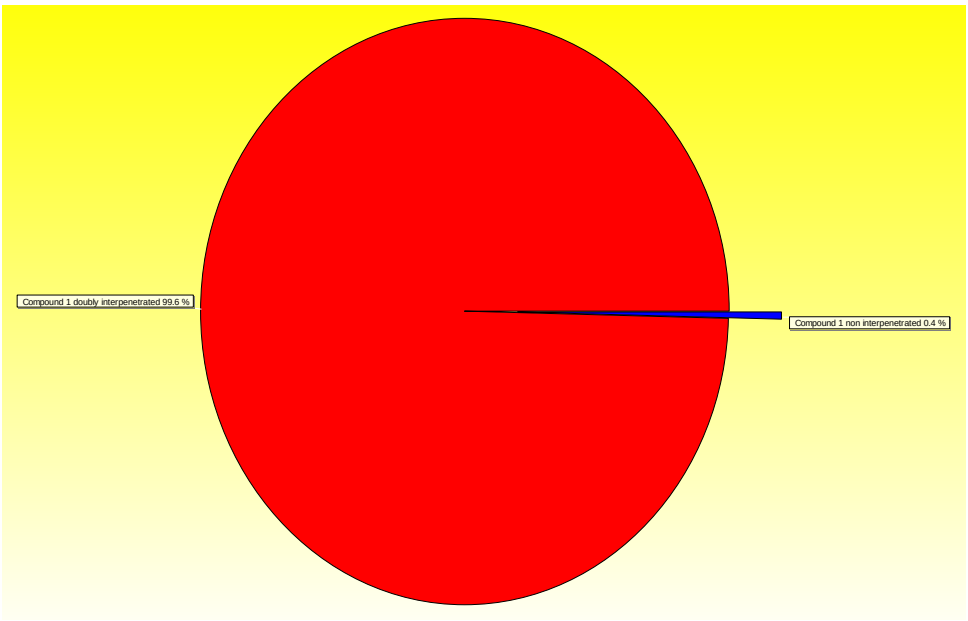

Figure S17: Quantification plot for activated **1** generated by X'Pert Highscore Plus after comparison with the non-interpenetrated (blue) and doubly interpenetrated (red) CIF data of **1.**

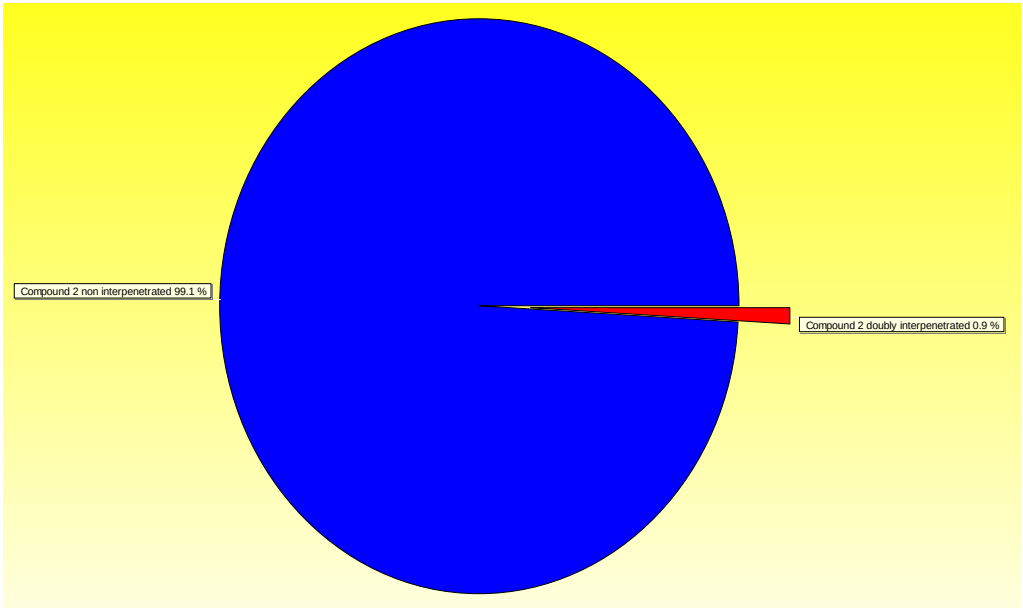

Figure S18: Quantification plot for as-synthesised **2** generated by X'Pert Highscore Plus after comparison with the non-interpenetrated (blue) and doubly interpenetrated (red) CIF data of **2**.

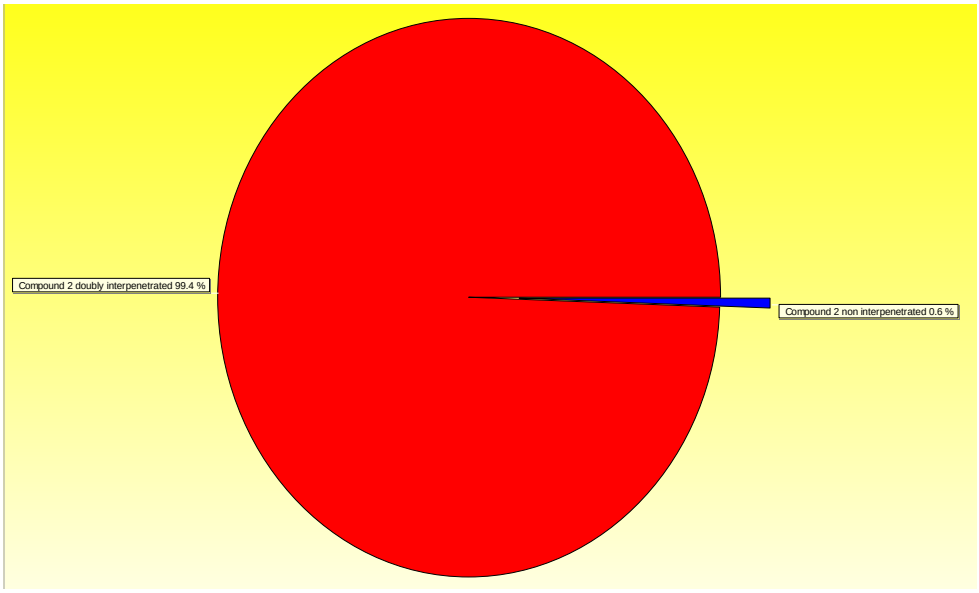

Figure S19: Quantification plot for activated **2** generated by X'Pert Highscore Plus after comparison with the non-interpenetrated (blue) and doubly interpenetrated (red) CIF data of **2**.

References:

1. J. Zhang, L. Wojtas, R. W. Larsen, M. Eddaoudi and M. J. Zaworotko, *J. Am. Chem. Soc.*, **2009**, *131*, 17040-17041.

2. H.-L. Jiang, Yo. Tatsu, Z.-H. Lu and Q. Xu, *J. Am. Chem. Soc.*, **2010**, *132*, 5586-5587.

3. A. Coelho, *J. Appl. Crystallogr.*, **2000**, *33*, 899–908.

4. Panalytical B. V. Almelo, The Netherland, **2009**, X'Pert Highscore Plus Version 2.2e.

CHAPTER 5

ISOLATION OF A STRUCTURAL INTERMEDIATE DURING SWITCHING OF INTERPENETRATION IN A METAL-ORGANIC FRAMEWORK

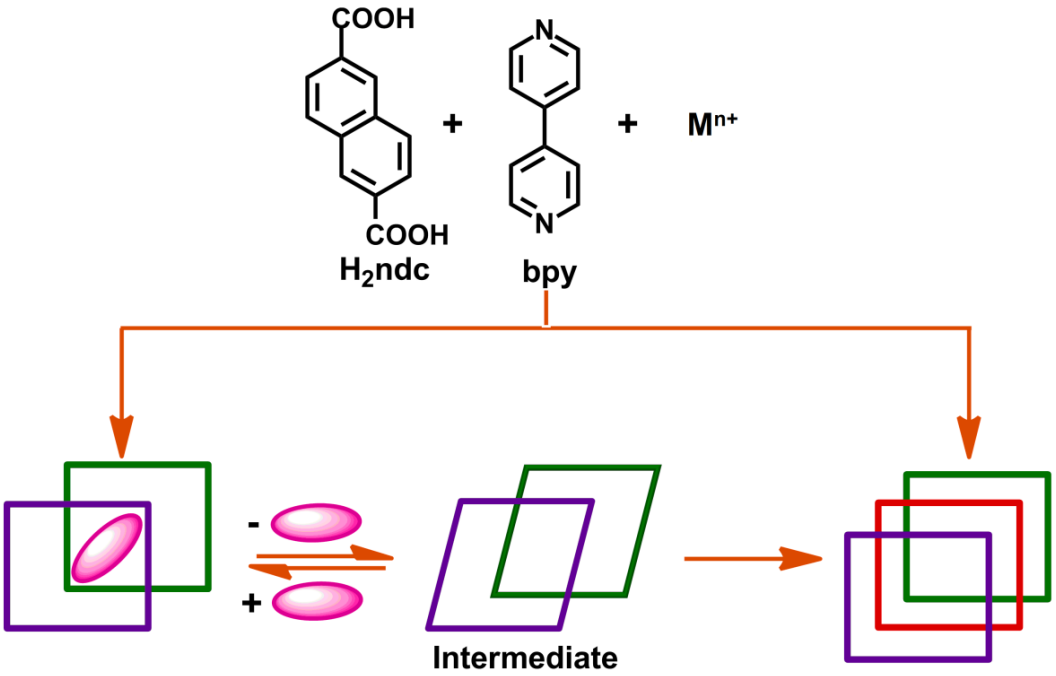

Author's Contribution

- Designed the project.
- Synthesised $[Co_2(ndc)_2(bpy)]$ crystals.
- Recorded all single-crystal to single-crystal transformations.
- Performed all additional studies such as PXRD, TGA and Rietveld refinements.
- Discussed and evaluated results with co-authors.
- Wrote manuscript with inputs from Raj Kumar Das and Prashant M. Bhatt.

Chemical Science

EDGE ARTICLE

View Article Online
View Journal | View Issue

Cite this: *Chem. Sci.*, 2015, **6**, 4986

Isolation of a structural intermediate during switching of degree of interpenetration in a metal–organic framework†

Himanshu Aggarwal, Raj Kumar Das, Prashant M. Bhatt and Leonard J. Barbour*

A known pillared layered metal–organic framework $[Co_2(ndc)_2(bpy)]$ is shown to undergo a change in degree of interpenetration from a highly porous doubly-interpenetrated framework (**2fa**) to a less porous triply-interpenetrated framework (**3fa**). The transformation involves an intermediate empty doubly-interpenetrated phase (**2fa′**) which has been isolated for the first time for this kind of phenomenon by altering the conditions of activation of the as-synthesized material. Interestingly, all the transformations occur in single-crystal to single-crystal fashion. Changes in degree of interpenetration have not been explored much to date and their implications with regard to the porosity of MOFs still remain largely unknown. The present study not only provides a better understanding of such dramatic structural changes in MOF materials, but also describes an original way of controlling interpenetration by carefully optimizing the temperature of activation. In addition to studying the structural mechanism of conversion from **2fa** to **3fa**, sorption analysis has been carried out on both the intermediate (**2fa′**) and the triply-interpenetrated (**3fa**) forms to further explain the effect that switching of interpenetration mode has on the porosity of the MOF material.

Received 18th May 2015
Accepted 11th June 2015

DOI: 10.1039/c5sc01796c

www.rsc.org/chemicalscience

Introduction

Owing to their high surface areas and porosity, metal–organic frameworks (MOFs) have been recognized as promising materials for gas sorption[1] and the separation[2] of substances.[3] Many groups have tried to enhance the surface areas of MOFs by increasing the length of the organic bridging ligands.[4] However, the presence of larger spaces in a framework frequently leads to network catenation, also known as interpenetration.[5] On the one hand, interpenetration promotes framework flexibility and guest selectivity[6] in MOFs, but on the other hand it also results in lower surface areas and void volumes.[7] Several reports have demonstrated that the degree of interpenetration can be controlled for certain MOFs by varying the conditions for crystallization such as choice of solvent,[8] temperature,[9,10] concentration,[10] *etc.*

Over the past few years many new MOFs have been prepared by successfully employing methodologies[8–10] for controlling the degree of interpenetration in order to obtain less dense (or more porous) frameworks. In a typical study, a MOF is first synthesized (mostly using solvothermal methods) and then activated/desolvated by heating at a relatively high temperature in order to obtain the guest-free form of the as-synthesized material. The activated sample is usually expected to retain its host framework integrity upon loss of solvent molecules from the channels. In some cases the activated material retains sufficient macroscopic integrity such that its structure can be elucidated by means of single crystal X-ray diffraction. However, in most instances the single crystals do not survive activation intact and the structure of the activated material therefore remains unknown.[11] Typically, in such cases thermogravimetric analysis (TGA) is used to confirm complete removal of guest molecules from the channels and the structural integrity of the host framework is inferred from X-ray powder diffraction (XRPD). Sorption data are then recorded with the assumption that the activated form has the identical (or at least similar) structure to that of the host framework of the as-synthesized material. Most of the time the sorption results are reasonable but several reports have mentioned unexpected loss of porosity upon activation of MOFs.[12–16]

Since our first report on the change in degree of interpenetration of a known MOF,[17] we have been interested in investigating this surprising phenomenon in more detail with a view to elucidating underlying mechanisms and to rationalizing the effect of such an extreme change on the porosity of other MOF materials. Since interpenetrated frameworks involve two or more independent grids with no formal bonds between them, they cannot be disentangled without breaking metal–ligand

Department of Chemistry and Polymer Science, University of Stellenbosch, Matieland 7602, Stellenbosch, South Africa. E-mail: ljb@sun.ac.za

† Electronic supplementary information (ESI) available: Synthetic procedure, detail physical methods, detailed crystallographic information, additional figures, Rietveld refinements, CO_2 sorption isotherm, additional XRPD patterns. CCDC 1052168–1052173. For ESI and crystallographic data in CIF or other electronic format see DOI: 10.1039/c5sc01796c

coordination bonds. "Soft" secondary building units (SBUs) have been reported[18] that involve partial breaking and formation of metal-chelate coordination bonds. However, the complete detachment of metal–ligand linkages requires a relatively large amount of energy, and thus any change in interpenetration mode is generally assumed to be quite unlikely. Indeed, there have been only a few reports of changes in interpenetration, either as a result of removal of coordinated solvent[19] upon heating at elevated temperatures, or by loss of solvent of crystallization[17,20] upon activation of crystals. Furthermore, the transformations generally involve concomitant degradation of crystal singularity. In order to better understand the mechanisms that govern solid-state phase transformations at the molecular level, and to rule out any possibility of recrystallization *via* an amorphous phase, monitoring such processes as single-crystal to single-crystal transformations is very important.[21]

Recently, we showed that two doubly pillared layered Cd(II) non-interpenetrated MOFs, [Cd(tp)(4,4′-bpy)] and [Cd(atp)(4,4′-bpy)], (tp = terephthalate; 4,4′-bpy = 4,4′-bipyridine and atp = 2-aminoterephthalate) convert to doubly-interpenetrated frameworks upon loss of solvent molecules from the channels.[20] Prior to that, we also showed that a doubly-interpenetrated MOF $[Zn_2(ndc)_2(bpy)]$ (ndc = 2,6-napthalene dicarboxylate, bpy = 4,4′-bipyridyl) changes to its triply-interpenetrated form upon loss of solvent under ambient conditions, and that the transformation occurs in single-crystal to single-crystal fashion.[17] The suggested mechanism involves bending of metal–ligand linkages with concomitant sliding of layers, ultimately resulting in concerted bond breaking and remaking to yield a new structure. It is possible that the transformation proceeds *via* an 'empty' doubly-interpenetrated phase that is crystallographically distinct from the as-synthesized material but, owing to the rapid transformation rate we were unable to observe any evidence for such an intermediate. Therefore it was not known whether the loss of solvent is concomitant with the change of interpenetration mode or if the transformation occurs in a stepwise fashion. In order to monitor the phenomenon in greater detail and to obtain more convincing evidence for the proposed mechanism, we have selected the analogous but more robust framework $[Co_2(ndc)_2(bpy)]$ for further study. Owing to the crystal field stabilization energy of Co(II), we expected the bond breaking and remaking process to be much slower in this particular case, thus enabling us to isolate an intermediate empty doubly-interpenetrated structure.

Results and discussion

The $[Co_2(ndc)_2(bpy)]$ framework has already been reported to form both doubly-[12] and triply-interpenetrated[22] structures under different conditions. Both of these forms have a three dimensional pillared layer structure containing $Co_2(COO)_2$ paddle-wheel secondary building units with 6-connected *pcu* net topology. Doubly-interpenetrated networks are quite well-known for this topology, whereas analogous triply-interpenetrated frameworks are far less common.[5c,6b,6c,22] The doubly-interpenetrated framework has high 'virtual porosity',[23] with *N*,*N*′-dimethylformamide (DMF) and water molecules occupying the channels, whereas the solvent-free triply-interpenetrated form is considerably less porous. To investigate a possible change in interpenetration upon activation, we first synthesised the twofold-interpenetrated (**2fa**) framework using the reported procedure.[12] The phase purity of the as-synthesized crystals was confirmed by comparing the X-ray powder diffraction (XRPD) patterns of the bulk sample with the simulated pattern of the reported doubly interpenetrated form (Fig. S1†).[12] The crystal structure of **2fa** contains 40% guest-accessible volume (calculated by Platon),[24] with one water and three DMF molecules per asymmetric unit, although the solvent molecules could not be modelled. Thermogravimetric analysis (TGA) shows a steady weight loss between room temperature and 120 °C, followed by a single step decomposition beyond 400 °C (Fig. S2†). Based on the TGA results, crystals were activated at 120 °C under dynamic vacuum for 12 hours. The XRPD diffractogram of the activated form was significantly different from that of the as-synthesized crystals but similar to those simulated for triply-interpenetrated $[Co_2(ndc)_2(bpy)]$[22] and the known threefold-interpenetrated structure of $[Zn_2(ndc)_2(bpy)]$ (**3f**) (Fig. 1).[17]

Although most of the crystals became opaque upon desolvation, several single crystals were observed to remain intact. Single-crystal diffraction (SCD) analysis of these crystals yielded the threefold-interpenetrated structure already reported in the literature.[22] This observation was consistent with our previous finding that a doubly-interpenetrated structure can convert to its triply-interpenetrated form upon removal of the guest molecules, and suggested that the occurrence of such a change in single-crystal to single-crystal fashion is not limited to only one system. In order to unequivocally rule out the possibility that a small number of threefold-interpenetrated crystals had not already been present before activation, we undertook to monitor the transformation using only one crystal, and to preserve its diffraction quality by activating under the mildest possible conditions.

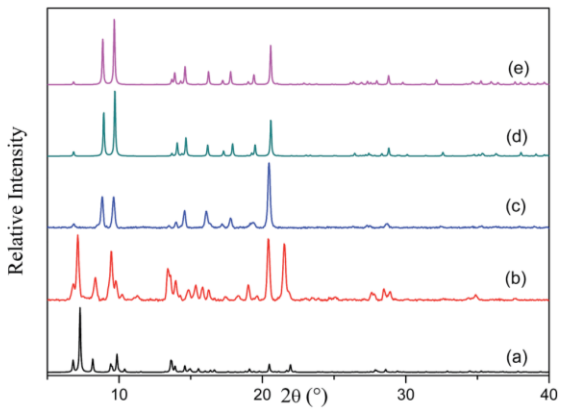

Fig. 1 XRPD patterns of (a) **2fa** simulated from the crystal structure, (b) as-synthesized **2fa** crystals, (c) **2fa** crystals after heating at 120 °C under dynamic vacuum, (d) **3fa** simulated from the crystal structure and (e) **3f** $[Zn_2(ndc)_2(bpy)]$ simulated from the crystal structure.

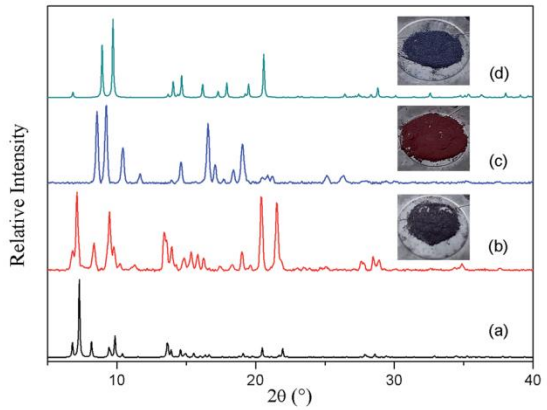

Fig. 2 XRPD patterns of (a) **2fa** simulated from the crystal structure, (b) as-synthesized crystals of **2fa**, (c) **2fa** crystals after heating at 80 °C under dynamic vacuum, (d) **3fa** simulated from the crystal structure.

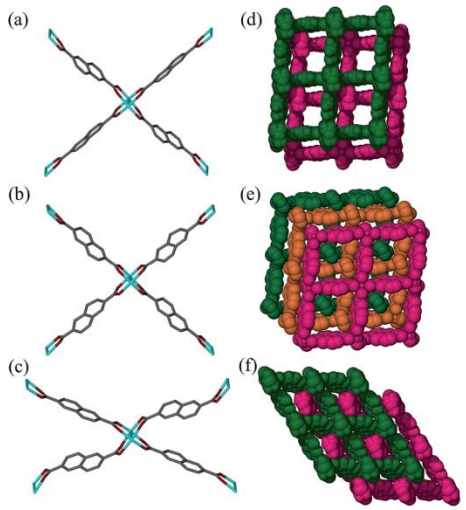

Fig. 3 Perspective view showing $Co_2(COO)_4$ paddle-wheel linkages in (a) **2fa**, (b) **3fa** and (c) **2fa′** and packing diagrams of (d) **2fa** (guest molecules omitted), (e) **3fa** and (f) **2fa′**.

To slow down the activation process, a single crystal was allowed to lose its solvent of crystallization simply by exposure to atmospheric conditions (its unit cell parameters were monitored at regular intervals to follow the progress of the transformation). After almost one week X-ray diffraction analysis revealed that the crystal had converted to its triply-interpenetrated form (**3fa**). Note that, in the case of $[Zn_2(ndc)_2(bpy)]$, conversion of **2f** to **3f** took place in only 6 hours at room temperature.[17] We further established that complete conversion of bulk **2fa** to **3fa** at room temperature required about 10–12 days (Fig. S3†), thus verifying that conversion of the cobalt complex is much slower than that of its zinc analogue, as we had anticipated. We therefore explored the possibility of isolating an intermediate structure with a view to obtaining more insight into the mechanism of transformation from **2fa** to **3fa**. When as-synthesized crystals were activated at 80 °C under dynamic vacuum for 12 hours, the XRPD pattern of the resultant material was substantially different from those simulated from the crystal structures of the doubly- and triply-interpenetrated forms (Fig. 2).

Surprisingly, SCD analysis of activated crystals taken from the bulk sample revealed a new doubly-interpenetrated structure (**2fa′**) devoid of DMF and water molecules (Fig. S4†), as also confirmed by TGA (Fig. S5†). The XRPD pattern of the activated crystals was compared with that simulated from the single-crystal structure to confirm the phase purity of the bulk sample (Fig. S6†). The structure of **2fa′** retains the connectivity of **2fa**, but, in order to compensate for the empty spaces resulting from guest removal, **2fa′** experiences extreme distortion of the metal–ligand linkages (Fig. 3c). As a result, the solvent accessible volume is reduced to 18%.[24]

Although the metal–ligand linkages involving both ndc and bpy are clearly bent, distortion of the former is more pronounced. This can be corroborated by examining the dihedral angles between the metal (*i.e.* $Co_2\cdots Co_2$) plane and the metal-carboxylate plane (θ), as well as the metal plane and the aromatic plane of ndc (ϕ) in both **2fa** and **2fa′** (Fig. 4). The dihedral angles increase sharply upon conversion from **2fa** to **2fa′**.

In the case of bpy, a similar assessment was made by measuring the torsion angle (δ) between the Co_2 cluster metal–metal axis and the Co–N linkage, and the torsion angle (ω) between the metal–metal axis and the aromatic part of bpy (Fig. 4). These angles are larger for **2fa′**, thus indicating bending of the metal–ligand linkages upon activation.

It is also clear from the measurements that the distortion of the (Co···Co)—ndc—(Co···Co) linkage is much greater than that of Co–bpy–Co, suggesting that the ndc linkers are in a more

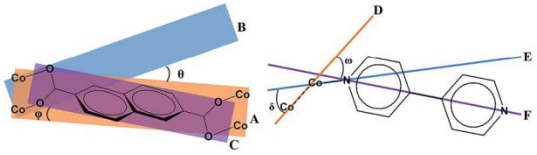

2fa				2fa′			
θ	φ	δ	ω	θ	φ	δ	ω
1.56(4)	2.98(5)	17.8(1) – 29.5(3)	21.7(1) – 27.46(4)	10.53(3)	7.41(6)	30.1(3) – 35.3(3)	33.7(1) – 36.8(1)
1.71(4)	7.81(4)	20.8(7) – 28.9(3)		18.63(4)	18.33(4)		
3.70(3)							
4.44(4)							

Fig. 4 Top: diagrammatic representation of key dihedral and torsion angles in **2fa** and **2fa′**. A: $Co_2\cdots Co_2$ metal atom plane; B: Co_2–carboxylate oxygen plane; C: aromatic plane of ndc; D: Co_2 cluster metal–metal axis; E: metal–nitrogen; F: N···N axis of bpy. Both crystallographic symmetry and geometrical disorders have been considered in measuring these parameters. Bottom: table of relevant angles in °.

strained configuration. With reference to Fig. 3c, The structure of **2fa′** is comparable to that of the well-known MOF [Zn_2(bdc)$_2$(bpy)] which, upon activation, yields a considerably distorted and less porous phase (but owing to steric factors, further conversion to a more highly interpenetrated form is improbable in that case).[25] Since ndc is longer than bdc, we observe even more distortion in the case of **2fa′**, as might be expected.

In our previous report describing a change in the degree of interpenetration for the [Zn_2(ndc)$_2$(bpy)] system we suggested a plausible mechanism for the transformation based on the available information:[17] the metal–ligand bonds should bend on solvent removal in order to minimize the free space in the structure and this distortion of the framework should have two consequences: (1) the metal–ligand bonds will become weaker and easier to break and (2) adjacent layers from two independent networks will move closer to each other. When the metal–ligand bonds become sufficiently bent and weakened, they will break and form more linear and stronger bonds with suitably located metal centers of another network. This triggers a cascade of further bond breaking and formation, ultimately resulting in transformation of **2fa** to **3fa**. For the following reasons we suggested bpy as the more plausible choice than ndc to become involved in bond breaking and making: (1) at each end bpy coordinates in a monodentate fashion while bidentate chelation by ndc is associated with greater binding energy and (2) in the analogous [Zn_2(bdc)$_2$(bpy)] system the metal–bpy–metal linkage has indeed been observed[25] to undergo severe distortion in order to minimize free space in the structure.

Notwithstanding the above, isolation of the intermediate structure **2fa′** provides more insight into the possible mechanism of transformation. It is clear from the structure of **2fa′** that the ndc linkage undergoes more severe distortion than does bpy. Furthermore, ndc is geometrically better placed than bpy to form a new attachment to a neighboring metal cluster of another network. There are two symmetry-independent ndc ligands in the structure of **2fa**; one of them forms a comparatively straight connection between two Co_2 clusters, with a node···node distance between two paddle-wheel units of 13.130 Å, while the other forms a relatively bent connection with a corresponding distance of 12.970 Å.‡ The shortest distance between two favorably oriented paddle-wheel nodes of different networks is 16.376 Å. Upon conversion to **2fa′** the corresponding Co···Co distances decrease to 13.025 Å and 12.446 Å, respectively. However, the latter ndc molecule could conceivably form a relatively straight connection between two paddle-wheel nodes of different networks without requiring any other major structural change; the distance between geometrically favorable paddle-wheels is only 14.284 Å (Fig. 5). On the other hand, in the case of bpy the distance between connected paddle-wheels is 11.195 Å in **2fa** and 11.204 Å in **2fa′**, whereas the shortest alternative distance (*i.e.* between paddle-wheel units of different frameworks) is 16.940 Å in **2fa** and 16.854 Å in **2fa′**.

The Co–O distances become elongated whereas the Co–N distances remain almost constant in **2fa′**, indicating weakening of metal carboxylate bonds as a direct consequence of activation, suggesting that **2fa′** is less stable than **2fa** (Table S1†).

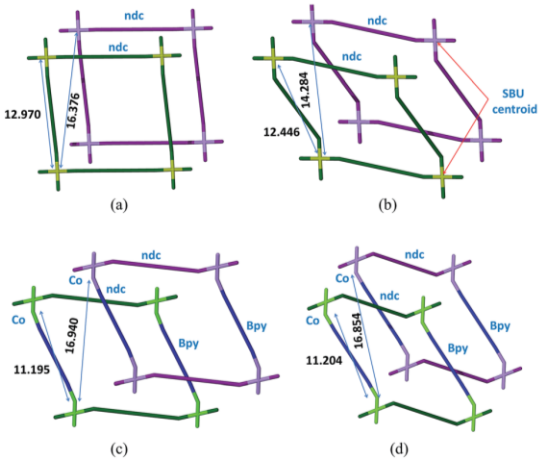

Fig. 5 Schematic representation showing extent of bending and internodal distances for ndc and bpy; (a and b) **2fa** and **2fa′** viewed perpendicular to bpy, respectively and (c and d) **2fa** and **2fa′** viewed perpendicular to ndc, respectively.

Upon further heating, it is reasonable to expect the Co–O bonds to become even weaker, ultimately leading to cleavage of the metal–ligand linkages involving ndc, followed by reattachment to energetically more favorable metal centers to yield an almost linear (Co···Co)–ndc–(Co···Co) linkage, and thus a triply-interpenetrated network. Although we do not rule out the possibility of simultaneous breaking of bpy linkers during this process, we believe it to be far less likely.

Having isolated the guest-free doubly-interpenetrated structure **2fa′**, we investigated whether it will convert to **3fa** (*i.e.* with the implication that **2fa′** is an intermediate phase during conversion from **2fa** to **3fa**). The same crystal was exposed to ambient conditions for several days after which single-crystal diffraction data were recollected. We thereby established that the crystal of **2fa′** had indeed converted to **3fa** in single-crystal to single-crystal fashion, thus demonstrating that **2fa′** is a metastable phase that ultimately converts to more stable **3fa**. Interestingly, the structure of **3fa** contains 16% solvent-accessible volume[24] with no guest molecules in the channels. When bulk **2fa′** crystals were immersed in fresh DMF for 24 hours, the resulting XRPD pattern was similar to that of **2fa**, showing that the transformation from **2fa** to **2fa′** is reversible (Fig. S7†). When **3fa** crystals were immersed in fresh DMF we observed no change in the XRPD patterns. We also heated **3fa** crystals in fresh DMF at 120 °C for 48 hours, but the resulting XRPD pattern remained unchanged. This suggests that the transformation from **2fa** to **3fa** is irreversible under these conditions (Fig. S8†).

To verify unequivocally that **2fa** converts to **3fa** *via* the structural intermediate phase **2fa′**, it was important to also record the initial transformation from **2fa** to **2fa′** in single-crystal to single-crystal fashion. Since the transformation from **2fa** to **2fa′** is a time consuming process at room temperature, gentle heating was used to bring about the conversion. Single-

crystal diffraction data were collected for a suitable crystal of **2fa** at 100 K in order to indisputably verify the starting phase. The temperature was then ramped to 313 K to gently heat the crystal, followed by recollection of single-crystal diffraction data, which yielded a structure quite similar to that of **2fa′** isolated from the activated of bulk crystals (the only difference being that the structure still contains some residual solvent, owing to the much lower activation temperature). The single-crystal conversion of **2fa** to **2fa′** and subsequent conversion of **2fa′** to **3fa** explains the series of events involved during the transformation from a doubly- to a triply-interpenetrated structure. It is clear that the doubly-interpenetrated framework transforms into its triply-interpenetrated analog *via* an intermediate doubly-interpenetrated guest-free structure, which is severely distorted (Scheme 1) but distinct from **2fa**. Indeed, **2fa′** is the first intermediate structure isolated to date for such types of transformations, and it substantiates the mechanism that we proposed in our previous report. Although we also attempted to record the transformation from **2fa** to **2fa′** to **3fa** on the same crystal, it did not survive the process intact; taken together, our results imply that selecting a suitable crystal that would survive both transformations intact is a matter of chance. However, we were able to monitor the bulk change from **2fa** to **3fa** proceeding *via* **2fa′** by using XRPD analysis of the same batch of crystals (Fig. S9†).

When gas sorption results are difficult to rationalize based on the as-synthesized host structure, it is generally assumed that the framework might have collapsed, thus resulting in less than anticipated surface area. The exact nature of this "collapse" is seldom investigated and the material is dismissed as unpromising. Given the often stated importance of developing new porous materials, it is surprising that little attention has been devoted to understanding the problems related to unexpected loss of porosity.

Since our first report on the change in degree of interpenetration of a MOF upon activation, we have maintained that this phenomenon might still be a relatively unappreciated reason for loss of porosity in similar materials. However, in both our previous reports[17,20] we were not able to isolate the empty structure of the less interpenetrated form (the activated structure) and we could therefore not provide sufficient evidence to support our argument. Gas sorption studies were carried out on both guest-free phases **2fa′** and **3fa** in order to compare their sorption properties. PXRD patterns were recorded for **2fa′** before and after the gas sorption measurements to rule out the possibility of conversion of **2fa′** to **3fa** during the sorption experiment (Fig. S10†). Sorption isotherms were recorded at 298 K for carbon dioxide, methane, ethane, propane and butane (Fig. 6). Sorption of CO_2 shows comparable gas uptake for both **2fa′** and **3fa** (Fig. S11†) and similar sorption trends were also observed for both phases in the case of methane. The similarity in gas uptake of CO_2, and methane can be attributed to the comparable void volumes for both **2fa′** and **3fa** as determined using the Platon software package.

For the higher alkanes clear differences were observed for the sorption behavior of the two forms. Form **3fa** shows greater uptake of propane and butane at low pressure, which may be due to the catenation effect.[26] However, in the case of **2fa′** there are clear steps between 2 to 5 bar for propane and 0.5 to 2 bar for butane, whereas no such steps are observed for **3fa**. Moreover, the propane and butane isotherms exhibit substantial hysteresis for **2fa′**. This phenomenon can be related to the so-called "gate opening effect", which is quite common for flexible/dynamic MOFs.[27] Indeed, it is interesting to note that **2fa′** shows greater uptake of these gases at higher pressure, which suggests enhancement of porosity, possibly due to gate opening. With regard to the sorption isotherms for ethane, a step is also apparent in the case of **2fa′**, albeit less pronounced than for propane or butane. However, for both **2fa′** and **3fa** the extent of hysteresis for ethane sorption is relatively insignificant and the total uptake at 20 bar is approximately the same.

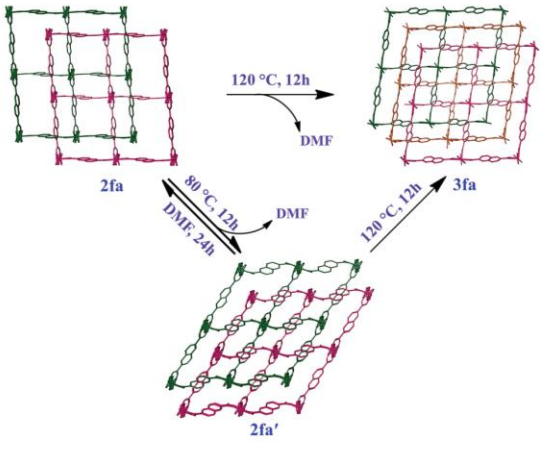

Scheme 1 Schematic representation showing bending and switching of interpenetration in the $[Co_2(ndc)_2(bpy)]$ system.

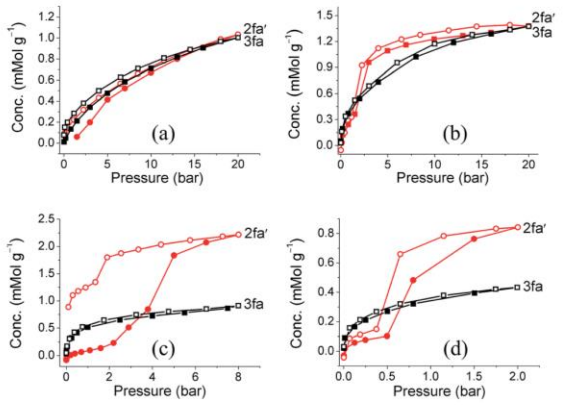

Fig. 6 (a) Methane (b) ethane, (c) propane and (d) butane sorption isotherms of **2fa′** (circles) and **3fa** (squares) at 298 K (shaded and open symbols represent adsorption and desorption, respectively).

Conclusions

The isolation and characterization of structural intermediates is crucial for understanding structure–property relationships in dynamic MOFs, and it also extends our knowledge of concepts such as permanent and transient porosity. The $[Co_2(ndc)_2(bpy)]$ system reported by Chen and co-workers was presumed to lose porosity upon activation, leading to lower than anticipated surface area for such a seemingly highly porous framework.[14] We believe that the activated framework isolated by Chen *et al.* was **3fa** and not **2fa′** (owing to activation at high temperature in their case). This highlights the notion that exact activation conditions can be critical for gas sorption studies. Although much attention is usually devoted to design criteria and crystallization methodologies, activation procedures receive comparatively little consideration. The control of interpenetration in MOFs has also received much attention and it is generally expected that once a less interpenetrated structure is isolated, it will retain its interconnectivity upon activation. In the present case the doubly-interpenetrated framework of $[Co_2(ndc)_2(bpy)]$ has indeed been produced by altering the crystallization conditions but upon activation at 120 °C it converts to its triply-interpenetrated form. However, under milder activation conditions the same material yields the empty twofold-interpenetrated structure. We also show that misleading results might be obtained if a sample is kept under ambient conditions for some time before the sorption data are recorded. To date the phenomenon of a change in degree of interpenetration and its effect on porosity has largely been overlooked. This study demonstrates the importance of considering dramatic structural rearrangements when rationalizing unexpected loss of porosity. We believe that the phenomenon needs more attention and that many more systems (both known and unknown) might experience similar changes. Indeed, these changes may go unnoticed owing to the difficulties involved in analyzing materials that lose crystal singularity upon activation.

Acknowledgements

We thank the National Research Foundation and Department of Science and Technology (SARCHI Program) for support of this work. PB also thanks the Claude Leon Foundation for financial support.

Notes and references

‡ In the case of ndc, the node···node distances between two paddle-wheel units is taken as the distance between the Co–Co centroids of the two metal clusters bridged by the ndc ligand. The same protocol was used to determine the shortest distance between two paddle-wheel nodes of different networks. In the case of bpy, the distance is measured between the two Co metal centers to which the ligand is attached. It should be noted that only the geometrically favorable Co centers are taken in to account while measuring the shortest distances between paddle-wheel units of different networks.

1 (*a*) H. Li, M. Eddaoudi, M. O'Keeffe and O. M. Yaghi, *Nature*, 1999, **402**, 276; (*b*) S. Horike, S. Shimomura and S. Kitagawa, *Nat. Chem.*, 2009, **1**, 695; (*c*) L. R. MacGillivray, *Metal–Organic Frameworks: Design and Application*, John Wiley & Sons, Inc., 2010.

2 J.-R. Li, R. J. Kuppler and H.-C. Zhou, *Chem. Soc. Rev.*, 2009, **38**, 1477.

3 (*a*) Y.-S. Bae, C. Y. Lee, K. C. Kim, O. K. Farha, P. Nickias, J. T. Hupp, S. T. Nguyen and R. Q. Snurr, *Angew. Chem., Int. Ed.*, 2012, **51**, 1857; (*b*) H. K. Chae, D. Y. Siberio-Pérez, J. Kim, Y. Go, M. Eddaoudi, A. J. Matzger, M. O'Keeffe and O. M. Yaghi, *Nature*, 2004, **427**, 523.

4 M. Eddaoudi, J. Kim, N. Rosi, D. Vodak, J. Wachter, M. O'Keeffe and O. M. Yaghi, *Science*, 2002, **295**, 469.

5 (*a*) H.-L. Jiang, T. A. Makala and H.-C. Zhou, *Coord. Chem. Rev.*, 2013, **257**, 2232; (*b*) S. R. Batten and R. Robson, *Angew. Chem., Int. Ed.*, 1998, **37**, 1460; (*c*) V. A. Blatov, L. Carlucci, G. Ciani and D. M. Proserpio, *CrystEngComm*, 2004, **6**, 377.

6 (*a*) S. Yang, X. Lin, W. Lewis, M. Suyetin, E. Bichoutskaia, J. E. Parker, C. C. Tang, D. R. Allan, P. J. Rizkallah, P. Hubberstey, N. R. Champness, K. M. Thomas, A. J. Blake and M. Schröder, *Nat. Mater.*, 2012, **11**, 710; (*b*) B. Chen, S. Ma, E. J. Hurtado, E. B. Lobkovsky and H.-C. Zhou, *Inorg. Chem.*, 2007, **46**, 8490; (*c*) M. Xue, S. Ma, Z. Jin, R. M. Schaffino, G.-S. Zhu, E. B. Lobkovsky, S.-L. Qiu and B. Chen, *Inorg. Chem.*, 2008, **47**, 6825.

7 Y. Lan, S.-L. Li, H.-L. Jiang and Q. Xu, *Chem.–Eur. J.*, 2012, **18**, 8076.

8 (*a*) H. M. Guo and Z.-M. Sun, *J. Mater. Chem.*, 2012, **22**, 15939; (*b*) L. Ma and W. Lin, *J. Am. Chem. Soc.*, 2008, **130**, 13834.

9 H.-L. Jiang, Y. Tatsu, Z.-H. Lu and Q. Xu, *J. Am. Chem. Soc.*, 2010, **132**, 5586.

10 J. Zhang, L. Wojtas, R. W. Larsen, M. Eddaoudi and M. J. Zaworotko, *J. Am. Chem. Soc.*, 2009, **131**, 17040.

11 (*a*) P. K. Thallapally, J. Tian, M. R. Kishan, C. A. Fernandez, S. J. Dalgarno, P. B. McGrail, J. E. Warren and J. L. Atwood, *J. Am. Chem. Soc.*, 2008, **130**, 16842; (*b*) B. Mu, F. Li, Y. Huanga and K. S. Walton, *J. Mater. Chem.*, 2012, **22**, 10172; (*c*) P. V. Dau, M. Kim, S. J. Garibay, F. H. L. Münch, C. E. Moore and S. M. Cohen, *Inorg. Chem.*, 2012, **51**, 5671; (*d*) S. Sanda, S. Parshamoni and S. Konar, *Inorg. Chem.*, 2013, **52**, 12866.

12 B. Chen, S. Ma, E. J. Hurtado, E. B. Lobkovsky, C. Liang, H. Zhu and S. Dai, *Inorg. Chem.*, 2007, **46**, 8705.

13 B.-Q. Ma, K. L. Mulfort and J. T. Hupp, *Inorg. Chem.*, 2005, **44**, 4912.

14 B. Chen, S. Ma, F. Zapata, E. B. Lobkovsky and J. Yang, *Inorg. Chem.*, 2006, **45**, 5718.

15 D. N. Dybtsev, M. P. Yutkin, E. V. Peresypkina, A. V. Virovets, C. Serre, G. Férey and V. P. Fedin, *Inorg. Chem.*, 2007, **46**, 6843.

16 S. Henke, A. Schneemann, S. Kapoor, R. Winter and R. A. Fischer, *J. Mater. Chem.*, 2012, **22**, 909.

17 H. Aggarwal, P. M. Bhatt, C. X. Bezuidenhout and L. J. Barbour, *J. Am. Chem. Soc.*, 2014, **136**, 3776.

18 (*a*) J. Seo, C. Bonneau, R. Matsuda, M. Takata and S. Kitagawa, *J. Am. Chem. Soc.*, 2011, **133**, 9005; (*b*) B. Xiao, P. J. Byrne, P. S. Wheatley, D. S. Wragg, X. Zhao, A. J. Fletcher, K. M. Thomas, L. Peters, J. S. O. Evans,

J. E. Warren, W. Zhou and R. E. Morris, *Nat. Chem.*, 2009, **1**, 289.

19 (*a*) S. B. Choi, H. Furukawa, H. J. Nam, D.-Y. Jung, Y. H. Jhon, A. Walton, D. Book, M. O'Keeffe, O. M. Yaghi and J. Kim, *Angew. Chem., Int. Ed.*, 2012, **51**, 8791; (*b*) J.-P. Zhang, Y.-Y. Lin, W. I.-X. Zhang and X.-M. Chen, *J. Am. Chem. Soc.*, 2005, **127**, 14162.

20 H. Aggarwal, P. Lama and L. J. Barbour, *Chem. Commun.*, 2014, **50**, 4543.

21 (*a*) T. Jacobs, G. O. Lloyd, J.-A. Gertenbach, K. K. Müller-Nedebock, C. Esterhuysen and L. J. Barbour, *Angew. Chem., Int. Ed.*, 2012, **51**, 4913; (*b*) S. Takamizawa, E.-I. Nakata, H. Yokoyama, K. Mochizuki and W. Mori, *Angew. Chem., Int. Ed.*, 2003, **42**, 4331; (*c*) R. K. Das, A. Aijaz, M. K. Sharma, P. Lama and P. K. Bharadwaj, *Chem.–Eur. J.*, 2012, **18**, 6866; (*d*) S. Sen, S. Neogi, K. Rissanen and P. K. Bharadwaj, *Chem. Commun.*, 2015, **51**, 3173.

22 (*a*) L.-P. Hsu, J.-Y. Wu and K.-L. Lu, *J. Inorg. Organomet. Polym. Mater.*, 2007, **17**, 259; (*b*) S. W. Lee, H. J. Kim, Y. K. Lee, K. Park, J.-H. Son and Y.-U. Kwon, *Inorg. Chim. Acta*, 2003, **353**, 151.

23 L. J. Barbour, *Chem. Commun.*, 2006, 1163.

24 A. L. Spek, *PLATON*, The University of Utrecht, Utrecht, The Netherlands, 1999.

25 B. Chen, C. Liang, J. Yang, D. S. Contreras, Y. L. Clancy, E. B. Lobkovsky, O. M. Yaghi and S. Dai, *Angew. Chem., Int. Ed.*, 2006, **45**, 1390.

26 (*a*) J. L. C. Rowsell and O. M. Yaghi, *J. Am. Chem. Soc.*, 2006, **128**, 1304; (*b*) C. E. Willans, S. French, L. J. Barbour, J.-A. Gertenbach, P. C. Junk, G. O. Lloyd and J. W. Steed, *Dalton Trans.*, 2009, 6480; (*c*) P. Nugent, Y. Belmabkhout, S. D. Burd, A. J. Cairns, R. Luebke, K. Forrest, T. Pham, S. Ma, B. Space, L. Wojtas, M. Eddaoudi and M. J. Zaworotko, *Nature*, 2013, **495**, 80; (*d*) S. Ma, D. Sun, M. Ambrogio, J. A. Fillinger, S. Parkin and H.-C. Zhou, *J. Am. Chem. Soc.*, 2007, **129**, 1858.

27 (*a*) N. Nijem, H. Wu, P. Canepa, A. Marti, K. J. Balkus Jr, T. Thonhauser, J. Li and Y. J. Chabal, *J. Am. Chem. Soc.*, 2012, **134**, 15201; (*b*) C. Gücüyener, J. van den Bergh, J. Gascon and F. Kapteijn, *J. Am. Chem. Soc.*, 2010, **132**, 17704; (*c*) A. Demessence and J. R. Long, *Chem.–Eur. J.*, 2010, **16**, 5902.

Supporting Information

Isolation of a Structural Intermediate During Switching of Degree of Interpenetration in a Metal-Organic Framework.

*Himanshu Aggarwal, Raj Kumar Das, Prashant M. Bhatt and Leonard J. Barbour**

Department of Chemistry and Polymer Science, University of Stellenbosch, Matieland 7602, Stellenbosch, South Africa

EXPERIMENTAL

Methods and materials. All chemicals were obtained commercially and used as received without further purification.

Synthesis of 2fa. The doubly-interpenetrated $[Co_2(ndc)_2(bpy)]$ metal-organic framework was synthesised following a previously reported procedure.[1]

Preparation of 3fa by activation of 2fa. Crystals of the triply-interpenetrated structure **3fa** were prepared by activating **2fa** crystals under dynamic vacuum at 120 °C for 12 hours in a Büchi glass oven. Crystals of **3fa** were also obtained when **2fa** crystals were removed from mother liquor and left standing under ambient conditions for approximately two weeks.

Preparation of 2fa′ by activation of 2fa. Crystals of the empty doubly interpenetrated structure **2fa′** were prepared by activating **2fa** crystals under dynamic vacuum at 80 °C for 12 hours in a Büchi glass oven.

Single-crystal X-ray diffraction (SCD). Intensity data were collected on a Bruker Apex II DUO CCD diffractometer with a multilayer monochromator. Mo-K_α radiation (λ= 0.71073 Å) was used for the experiments. The temperature of the crystal was controlled using an Oxford Cryostream 700 Plus. Data reduction was carried out by means of standard procedures using the Bruker software package SAINT[2] while absorption corrections and correction of other systematic errors were carried out using SADABS.[3] The structures were solved by direct methods using SHELXS-97 and refined using SHELXL-97.[4] X-Seed[5] was used as the graphical interface for the SHELX program suite. Hydrogen atoms were placed in calculated positions using riding models. In the case of **2fa** the bpy linker is disordered over three positions (Figure S12). As a result, the thermal parameters of the bpy fragment are

substantially different, resulting in some A and B level alerts in the checkcif report. Moreover, one of the nitrogen atoms (N2A) was refined isotropically. The disorder was modelled to the best of our ability to make sense of the electron density maps. The remaining electron density within the channel was removed using the SQUEEZE routine of PLATON[24]. The solvent-accessible void volumes were also calculated using PLATON.

Single-crystal to single-crystal conversion of 2fa to 3fa. A single crystal of **2fa** was left at room temperature. The unit cell parameters for the same crystal were checked at regular intervals to monitor the progress of the transformation. Based on these parameters, the conversion appeared to be complete after almost one week and the single-crystal X-ray diffraction data analysis revealed that the system had converted to its triply-interpenetrated form (**3fa**).

Single-crystal to single-crystal conversion of 2fa′ to 3fa. A suitable single crystal of **2fa′** isolated from the bulk material was left at room temperature. The unit cell parameters of the same crystal were checked at regular intervals to monitor the progress of the transformation. After 3 to 4 days the conversion appeared to be complete and single-crystal X-ray diffraction analysis revealed that the system had converted to its triply-interpenetrated form (**3fa**).

Single-crystal to single-crystal conversion of 2fa to 2fa′. Since the transformation from **2fa** to **2fa′** is a time consuming process at room temperature, gentle heating was used to bring about the conversion. A suitable crystal of as-synthesised material was glued to the end of a glass fibre and SCD data were recorded at 100 K, yielding the structure of **2fa**. The temperature was then ramped to 313 K at a rate of 120 K h^{-1} and kept constant while unit cell parameters were determined repeatedly. Once the unit cell parameters indicated apparently complete conversion of **2fa** to **2fa′**, the temperature was then decreased back to 100 K. Single crystal X-ray diffraction data were again recorded, revealing a structure quite similar to that of **2fa′** isolated from the activation of bulk crystals.

Single-crystal X-ray diffraction (SCD)

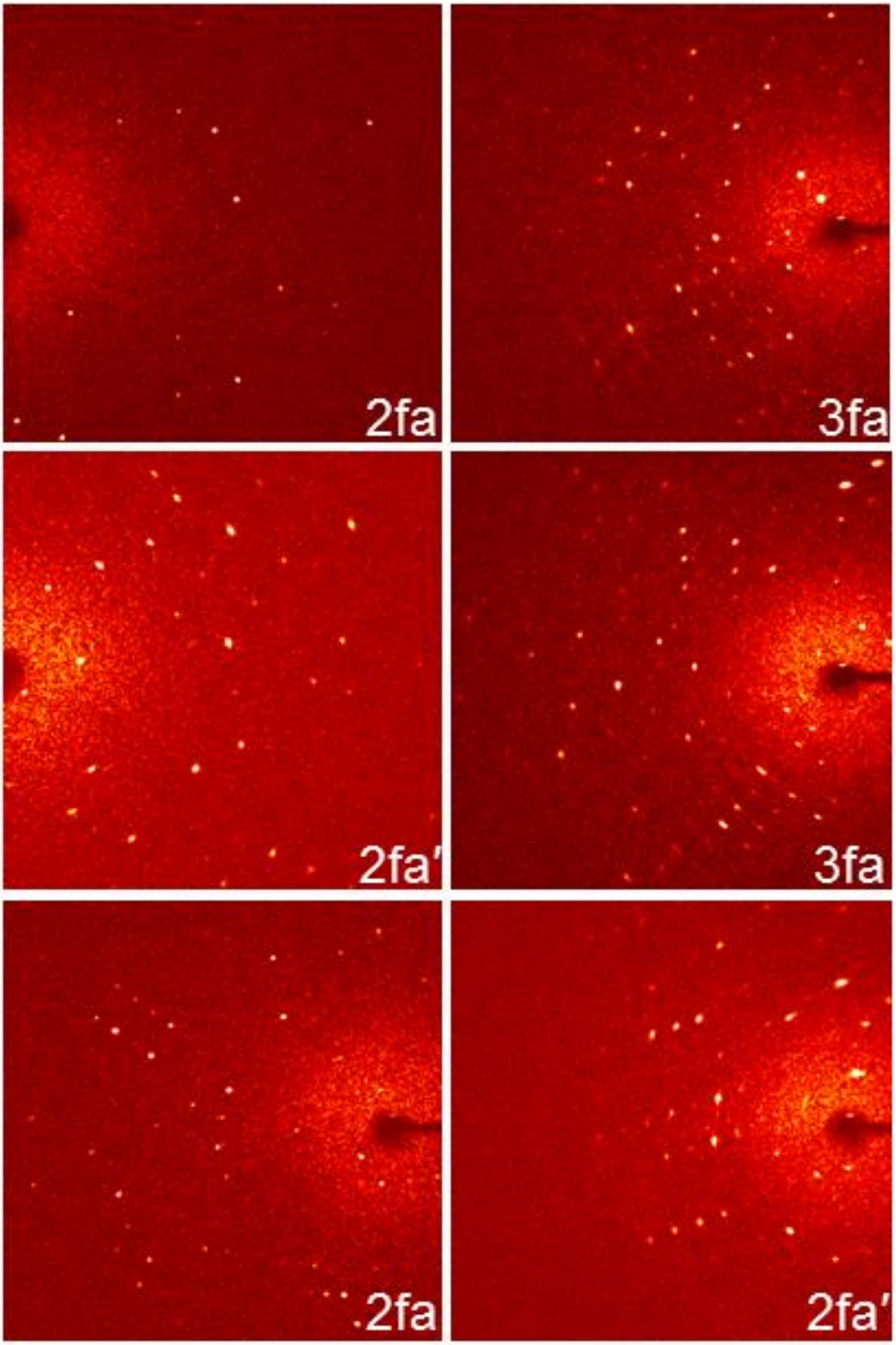

Diffraction patterns for three single-crystal to single-crystal transformations: **2fa to 3fa** (top), **2fa′ to 3fa** (middle) and **2fa to 2fa′** (bottom).

Crystal Data and Structure Refinement:

Identification code	**LJB_2fa_1**	**LJB_3fa_1**
Empirical formula	$C_{34}H_{20}Co_2N_2O_8$	$C_{51}H_{30}Co_3N_3O_{12}$
Formula weight	702.38	1053.57
Temperature/K	100(2)	296(2)
Crystal system	triclinic	monoclinic
Space group	*P*-1	*C*2
a/Å	12.956(3)	17.173(6)
b/Å	13.122(3)	19.784(7)
c/Å	13.752(3)	13.887(5)
α/°	84.973(3)	90.00
β/°	67.595(3)	95.771(4)
γ/°	83.245(3)	90.00
Volume/Å^3	2144.0(8)	4694(3)
Z	2	4
ρ_{calc}g/cm^3	1.088	1.491
μ/mm^{-1}	0.814	1.115
F(000)	712.0	2136.0
Crystal size/mm^3	0.2 × 0.08 × 0.06	0.24 × 0.14 × 0.04
Radiation	MoKα (λ = 0.71073)	MoKα (λ = 0.71073)
2θ range for data collection/°	3.2 to 52.12	2.94 to 56.76
Index ranges	-16 ≤ h ≤ 16, -16 ≤ k ≤ 16, -16 ≤ l ≤ 16	-22 ≤ h ≤ 22, -26 ≤ k ≤ 26, -18 ≤ l ≤ 18
Reflections collected	21004	56788
Independent reflections	8409 [R_{int} = 0.0506, R_{sigma} = 0.0733]	11722 [R_{int} = 0.0710, R_{sigma} = 0.0615]
Data/restraints/parameters	8409/42/392	11722/1/467
Goodness-of-fit on F^2	1.038	1.052
Final R indexes [I>=2σ (I)]	R_1 = 0.0534, wR_2 = 0.1270	R_1 = 0.0615, wR_2 = 0.1659
Final R indexes [all data]	R_1 = 0.0801, wR_2 = 0.1375	R_1 = 0.0938, wR_2 = 0.1840
Largest diff. peak/hole / e Å^{-3}	0.85/-1.29	1.16/-1.11
Mosaicity	0.35	0.40
CCDC Number	1052168	1052172

Identification code	**LJB_2fa'_1**	**LJB_3fa_2**
Empirical formula	$C_{17}H_{10}CoNO_4$	$C_{51}H_{30}Co_3N_3O_{12}$
Formula weight	351.19	1053.57
Temperature/K	296(2)	100(2)
Crystal system	triclinic	monoclinic
Space group	*P*-1	*C*2
a/Å	7.7116(7)	17.0391(8)
b/Å	10.2889(10)	20.0278(10)
c/Å	11.0085(10)	13.8334(7)
α/°	71.4300(10)	90.00
β/°	86.2820(10)	96.243(3)
γ/°	82.2650(10)	90.00
Volume/Å^3	820.22(13)	4692.7(4)
Z	2	4
ρ_{calc}g/cm^3	1.422	1.491
μ/mm^{-1}	1.063	1.115
F(000)	356.0	2136.0
Crystal size/mm^3	0.12 × 0.05 × 0.02	0.13 × 0.05 × 0.02
Radiation	MoKα (λ = 0.71073)	MoKα (λ = 0.71073)
2θ range for data collection/°	3.9 to 56.6	2.96 to 56.88
Index ranges	-10 ≤ h ≤ 10, -13 ≤ k ≤ 13, -14 ≤ l ≤ 14	-22 ≤ h ≤ 22, -26 ≤ k ≤ 26, -18 ≤ l ≤ 18
Reflections collected	23571	43655
Independent reflections	4064 [R_{int} = 0.0574, R_{sigma} = 0.0421]	11692 [R_{int} = 0.0883, R_{sigma} = 0.0893]
Data/restraints/parameters	4064/24/236	11692/46/443
Goodness-of-fit on F^2	1.062	1.026
Final R indexes [I>=2σ (I)]	R_1 = 0.0492, wR_2 = 0.1217	R_1 = 0.0588, wR_2 = 0.1373
Final R indexes [all data]	R_1 = 0.0720, wR_2 = 0.1331	R_1 = 0.1141, wR_2 = 0.1654
Largest diff. peak/hole / e Å^{-3}	1.60/-0.53	1.44/-1.42
Mosaicity	0.41	0.40
CCDC Number	1052169	1052173

Identification code	**LJB_2fa_2**	**LJB_2fa'_2**
Empirical formula	$C_{34}H_{20}Co_2N_2O_8$	$C_{17}H_{10}CoNO_4$
Formula weight	702.38	351.19
Temperature/K	100(2)	100(2)
Crystal system	triclinic	triclinic
Space group	*P*-1	*P*-1
a/Å	12.9698(12)	7.6397(12)
b/Å	13.1304(12)	10.4311(17)
c/Å	13.7579(13)	10.9968(18)
α/°	85.0410(10)	71.121(12)
β/°	68.0140(10)	87.061(12)
γ/°	83.544(2)	83.361(12)
Volume/Å^3	2156.3(3)	823.5(2)
Z	2	2
ρ_{calc}g/cm^3	1.082	1.416
μ/mm^{-1}	0.809	1.059
F(000)	712.0	356.0
Crystal size/mm^3	0.2 × 0.12 × 0.04	0.19 × 0.11 × 0.05
Radiation	MoKα (λ = 0.71073)	MoKα (λ = 0.71073)
2θ range for data collection/°	3.12 to 56.72	3.92 to 50.32
Index ranges	-17 ≤ h ≤ 17, -17 ≤ k ≤ 17, -18 ≤ l ≤ 18	-9 ≤ h ≤ 9, -12 ≤ k ≤ 12, -13 ≤ l ≤ 13
Reflections collected	54070	8403
Independent reflections	10710 [R_{int} = 0.0381, R_{sigma} = 0.0303]	2879 [R_{int} = 0.0861, R_{sigma} = 0.1013]
Data/restraints/parameters	10710/20/458	2879/6/251
Goodness-of-fit on F^2	1.096	1.087
Final R indexes [I>=2σ (I)]	R_1 = 0.0391, wR_2 = 0.0989	R_1 = 0.0958, wR_2 = 0.2632
Final R indexes [all data]	R_1 = 0.0487, wR_2 = 0.1023	R_1 = 0.1276, wR_2 = 0.2806
Largest diff. peak/hole / e Å^{-3}	1.26/-1.07	1.28/-0.72
Mosaicity	0.40	0.40
CCDC Number	1052170	1052171

Thermogravimetric analysis. Thermal analyses were carried out using a TA Instruments Q500 thermogravimetric analyser.

Gas sorption measurement. An Intelligent Gravimetric Analyser (IGA-002 supplied by Hiden Analytical Ltd, Warrington, UK)[6] was used to record sorption isotherms at 298 K for samples of **2fa′** and **3fa**. The instrument facilitates precise measurement of mass change and control of pressure and temperature, and is equipped with an advanced pressure rating allowing measurement up to 20 bar. The pressure is monitored using a pressure transducer with a range of 0-20 bar and buoyancy effects are corrected for. Temperature control is maintained to an accuracy of ca. 0.05 °C by a refrigerated recirculating bath. Data collection is controlled by Real-Time Processing computer software,[7] which continually analyses the equilibrium using least-squares regression to extrapolate a value of the asymptote.

X-ray powder diffraction studies (XRPD). The diffractograms were recorded with a Bruker D2 PHASER equipped with a Lynxeye 1D detector and Ni-filtered copper Kα radiation (30 kV, 10 mA generator parameters; restricted by a 1.0 mm divergence slit and a 2.5° Soller collimator) with a 0.02° step width. The phase purity of the as-synthesised **2fa** and the activated forms **2fa′** and **3fa** was confirmed by comparison of experimental XRPD with the simulated XRPD patterns from the respective crystal structures. XRPD was used to study all the conversions under different conditions.

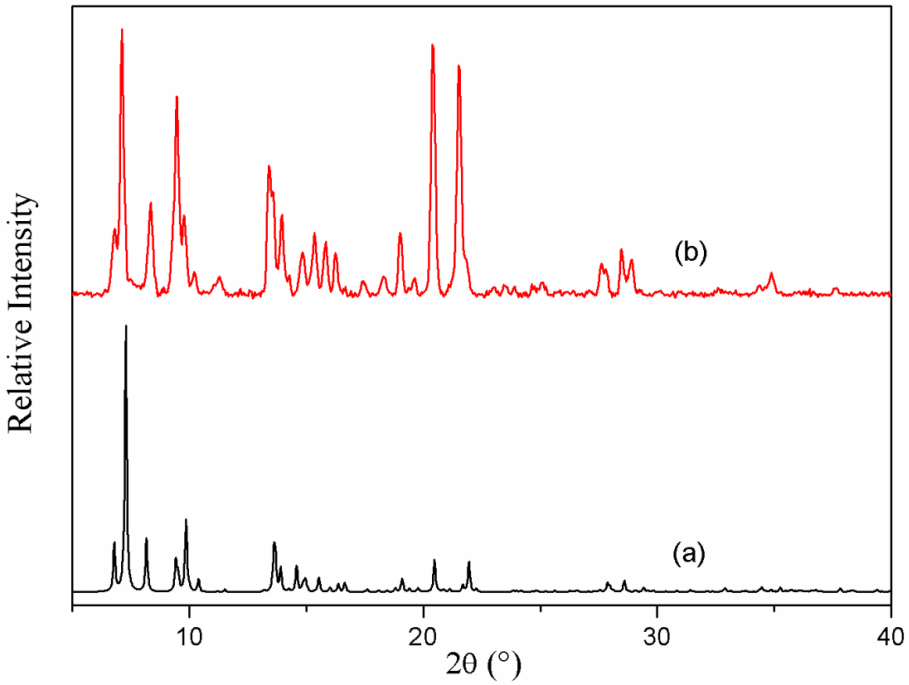

Figure S1: (a) simulated XRPD pattern of **2fa** from crystal structure, (b) XRPD patterns of as-synthesised **2fa**.

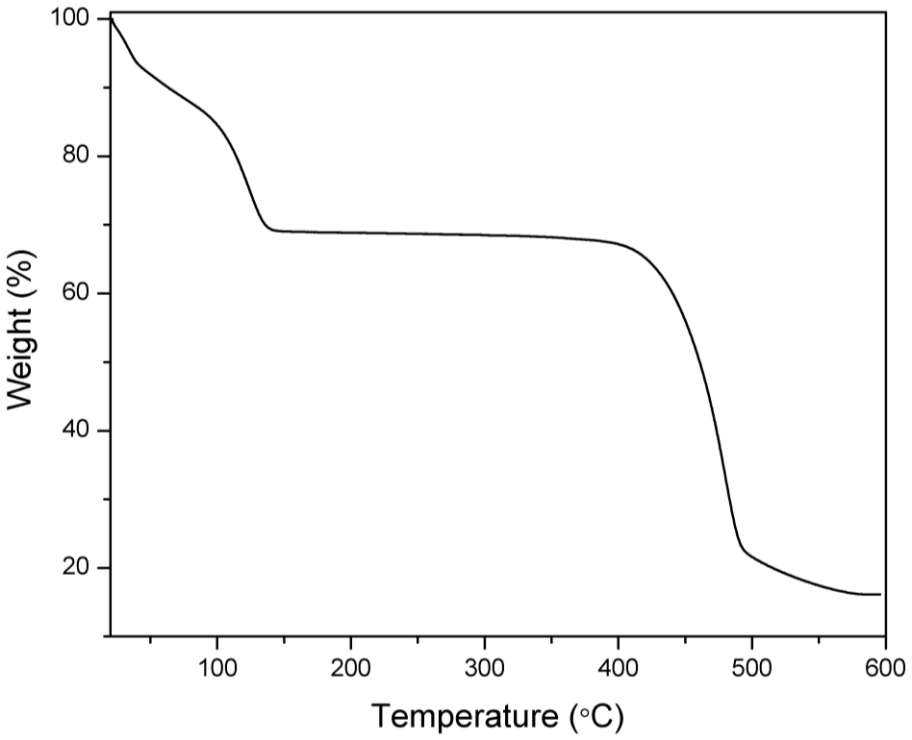

Figure S2: TGA analysis of the as-synthesised crystals of **2f**

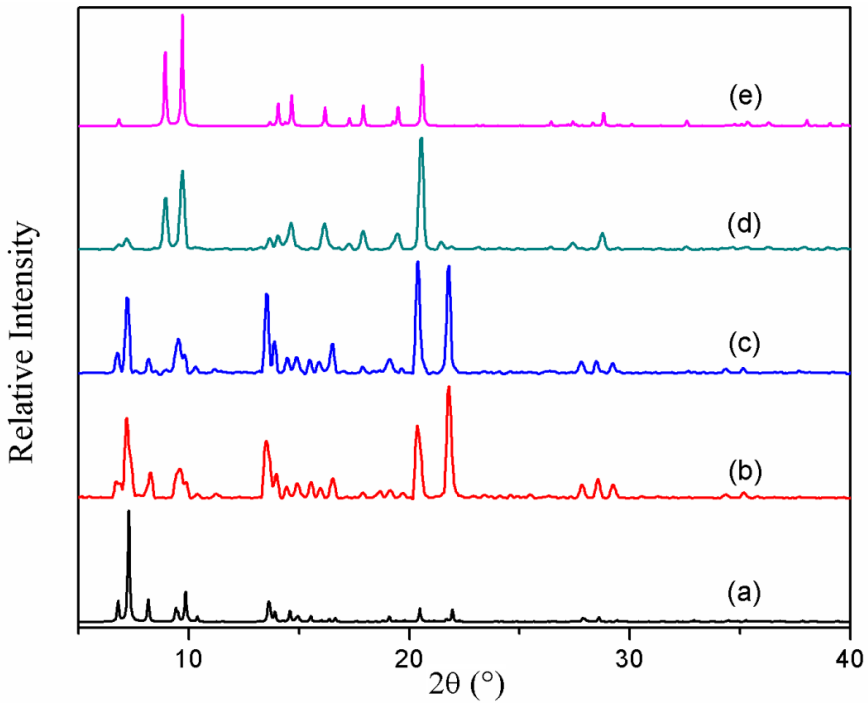

Figure S3: (a) Simulated XRPD pattern of **2fa** from crystal structure, (b) XRPD pattern of as-synthesised **2fa**. (c) XRPD of the **2fa** sample after on exposure to ambient conditions for 5 days, (d) XRPD of the **2fa** sample after exposure to ambient condition for 10 days (e) simulated XRPD pattern of **3fa** from crystal structure.

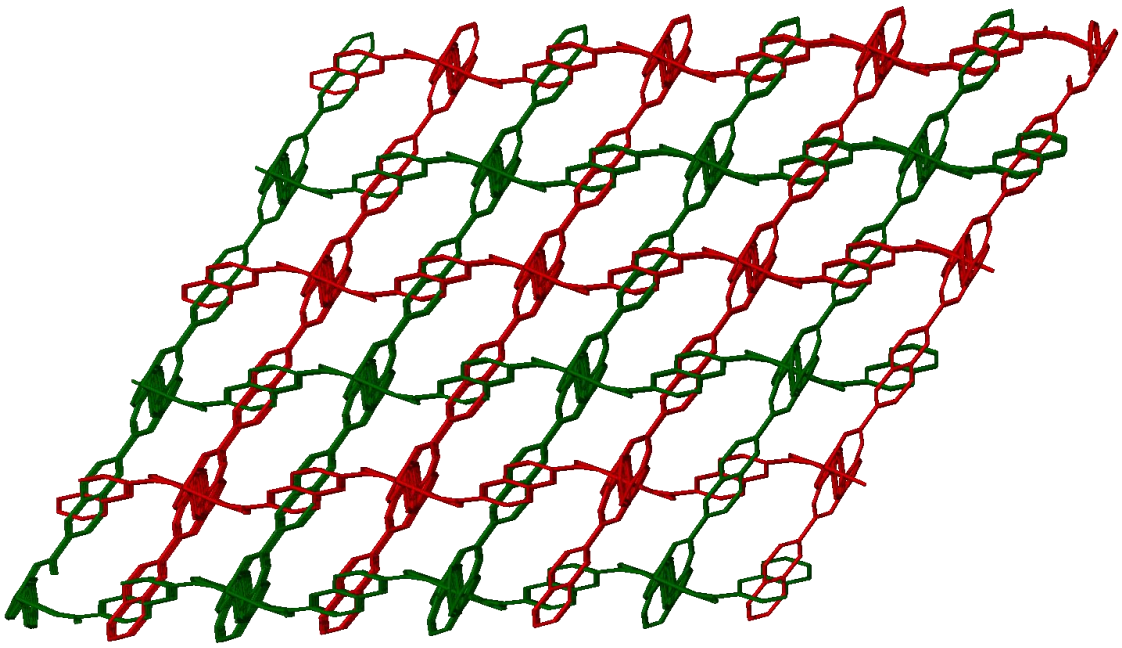

Figure S4: Packing diagram of **2fa′** (H atoms have been removed for clarity)

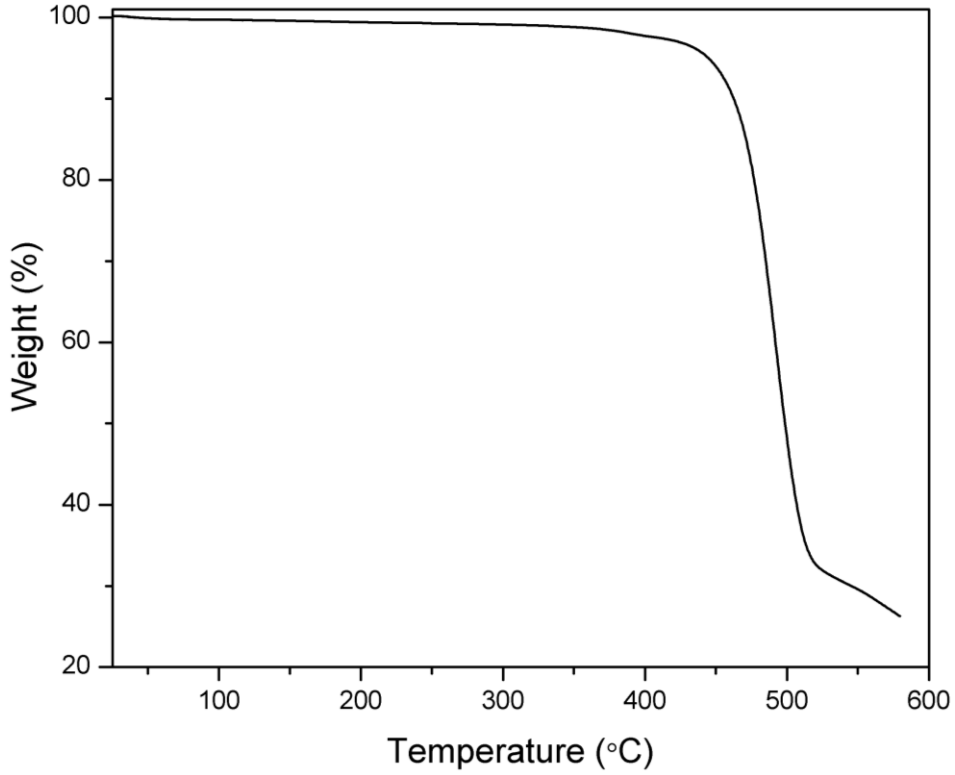

Figure S5: TGA analysis of **2fa′** sample.

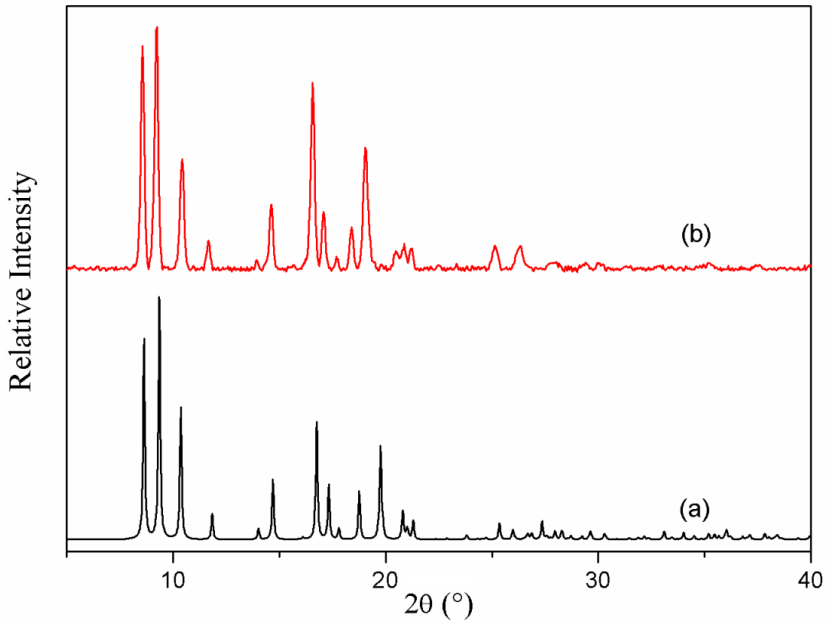

Figure S6: (a) simulated XRPD pattern of **2fa′** from crystal structure, (b) XRPD patterns of as-synthesised **2fa′**.

Table S1: Comparison of Co-O and Co-N bond distances in 2fa and 2fa′

2fa		2fa′	
Co1—O5	2.012(1)	Co1—O4^{i}	2.007(3)
Co1—O7^{i}	2.025(1)	Co1—O3	2.032(3)
Co1—O3^{ii}	2.029(2)	Co1—O2^{i}	2.058(2)
Co1—O1	2.097(2)	Co1—O1	2.176(3)
Co1—Co2	2.764(1)		
O3—Co1^{iv}	2.029(2)		
O4—Co2^{iv}	2.080(2)		
O7—Co1^{v}	2.025(1)		
O8—Co2^{v}	2.020(1)		
Co2—O8^{i}	2.020(1)		
Co2—O6	2.023(1)		
Co2—O2	2.025(2)		
Co2—O4^{ii}	2.080(2)		
Average Co—O	**2.039(1)**	**Average Co—O**	**2.068(4)**
Co2—N1A	2.055(7)	Co1—N1A	2.056(20)
Co2—N1C	2.016(13)	Co1—N1B	2.077(18)
Co2—N1B	2.104(15)		
Co1—N2A^{iii}	2.068(4)		
Co1—N2B^{iii}	2.070(18)		
Co1—N2C^{iii}	2.091(19)		
Average Co—N	**2.067(5)**	**Average Co—N**	**2.067(13)**
(i) x, -1+y, z; (ii) -1+x, y, z; (iii) x, y, 1+z; (ii) (iv) 1+x, y, z; (v) x, 1+y, z; (vi) x, y, -1+z.		(i) 1-x, 1-y, 1-z; (ii) 1-x, 2-y, -z; (iii) -x, 1-y, 2-z; (iv) 2-x, 2-y, 1-z.	

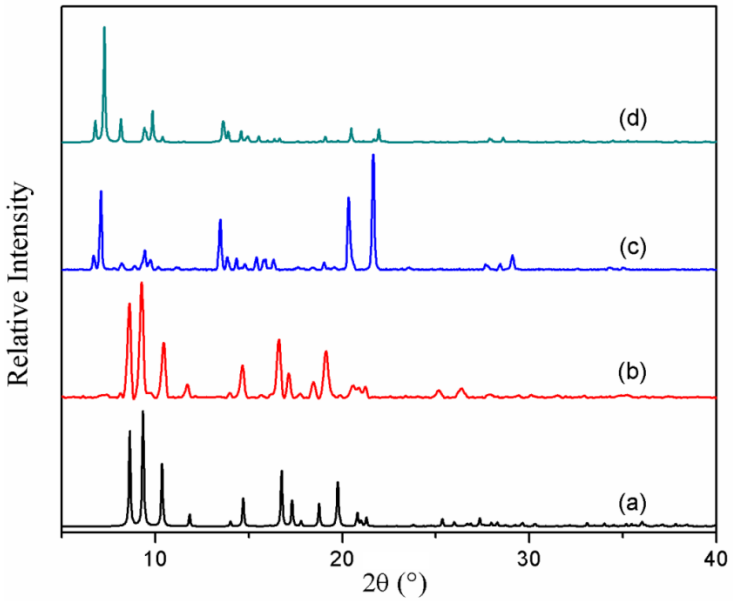

Figure S7: (a) Simulated XRPD pattern of **2fa′** from the SCD structure, (b) XRPD pattern of bulk **2fa′**, (c) XRPD pattern of **2fa′** after immersion in fresh DMF at RT for 24 hours and (d) simulated XRPD pattern of **2fa** from SCD data.

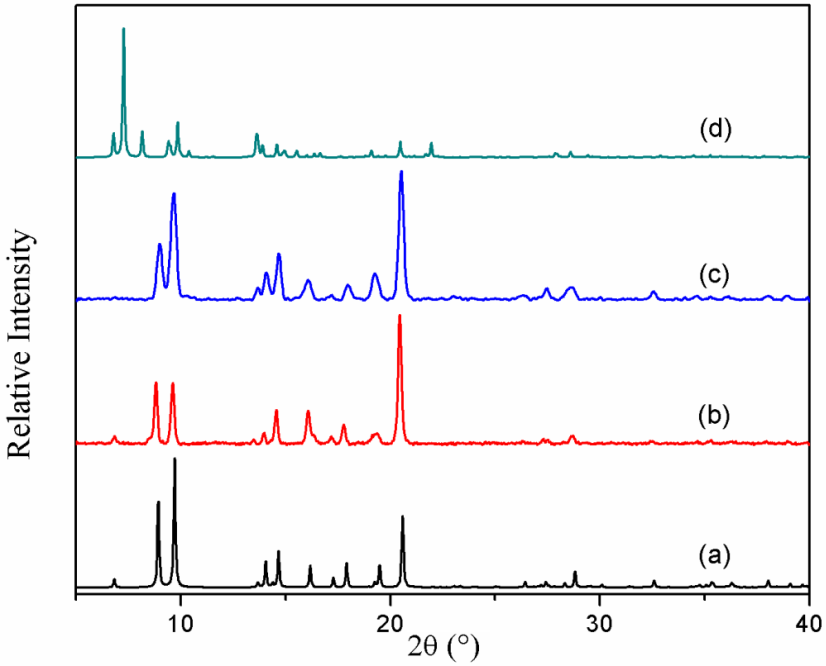

Figure S8: a) Simulated XRPD pattern of **3fa** from the SCD structure, (b) XRPD pattern of bulk **3fa**, (c) XRPD pattern of **3fa** after immersion in fresh DMF at 120 °C for 48 hours and (d) simulated XRPD pattern of **2fa** from SCD data.

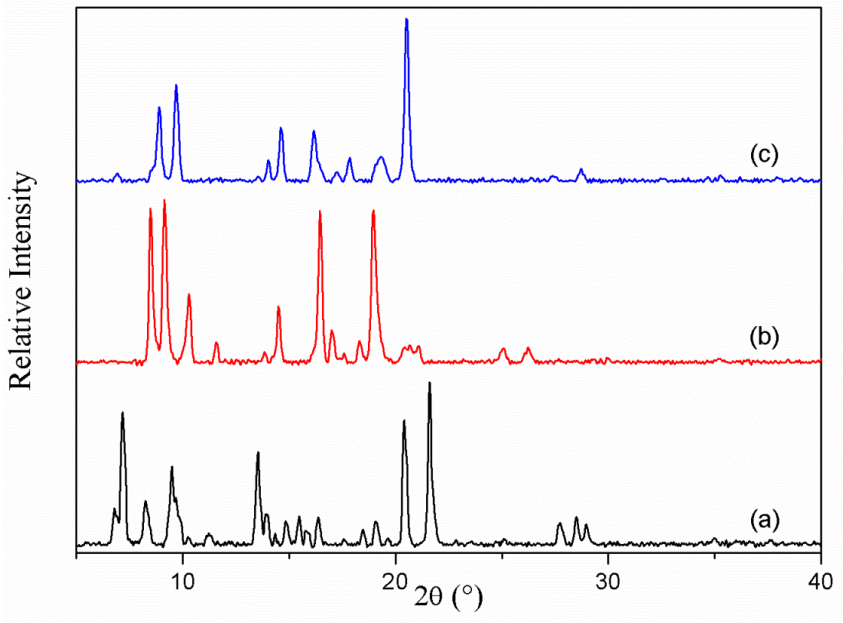

Figure S9: (a) XRPD pattern of as-synthesised **2fa**. (b) XRPD patterns of the sample after heating at 80 °C under dynamic vacuum, (c) XRPD pattern of 80 °C activated sample after further activation at 120 °C under dynamic vacuum. **(These XRPD patterns clearly show subsequent conversion from 2fa to 2fa′ to 3fa)**

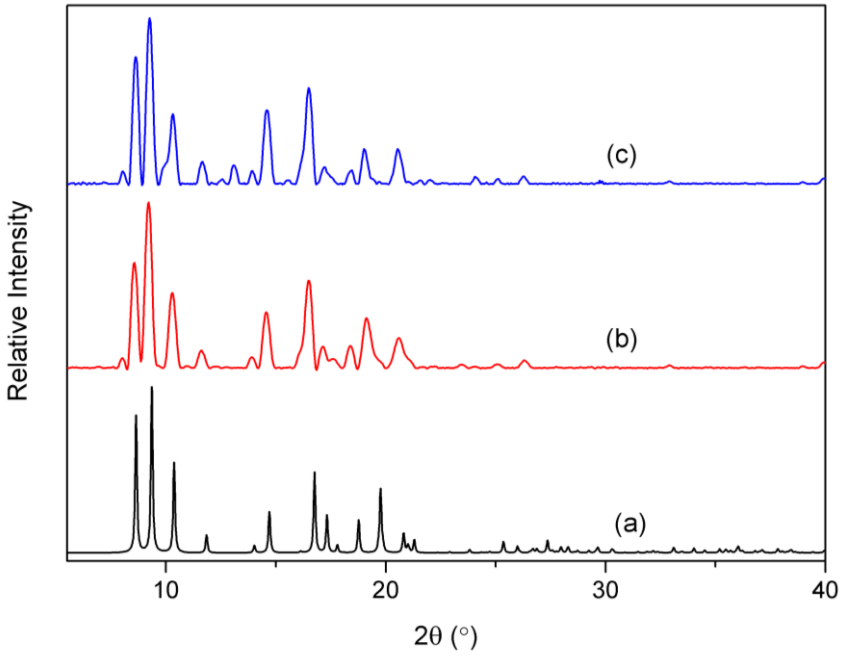

Figure S10: (a) Simulated XRPD pattern of **2fa′** from the SCD structure, (b) XRPD pattern of bulk **2fa′** before sorption experiment, (c) XRPD pattern of bulk **2fa′** after sorption experiment.

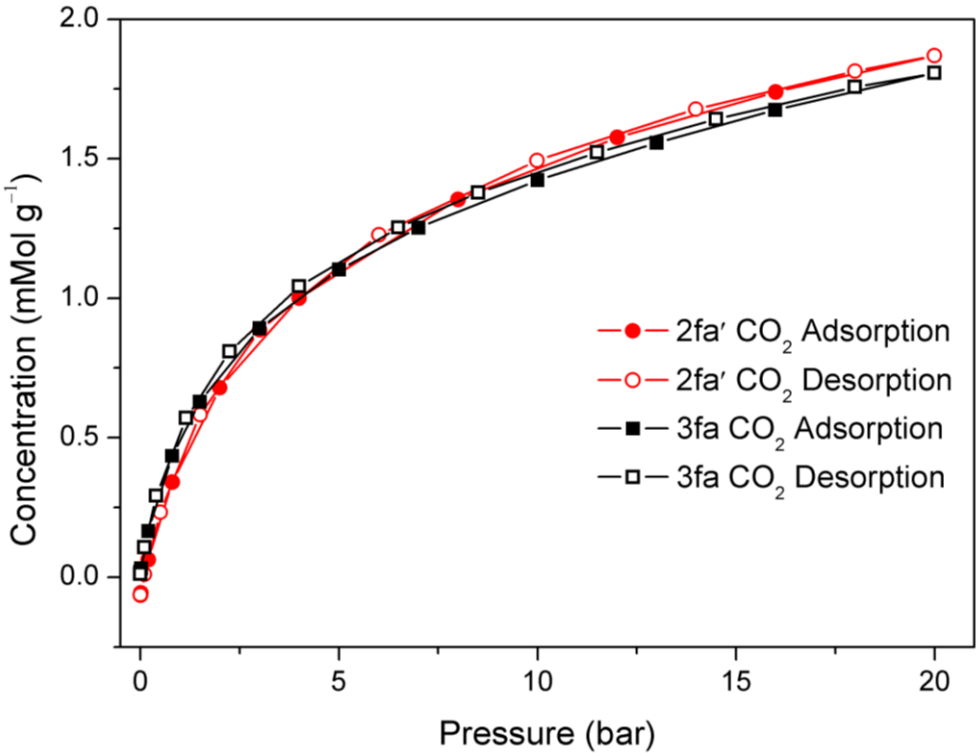

Figure S11: CO_2 sorption isotherm of **2fa′**and **3fa** at 298K.

Measurement of dihedral and torsion angles:

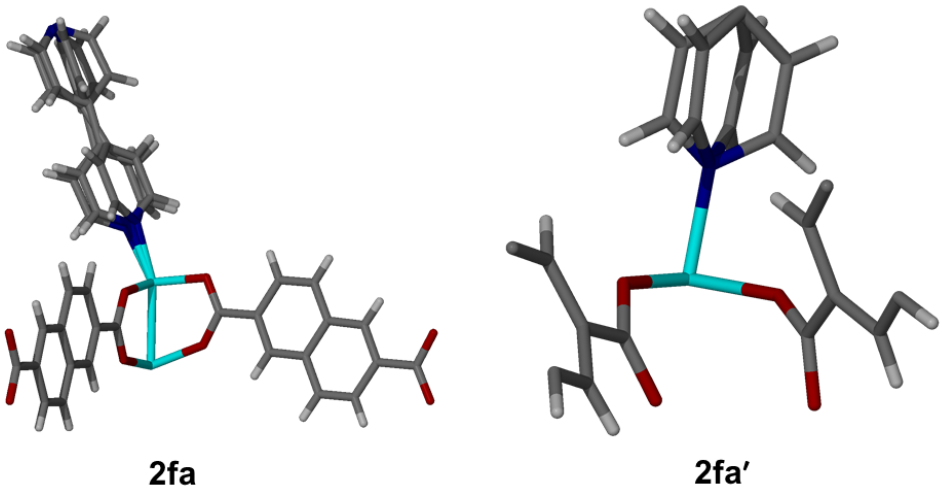

Figure S12: Asymmetric units of 2fa and 2fa′

The dihedral angles between metal plane and metal-carboxylate plane (θ) as well as metal plane and the aromatic plane of ndc (φ) in both **2fa** and **2fa′** structures were measured. There are two crystallographically distinct ndc linkers with four different carboxylates and two different aromatic units in **2fa**. As a result, a total of four θ and two φ values were determined. In the case of the bpy linker, similar measurements were made by measuring the torsion angle

(δ) between the metal-metal axis and the metal-N linkages and torsion angle (ω) between metal-metal axis and aromatic part of bpy. Since bpy is disordered over three positions in **2fa** (as shown above), torsion angles for each individual subunit were measured and the complete range reported. Similar measurement were carried out for **2fa'**.

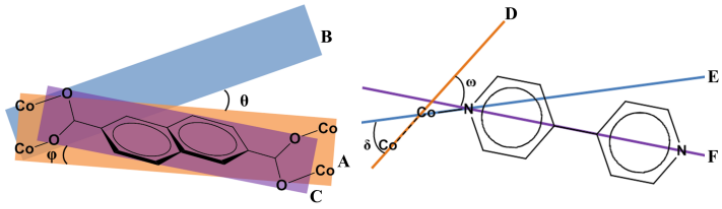

2fa				2fa'			
θ	φ	δ	ω	θ	φ	δ	ω
1.56(4)	2.98(5)	17.8(1) – 29.5(3)	21.7(1) – 27.46(4)	10.53(3)	7.41(6)	30.1(3) – 35.3(3)	33.7(1) – 36.8(1)
1.71(4)	7.81(4)	20.8(7) – 28.9(3)		18.63(4)	18.33(4)		
3.70(3)							
4.44(4)							

Top: diagrammatic representation of key dihedral and torsion angles in **2fa** and **2fa'**. A: $Co_2\cdots Co_2$ metal atom plane; B: Co_2-carboxylate oxygen plane; C: aromatic plane of ndc; D: Co_2 cluster metal-metal axis; E: metal-nitrogen; F: N···N axis of bpy. Both crystallographic symmetry and geometrical disorders have been considered in measuring these parameters. **Bottom**: table of relevant angles in °.

Measurement of metal-metal distances between two paddlewheels:

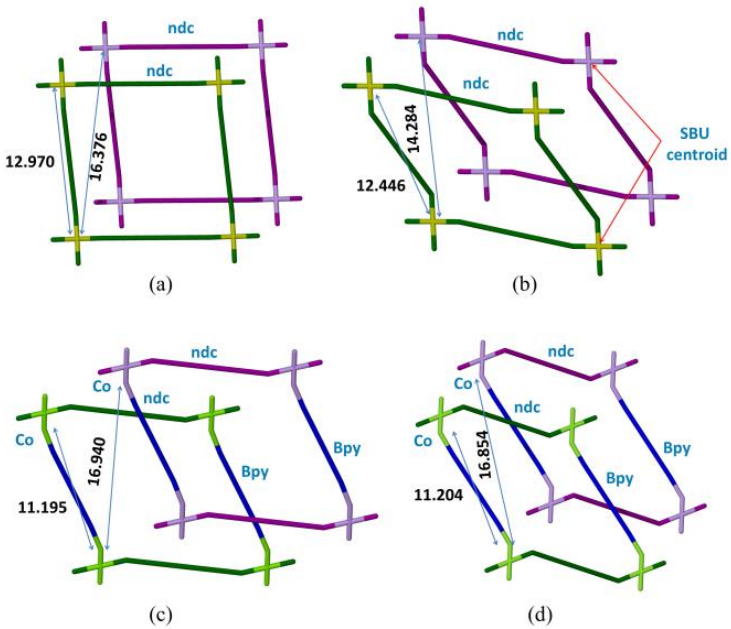

In the case of ndc, the node···node distances between two paddlewheel units is taken as the distance between the Co–Co centroids of the two metal clusters bridged by the ndc ligand. The same protocol was used to determine the shortest distance between two paddlewheel

nodes of different networks. In the case of bpy, the distance is measured between the two Co metal centers to which the ligand is attached. It should be noted that only the geometrically favourable Co centers are taken in to account while measuring the shortest distances between paddlewheel units of different networks.

Rietveld Refinement

The observed X-ray powder patterns were refined using the Rietveld[8] method. The program TOPAS was employed, using the corresponding published single-crystal X-ray structures as starting models. The resultant difference plots thus generated are given below.

NOTE:

For Rietveld refinements, the background was not subtracted for any of the three XRPD patterns. The XRPD patterns were originally collected on Bruker D2 phaser equipped with a Cu source. Owing to the presence of Co ions, each pattern contained a significant background signal, which was subtracted (for clarity) when comparing the XRPD patterns with simulated patterns obtained from single-crystal data.

Table S3 Final Rietveld refinement parameters for the three structures:

Compound	**2fa**	**2fa′**	**3fa**
$R_p$fitted	0.010	0.008	0.018
${}_wR_p$fitted	0.014	0.011	0.024
Bragg R-factor	2.073	1.403	0.286
GoF (χ)	2.04	1.64	1.21
Temperature (K)	298(2)	298(2)	298(2)
Space group	*P-1*	*P-1*	*C2*
a (Å)	12.9377(46)	7.7014(47)	17.2570(74)
b (Å)	13.0741(27)	10.2658(63)	19.832(12)
c (Å)	13.7277(62)	10.9889(87)	13.9305(46)
α, (°)	85.656(54)	71.535(59)	90
β (°)	67.731(66)	86.330(52)	95.586(37)
γ (°)	84.071(55)	82.285(38)	90

Table S4: Comparison of Rietveld parameters with the single crystal unit cell parameters for 2fa

Compound	**2fa**	
	XRPD (Rietveld)	SCD (SHELXL)
Temperature (K)	298	100
Space group	*P-1*	*P-1*
a (Å)	12.9377(46)	12.9698(12)
b (Å)	13.0741(27)	13.1304(12)
c (Å)	13.7277(62)	13.7579(13)
α, (°)	85.656(54)	85.0410(10)
β (°)	67.731(66)	68.0140(10)
γ (°)	84.071(55)	83.544(2)

Table S5: Comparison of Rietveld parameters with the single crystal unit cell parameters for 2fa′

Compound	**2fa′**	
	XRPD (Rietveld)	SCD (SHELXL)
Temperature (K)	298	296
Space group	*P-1*	*P-1*
a (Å)	7.7014(47)	7.7116(7)
b (Å)	10.2658(63)	10.2889(10)
c (Å)	10.9889(87)	11.0085(10)
α, (°)	71.535(59)	71.4300(10)
β (°)	86.330(52)	86.2820(10)
γ (°)	82.285(38)	82.2650(10)

Table S6: Comparison of Rietveld parameters with the single crystal unit cell parameters for 3fa.

Compound	**3fa**	
	XRPD (Rietveld)	SCD (SHELXL)
Temperature (K)	298	296
Space group	*C2*	*C2*
a (Å)	17.2570(74)	17.173(6)
b (Å)	19.832(12)	19.784(7)
c (Å)	13.9305(46)	13.887(5)
α, (°)	90	90
β (°)	95.586(37)	95.771(4)
γ (°)	90	90

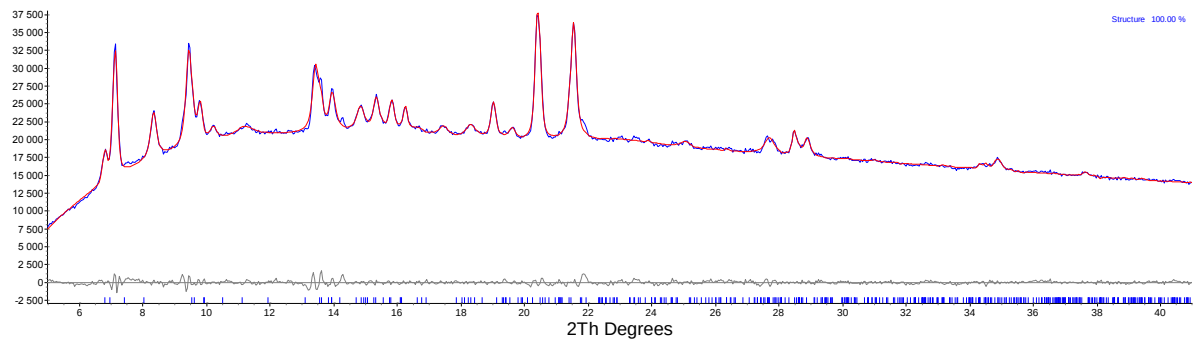

Figure S13: Observed (blue) and simulated (red) X-ray powder diffractograms (the latter obtained from Rietveld refinement) as well as the difference plot (grey) for **2fa**.

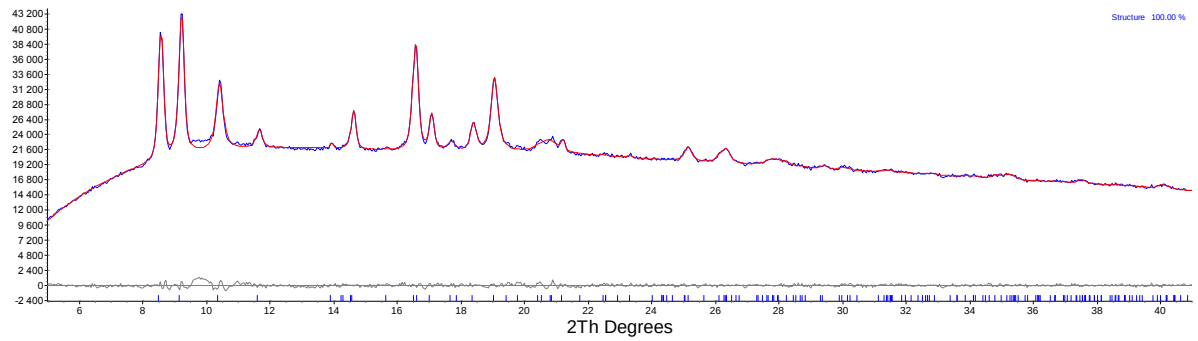

Figure S14: Observed (blue) and simulated (red) X-ray powder diffractograms (the latter obtained from Rietveld refinement) as well as the difference plot (grey) for **2fa′**.

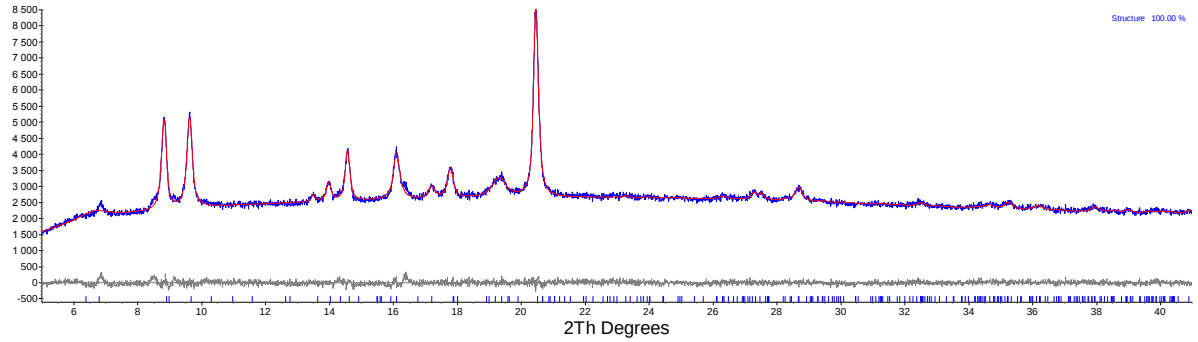

Figure S15: Observed (blue) and simulated (red) X-ray powder diffractograms (the latter obtained from Rietveld refinement) as well as the difference plot (grey) for **3fa**.

References

1. B. Chen, S. Ma, E. J. Hurtado, E. B. Lobkovsky, C. Liang, H. Zhu, S. Dai, *Inorg. Chem.* 2007, **46**, 8705.
2. SAINT Data Reduction Software, Version 6.45; Bruker AXS Inc., Madison, WI, 2003.
3. (a) SADABS, Version 2.05; Bruker AXS Inc., Madison, WI, 2002; (b) R. H. Blessing, *Acta Crystallogr., Sect. A: Found. Crystallogr*. 1995, **51**, 33.
4. G. M. Sheldrick, *Acta Crystallogr., Sect. A: Found. Crystallogr*. 2008, **64**, 112.
5. L. J. Barbour, *J. Supramol. Chem*. 2001, **1**, 189.
6. M. J. Benham, D. K. Ross, *Z. Phys. Chem.*, 1989, **163**, 25.
7. (a) C. R. Reid, I. P. O'Koye and K. M. Thomas, *Langmuir*, 1998, **14**, 2415; (b) C. R. Reid and K. M. Thomas, *Langmuir*, 1999, **15**, 3206; (c) A. W. Harding, N. J. Foley, P. R. Norman, D. C. Francis and K. M. Thomas, *Langmuir*, 1998, **14**, 3858; (d) I. P. O'Koye, M. Benham and K. M. Thomas, *Langmuir*, 1997, **13**, 4054.
8. A. Coelho, *J. Appl. Crystallogr.*, 2000, **33**, 899.

CONCLUSION

The aim of utilising metal-organic frameworks (MOFs) for gas sorption and storage led to the design of highly porous structures with large void spaces. But it was soon realised that when the empty spaces are large enough, interpenetration becomes likely. Since interpenetration is considered a drawback in designing materials with large surface areas it became desirable to control interpenetration in MOFs. To this end, crystallisation methodologies have been modified in one way or another and numerous non- or less interpenetrated MOFs have been reported to date. Although better control over crystallisation conditions has been very crucial to solving the problem of interpenetration, the possible conversion of these structures to their already reported dense (i.e. more highly interpenetrated) forms has always been overlooked.

The work presented here has provided a detailed account of switching of degree of interpenetration and its effects on porosity of MOFs, an important phenomenon that had been previously ignored. Not only have various MOF structures been studied for change of interpenetration, but a plausible mechanism has also been postulated in order to rationalise the phenomenon in detail. It is also interesting to note that such changes are not limited to any one type of metal ion, linker or coordination network. Moreover, such a dramatic change has been monitored in single-crystal to single-crystal (SCSC) fashion for the very first time by recording the structures before and after the transformation using the same crystal. Although SCSC transformations resulting from activation are quite common in studies of porous coordination compounds, the change of interpenetration mode has certainly pushed the limits of such transformations.

Furthermore, the isolation of an intermediate structure (**2fa′**) during switching of degree of interpenetration has provided clear insights into the phenomenon. The intermediate structure shows that the assumptions that we made in the case of **[Zn_2(ndc)$_2$(bpy)]** were reasonable. The gas sorption analysis on the intermediate structure not only revealed the differences in the gas uptake between a less interpenetrated form (**2fa′**) and a more interpenetrated form (**3fa**), but has also drawn attention to the fact that the activation conditions can be as crucial as the crystallisation conditions. Designing a less interpenetrated framework by cleverly altering the conditions of crystallisation may be irrelevant if the activation conditions are inappropriate.

The current work highlights the phenomenon of change in degree of interpenetration in three different MOFs, out of which, two MOFs {**[Zn_2(ndc)$_2$(bpy)] and [Co_2(ndc)$_2$(bpy)]**}

have been reported for loss of porosity upon activation. Although such a dramatic change seems quite improbable, a close investigation is required in order to determine if it is more general. It is therefore very important to extend the study to more robust systems. Future work could be based on the well-known IRMOFs, which are considered quite robust and have been well studied for their sorption properties. On the whole, the change in degree of interpenetration in metal-organic frameworks needs much more attention and such changes should not be ruled out as one of the key factors affecting loss of porosity in MOF materials.

APPENDIX

The attached CD contains the following files

- CIF data files and CIF check reports for all the structures of Chapter 3.
- A video file explaining mechanism of change of interpenetration in case of $[Zn_2(ndc)_2(bpy)]$.
- CIF data files and CIF check reports for all the structures of Chapter 5.